MAGNETOM Flash

Issue Number 95 · 6/2025
RSNA Edition

magnetomworld.siemens-healthineers.com

Not for distribution in the U.S.

SIEMENS
Healthineers

12

High-resolution
pancreaticobiliary MRI

36

Pediatric[2] kidney MR Elastography

56

Clinical utility of DANTE
T1-SPACE imaging

Editorial Comment

Abdominal Imaging

Neurological Imaging

Wideband Black-Blood CMR[3]

Protocol guidance of gynecological MRI

Musculoskeletal Imaging

Cardiovascular Imaging

Women's Health

Access to Care

Meet Siemens Healthineers

[1]*Work in progress. The application is currently under development and is not for sale in the U.S. and in other countries. Its future availability cannot be ensured.*

[2]*MR scanning has not been established as safe for imaging fetuses and infants less than two years of age. The responsible physician must evaluate the benefits of the MR examination compared to those of other imaging procedures.*

[3]*The MRI restrictions (if any) of the metal implant must be considered prior to patient undergoing MRI exam. MR imaging of patients with metallic implants brings specific risks. However, certain implants are approved by the governing regulatory bodies to be MR conditionally safe. For such implants, the previously mentioned warning may not be applicable. Please contact the implant manufacturer for the specific conditional information. The conditions for MR safety are the responsibility of the implant manufacturer, not of Siemens Healthineers.*

Cover images from *Examining MSK Implants with Lower-Field MRI* by Bianca Samsula, Markus Lentschig, et al. (ZEMODI - MVZ Zentrum für moderne Diagnostik, Bremen, Germany)

Professor Min Chen, M.D., Ph.D., is a professor of Radiology and a doctoral supervisor at Peking Union Medical College and Peking University Health Science Center in Beijing, China.

Professor Chen is currently president-elect of the Chinese Society of Radiology and president of the Society of Chinese Medical Imaging Technology. He is the former director of the Department of Radiology and Medical Image Center in Beijing Hospital.

He mainly focuses on advancing research in MRI, especially abdominal and pelvic imaging. Professor Chen is the principal director of the Natural Science Foundation of China and the Natural Science Foundation of Beijing. He has published more than 100 scientific papers as the first or corresponding author.

Bridging Precision, AI, and Global Collaboration in MRI

It is both a privilege and a pleasure to introduce this RSNA 2025 edition of MAGNETOM Flash. MRI is currently experiencing a transformation, as precision engineering, artificial intelligence (AI), and global collaboration converge to create a more intelligent, efficient, and equitable imaging landscape.

AI has become integral to the MRI ecosystem, not only accelerating reconstruction and improving image quality, but also advancing clinical interpretation, quantitative analysis, and workflow automation. As healthcare systems face rapid growth in patient volumes, intelligent tools that extend expertise and sustain diagnostic excellence are becoming essential. Equally important is a shared commitment to validation and standardization, as this will ensure that emerging technologies are not only innovative but also reproducible and accessible.

The works presented in this edition exemplify this vision. From accelerated neuroimaging and oncologic precision mapping to musculoskeletal low-field applications, cardiovascular innovation, and standardized women's health protocols, each article shows how technology and collaboration will define the future of MRI.

Neurological imaging: Innovation improves speed, comfort, and quality

Neuro MRI continues to advance at an extraordinary pace, transforming how we approach speed, precision, and patient experience. A new generation of technologies are harnessing deep learning, optimized acquisition strategies, and ultra-high fields to redefine the boundaries of clinical neuroimaging.

The pursuit of faster imaging without compromise is central to this evolution [1]. Altmann et al. demonstrate how deep learning-based reconstruction (Deep Resolve) enables ultra-fast pediatric[1] brain MRI within seconds per plane. Diagnostic-quality imaging can now be achieved without sedation, addressing one of the most persistent challenges in pediatric neuroimaging. The impact is impressive: higher completion rates, fewer sedation-related risks, and a reduced reliance on CT for rapid checks when radiation exposure is a concern.

Beyond pediatrics, intelligent acceleration is revolutionizing everyday clinical workflows in neuro MRI [2]. Buxi and Sud illustrate how deep learning has redefined the concept of routine imaging through two-minute MRI protocols on the MAGNETOM Vida platform. By combining Deep Resolve with advanced acceleration techniques such as SMS and GRAPPA, they demonstrate that full neuro examinations can be completed in a fraction of the usual scan time while still maintaining diagnostic integrity. This evolution reflects a new clinical mindset: Rapid imaging no longer means reduced quality, but rather an optimized workflow, enhanced patient throughput, and a patient friendly imaging experience.

Vessel wall and perfusion imaging continue to push the frontiers of neuro MRI capabilities [3]. Fushimi et al. demonstrate the clinical power of DANTE-prepared T1-SPACE imaging for intracranial vessel wall visualization. The DANTE pre-pulse efficiently suppresses flowing blood signals while preserving static tissue, enabling high-resolution, isotropic 0.6 mm imaging that is compatible with compressed sensing and deep learning acceleration.

---

[1]MR scanning has not been established as safe for imaging fetuses and infants less than two years of age. The responsible physician must evaluate the benefits of the MR examination compared to those of other imaging procedures.

Similarly, Wang et al. show how ASL perfusion imaging can now be reliably performed at 7T through optimized labeling and readout schemes. The collaboration between USC and PLA General Hospital successfully mitigated field inhomogeneity, transverse relaxation penalties, and image distortions, producing high-resolution perfusion maps that reveal collateral flow patterns and even small perfusion deficits.

Finally, technological innovation in MRI is increasingly human-centered. Fernandes Arêas presents practical strategies for managing claustrophobic patients using the 0.55T MAGNETOM Free.Max. The ultra-wide 80 cm bore, the flexible coil design, and Deep Resolve preserve image quality even when the upper coil element is removed to help reduce anxiety [4].

Together, these advances mark a cohesive transformation in neuroimaging. Deep learning has redefined speed, UHF MRI has expanded diagnostic reach, and patient-centered design has made imaging more inclusive. The integration of these innovations moves neuro MRI toward a future where precision, comfort, and efficiency are inseparable – and where technology improves both the imaging and the experience of care itself.

Abdominal imaging: Translating technological advances into clinical practice

Abdominal MRI is experiencing a remarkable transformation – one that is being driven by synergistic advances in gradient technology, motion-robust acquisition, and intelligent reconstruction. This issue illustrates how these innovations are enhancing diagnostic precision, streamlining workflows, and expanding accessibility across a wide spectrum of abdominal diseases.

The introduction of ultra-high-gradient 3T MRI with the MAGNETOM Cima.X (200 mT/m, 200 T/m/s) represents a major leap forward in pancreatic imaging. Zhu and colleagues demonstrate how this system, when combined with deep learning reconstruction for T2-weighted and diffusion-weighted imaging, achieves submillimeter resolution and sharper depiction of fine septations, mural nodules, and central stellate scars. These fine details are critical for precise diagnosis of serous cystadenoma, and of premalignant and malignant cystic lesions. In pancreaticobiliary imaging, MAGNETOM Cima.X provides unprecedented clarity in depicting ductal morphology and diffusion-restricted inflammatory patterns, offering non-invasive differentiation between IgG4-related disease and pancreatic cancer or cholangiocarcinoma. Moreover, the ability to monitor post-therapy changes through DWI introduces a new dimension of longitudinal disease assessment – linking diagnostic imaging with treatment response and surgical decision-making.

The growing emphasis on early detection is also redefining liver imaging. Choi highlights how abbreviated and non-contrast MRI protocols have emerged as efficient and reproducible tools for hepatocellular carcinoma (HCC) surveillance. These techniques, validated across multicenter trials, outperform ultrasound in sensitivity for early HCC while reducing operator dependency. By minimizing scan duration and eliminating contrast use, abbreviated MRI is now feasible as a tool for practical population-scale surveillance programs that combine diagnostic rigor with accessibility, which shows how simplification can drive precision [5, 6].

Progress in motion-tolerant acquisition is reflected in the evolution of GRASP MRI. Initially conceptualized more than a decade ago, GRASP integrates radial sampling, compressed sensing, and parallel imaging into a unified framework for free-breathing dynamic MRI [7]. Feng and colleagues show that the combination of flexibility and reliability is particularly valuable for patients unable to perform consistent breath-holds.

Quantitative MRI continues to enrich abdominal assessment by offering reproducible tissue biomarkers. Serai and colleagues extend magnetic resonance elastography (MRE) to pediatric kidney transplantation, demonstrating that renal stiffness measured by MRE correlates strongly with histological fibrosis and graft health [8]. This development brings us closer to noninvasive transplant monitoring, enabling early detection of rejection and fibrosis while reducing biopsy dependence.

These innovations reflect a cohesive movement toward precision and practicality. Abdominal MRI is evolving from a morphology-based modality to become a comprehensive quantitative ecosystem – one that captures structural, functional, and mechanical information in a single examination. The integration of high-performance gradient systems, deep learning reconstruction, and motion-robust dynamic imaging makes imaging workflows more reproducible, accessible, and patient-centered. As these technologies mature, their impact will expand and redefine what is possible in abdominal radiology. They will improve early diagnosis, personalize follow-up, and democratize access to advanced imaging. This evolution shows how innovation grounded in clinical relevance translates into meaningful progress for patients and practitioners alike, building a strong foundation for the continued advancement of MRI across specialties.

MSK imaging: Technical breakthroughs and clinical value of 0.55T MRI

As the volume of musculoskeletal implant surgeries grows, the need for accurate diagnosis of implant-related[2] pathologies has become increasingly pressing. The two articles on the 0.55T MAGNETOM Free. Platform offer valuable insights into addressing this clinical challenge.

X-ray and CT imaging have long had limited utility in these cases, and while MRI is an alternative, traditional

high-field systems (1.5T, 3T) are hampered by severe metal-induced artifacts, which undermine diagnostic accuracy [9, 10]. The 0.55T system directly targets this pain point. As shown in the work from ZEMODI in Bremen and the University of California, San Francisco (UCSF), the 0.55T system has unique advantages compared to high-field MRI systems when it comes to imaging metal implants. The 0.55T system leverages its inherent low-field-strength advantage to drastically reduce susceptibility artifacts around implants. Its wide-bore design also fills a practical gap, accommodating claustrophobic or over-weight patients, who often face barriers to standard imaging, which adds real-world clinical value.

Overall, these findings show that the MAGNETOM Free. Platform is more than just a complement to high-field MRI. It expands the clinical toolkit, and moves post-musculoskel-etal-implant care toward greater precision and inclusivity, all of which addresses unmet needs in current diagnostic workflows.

Cardiovascular imaging: Advancing cardiovascular and neurovascular MRI through technical innovation

Significant advancements have been made in CMRI, particularly by optimizing imaging protocols to improve diagnostic efficacy for patients with implantable cardiac devices.[2] Wideband black-blood LGE imaging effectively reduces hyperintensity artifacts, significantly improving the visualization of myocardial scars. This advancement is crucial for accurately diagnosing and managing cardio-vascular diseases in patients with ICDs – a population that continues to grow due to the rising prevalence of heart failure and arrhythmias.

Women's health: Optimized protocols for uterus and ovaries guided by ESUR recommendations

Shagalov and Roccia present a practical and anatomically grounded framework for uterine and ovarian MRI, guided by the European Society of Urogenital Radiology (ESUR) recommendations [12, 13]. Their work exemplifies how consensus-based guidance can be transformed into stan-dardized, reproducible, and time-efficient clinical practice.

By merging guideline-based standardization with intelligent acceleration, the authors provide a model for accessible, high-quality pelvic MRI across practice environ-ments. Their contribution encapsulates the broader mes-sage of this issue: Precision, (artificial) intelligence, and collaboration together make advanced imaging both effi-cient and equitable.

Access to care: Expanding equity through mobile and resilient MRI

Expanding global access to MRI requires both greater system portability and operational resilience. Christensen presents a timely and comprehensive overview of mobile MRI as a dynamic and evolving solution to one of health-care's most persistent challenges: geographic inequality. Christensen looks beyond mere mobility to highlight critical innovations such as helium-free systems and power-save modes, which tackle core operational and environmental limitations of traditional MRI [14]. The inte-gration of AI and remote scanning – rightly emphasized as a game-changer – further enhances the model's viability by centralizing expertise and streamlining workflows.

Complementing this approach, Sharma et al. address another critical barrier: unreliable infrastructure [15]. By enabling automatic recovery after power interruptions without the need for helium refills or specialized engineer-ing support, systems with DryCool technology challenge the conventional dependence on a stable power grid. DryCool technology increases the feasibility of sustainable imaging in challenging settings.

These innovations represent a dual-front strategy for addressing healthcare inequality: Mobile MRI units over-come geographical barriers by bringing imaging capabili-ties directly to patients, while technologies such as DryCool technology address infrastructural vulnerabilities that can immobilize a scanner even when it is in place.

Conclusion
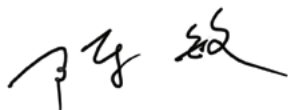
As we look ahead, the promise of MRI lies both in technical sophistication and in our shared responsibility to make these innovations clinically meaningful and globally acces-sible. From ultra-fast neuroimaging to AI-driven abdominal diagnostics, from low-field musculoskeletal solutions to sustainable mobile MRI systems, the progress reflected in this issue highlights our field's continuous, collaborative evolution.

True innovation in MRI is not achieved in isolation. It thrives in collaboration, validation, and shared purpose. Through initiatives like RSNA and MAGNETOM Flash, we continue to foster this spirit of cooperation, connecting engineers, scientists, and clinicians worldwide. The result is a growing ecosystem where intelligence and empathy go hand in hand, and technology improves not just perfor-mance, but patient care itself.

I extend my deepest gratitude to all contributors and readers, whose passion is the driving force of this

---

[2]The MRI restrictions (if any) of the metal implant must be considered prior to patient undergoing MRI exam. MR imaging of patients with metallic implants brings specific risks. However, certain implants are approved by the governing regulatory bodies to be MR conditionally safe. For such implants, the previously mentioned warning may not be applicable. Please contact the implant manufacturer for the specific conditional information. The conditions for MR safety are the responsibility of the implant manufacturer, not of Siemens Healthineers.

evolution. May this edition inspire continued dialogue and discovery as we shape the next era of magnetic resonance imaging together.

Professor Min Chen

References

1 Altmann S, Grauhan NF, Brockstedt L, Kondova M, Schmidtmann I, Roman P, et al. Ultrafast Brain MRI with Deep Learning Reconstruction for Suspected Acute Ischemic Stroke. Radiology. 2024;310(2):e231938.

2 Rastogi A, Brugnara G, Foltyn-Dumitru M, Mahmutoglu MA, Preetha CJ, Kobler E, et al. Deep-learning-based reconstruction of undersampled MRI to reduce scan times: a multicentre, retrospective, cohort study. Lancet Oncol. 2024;25(3):400–410.

3 Kharaji M, Canton G, Guo Y, Mosi MH, Zhou Z, Balu N, et al. DANTE-CAIPI Accelerated Contrast-Enhanced 3D T1: Deep Learning-Based Image Quality Improvement for Vessel Wall MRI. AJNR Am J Neuroradiol. 2025;46(1):49–56.

4 Thorpe S, Salkovskis PM, Dittner A. Claustrophobia in MRI: the role of cognitions. Magn Reson Imaging. 2008;26(8):1081–8.

5 Kim DH, Yoon JH, Choi MH, Lee CH, Kang TW, Kim HA, et al. Comparison of non-contrast abbreviated MRI and ultrasound as surveillance modalities for HCC. J Hepatol. 2024;81(3):461–470.

6 Rhee H, Kim MJ, Kim DY, An C, Kang W, Han K, et al. Noncontrast Magnetic Resonance Imaging vs Ultrasonography for Hepatocellular Carcinoma Surveillance: A Randomized, Single-Center Trial. Gastroenterology. 2025;168(6):1170–1177.e12.

7 Feng L, Grimm R, Block KT, Chandarana H, Kim S, Xu J, et al. Golden-angle radial sparse parallel MRI: combination of compressed sensing, parallel imaging, and golden-angle radial sampling for fast and flexible dynamic volumetric MRI. Magn Reson Med. 2014;72(3):707–17.

8 Joshi M, Dillman JR, Towbin AJ, Serai SD, Trout AT. MR elastography: high rate of technical success in pediatric and young adult patients. Pediatr Radiol. 2017;47(7):838–843.

9 Kelsey LJ, Seiberlich N, Bapuraj J, Rivas F, Masotti M, Gulani V, et al. Clinical MR imaging of patients with spinal hardware at 0.55T: comparison of diagnostic assessment and metal artifact appearance with 1.5T. Eur Spine J. 2025;34(4):1495–1504.

10 Feuerriegel GC, Sutter R. Managing hardware-related metal artifacts in MRI: current and evolving techniques. Skeletal Radiol. 2024;53(9):1737–1750.

11 Seginer A, Niry D, Furman-Haran E, Kolb H, Schmidt R. Reducing blood flow pulsation artifacts in 3D time-of-flight angiography by locally scrambling the order of the acquisition at 3 T and 7 T. Magn Reson Med. 2024;92(5):2081–2090.

12 Nougaret S, Horta M, Sala E, Lakhman Y, Thomassin-Naggara I, Kido A, et al. Endometrial Cancer MRI staging: Updated Guidelines of the European Society of Urogenital Radiology. Eur Radiol. 2019;29(2):792–805.

13 Thomassin-Naggara I, Dolciami M, Chamie LP, Guerra A, Bharwani N, Freeman S, et al. ESUR consensus MRI for endometriosis: indications, reporting, and classifications. Eur Radiol. 2025. Epub ahead of print.

14 Deoni SCL, Medeiros P, Deoni AT, Burton P, Beauchemin J, D'Sa V, et al. Development of a mobile low-field MRI scanner. Sci Rep. 2022;12(1):5690.

15 Chaban YV, Vosshenrich J, McKee H, Gunasekaran S, Brown MJ, Atalay MK, et al. Environmental Sustainability and MRI: Challenges, Opportunities, and a Call for Action. J Magn Reson Imaging. 2024;59(4):1149–1167.

Editorial Note

I am very happy to welcome André Fischer as Associate Editor. André brings extensive experience in cardiovascular and neurological MRI, and I am delighted that he will join me in shaping the future of *MAGNETOM Flash*.

Please join me in welcoming him to the team.
Antje Hellwich

Editorial Board

We appreciate your comments. Please contact us at **magnetomworld.team@siemens-healthineers.com**

Review Board

Advances in Ultra-High-Gradient MRI: High-Resolution Imaging for Accurate Diagnosis of Pancreatic Cystic Lesions

Bowen Wu[1], Yitong Lu[1], Yueluan Jiang[2], Xiaoye Wang[3], Liang Zhu[1]

[1]Department of Radiology, Peking Union Medical College Hospital, Beijing, China
[2]MR Research Collaboration Team, Siemens Healthineers Ltd., Beijing, China
[3]MR Clinical Marketing, Siemens Healthineers Ltd., Beijing, China

Introduction

Pancreatic cystic lesions (PCLs) are relatively common in clinical practice, and the detection rate has been increasing with the widespread application of computed tomography (CT) and magnetic resonance imaging (MRI). These lesions encompass a broad spectrum of diseases with similar imaging features, ranging from non-neoplastic cysts and benign tumors to premalignant and frankly malignant neoplasms. Accurate diagnosis is therefore challenging. Benign lesions may be misinterpreted as malignancies, leading to over-treatment, while early-stage cancer may be overlooked, delaying appropriate treatment. MRI possesses distinct advantages in the diagnosis of PCLs, owing to its non-invasiveness, its lack of ionizing radiation, its superior soft-tissue contrast, and its multiparametric imaging capabilities. Moreover, high-resolution MRI enabled by an ultra-high-gradient system and deep-learning reconstruction delineates subtle internal structures of PCLs and provides critical diagnostic clues.
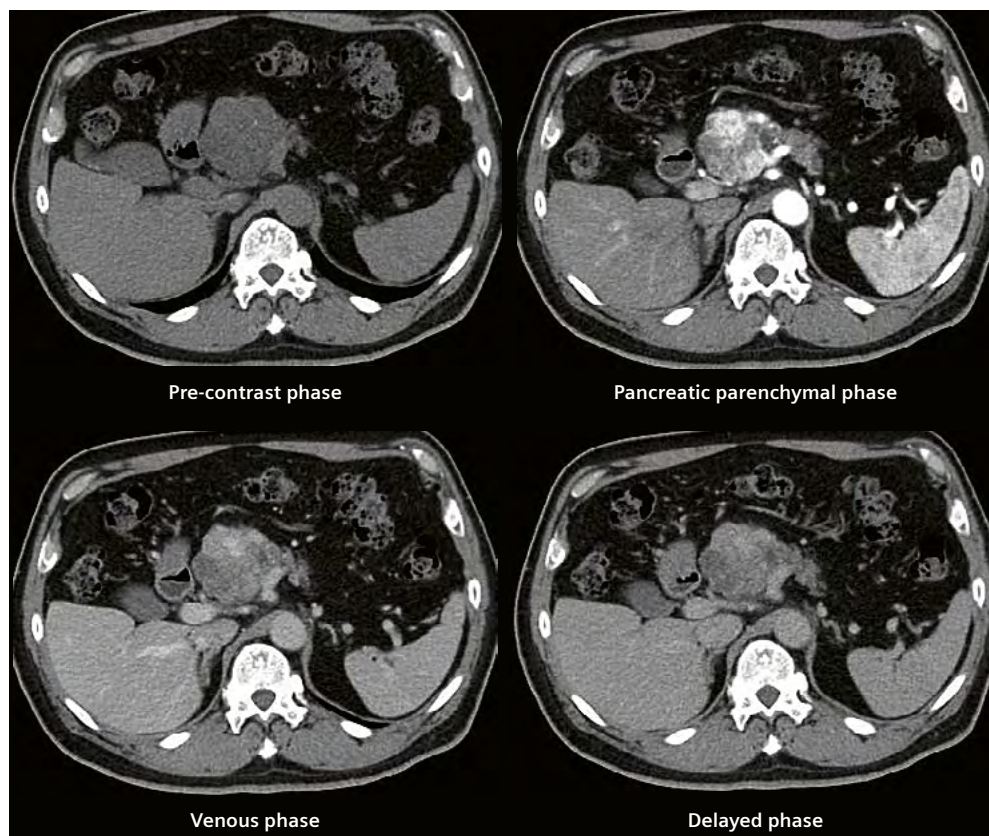
1 Contrast-enhanced CT demonstrates a mass with punctate calcifications and heterogeneous hyperenhancement during the pancreatic parenchymal phase, with partial washout in later phases. This raised suspicions of a pancreatic neuroendocrine tumor.

Pre-contrast phase

Pancreatic parenchymal phase

Venous phase

Delayed phase

At Peking Union Medical College Hospital, the pancreatic multidisciplinary team (MDT) combines clinical expertise, advanced imaging techniques, and complementary multi-modality information to enhance diagnostic accuracy. Here, we present a representative case from our hospital that illustrates how high-resolution MRI on the 3T MAGNETOM Cima.X served as a problem-solving tool for a challenging case.

Patient history

A 65-year-old male presented with occasional abdominal distension since May 2024, sometimes accompanied by right upper quadrant pain that resolved spontaneously. In May 2025, a chest CT performed during routine health screening incidentally revealed a hypodense lesion in the pancreatic head. Contrast-enhanced CT demonstrated a mass with punctate calcifications and heterogeneous hyperenhancement during the pancreatic parenchymal phase, with partial washout in later phases. This raised suspicions of a pancreatic neuroendocrine tumor (Fig. 1). PET/CT showed an increased maximum standardized uptake (SUVmax) value of 3.3, suggesting a low-grade malignant lesion.

The case was reviewed by the pancreatic MDT. Based on the patient's clinical history and the imaging findings, the possibility of a serous cystadenoma was suspected. High-resolution MRI was recommended for further clarification.

Imaging findings

High-resolution abdominal MRI and MRCP were performed on our 3T MAGNETOM Cima.X scanner. The ultra-high-gradient system provided unprecedented delineation of internal details:

- Axial high-resolution deep learning fat-saturated T2WI revealed a central stellate scar with fine honeycomb-like septations within the pancreatic head lesion. These were less clearly visualized on conventional T2WI (Fig. 2).
- The hypervascular nodular areas seen on CT corresponded to dense fibrous septa on MRI, producing a lace-like appearance that is consistent with a microcystic lesion rather than a solid tumor.
- High-resolution deep learning ZOOMit DWI demonstrated sharper lesion boundaries and internal heterogeneity than conventional DWI. Corresponding ADC maps showed diffuse high signal intensity, supporting the cystic nature of the lesion rather than a neuroendocrine tumor. The apparent diffusion restriction in hypervascular areas was attributed to the very dense septations, which leads to water diffusion within the small cells (Fig. 3).

Diagnosis and outcome

To further exclude malignancy, the patient underwent fine-needle biopsy with endoscopic ultrasound. The histopathology was negative for malignant cells. Finally, the patient was diagnosed with a benign serous cystadenoma of the pancreas. Surgical intervention was deemed unnecessary, and the patient was discharged.

"As a pancreatic surgeon, I frequently encounter patients with cystic lesions who are deeply anxious about potential malignancy. While surgical excision is sometimes necessary, the ability to accurately identify benign lesions and intervene only when appropriate is equally critical. The ultra-high gradient strength and deep learning reconstruction of MAGNETOM Cima.X deliver high-resolution T2WI and DWI that are superior to conventional MRI, providing surgeons with the confidence to avoid overtreatment and to recognize early malignant changes when present. Such imaging advances are invaluable for clinical decision-making."

Professor Xianlin Han
Department of General Surgery, Peking Union Medical College Hospital, Beijing, China

T2_BLADE_trig, 1.1 × 1.1 × 6.0 mm³

DL HASTE, 0.5 × 0.5 × 4.0 mm³
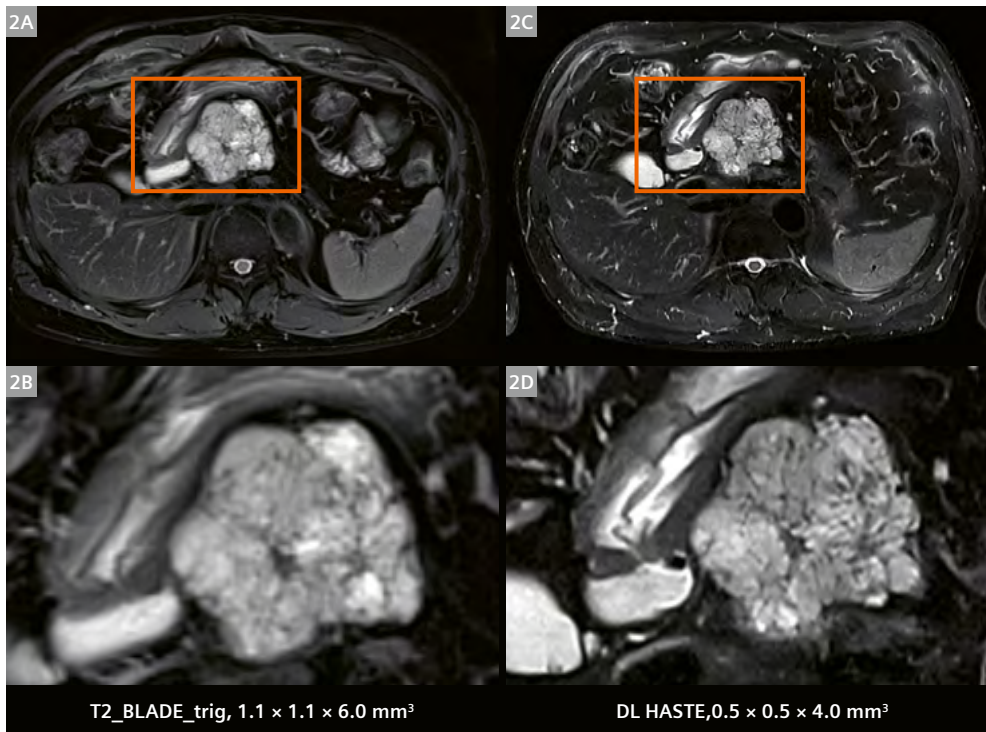
2 Axial high-resolution deep learning fat-saturated T2WI **(2C, D)** reveals a central stellate scar with fine honey-comb-like septations within the pancreatic head lesion. These were less clearly visualized on conventional T2WI **(2A, B)**.

Con DWI b = 800 s/mm², 1.5 × 1.5 × 4.0 mm³

DL ZOOMit DWI b = 800 s/mm², 1.0 × 1.0 × 3.0 mm³

Con DWI ADC

DL ZOOMit DWI ADC
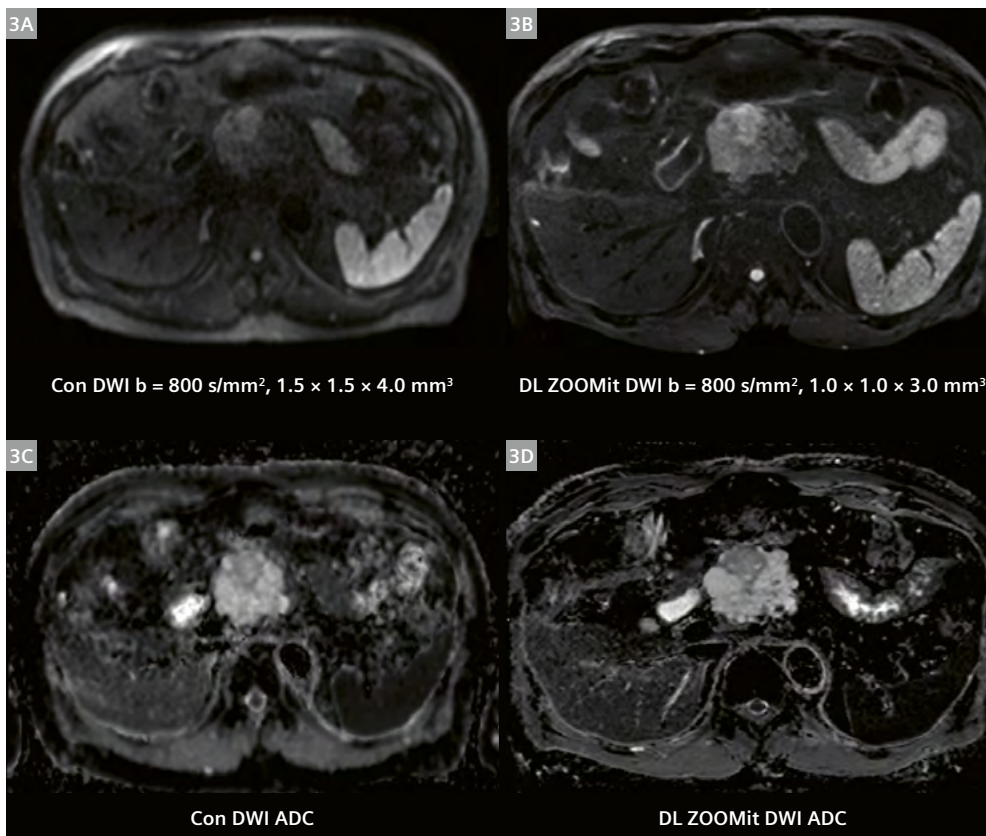
3 High-resolution deep-learning ZOOMit DWI **(3B)** demonstrates sharper lesion boundaries and internal heterogeneity than conventional DWI **(3A)**. Corresponding ADC maps **(3C, D)** show diffusely high signal intensity, supporting the cystic nature of the lesion rather than a neuroendocrine tumor.

	Con T2WI axial	HR T2WI axial	Con DWI	HR DWI
Field of view (mm³)	360 × 360	380 × 309	380 × 309	300 × 208
Matrix	320 × 320	384 × 269	128 × 128	150 × 150
Spatial resolution (mm³)	1.1 × 1.1 × 6.0	0.5 × 0.5 × 3.0	1.5 × 1.5 × 4.0	1.0 × 1.0 × 3.0
Slices	25	48	38	48
Echo time (ms)	85	89	56	50
Repetition time (ms)	2390	666	2000	2400
Averages	1	1	1, 4	1, 8
Diffusion gradients	–	–	3	3
B values (s/mm²)	–	–	50, 800	50, 800
Bandwidth (Hz/pixel)	710	420	2298	1960
Acquisition time (min:s)	3:00	0:42	2:04	3:20
Fat suppression	SPAIR	SPAIR	SPAIR	Fat saturation
DL reconstruction	--	On	--	On
Sequence	BLADE	HASTE	SE-EPI	ZOOMit SE-EPI
Scanner	MAGNETOM Skyra	MAGNETOM Cima.X	MAGNETOM Skyra	MAGNETOM Cima.X
Interpolation	Off	On	On	On
Resp. control	Trigger	Breath-hold	Trigger	Trigger
Acceleration factor	2	4	2	2
Acceleration mode	GRAPPA	GRAPPA	SMS, GRAPPA	GRAPPA

Table 2: Examination protocol
Con = conventional; HR = high resolution; DL = deep learning

Discussion

This case demonstrates the critical role of high-resolution MRI in the differential diagnosis of pancreatic cystic lesions. Conventional CT and MRI may suggest solid or malignant tumors, whereas high-resolution MRI – enabled by the MAGNETOM Cima.X with a 200 mT/m amplitude and a 200 T/m/s slew rate – allows confident identification of key features with a smaller voxel size (e.g., axial T2WI 0.5 × 0.5 × 3 mm³ vs. 1.1 × 1.1 × 6 mm³) and a short acquisition time (e.g., cor T2WI in 18 seconds within one breath-hold vs. 3–4 minutes). These features include stellate scars, fine septations, internal hemorrhage, and mural nodules. These subtle imaging features form the basis for distinguishing benign cystic lesions from premalignant or malignant lesions, directly influencing patient management.
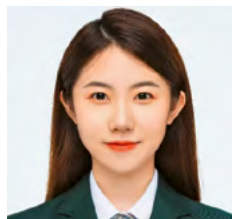
Bowen Wu, Radiographer   Yitong Lu, Radiographer   Professor Liang Zhu, M.D.

Contact

Liang Zhu, M.D.
Associate Professor, Department of Radiology
Peking Union Medical College Hospital
Shuaifuyuan No. 1, Dongcheng District
Beijing, 100730
China
zhuliang_pumc@163.com

High-Resolution Pancreaticobiliary MR Imaging with MAGNETOM Cima.X: Two Cases of IgG4-Related Diseases

Yitong Lu[1], Bowen Wu[1], Yueluan Jiang[2], Xiaoye Wang[3], Liang Zhu[1]

[1]Department of Radiology, Peking Union Medical College Hospital, Beijing, China
[2]MR Research Collaboration Team, Siemens Healthineers Ltd., Beijing, China
[3]MR Clinical Marketing, Siemens Healthineers Ltd., Beijing, China

Introduction

IgG4-related disease (IgG4-RD) is a rare autoimmune disorder that can involve multiple organs. The clinical manifestation and radiological appearance of pancreaticobiliary system involvement often closely mimics pancreatic cancer or cholangiocarcinoma, which may lead to unnecessary surgical resections. Accurate differentiation between IgG4-RD and pancreaticobiliary malignancies is therefore essential for appropriate treatments.

Recent advances in magnetic resonance imaging (MRI), particularly with the development of ultra-high-gradient systems and deep learning reconstruction, provide superior spatial resolution and contrast compared to conventional systems. This enables the detection of subtle imaging features, such as the duct-penetrating sign of the pancreas, and symmetric thickening and diffusion restriction of the biliary wall, which provide important clues for an accurate diagnosis.

In this report, we present two cases of IgG4-related autoimmune pancreatitis with or without associated sclerosing cholangitis, where high-resolution images from the 3T MAGNETOM Cima.X provided critical diagnostic information and enabled accurate distinction from malignancy.

Case 1

Patient history

A 49-year-old male presented with obstructive jaundice for a week, and a history of intermittent abdominal bloating for six months. Initial MRI from an external institution revealed a mass in the pancreatic head with a "double-duct sign." Serum CA 19-9 was slightly increased (40.1 U/mL). The patient was suspected of having pancreatic head carcinoma and referred to our hospital for further workup.

At our institution, contrast-enhanced CT revealed a soft-tissue mass in the pancreatic head with a "double-duct sign," while PET/CT demonstrated increased FDG uptake of the pancreatic head lesion (SUVmax 8.9). Serum IgG4 was within normal range (791 mg/L). With a preliminary diagnosis of pancreatic head mass with obstructive jaundice, this case was presented for discussion in the pancreatic multidisciplinary team (MDT). Based on the clinical history and imaging findings, atypical focal autoimmune pancreatitis (AIP) was suspected, and high-resolution contrast-enhanced pancreatic MRI and MR cholangiopancreatography (MRCP) were suggested.

1 High-resolution DL HASTE T2-weighted imaging (right) clearly demonstrates the pancreatic duct-penetrating sign.

Conventional T2WI HASTE — MAGNETOM Cima.X HR T2WI DL HASTE

Imaging findings

MR imaging from the 3T MAGNETOM Cima.X revealed the following:

Coronal high-resolution deep learning T2-weighted imaging (HR DL T2WI) demonstrated a narrowed but non-obstructed main pancreatic duct (MPD) traversing the pancreatic head mass. This is the "duct-penetrating sign," and it favors AIP over pancreatic carcinoma (Fig. 1).

Axial HR DL HASTE T2WI clearly depicted the Santorini's duct, which was spared from the pancreatic head lesion. Such details were not shown on conventional BLADE T2WI (Fig. 2).

DL ZOOMit DWI showed a sharply delineated hyper-intense lesion in the pancreatic head, corresponding to heterogeneous hypo-enhancement in the pancreatic arterial phase and homogeneous hyper-enhancement in the delayed phase, consistent with focal AIP (Fig. 3).

Diagnosis and outcome

According to the information from high-resolution MRI, the diagnosis was probable seronegative IgG4-related autoimmune pancreatitis. Further pancreatic biopsy revealed chronic pancreatitis with >10 IgG4+ plasma cells/high-power field (HPF), consolidating the diagnosis. After four weeks of corticosteroid therapy (CST), the patient's jaundice was resolved, and follow-up MRI demonstrated regression of the lesion and resolved biliary obstruction.
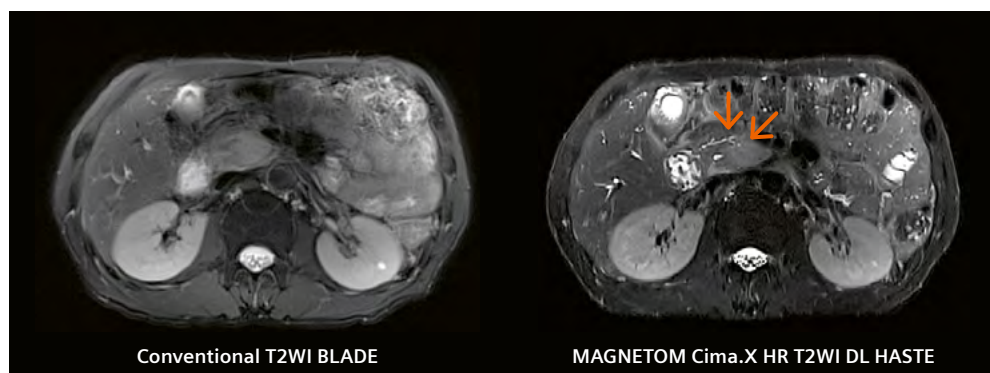
2 High-resolution DL HASTE T2-weighted imaging (right) clearly demonstrates the accessory pancreatic duct.

Conventional T2WI BLADE

MAGNETOM Cima.X HR T2WI DL HASTE
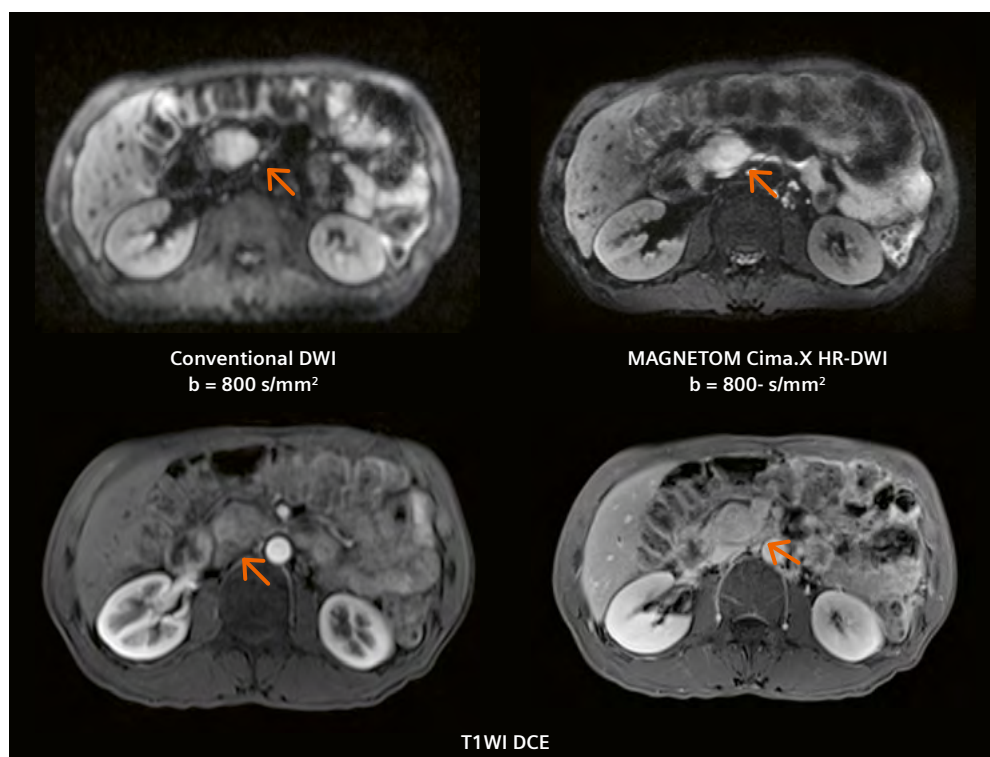
3 High-resolution DL ZOOMit DWI (top right) clearly delineates the lesions in the pancreatic head.

Conventional DWI
b = 800 s/mm²

MAGNETOM Cima.X HR-DWI
b = 800- s/mm²

T1WI DCE

"Upper abdominal MRI is inherently challenging, and hardware performance is essential for consistently achieving diagnostic-quality images. While ductal dilatation is relatively easy to depict, subtle features such as a narrowed but non-obstructed MPD penetrating the mass, or fine biliary wall changes, are significantly more challenging for imaging techniques. The ultra-high-gradient performance of the MAGNETOM Cima.X, combined with deep learning-based reconstruction, delivers high-resolution T2WI and DWI that is unobtainable with conventional MRI. These advances could greatly enhance the performance of MRI and provide a powerful problem-solving tool for clinical doctors."

Professor Feng Feng
Department of Radiology, Peking Union Medical College Hospital, Beijing, China

Case 2

Patient history

A 69-year-old male presented with generalized pruritus following medication for conjunctivitis. Liver function tests showed elevated liver enzymes and bilirubin levels (ALT 308 U/L, AST 139 U/L, GGT 546 U/L, ALP 261 U/L, TBil 28.6 µmol/L). His serum CA 19-9 level fluctuated between 26 and 36 U/mL, while his carcinoembryonic antigen (CEA) level was mildly elevated (5.8 ng/mL). CT and MRI suggested distal common bile duct stricture, pancreatic head enlargement, and main pancreatic duct dilatation. Endoscopic ultrasound demonstrated common bile duct wall thickening.

Based on the abovementioned information from the external institution, the consulting gastroenterologist raised suspicion for IgG4-related autoimmune pancreatitis and sclerosing cholangitis. Serum IgG4 was markedly elevated (6213 mg/dL). High-resolution MRI and MRCP were requested to rule out pancreaticobiliary malignancies.

Imaging findings

MR imaging from the 3T MAGNETOM Cima.X revealed the following:

Compared with conventional HASTE T2WI, the HR DL T2WI more clearly revealed biliary wall thickening, pancreatic head swelling, and subtle main pancreatic duct dilatation in the body (Fig. 4).

On HR-DL T2WI, the irregularity and slight dilation of the MPD in the pancreatic body and tail was more clearly seen than on the conventional BLADE (Fig. 5).

Conventional DWI showed tape-like hyperintensity along the common bile duct and cystic duct region. HR DL ZOOMit DWI demonstrated sharply delineated "tram-track" and ring-like hyperintensity, which was precisely confined to the thickened biliary wall. The image pattern of diffusion restriction corresponds perfectly to hyperenhancement of the biliary wall on contrast-enhanced sequences (Fig. 6).
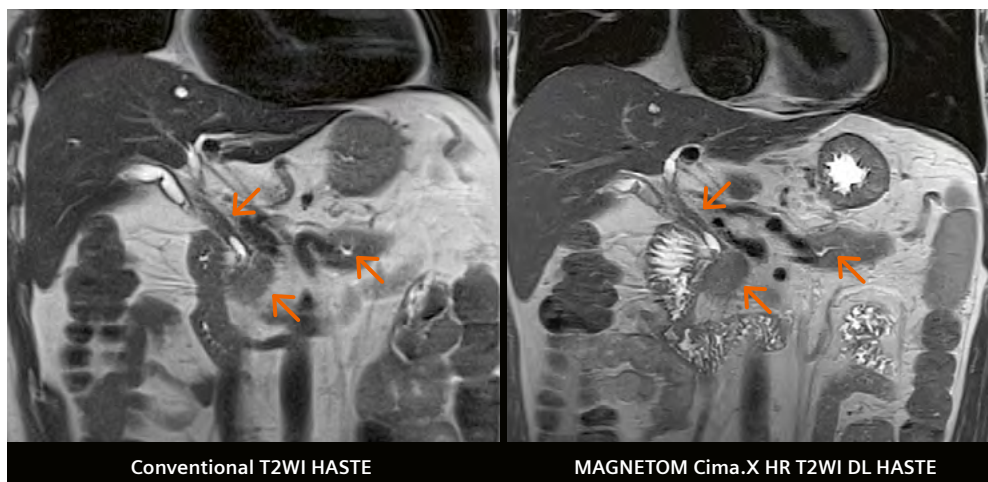
4 High-resolution DL-T2WI (right) clearly shows the thickening of the main bile duct wall.

Conventional T2WI HASTE

MAGNETOM Cima.X HR T2WI DL HASTE

Diagnosis and outcome

The diagnosis was IgG4-related autoimmune pancreatitis with associated sclerosing cholangitis. After four weeks of CST, follow-up high-resolution MRI showed dramatic regression of both pancreatic and biliary abnormalities (Fig. 7).
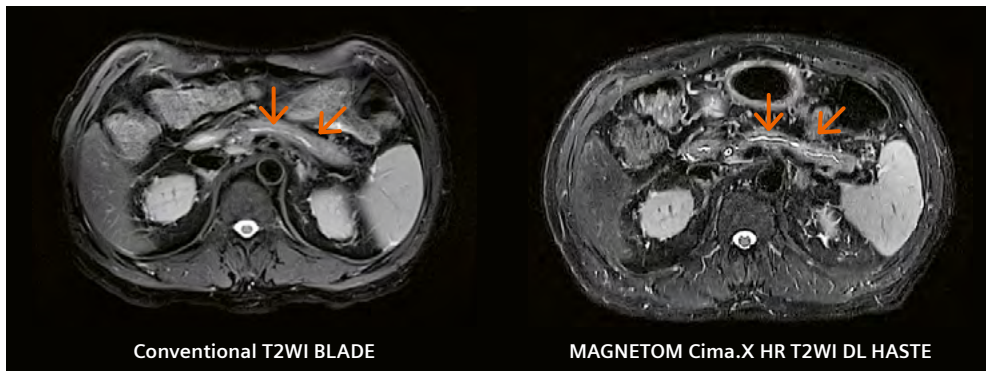
Conventional T2WI BLADE   **MAGNETOM Cima.X HR T2WI DL HASTE**

5 High-resolution DL T2WI (right) clearly demonstrates morphological abnormalities in the pancreatic duct.

Conventional DWI
b = 800 s/mm²   **MAGNETOM Cima.X HR-DWI**
b = 800 s/mm²   **T1WI Dixon DCE**

6 High-resolution DL T2WI (right) clearly demonstrates morphological abnormalities in the pancreatic duct.

HR-T2WI DL-HASTE cor   **HR-T2WI DL-HASTE**
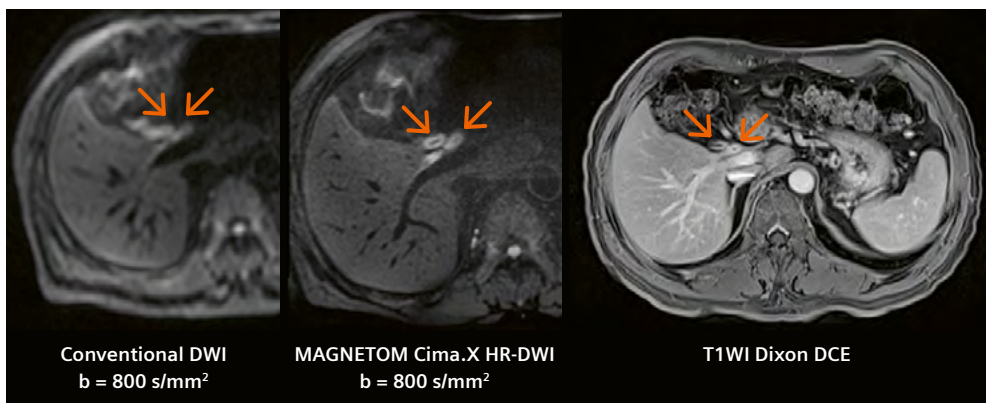
HR-DWI
b = 800 s/mm²   **T1WI Dixon DCE**
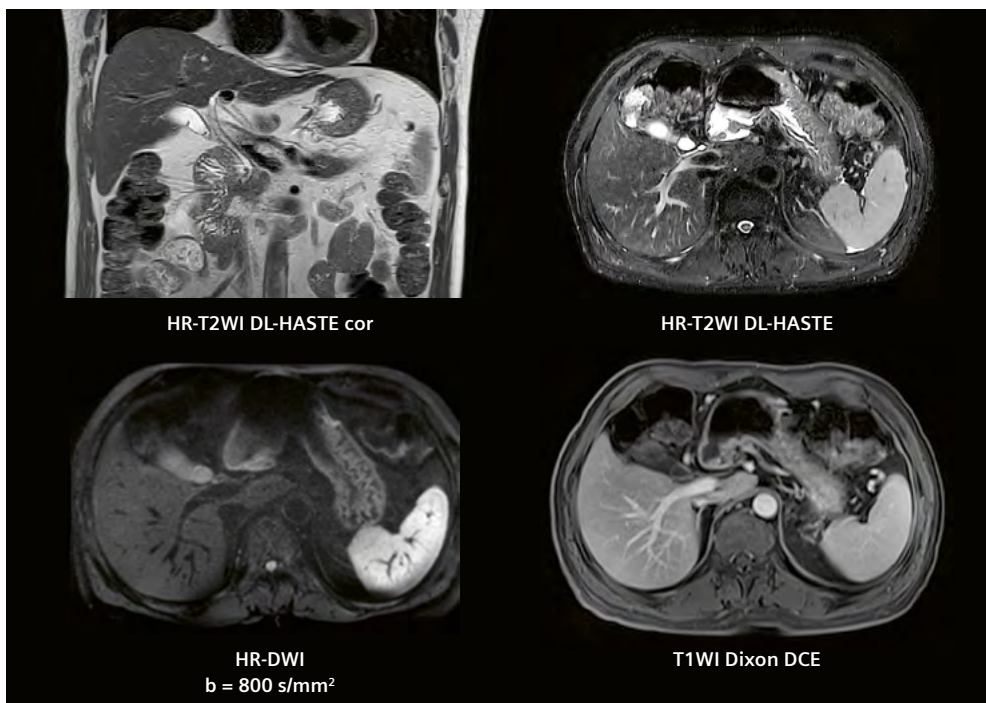
7 Posttreatment MRI.

	Con T2WI cor	HR T2WI cor	Con T2WI ax	HR T2WI ax	Conv DWI	HR DWI
Field of view (mm³)	360 × 360	400 × 400	360 × 360	380 × 309	380 × 309	300 × 208
Matrix	320 × 320	448 × 358	320 × 320	384 × 269	128 × 128	150 × 150
Spatial resolution (mm³)	1.1 × 1.1 × 4.0	0.45 × 0.45 × 4.0	1.1 × 1.1 × 6.0	0.5 × 0.5 × 3.0	1.5 × 1.5 × 4.0	1.0 × 1.0 × 3.0
Slices	32	32	25	48	38	48
Echo time (ms)	92	87	85	89	56	50
Repetition time (ms)	2000	567	2390	666	2000	2400
Averages	1	1	1	1	1, 4	1, 8
Diffusion gradients	–	–	–	–	3	3
B values (s/mm²)	–	–	–	–	50, 800	50, 800
Bandwidth (Hz/pixel)	710	657	710	420	2298	1960
Acquisition time (min:s)	1:30	0:18	3:00	0:42	2:04	3:20
Fat suppression	–	–	SPAIR	SPAIR	SPAIR	Fat saturation
DL reconstruction	–	On	–	On	–	On
Sequence	HASTE	HASTE	BLADE	HASTE	SE-EPI	ZOOMit SE-EPI
Scanner	MAGNETOM Skyra	MAGNETOM Cima.X	MAGNETOM Skyra	MAGNETOM Cima.X	MAGNETOM Skyra	MAGNETOM Cima.X
Interpolation	Off	On	Off	On	On	On
Resp. control	Trigger	Breath-hold	Trigger	Breath-hold	Trigger	Trigger
Acceleration factor	3	4	2	4	2	2
Acceleration mode	GRAPPA	GRAPPA	GRAPPA	GRAPPA	SMS, GRAPPA	GRAPPA

Table 1: Examination protocol: Con = conventional, HR = high resolution, DL = deep learning, cor = coronal, ax = axial

Discussion

Both cases highlight the critical role of ultra-high-gradient MRI in differentiating IgG4-related disease from pancreaticobiliary malignancies. Conventional MRI and CT may demonstrate mass-like lesions with upstream MPD and biliary dilatation, mimicking malignancy. The hypermetabolism of the lesion with active inflammation may be even more misleading. However, the diagnostic clues for autoimmune pancreatitis – such as the subtle duct changes and multi-focal involvement – require high-resolution imaging for confident identification.

The MAGNETOM Cima.X, equipped with a 200 mT/m amplitude and a 200 T/m/s slew rate, enables high-resolution T2WI and DWI with deep learning reconstruction. This permits clear visualization of subtle pancreatic parenchymal signal intensity, ductal morphology, and biliary wall alterations, which is critical for distinguishing IgG4-RD from malignancies.

Contact

Liang Zhu, M.D.
Associate Professor, Department of Radiology
Peking Union Medical College Hospital
Shuaifuyuan No. 1, Dongcheng District
Beijing, 100730
China
zhuliang_pumc@163.com
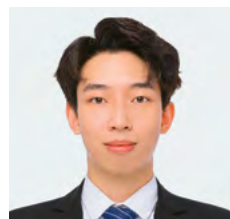
Yitong Lu, Radiographer   Bowen Wu, Radiographer   Professor Liang Zhu, M.D.

Surveillance of Hepatocellular Carcinoma using MRI

Joon-Il Choi, M.D., Ph.D.

Department of Radiology, Seoul St. Mary's Hospital,
The Catholic University of Korea, Seoul, Republic of Korea

Introduction

Hepatocellular carcinoma (HCC) is the most common primary liver cancer and one of the leading causes of cancer-related mortality worldwide [1]. The prognosis of HCC largely depends on the stage at which it is diagnosed. When detected at an early stage, curative treatment options such as surgical resection, liver transplantation, and locoregional therapies can significantly improve survival rates, with five-year survival exceeding 60% [2–4]. However, due to the often asymptomatic nature of early-stage HCC, most cases are diagnosed at an advanced stage, when treatment options are limited, resulting in poor prognoses [5].

To improve patient outcomes, major liver societies, including the European Association for the Study of the Liver (EASL) and the American Association for the Study of Liver Diseases (AASLD), recommend biannual surveillance for high-risk individuals, particularly those with liver cirrhosis [2, 4]. The current standard surveillance modality is ultrasonography (US) with or without serum alpha-fetoprotein (AFP) testing. US is widely used due to its cost-effectiveness, accessibility, and lack of ionizing radiation. However, its diagnostic performance in detecting early-stage HCC is suboptimal. A recent meta-analysis has reported that the sensitivity of US in detecting early-stage HCC (Barcelona Clinic Liver Cancer [BCLC] Stage 0 or A) is approximately 47%, with surveillance failure occurring in nearly one-third of cases [6].

Several factors contribute to the limitations of US, including patient-related variables such as obesity, liver macronodularity, and suboptimal echogenic windows, which reduce lesion detectability. In addition, the operator dependency of US can lead to variability in diagnostic accuracy [7–9]. Given these limitations, there is increasing interest in alternative imaging modalities that can enhance early detection rates, reduce false negatives, and improve overall surveillance efficacy [7, 10, 11]. MRI has emerged as a promising alternative due to its superior soft tissue contrast, ability to detect small HCC lesions, and independence from operator variability [12]. Furthermore, MRI provides a more comprehensive evaluation of liver nodules, offering functional and structural imaging techniques that improve lesion characterization. These advantages position MRI as a valuable tool in HCC surveillance, particularly for high-risk patients with suboptimal US visualization.

MRI methods for HCC surveillance

Several MRI protocols have been developed to optimize surveillance for HCC while addressing concerns about cost, scan time, and contrast agent administration. The four MRI protocols are: full-protocol contrast-enhanced MRI, abbreviated MRI (AMRI) with hepatobiliary-specific contrast agents (HBAs), AMRI with extracellular contrast mediums (ECCMs), and non-contrast MRI (NC-MRI, also a form of AMRI) [13]. Compared to full-protocol MRI, AMRI significantly reduces both cost and scan time by eliminating unnecessary imaging sequences while maintaining high diagnostic accuracy, making it a more practical and accessible option for HCC surveillance.

1) Full-protocol MRI: This technique involves the use of multiphase dynamic imaging with gadolinium-based contrast agents, particularly HBAs such as gadoxetic acid. This protocol offers the highest sensitivity for detecting small HCC lesions and allows for functional assessment of liver parenchyma [7]. However, its limitations include high cost, prolonged scan times, limited accessibility, and concerns about gadolinium accumulation, especially in patients with impaired renal function [13].

2) AMRI with HBAs: Abbreviated MRI protocols aim to reduce scan time while maintaining diagnostic accuracy. They typically include fewer imaging sequences. AMRI with gadoxetic acid is designed to preserve the high sensitivity of hepatobiliary phase imaging for lesion detection, while shortening overall exam time by excluding the dynamic contrast-enhanced sequences typically used for lesion characterization. The workflow is further optimized by administering the contrast agent in the waiting area prior to scanning, eliminating delays during the MRI session itself. AMRI with HBAs typically includes hepatobiliary phase imaging, diffusion-weighted imaging (DWI), and T2-weighted imaging (T2WI), with total acquisition time – including preparation and setup – reported to be under 15 minutes [13]. With continued advancements in imaging technology and the integration of deep learning methods, this acquisition time is expected to decrease even further [14, 15].

3) AMRI with ECCMs: This sequence involves dynamic contrast-enhanced AMRI consisting of fat-saturated T1-weighted imaging (T1WI) before and after contrast administration, covering key phases such as arterial, portal venous, and delayed phases using an ECCM. By focusing solely on the dynamic contrast-enhanced sequences and excluding others like DWI and T2WI, AMRI with ECCMs shortens the overall scan time. A primary advantage of this approach is its ability to capture the hallmark imaging features required for a definitive HCC diagnosis, eliminating the need for additional confirmatory imaging [13]. Compared to AMRI with HBAs, this protocol offers a simpler workflow and fewer patient compliance issues. However, it lacks the hepatobiliary phase, which can be critical for detecting small or well-differentiated HCCs [16, 17]. AMRI with HBAs typically provides superior sensitivity for early-stage or subcentimeter lesions, but at the expense of longer scan times and increased cost, since HBAs are more expensive than ECCMs.

4) NC-MRI: This typically includes DWI and T2WI, with optional in- and opposed-phase T1WI. It is the simplest and most cost-effective of the AMRI strategies, avoiding gadolinium-related risks and costs. DWI is central to lesion detection in NC-MRI and has shown excellent sensitivity and specificity for HCC, with one prospective study reporting values of 83% and 98%, respectively [18]. Most NC-MRI protocols use free-breathing or respiratory-triggered DWI with multiple b-values, typically ranging from 0 to 800 s/mm², though the optimal b-value combination remains unclear [13]. Since NC-MRI lacks hepatobiliary phase imaging and dynamic contrast imaging, achieving high-quality DWI is critical for effective surveillance. T2WI supports both lesion detection and characterization. Moderately weighted T2WI sequences are preferred, due to better lesion conspicuity and higher signal-to-noise ratio, although more validation is needed [19, 20]. Advances in imaging, including deep learning, may allow for the acquisition of both moderate and heavy T2WI without significantly increasing scan time. T1WI with dual echo, which assesses intralesional fat – an ancillary feature favoring HCC – can also be added with minimal time burden, as it is easily acquired in a single breath-hold.

Each of these protocols offers distinct advantages and limitations, and ongoing prospective studies aim to determine the optimal approach for HCC surveillance.

Performing NC-MRI

Despite increasing interest in AMRI for HCC surveillance, there is no consensus on the optimal MRI protocol. As a researcher and a clinician, I chose NC-MRI for its shorter acquisition time, which improves workflow and patient compliance, and for the absence of contrast agents, which reduces costs and potential adverse effects. The use of gadolinium-based contrast agents in HCC surveillance remains a topic of debate. Recent studies have reported gadolinium deposition in the brain of patients who have undergone repeated contrast-enhanced MRI exams, raising concerns about the long-term effects. Additionally, some reports suggest a potential association between gadolinium exposure and the development of Parkinson's disease. Given these concerns, the justification for administering MRI contrast agents in surveillance populations – who are at risk of HCC but have not yet been diagnosed with the disease – remains controversial, especially when considering the potential risks versus benefits in this setting. While concerns exist regarding its sensitivity, retrospective studies have shown NC-MRI to be comparable to full-protocol MRI, with reported sensitivities of 86%–87% and specificities of 90%–94%. The inclusion of DWI and
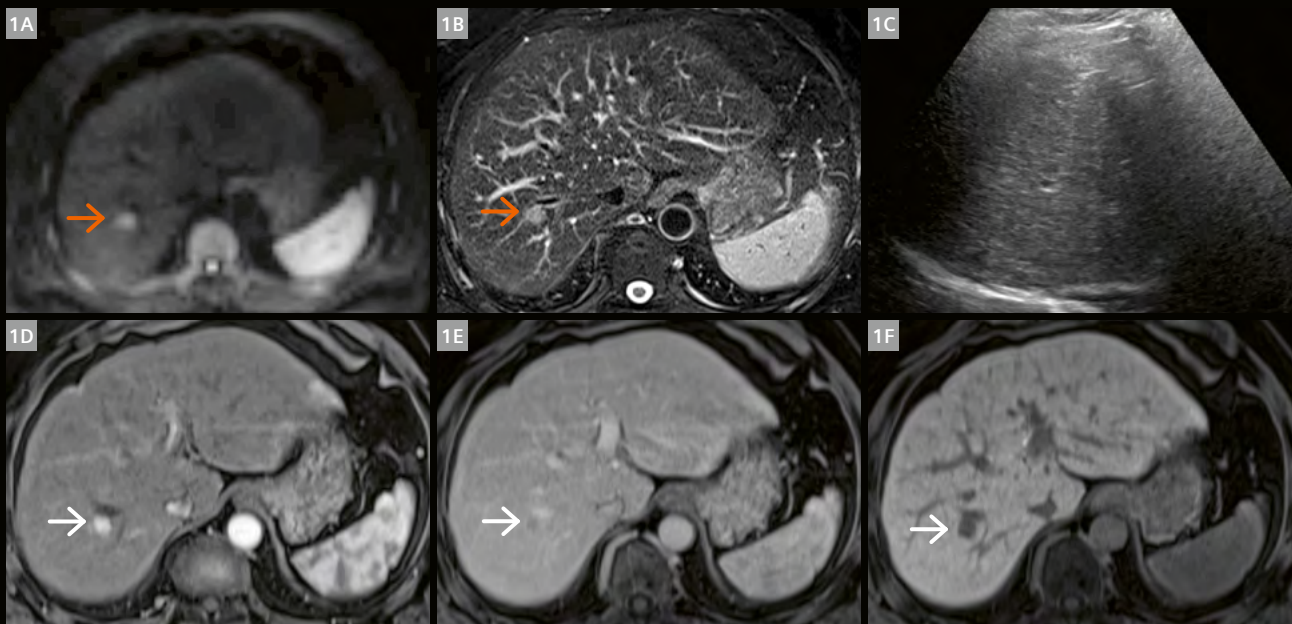
1 A 57-year-old man who was diagnosed with HCC by NC-MRI. The disease was not detected on US. On DWI (**1A**, b-value = 500 s/mm²) and T2WI (**1B**), there is a small diffusion-restricted and T2-high-signal nodular lesion in S7 of the liver (arrows). However, on US (**1C**), no mass is detected. After the injection of gadoxetic acid, an arterial-enhancing mass (**1D**) with washout on portal venous phase (**1E**) and a defect on hepatobiliary imaging (HBI) (**1F**) are noted.

2 A 63-year-old man who was diagnosed with HCC by NC-MRI. The disease was not detected on US. On DWI (**2A**, b-value = 500 s/mm²), there is an ill-defined mass in the caudate lobe of the liver (arrow). On T2WI (**2B**), this mass shows iso-signal (arrow). On US (**2C**), the caudate lobe is not clearly visible due to a poor sonic window. On arterial phase, contrast-enhanced CT scan (**2D**), there is an enhancing HCC in S1 of the liver.
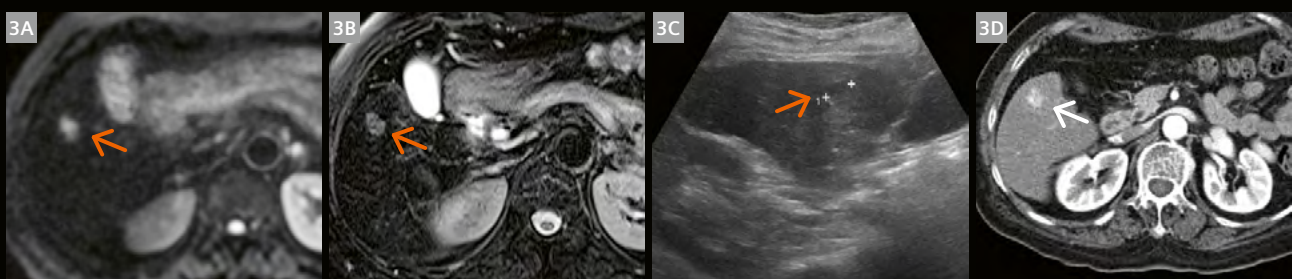
3 A 74-year-old woman who was diagnosed with HCC by both NC-MRI and US. On DWI (**3A**, b-value = 500 s/mm²) and T2WI (**3B**), there is a small diffusion-restricted and T2-high-signal nodular lesion in S5 of the liver (arrows). Also on US (**3C**), there is a low echoic mass corresponding to a nodular lesion on MRI. On arterial phase, contrast-enhanced CT scan (**3D**), there is an enhancing HCC in S5 of the liver.

T2WI sequences ensures effective lesion detection, and although meta-analyses suggest slightly lower sensitivity than contrast-enhanced AMRI (85% vs. 88%), the advantages of NC-AMRI – shorter scan times, lower costs, and improved accessibility – support its feasibility as a surveillance tool for HCC.

Two prospective studies comparing NC-MRI and US as surveillance tools for HCC were recently published by Korean researchers. The MAGNUS-HCC study evaluated annual NC-MRI against biannual US in a single-arm setting [21], while the MIRACLE-HCC study compared biannual NC-MRI with biannual US in a randomized, dual-arm design [22].

In the MAGNUS-HCC study, the authors reported that NC-MRI was superior to US as a surveillance tool. In that study, 208 participants in six institutes underwent 980 US and 516 NC-MRI examinations during 30 months of follow-up. Thirty-four HCCs were diagnosed in 31 participants, with 20 (64.5%) classified as very early-stage and 11 (35.5%) as early-stage HCC. NC-MRI alone detected 13 HCCs in 12 participants (Figs. 1, 2), whereas US alone identified four HCCs in four participants. Both modalities detected 12 HCCs in 10 participants (Fig. 3), but no cases were found solely by US when both methods were used together. Five HCCs in five participants went undetected by both NC-MRI and US, with some lesions being false positives on US or later diagnosed through elevated AFP levels and dynamic imaging. The sensitivity of annual NC-MRI (71.0%) was marginally higher than that of biannual US (45.2%, p = 0.077). NC-MRI showed a significantly higher diagnostic yield (DY) than US (4.26% vs. 1.43%, p <0.001), with a similar false referral rate (FRR) (2.91% vs. 3.06%, p = 0.885). A simulation alternating between US and NC-MRI every six months significantly improved sensitivity to 83.9% compared to biannual US alone (p = 0.006). It also yielded higher positive predictive value (43.3%) and DY (2.66%), though the FRR showed no significant difference.

In the MIRACLE-HCC study, 414 participants in a single institute were enrolled and randomly assigned to either the US group (n = 207) or the MRI group (n = 207). HCCs were diagnosed in 23 participants from the US group, and in 25 participants from the MRI group. The detection rates for BCLC Stage 0 or A tumors were similar between the two groups (8% for US vs. 12% for MRI). However, BCLC Stage 0 tumors were more frequently identified in the MRI group (8%) than in the US group (3%). Additionally, the MRI group exhibited a lower FRR (0.7% [95% confidence interval, 0.4%–1.2%] vs. 3.1% [2.3%–4.1%], P < 0.001) compared to the US group.

These studies provide valuable insights into the potential role of NC-MRI in HCC surveillance and its comparative effectiveness against the current standard of care (biannual US).

Conclusions

AMRI protocols, including those using hepatobiliary-specific contrast agents, extracellular contrast agents, and non-contrast techniques, are promising alternatives to conventional US for HCC surveillance, offering improved sensitivity for early-stage tumor detection and reduced operator dependency. Among these protocols, NC-MRI stands out for its simplicity, absence of gadolinium-related risks, shorter scan time, and cost-effectiveness – making it particularly suitable for repeated surveillance in high-risk populations. Recent prospective studies have demonstrated that NC-MRI performs comparably or is even superior to biannual US in terms of sensitivity, diagnostic yield, and false referral rate. This further supports its feasibility as a practical surveillance tool. As imaging technology continues to advance and as evidence accumulates, AMRI – especially streamlined protocols like NC-MRI – may play an increasingly central role in optimizing HCC surveillance strategies.

References

1 Bray F, Laversanne M, Sung H, Ferlay J, Siegel RL, Soerjomataram I, et al. Global cancer statistics 2022: GLOBOCAN estimates of incidence and mortality worldwide for 36 cancers in 185 countries. CA: Cancer J Clin. 2024;74(3):229-263.

2 European Association for the Study of the Liver. EASL Clinical Practice Guidelines on the management of hepatocellular carcinoma. Journal Hepatol. 2025;82(2):315-374.

3 Llovet JM, Kelley RK, Villanueva A, Singal AG, Pikarsky E, Roayaie S, et al. Hepatocellular carcinoma. Nat Rev Dis Primers. 2021;7(1):6.

4 Singal AG, Llovet JM, Yarchoan M, Mehta N, Heimbach JK, Dawson LA, et al. AASLD Practice Guidance on prevention, diagnosis, and treatment of hepatocellular carcinoma. Hepatology. 2023;78(6):1922-1965.

5 Moon AM, Singal AG, Tapper EB. Contemporary Epidemiology of Chronic Liver Disease and Cirrhosis. Clin Gastroenterol Hepatol. 2020;18(12):2650-2666.

6 Tzartzeva K, Obi J, Rich NE, Parikh ND, Marrero JA, Yopp A, et al. Surveillance Imaging and Alpha Fetoprotein for Early Detection of Hepatocellular Carcinoma in Patients With Cirrhosis: A Meta-analysis. Gastroenterology. 2018;154(6):1706-1718.e1.

7 Kim SY, An J, Lim YS, Han S, Lee JY, Byun JH, et al. MRI With Liver-Specific Contrast for Surveillance of Patients With Cirrhosis at High Risk of Hepatocellular Carcinoma. JAMA Oncol. 2017;3(4):456-463.

8 Kim YY, An C, Kim DY, Aljoqiman KS, Choi JY, Kim MJ. Failure of hepatocellular carcinoma surveillance: inadequate echogenic window and macronodular parenchyma as potential culprits. Ultrasonography. 2019;38(4):311-320.

9 Sinn DH, Yi J, Choi MS, Choi D, Gwak GY, Paik YH, et al. Incidence and risk factors for surveillance failure in patients with regular hepatocellular carcinoma surveillance. Hepatol Int. 2013;7(4):1010-8.

10 Park JH, Park MS, Lee SJ, Jeong WK, Lee JY, Park MJ, et al. Contrast-enhanced US with Perfluorobutane for Hepatocellular Carcinoma Surveillance: A Multicenter Diagnostic Trial (SCAN). Radiology. 2019;292(3):638-646.

11 Yoon JH, Lee JM, Lee DH, Joo I, Jeon JH, Ahn SJ, et al. A Comparison of Biannual Two-Phase Low-Dose Liver CT and US for HCC Surveillance in a Group at High Risk of HCC Development. Liver Cancer. 2020;9(5):503-517.

12 Kim DH, Choi SH, Shim JH, Kim SY, Lee SS, Byun JH, et al. Magnetic Resonance Imaging for Surveillance of Hepatocellular Carcinoma: A Systematic Review and Meta-Analysis. Diagnostics (Basel). 2021;11(9):1665.

13 Park HJ, Seo N, Kim SY. Current Landscape and Future Perspectives of Abbreviated MRI for Hepatocellular Carcinoma Surveillance. Korean J Radiol. 2022;23(6):598-614.

14 Herrmann J, Gassenmaier S, Nickel D, Arberet S, Afat S, Lingg A, et al. Diagnostic Confidence and Feasibility of a Deep Learning Accelerated HASTE Sequence of the Abdomen in a Single Breath-Hold. Invest Radiol. 2021;56(5):313-319.

15 Shanbhogue K, Tong A, Smereka P, Nickel D, Arberet S, Anthopolos R, et al. Accelerated single-shot T2-weighted fat-suppressed (FS) MRI of the liver with deep learning-based image reconstruction: qualitative and quantitative comparison of image quality with conventional T2-weighted FS sequence. Eur Radiol. 2021;31(11):8447-8457.

16 Min JH, Kim JM, Kim YK, Kang TW, Lee SJ, Choi GS, et al. Prospective Intraindividual Comparison of Magnetic Resonance Imaging With Gadoxetic Acid and Extracellular Contrast for Diagnosis of Hepatocellular Carcinomas Using the Liver Imaging Reporting and Data System. Hepatology. 2018;68(6):2254-2266.

17 Paisant A, Vilgrain V, Riou J, Oberti F, Sutter O, Laurent V, et al. Comparison of extracellular and hepatobiliary MR contrast agents for the diagnosis of small HCCs. J Hepatol. 2020;72(5):937-945.

18 Sutherland T, Watts J, Ryan M, Galvin A, Temple F, Vuong J, et al. Diffusion-weighted MRI for hepatocellular carcinoma screening in chronic liver disease: Direct comparison with ultrasound screening. J Med Imaging Radiat Oncol. 2017;61(1):34-39.

19 Coates GG, Borrello JA, McFarland EG, Mirowitz SA, Brown JJ. Hepatic T2-weighted MRI: a prospective comparison of sequences, including breath-hold, half-Fourier turbo spin echo (HASTE). J Magn Reson Imaging. 1998;8(3):642-9.

20 Schwartz LH, Seltzer SE, Tempany CM, Silverman SG, Piwnica-Worms DR, Adams DF, et al. Prospective comparison of T2-weighted fast spin-echo, with and without fat suppression, and conventional spin-echo pulse sequences in the upper abdomen. Radiology. 1993;189(2):411-6.

21 Kim DH, Yoon JH, Choi MH, Lee CH, Kang TW, Kim HA, et al. Comparison of non-contrast abbreviated MRI and ultrasound as surveillance modalities for HCC. J Hepatol. 2024;81(3):461-470.

22 Rhee H, Kim MJ, Kim DY, An C, Kang W, Han K, et al. Noncontrast Magnetic Resonance Imaging Vs Ultrasonography for Hepatocellular Carcinoma Surveillance: A Randomized, Single-Center Trial. Gastroenterology. 2025:S0016-5085(25)00049-6.

Contact

Joon-Il Choi, M.D., Ph.D.
Department of Radiology
Seoul St. Mary's Hospital
College of Medicine
The Catholic University of Korea
222 Banpo-daero, Seocho-gu
Seoul 06591
Korea
Tel: +82-2-2258-1431
dumkycji@gmail.com

GRASP MRI: A Decade of Innovation from Bench to Bedside

Li Feng, Kai Tobias Block, Hersh Chandarana, Daniel K Sodickson

[1]Bernard and Irene Schwartz Center for Biomedical Imaging, Department of Radiology,
 New York University Grossman School of Medicine, New York, NY, USA
[2]Center for Advanced Imaging Innovation and Research (CAI2R), Department of Radiology,
 New York University Grossman School of Medicine, New York, NY, USA

Introduction

Magnetic resonance imaging (MRI) is a powerful and versatile imaging modality that plays an essential role in clinical diagnosis. It offers excellent soft-tissue contrast, multiparametric information, and flexible imaging protocols, enabling comprehensive evaluation of a wide range of diseases without exposing patients to ionizing radiation. Nevertheless, the relatively slow imaging speed of MRI remains a significant challenge compared to other imaging modalities, making MRI exams susceptible to motion artifacts and limiting its suitability for dynamic imaging applications. Long acquisition times also necessitate breath-holding during imaging of moving organs such as the liver and the heart, which can be difficult or impractical for many patients. These challenges together have resulted in an MRI workflow that remains complex and cumbersome, even after decades of routine clinical use.

Over the past few decades, major advances in fast imaging techniques have been made to address these limitations, and these efforts have led to remarkable improvements in image quality, acquisition speed, and overall diagnostic performance. Among these developments, Golden-angle RAdial Sparse Parallel (GRASP) MRI stands out as a rapid, motion-robust dynamic imaging approach that enables free-breathing acquisition without the need for breath-holding [1]. GRASP combines compressed sensing and parallel imaging with golden-angle radial sampling into a unified framework. This combination not only enables faster imaging but also establishes a new paradigm of rapid, continuous MRI with improved motion robustness, greater workflow efficiency, and enhanced flexibility for clinical use [2].

Since its introduction in 2012, GRASP MRI has been widely adopted both in research and clinical settings and has been applied across a variety of organ systems [3], including the brain [4], neck [5], breast [6], liver [7], kidneys [8], bowel [9], prostate [10], and bladder [11]. Since 2017, GRASP MRI has also been commercially available on MRI systems from Siemens Healthineers with FDA clearance for routine diagnostic use. This progress reflects not only the technical strengths of GRASP MRI but also its adaptability to real-world clinical workflows, particularly for patients with limited breath-hold capacity [12, 13]. Over the past decade, the original GRASP technique has also evolved into multiple advanced versions, extending the capabilities toward motion-resolved reconstruction [14], time-resolved 4D MRI [15], real-time motion tracking [16], multiparametric mapping [17], and deep learning-based reconstruction [18]. These new developments have broadened the scope and clinical impact of GRASP MRI from traditional diagnostic imaging to emerging applications in image-guided treatment.

The goal of this article is to present an overview of GRASP MRI, covering its technical foundation, major advances, and clinical applications. We also share our decade-long journey at New York University (NYU) with GRASP MRI, including the history of its inception, development, and successful translation into routine clinical use. The review begins with a historical overview that outlines the motivation and early development of GRASP MRI. This is followed by a detailed summary of the technical framework, clinical implementation, and impact. The subsequent two sections then highlight different methodological extensions and variants of GRASP MRI and their applications. Finally, we conclude the review with a discussion of current limitations of this technique and its future directions. By the end of the review, we hope to provide readers with a clear understanding of how GRASP MRI works, what has been achieved, and where this technique is headed next.

GRASP MRI: A historical overview
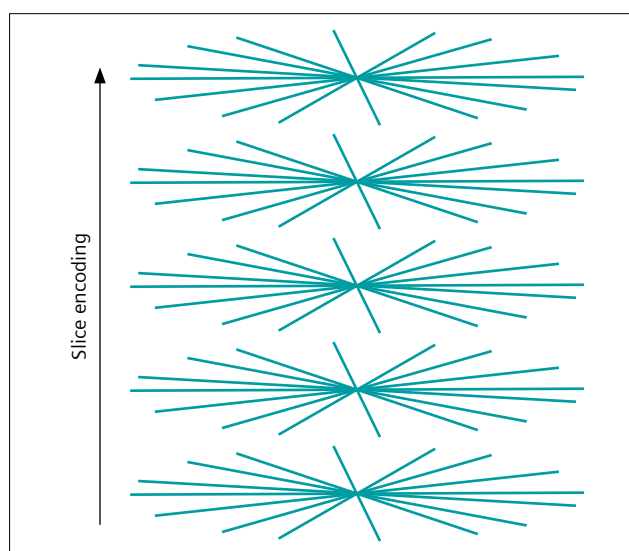
The origins of GRASP MRI go back to the year 2010, when researchers at NYU were pursuing two separate but complementary paths of investigation that ultimately converged into what became the GRASP technique. The first direction focused on combining compressed sensing with parallel imaging to achieve highly accelerated dynamic MRI using undersampled Cartesian *k*-space trajectories.

At that time, compressed sensing was still a relatively new concept but had quickly gained substantial attention in the MRI community [19–21]. The NYU team was among the early groups to demonstrate that integrating compressed sensing with parallel imaging in a sensitivity encoding (SENSE) reconstruction framework could outperform either approach alone for accelerated dynamic imaging [22]. This reconstruction strategy was successfully applied to several applications, including myocardial perfusion MRI [22, 23], real-time cardiac cine MRI [24–26], phase-contrast cine MRI [27], and quantitative MR parameter mapping [28]. These early efforts in combining compressed sensing and parallel imaging laid the groundwork for what later evolved

1 Stack-of-stars sampling trajectory. Radial sampling is used for in-plane encoding, while Cartesian encoding is applied along the slice direction. This hybrid strategy preserves the motion robustness of radial trajectories while maintaining key advantages of Cartesian-based slice encoding, such as robust fat suppression and compatibility with parallel imaging reconstruction.
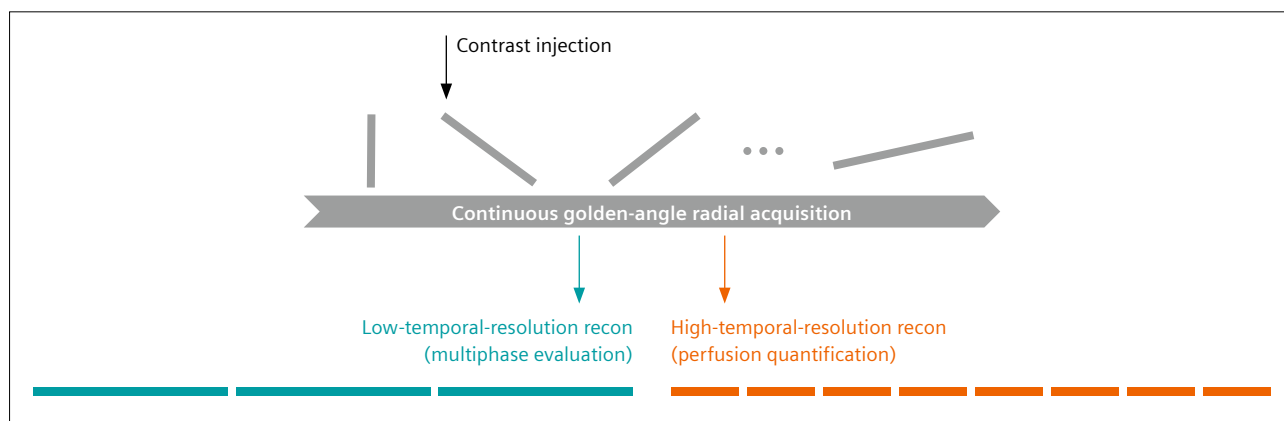
into GRASP MRI and has since become standard in modern iterative MRI reconstruction.

The second direction centered on evaluating a fat-saturated, T1-weighted stack-of-stars 3D gradient echo (GRE) sequence called Radial VIBE (now known as StarVIBE), which was developed by Siemens Healthineers in 2010 for motion-robust imaging [29]. While the concept of stack-of-stars for radial sampling had been introduced in the late 1990s [30], it was not broadly available on commercial MRI scanners with vendor support until the release of Radial VIBE. As an extension of the VIBE sequence family from Siemens Healthineers, Radial VIBE employs a hybrid radial-Cartesian trajectory, implementing radial sampling for in-plane acquisition and Cartesian sampling along the slice encoding direction [31], as shown in Figure 1. The sequence was released as a research (WIP) package on the Siemens Healthineers MRI platform, with thorough optimization of key technical elements such as gradient delay correction and fat suppression, both of which are essential for routine clinical use. In the same year, NYU became the first academic institution to adopt Radial VIBE for clinical patient studies, and preliminary results were published the following year [32]. The main motivation for using this sequence in the study was to leverage its motion robustness for free-breathing, contrast-enhanced multiphase liver MRI.

By 2011, NYU investigators, including both radiologists and MRI physicists, began working together to integrate compressed sensing and parallel imaging with stack-of-stars sampling. Around this time, Kai Tobias Block, the lead developer of the Radial VIBE sequence, joined NYU as a faculty member, bringing strong expertise in radial imaging. The arrival of Tobias catalyzed the convergence of the previously separate research directions into a unified framework. Initially, the integration did not include golden-angle sampling, even though this was a built-in feature of the Radial VIBE sequence. However, the team quickly

2 Flexibility of golden-angle radial sampling. The continuously rotating golden-angle acquisition enables retrospective reconstruction at different temporal resolutions for tailored clinical needs, such as low-temporal-resolution images for conventional multiphase assessment and high-temporal-resolution series for perfusion quantification.

recognized that golden-angle sampling offers great potential for continuous data acquisition in accelerated dynamic imaging, enabling flexible retrospective reconstruction that is particularly well suited for dynamic contrast-enhanced MRI (DCE-MRI) [33, 34]. This eliminated the need to predefine the desired temporal resolution or specify in advance how each contrast-enhanced phase should be acquired. Instead, all reconstruction parameters could be defined retrospectively after data acquisition. For example, in DCE-MRI, the same dataset can be reconstructed with a lower temporal resolution for qualitative clinical assessment or with a higher temporal resolution for quantitative perfusion analysis [6, 35], as illustrated in Figure 2. The name GRASP MRI was selected in 2012 during a brainstorming session. The team was enthusiastic about the technique's potential to transform clinical workflows by enabling free-breathing, high-resolution dynamic imaging that combines speed, flexibility, and motion robustness within a single framework.

Technical components of GRASP: A link to the past

GRASP MRI integrates multiple technical components spanning both data acquisition and image reconstruction. On the acquisition side, it employs a golden-angle radial sampling scheme, initially implemented using the stack-of-stars trajectory and later extended to other radial sampling schemes. On the reconstruction side, GRASP combines compressed sensing and parallel imaging with spatiotemporal regularization to recover dynamic images from undersampled data. In fact, these acquisition and reconstruction strategies were previously proposed independently in earlier works, but their synergy in GRASP ultimately enabled a practical, rapid, and motion-robust solution for dynamic MRI. This section revisits these components from a historical perspective and highlights how their integration provides key advantages in imaging speed, motion robustness, and reconstruction flexibility.

Golden-angle radial sampling
Radial sampling has a long and influential history and was, in fact, the first data acquisition strategy demonstrated by Paul Lauterbur in his pioneering MRI experiments [36]. With the advent of Fourier imaging, however, Cartesian sampling quickly became the standard because of its simplicity and better tolerance to system imperfections. Clinical adoption of radial sampling was initially very limited for several reasons [31]. First, since data are collected on a non-Cartesian grid, image reconstruction from radial data requires computationally intensive algorithms, such as the "gridding" method. Second, because each view in radial sampling is acquired at a different angle (referred to as a "spoke"), the method is sensitive to gradient delays and

off-resonance effects. Third, repeated sampling of the k-space center in radial MRI reduces the effectiveness of fat saturation and leads to undesired contrast mixing, which hinders its use in certain applications such as turbo spin-echo (TSE) imaging.

While radial sampling remained primarily a research tool for decades, important advances have expanded its capabilities and clinical translation. As early as the 1990s, studies demonstrated that radial trajectories offer greater motion robustness than Cartesian sampling [37, 38]. In the meantime, sliding-window or view-sharing reconstruction strategies were developed for continuous data acquisition in real-time dynamic imaging [39–41]. Radial sampling has since been applied not only to standard T1-weighted acquisition, but also to T2-weighted MRI [42], gradient- and spin-echo (GRASE) imaging [43], quantitative parameter mapping [44, 45], ultrashort echo time (UTE) imaging [46, 47], and other specialized applications [48–50]. The concept of stack-of-stars sampling, which is widely adopted today, was initially proposed for contrast-enhanced MR angiography by Peters et al. in the late 1990s to balance motion robustness and acquisition efficiency [30].

The concept of golden-angle radial sampling was first introduced at the 2005 ISMRM Annual Meeting, where it was demonstrated by Winkelmann et al. for single-shot T1 mapping with a Look-Locker sequence [51]. This work was soon expanded into a full publication in 2007, which described how golden-angle ordering optimizes k-space coverage for time-resolved MRI [33]. The key advantage of golden-angle sampling lies in its flexibility, which allows a single dataset to be retrospectively reconstructed at multiple temporal resolutions to address different clinical questions. At the 2006 ISMRM Annual Meeting, well before the development of GRASP, the feasibility of applying this idea to dynamic imaging had been demonstrated for DCE-MRI using view-sharing reconstruction [34]. In addition, the flexibility of golden-angle radial sampling allows retrospective sorting of acquired spokes according to underlying respiratory or cardiac states [52], an idea later implemented in the eXtra-Dimensional GRASP (XD-GRASP) technique [14].

Golden-angle radial sampling has since been refined in two main directions that continue to be widely explored. The first was the introduction of the tiny golden-angle scheme [53], designed to minimize eddy-current artifacts sometimes observed in 2D radial imaging due to the large gradient jumps between adjacent spokes [54]. The second extended golden-angle sampling to true 3D radial acquisitions based on the Koosh-ball pattern, from which two notable rotation strategies were proposed: one derived from 2D golden means [55] and the other from spiral phyllotaxis [56]. These 3D variants enable isotropic coverage and spatial resolution, which have proven particularly valuable in cardiovascular and lung MRI [57–60].

Among the various radial sampling schemes, stack-of-stars has been the most widely adopted on modern MRI scanners. There are several reasons for the widespread adoption [31]. First, the hybrid sampling scheme provides an effective balance between motion robustness and spatial encoding efficiency. Radial in-plane sampling offers improved tolerance to motion artifacts compared to Cartesian sampling, while Cartesian encoding along the slice direction simplifies reconstruction compared to full 3D radial imaging. This is particularly advantageous in applications like abdominal MRI, where isotropic spatial resolution and volumetric coverage are not always necessary. Second, Cartesian encoding along the slice direction supports effective fat suppression with conventional methods, which is essential for many routine clinical protocols. This implementation also enables reconstruction of different image slices in parallel after disentangling the slice dimension using a one-dimensional fast Fourier transform (FFT), thereby facilitating faster reconstruction. These practical benefits, along with technical improvements in hardware design, gradient-delay correction, and robust vendor support, have made radial sampling clinically viable. The Radial VIBE sequence from Siemens Healthineers represented the first implementation of stack-of-stars acquisition by a major vendor, and it has since been widely deployed in routine practice.

Radial MRI reconstruction and the synergy with compressed sensing

Before the advent of compressed sensing, reconstruction from radial MRI data primarily relied on relatively straightforward methods such as gridding and view-sharing. View-sharing, in particular, was widely explored for dynamic radial MRI reconstruction, as it allowed acquired spokes to be retrospectively grouped into overlapping temporal frames to achieve high frame rates, albeit with a potential risk of temporal blurring. While standard view-sharing reconstruction was conceptually simple and computationally efficient, it did not fully address the challenge of undersampling artifacts. Improved techniques, such as *k*-space weighted image contrast (KWIC) [61] and highly constrained projection reconstruction (HYPR) [50], were later developed to address these challenges, but various limitations complicated their practical use, and these methods did not achieve widespread clinical adoption.

In the early 2000s, several years after parallel imaging was proposed for accelerated MRI [62–64], different research groups began to adapt the concept for radial acquisition [65–67]. However, the use of parallel imaging, whether through image-domain methods such as SENSE or through *k*-space-domain methods such as Generalized Autocalibrating Partially Parallel Acquisitions (GRAPPA), has been primarily confined to Cartesian MRI, and clinical adoption of non-Cartesian parallel imaging has remained limited. This is largely due to the more complex reconstruction process and substantially higher computational demand for inverting large, ill-conditioned encoding matrices [68]. A practical exception has been the application along the slice-encoding direction in stack-of-stars imaging. As early as 2005, GRAPPA was successfully combined with stack-of-stars sampling to accelerate slice encoding [69]. Reconstruction was performed by first applying GRAPPA along the slice dimension, followed by gridding for in-plane reconstruction.

A major shift occurred in the mid-2000s with the introduction of compressed sensing to MRI [19]. At the 2005 ISMRM Annual Meeting, Lustig and colleagues presented L1-constrained reconstruction for accelerated imaging, initially using randomly perturbed spiral undersampling to maximize incoherence [70]. At the same meeting, Velikina demonstrated the use of spatial total variation (TV) constraints for reconstructing undersampled MRI data [71]. In 2006, Lustig et al. expanded these ideas to variable-density Cartesian undersampling [72] and introduced the k-t SPARSE framework for dynamic MRI [73]. In the same year, researchers from Siemens Corporate Research applied L1 constraints to undersampled radial MRI in phantom studies, marking the first demonstration of compressed sensing for radial trajectories [74].

In 2007, Lustig et al. published the landmark "Sparse MRI" paper [19], now a foundational work in the field. In the same year, two groups independently demonstrated the combination of compressed sensing with radial sampling. In the first work, Ye et al. used the Focal Underdetermined System Solver (FOCUSS) algorithm to iteratively solve for sparse solutions [75], while Block et al. applied a spatial TV constraint for image reconstruction from undersampled radial MRI data [21]. Researchers also recognized the potential combination of compressed sensing with parallel imaging to further improve reconstruction performance [22, 76, 77]. This synergy arises for two main reasons. First, the coil-sensitivity encoding in parallel imaging helps to suppress aliasing artifacts from undersampling, thereby facilitating more effective compressed sensing reconstruction. Second, the L1 constraint in compressed sensing helps to mitigate noise amplification in parallel imaging, particularly at high acceleration rates. The work presented by Block et al. in 2007 also proposed incorporating parallel imaging into radial compressed sensing reconstruction using the SENSE framework, which is generally considered the first demonstration of this combination [21]. In 2008, Liu et al. proposed Sparse-SENSE, which combined compressed sensing and SENSE for Cartesian sampling [77]. Soon after that, Otazo et al. extended this method to k-t SPARSE-SENSE for dynamic Cartesian MRI with a time-varying, variable-density random undersampling scheme [22].

In addition to specific sampling strategies, compressed sensing reconstruction requires a sparsifying transform. Early compressed sensing reconstruction for dynamic MRI focused on two options. The first approach, initially implemented in the k-t SPARSE framework, used a temporal FFT to exploit temporal sparsity [73]. The use of temporal FFT for dynamic MRI reconstruction had been introduced earlier by Tsao et al. in their k-t Broad-use Linear Acquisition Speed-up Technique (BLAST) method in 2003 [78], though not in the context of compressed sensing. The second approach, demonstrated by Adluru et al. for both Cartesian and radial MRI, enforced a temporal TV constraint for dynamic compressed sensing MRI reconstruction [79, 80]. While both approaches proved to be effective, a study in 2013 by Feng et al. compared the two temporal sparsity constraints and found that temporal TV outperformed temporal FFT for dynamic compressed sensing MRI reconstruction [24]. Since then, temporal TV has become one of the commonly used sparsifying transforms in iterative dynamic MRI reconstruction, including GRASP MRI.

At the 2012 ISMRM Annual Meeting, the NYU team presented GRASP MRI that combined compressed sensing and parallel imaging with stack-of-stars golden-angle radial sampling, and demonstrated its performance in various motion-robust DCE-MRI applications [81]. In many respects, GRASP MRI represented a natural evolution of earlier efforts, particularly as a synergy between the static radial MRI reconstruction framework of Block et al. and the k-t SPARSE-SENSE approach [1]. More importantly, GRASP MRI demonstrated for the first time that rapid, continuous golden-angle radial acquisition could enable free-breathing body MRI with retrospectively selectable temporal resolution. This innovation overcame major limitations of earlier techniques and established a new paradigm for dynamic imaging with great flexibility.

Clinical translation and impact

The successful translation of GRASP into clinical practice has been a major factor contributing to its broad impact. This achievement has distinguished GRASP MRI from many other dynamic MRI reconstruction techniques developed over the past decades, as bringing new reconstruction methods into routine use often falters due to obstacles at multiple levels. This section summarizes the collaborative efforts between NYU and the teams at Siemens Healthineers that made this transition possible.

Workflow integration in collaboration with Siemens Healthineers
The first GRASP reconstruction pipeline was implemented in MATLAB (MathWorks Inc., Natick, MA, USA) using spatiotemporal TV constraints with separate parameters controlling the balance between spatial and temporal regularizations. At that time, however, several barriers hindered the clinical translation of GRASP MRI.

First, iterative reconstruction is typically computationally demanding. For example, the initial MATLAB implementation of GRASP required ~15–30 minutes to reconstruct a single slice. Second, even if image reconstruction could be accomplished in a reasonable timeframe, integrating it into the MRI scanner workflow and automatically transferring the resulting images to the PACS system posed a significant challenge. Overcoming these challenges required a sustained team effort, driven not only by technical innovation but also by strong support from the NYU leadership, collaborating radiologists, and the IT department, whose contributions were essential at every stage. Together, these efforts established the groundwork for subsequent improvements and optimizations in partnership with Siemens Healthineers.

To address the computational bottleneck, Robert Grimm, then a Ph.D. student jointly affiliated with the Friedrich-Alexander University of Erlangen-Nuremberg and Siemens, visited NYU for six months in 2012. He re-implemented the entire GRASP reconstruction pipeline in C++, which substantially accelerated image reconstruction. With parallel computing, reconstruction time for an entire 3D volume was reduced to under 30 minutes, compared to 15–30 minutes per slice in MATLAB. This marked the first major step toward practical clinical translation.

The challenge of clinical translation was addressed in 2013 by Kai Tobias Block, who developed the Yarra framework [82], a software tool that has been used at NYU since then. Yarra connects the MRI scanner to an external reconstruction server and the PACS system. After a scan is completed, the technologist simply enters the accession number into Yarra on the scanner console. The MRI raw data are then automatically transferred to the external server, where the C++ GRASP pipeline reconstructs 4D dynamic images. Once reconstruction is done, Yarra automatically sends the images into PACS. This workflow is fully automated and requires only a single click on the scanner. Yarra also supports the scheduled transfer of raw data to outside servers (e.g., overnight when the scanner is idle). Over the past decade, this framework has proven to be a powerful solution for translating iterative reconstruction into routine clinical practice.

Soon after GRASP was implemented and evaluated clinically at NYU, Siemens Healthineers began integrating the technique directly into its MRI systems. After multiple years of optimization, GRASP MRI was formally introduced by Siemens Healthineers as a product with FDA clearance at the 2017 European Congress of Radiology (ECR) under the name GRASP-VIBE. Since then, GRASP MRI has been available worldwide on the MRI platform from Siemens Healthineers and has been adopted by numerous clinical sites.

Limitations of standard GRASP MRI

Despite its simplicity and robustness, the standard GRASP framework has several limitations that continue to affect its performance in clinical practice.

One issue is latency. Although Yarra has enabled the routine use of GRASP MRI, a 10-to-60-minute delay remains between the completion of a scan and the availability of reconstructed images for interpretation. While this latency does not usually affect non-emergent patient care, it reduces workflow efficiency. To assist technologists, time-averaged images are generated on the scanner immediately after acquisition to verify scan quality and contrast injection. However, while these images are useful for quick checks, they cannot replace the fully reconstructed dynamic image series required for diagnosis. Meanwhile, although this was further optimized in the GRASP-VIBE implementation from Siemens Healthineers with improved algorithms and integration, the slow reconstruction speed inherent to iterative methods remains a major bottleneck.

Another limitation involves imperfect bolus timing. In conventional contrast-enhanced multiphase MRI, a bolus timing step is typically required to ensure optimal capture of the arterial phase. GRASP MRI omits this step for simplicity, which can lead to suboptimal arterial phase timing. The flexibility of GRASP MRI to reconstruct images with shifted data sorting can mitigate this limitation, but this requires additional processing and cannot fully substitute for optimized prospective bolus timing.

A third challenge is the presence of residual streaking artifacts. In radial MRI, gradient imperfections and off-resonance effects often generate bright peripheral hotspots, which in turn give rise to strong streaking artifacts that propagate throughout the image [83]. These artifacts are difficult to suppress completely with standard iterative reconstruction, and they may impact relevant anatomy and potentially reduce diagnostic confidence in certain scenarios.

Motion blurring is another limitation, especially in moving organs such as the liver. Although radial sampling is inherently more robust to motion than Cartesian sampling, it is not immune to motion effects [84]. In radial MRI, motion causes image blurring rather than ghosting, which impairs the visualization of fine anatomical structures and dynamic contrast patterns. Such blurring can reduce the accuracy of detecting small lesions or subtle enhancement differences. This has, to some extent, limited the use of standard GRASP MRI in the upper abdomen for imaging the liver, pancreas, and surrounding structures.

Many of these challenges are not unique to GRASP MRI but are also encountered in other radial MRI techniques. Over the past decade, various solutions have been proposed to address these limitations, including several contributions from the NYU team, which will be discussed in detail in the next section. Briefly, long reconstruction times can be accelerated with deep learning-based methods (see DeepGRASP). Suboptimal bolus timing can be alleviated with contrast-guided data sorting (see RACER-GRASP) or by leveraging high-temporal-resolution reconstruction (see GRASP-Pro). Residual streaking artifacts can be reduced using an approach called "unstreaking", while motion-related blurring can be mitigated through motion-resolved reconstruction (see XD-GRASP), adaptive data weighting (see RACER-GRASP), or sub-second temporal resolution reconstruction (see GRASP-Pro). Collectively, these solutions are expected to further improve the performance and clinical reliability of GRASP MRI.

Variants of GRASP: Advances and extensions

Since its original development, GRASP MRI has inspired a wide range of methodological extensions aimed at addressing various limitations and expanding its clinical and research applications. These variants build upon the GRASP framework through innovations in data acquisition, reconstruction strategies, and computational modeling, leading to improved spatiotemporal resolution, motion robustness, and flexibility across different organ systems and imaging needs. This section provides a brief overview of major GRASP variants developed by the NYU team over the past decade and highlights their potential applications.

XD-GRASP

Although radial sampling offers improved robustness to motion, motion-induced blurring can still degrade image quality, particularly in patients with irregular or deep breathing. The eXtra-Dimensional GRASP (XD-GRASP) technique was developed to address this limitation by sorting continuously acquired radial spokes according to underlying motion information, which generates an additional motion-resolved dimension [14]. The use of golden-angle radial sampling provides the flexibility to achieve adequate k-space coverage after motion-based data sorting, while compressed sensing reconstruction with a temporal sparsity constraint is applied to suppress undersampling artifacts caused by data binning. Compared with conventional motion correction approaches such as image registration, XD-GRASP provides more robust and effective motion management [85] and also yields additional motion information that may be of clinical value [86–89]. This approach has demonstrated superior performance over standard GRASP in free-breathing liver DCE-MRI [90], cardiac imaging [14], and other motion-sensitive applications [85, 86, 89].

GROG-GRASP

In standard GRASP reconstruction, gridding is performed within each iterative step, which prolongs reconstruction time compared with iterative Cartesian reconstruction

that relies only on standard FFT. GROG-GRASP incorporates the GRAPPA Operator Gridding (GROG) technique, originally proposed by Seiberlich et al. as an alternative to conventional gridding [91, 92], to pre-shift radial data onto a Cartesian grid using coil sensitivity information [93]. This preprocessing step applies parallel imaging to estimate *k*-space data on a Cartesian grid from nearby radial samples, enabling the subsequent iterative reconstruction to be performed entirely in Cartesian space. As a result, computationally expensive gridding operations are not needed, and the reconstruction efficiency can be improved.

RACER-GRASP

Respiratory-weighted, Aortic Contrast Enhancement-guided and coil-unstReaking GRASP (RACER-GRASP) addresses several limitations of GRASP collectively [94].

First, it introduces a contrast-guided data-sorting strategy to optimize arterial phase reconstruction. Second, it employs motion-weighted reconstruction (also known as soft gating), which assigns different weights to radial *k*-space data based on their underlying respiratory states, thereby reducing contributions from unfavorable motion phases. Unlike XD-GRASP, which explicitly bins data into multiple motion phases, RACER-GRASP does not require full motion-resolved reconstruction and is advantageous in terms of efficiency. Third, RACER-GRASP incorporates an "unstreaking" algorithm to suppress residual streaking artifacts [95]. By applying coil-wise soft weighting before iterative reconstruction, this method attenuates the contribution of coil elements prone to strong streaks. Together, these strategies improve arterial phase delineation, reduce motion blurring, and enable more effective suppression of streaking artifacts.

3D Koosh-Ball GRASP

While GRASP is commonly implemented with stack-of-stars sampling, it is not limited to this approach. True 3D radial sampling, such as the Koosh-ball trajectory, provides isotropic volumetric coverage and spatial resolution, which are advantageous for applications like cardiovascular imaging. Building on this concept, the NYU team and collaborators from the University of Lausanne jointly developed a free-running 5D whole-heart MRI framework, which combines golden-angle 3D radial Koosh-ball sampling for continuous data acquisition with XD-GRASP for cardiac- and respiratory-resolved reconstruction [96]. This framework has since been extended to other applications, such as flow MRI (5D flow) [97] and 4D lung MRI [89], enabling motion-resolved volumetric imaging with promising clinical value.

GRASP-Pro

Standard GRASP reconstruction relies on spatiotemporal TV constraints for dynamic image reconstruction. GRASP-Pro improves this by incorporating a low-rank subspace model that more effectively captures temporal correlations across frames [98]. In this framework, dynamic images are represented within a low-rank subspace by projection onto a pre-estimated temporal basis. This reduces the number of unknowns for the reconstruction, thereby improving both image quality and computational efficiency. This strategy also supports dynamic reconstruction at ultrahigh temporal resolution [15]. For example, GRASP-Pro has been applied to 4D liver DCE-MRI with sub-second temporal resolution, which inherently resolves respiratory motion and therefore eliminates the need for additional motion compensation [99], as shown in Figure 3. It also enables simultaneous reconstruction of multiple arterial phases to fully remove the need for conventional bolus timing or contrast-guided
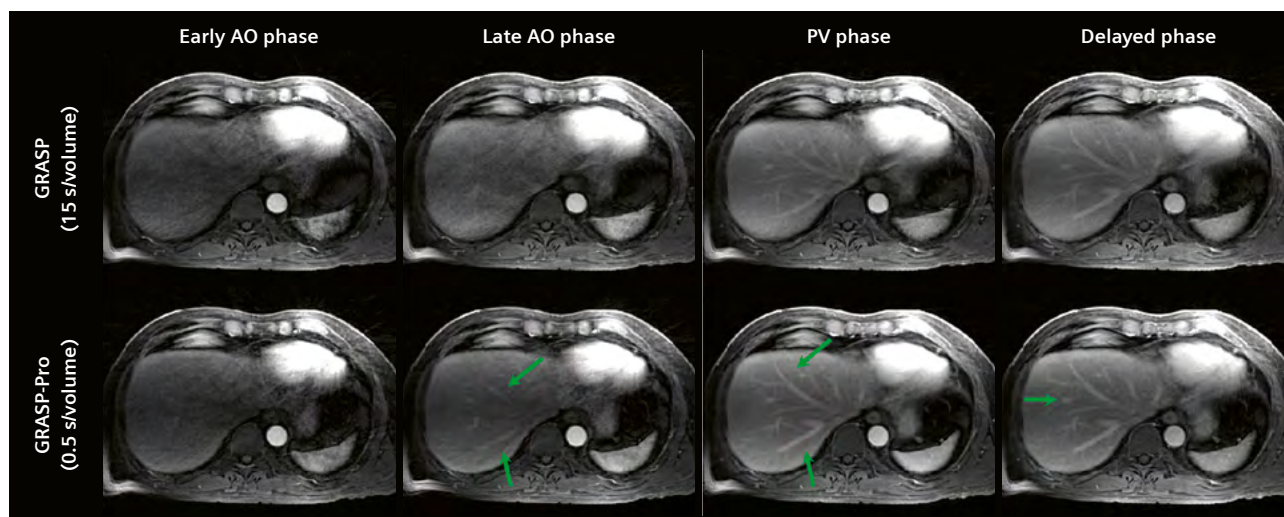
3 Comparison between standard GRASP MRI and GRASP-Pro with sub-second temporal resolution. Acquiring a full 3D volume within one second intrinsically resolves respiratory motion without the need for additional motion correction.
Figure reproduced from NMR in Biomedicine (2024;37(12):e5262) with permission from the journal.

data sorting. In addition to liver imaging, GRASP-Pro has been applied to DCE-MRI of the breast with sub-second temporal resolution to enable more accurate perfusion quantification [100].

MP-GRASP

Standard GRASP MRI typically uses a steady-state acquisition without magnetization preparation. Magnetization-Prepared GRASP (MP-GRASP) incorporates magnetization-preparation pulses to provide additional contrast and enable improved contrast or quantitative parameter mapping [17]. This approach facilitates several advanced applications, including free-breathing T1 mapping with inversion-recovery preparation [17, 101, 102], non-contrast dynamic 4D MRA using arterial spin labeling (ASL) [103], and free-breathing chemical exchange saturation transfer (CEST) MRI [104].
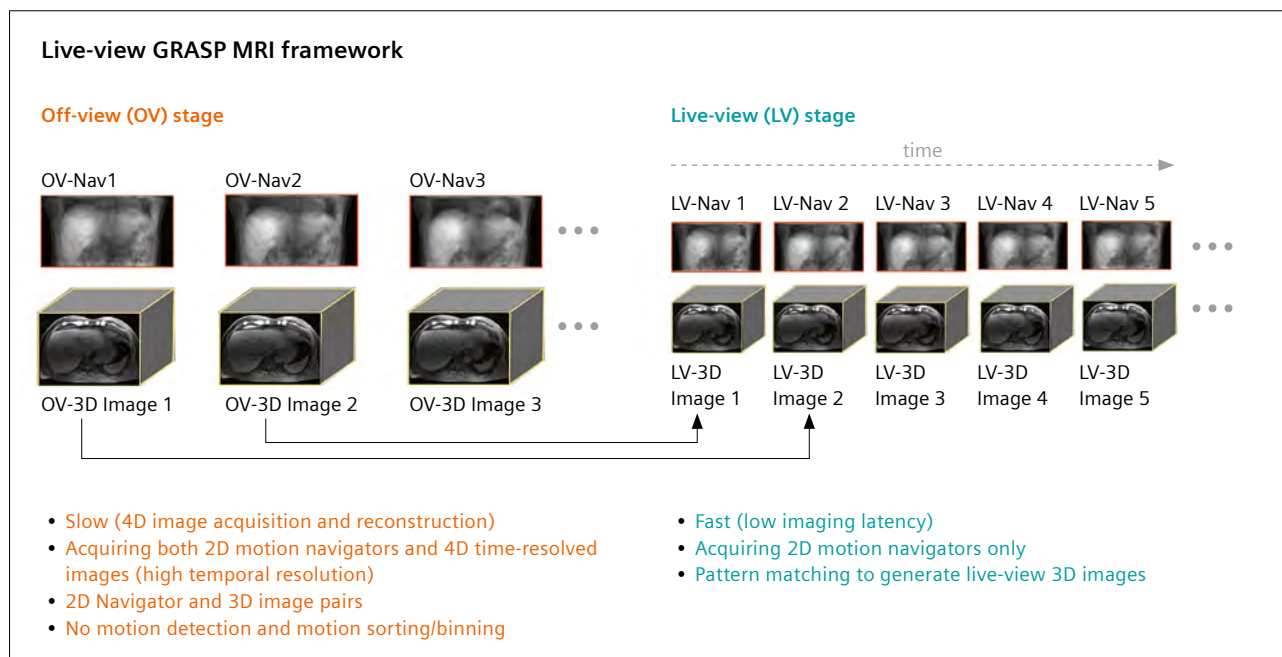
Multi-Echo GRASP MRI

In parallel with the development of different GRASP variants, stack-of-stars acquisitions were also adapted for multi-echo imaging by acquiring multiple echoes within each TR by the different research teams [105, 106]. This enables free-breathing fat/water separation and R2* estimation, which is particularly valuable for liver MRI exams, where separating fat and water signal is essential for assessing steatosis and other metabolic conditions. Beyond liver imaging, multi-echo stack-of-stars has

also shown potential clinical value in breast MRI, where improved fat suppression enhances diagnostic performance [107]. This imaging scheme was later combined with GRASP for DCE-MRI to enable simultaneous dynamic imaging and fat quantification at each contrast phase [108]. More recently, multi-echo acquisition has also been incorporated into MP-GRASP for water-specific parameter quantification [17, 109], a direction that is gaining increasing attention in liver imaging, where fat is known to be a confounding factor for quantitative measurements.

Live-View GRASP

Live-View GRASP is an extension of GRASP MRI for real-time image-guided interventions, such as MRI-guided radiation therapy [16]. A major challenge in this application is the inherent latency of 3D MRI, arising from time-consuming data acquisition and image reconstruction, which often exceeds the clinical requirements for real-time guidance. To address this challenge, several novel techniques, including Live-View GRASP, have been proposed [16, 110–112]. In Live-View GRASP, the imaging workflow is divided into two stages: an offline or off-view stage, and a live-view stage, as shown in Figure 4. During the offline stage, free-breathing time-resolved 4D (3D + motion) images are acquired and reconstructed to form a motion-resolved image database, where each 3D image in the database is linked to a low-resolution 2D navigator that represents a specific respiratory state. During the live-view stage, only

Live-view GRASP MRI framework

Off-view (OV) stage

OV-Nav1   OV-Nav2   OV-Nav3

OV-3D Image 1   OV-3D Image 2   OV-3D Image 3

Live-view (LV) stage

time

LV-Nav 1   LV-Nav 2   LV-Nav 3   LV-Nav 4   LV-Nav 5

LV-3D Image 1   LV-3D Image 2   LV-3D Image 3   LV-3D Image 4   LV-3D Image 5

- Slow (4D image acquisition and reconstruction)
- Acquiring both 2D motion navigators and 4D time-resolved images (high temporal resolution)
- 2D Navigator and 3D image pairs
- No motion detection and motion sorting/binning

- Fast (low imaging latency)
- Acquiring 2D motion navigators only
- Pattern matching to generate live-view 3D images

4   Live-View GRASP MRI framework. The workflow consists of two stages: an offline (or off-view) learning stage and a live-view stage. In the offline stage, free-breathing, time-resolved 4D (3D + motion) images are acquired and reconstructed to build a motion-resolved database, where each 3D image is linked to a corresponding low-resolution 2D navigator. During the live-view stage, only 2D navigators are acquired in real time and matched to the database to retrieve the best-corresponding 3D image with minimal latency.
Figure reproduced from Magnetic Resonance in Medicine (2023;90(3):1053–1068) with permission from the journal.

2D navigators are acquired in real time and can be rapidly matched to the offline database for retrieving the best-matching 3D image. This imaging strategy shifts the computational burden to the offline stage, which can be performed prior to treatment, while enabling fast and efficient live-view imaging during therapy.

DeepGrasp

DeepGrasp is a recent innovation that integrates self-supervised deep learning into the GRASP framework [18, 113]. Building on the low-rank subspace model of GRASP-Pro, DeepGrasp incorporates subspace modeling into a neural network-based reconstruction pipeline. This accelerates image reconstruction substantially while maintaining image quality, even when reconstructing large numbers of dynamic frames. Importantly, self-supervised learning in DeepGrasp avoids the need for fully sampled training data, which are not available from in vivo GRASP scans. More recently, an all-in-one DeepGrasp model has been developed to generalize this technique across different organs, spatial resolutions, and temporal frames within a single trained model, with preliminary results shown in Figure 5. Such a unified approach holds the potential to streamline clinical deployment by reducing the need for

retraining, while preserving the flexibility and robustness across different dynamic imaging applications.

Discussion and future directions

GRASP has demonstrated remarkable versatility and impact across a wide range of imaging applications. Its flexibility in data acquisition, robustness to motion, and compatibility with advanced reconstruction methods have made it a powerful framework in both research and clinical settings. This section briefly outlines the current limitations of the GRASP framework and highlights emerging directions being actively explored by the NYU team to further expand its utility.

GRASP MRI with different sampling trajectories

While radial sampling offers several key advantages, including intrinsic motion robustness, flexible data sorting, and the feasibility of self-navigation, it is not a one-size-fits-all trajectory for all clinical applications. For example, radial sampling is less suited than other trajectories for T2-weighted imaging and diffusion MRI. Moreover, with the renewed interest in low-field MRI, where improved B0 homogeneity mitigates limitations that typically
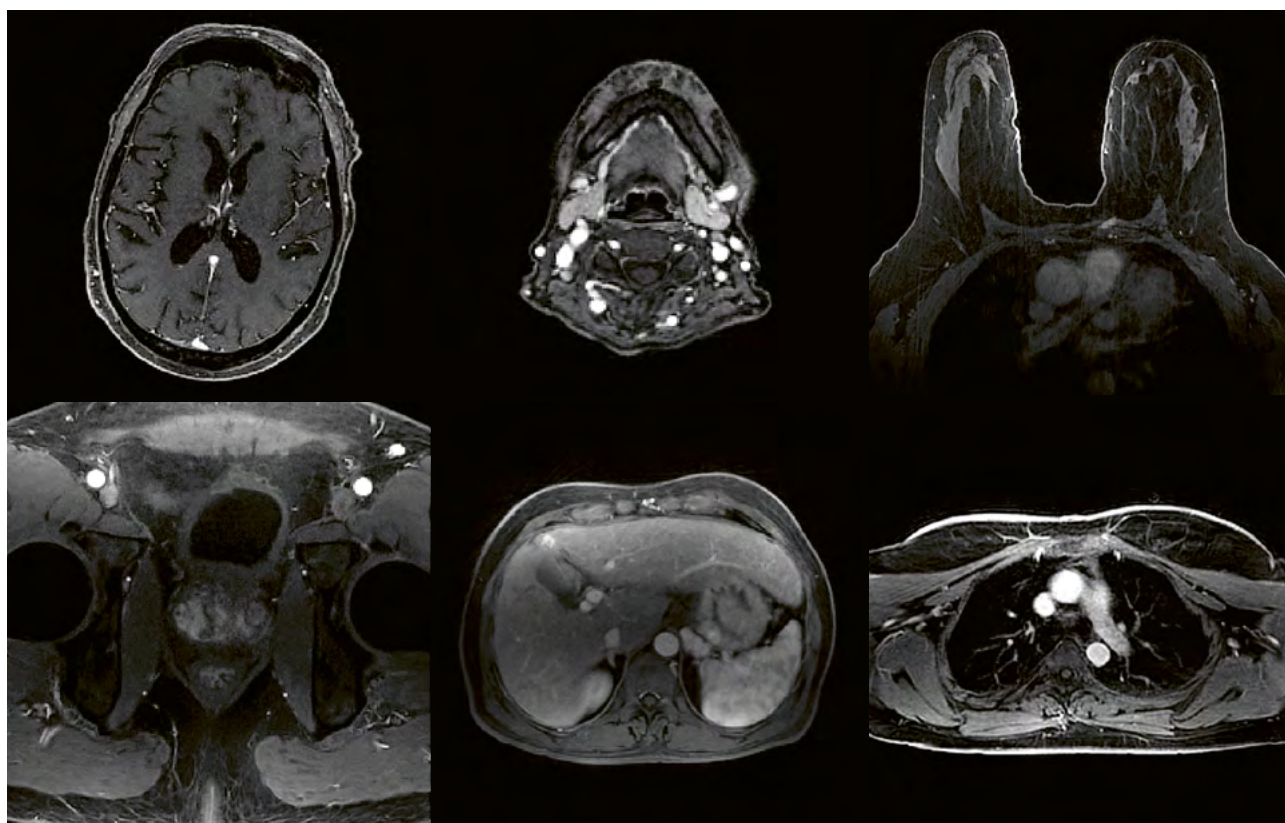
5 Preliminary results from a unified DeepGRASP reconstruction model. An all-in-one DeepGrasp network can be trained once and then applied to perform GRASP reconstruction across different organs, spatial resolutions, and temporal frames, enabling a single model to handle a wide range of reconstruction tasks without task-specific retraining.

hinder the broad use of non-Cartesian sampling with long readouts at high field (e.g., spiral sampling), it has become evident that radial trajectories may not always be the optimal choice at reduced field strengths [114].

To address these limitations, extending GRASP MRI beyond radial sampling is an important future direction. The NYU team recently began exploring spiral sampling, whose high signal-to-noise ratio and efficient coverage may be advantageous for low-field applications, as well as PROPELLER sampling for T2-weighted and diffusion-weighted imaging. These multifaceted sampling schemes aim to retain the strengths of GRASP while improving image quality and efficiency in applications where radial sampling may fall short. Preliminary results in these directions have been encouraging, as reported in several conference abstracts [115–119].

Further extension of deep learning-based GRASP

Building upon the initial development of DeepGrasp, future directions in the era of artificial intelligence (AI) are expected to focus increasingly on deep learning-based frameworks that move beyond pure reconstruction. One promising direction includes joint MRI reconstruction and denoising, in which neural networks simultaneously recover undersampled data and suppress noise. This could be particularly valuable for low-field MRI and applications requiring high spatial resolution. Another emerging direction is joint reconstruction and quantification with MP-GRASP, where MRI parameter estimation (e.g., T1, T2, and perfusion) is directly integrated into the reconstruction process rather than performed as a separate step, as demonstrated in early studies [120–123]. Such approaches hold the potential to further shorten scan times, reduce variability across patients and imaging sites, and accelerate the standardization of quantitative MRI for broader clinical implementation.

Integration with MRI-guided therapy

Another exciting direction for GRASP MRI lies in its use for image-guided therapy, particularly MRI-guided radiation therapy. In fact, the XD-GRASP technique has already been well recognized in the radiation therapy field [124] and adopted in several abdominal cancer treatment protocols on MRI-linac systems, where it provides a robust capability for respiratory-resolved 4D imaging to support treatment planning and motion management [125]. More recently, novel extensions such as Live-View GRASP and similar techniques [110–112] have been proposed to overcome the latency bottlenecks of conventional 3D MRI by separating the imaging workflow into an offline learning stage and a live-view stage. This enables near-instantaneous 3D image updates during treatment to facilitate high-fidelity motion tracking and adaptive response during radiation delivery.

These innovations expand the role of MRI beyond traditional diagnostics and toward image-guided therapy. Future developments are expected to focus on deeper integration of GRASP MRI with treatment planning systems, real-time motion tracking, and adaptive dose delivery. However, successful clinical translation of these methods will depend on close collaboration between academic researchers and industry partners to ensure robust implementation and rigorous validation.

Conclusion

This article summarized a decade of work from the NYU team in developing, translating, disseminating, and extending the GRASP MRI technique. It also described the historical context in which GRASP was conceived, building upon prior innovations in radial MRI, compressed sensing reconstruction, and dynamic imaging. From the initial implementation as a motion-robust technique for free-breathing DCE-MRI, GRASP has evolved into a versatile framework that supports a wide range of acquisition and reconstruction strategies, as summarized in this article. Looking ahead, the future of GRASP lies in further developing its capabilities across diverse sampling trajectories and field strengths, as well as in further integration with therapeutic applications, real-time imaging strategies, and intelligent reconstruction methods. With continued innovation and clinical translation, GRASP MRI may be expected to play an important role in further improving patient care in times to come.

Financial disclosure

The authors of this article have patents on the GRASP and XD-GRASP techniques.

References

1   Feng L, Grimm R, Block KT, Chandarana H, Kim S, Xu J, et al. Golden-angle radial sparse parallel MRI: combination of compressed sensing, parallel imaging, and golden-angle radial sampling for fast and flexible dynamic volumetric MRI.
Magn Reson Med. 2014;72(3):707–17.
2   Sodickson DK, Feng L, Knoll F, Cloos M, Ben-Eliezer N, Axel L, et al. The rapid imaging renaissance: sparser samples, denser dimensions, and glimmerings of a grand unified tomography. In: Gimi B, Molthen RC, editors. Medical Imaging 2015: Biomedical Applications in Molecular, Structural, and Functional Imaging. Proceedings Volume 9417; SPIE Medical Imaging; 2015 Feb 21–26; Orlando, FL, USA; p. 94170G.
3   Feng L, Benkert T, Block KT, Sodickson DK, Otazo R, Chandarana H. Compressed sensing for body MRI.
J Magn Reson Imaging. 2017;45(4):966–987.
4   Demerath T, Blackham K, Anastasopoulos C, Block KT, Stieltjes B, Schubert T. Golden-Angle Radial Sparse Parallel (GRASP) MRI differentiates head & neck paragangliomas from schwannomas.
Magn Reson Imaging. 2020;70:73–80.

5 Seo M, Yoon J, Choi Y, Nickel D, Jang J, Shin NY, et al. Image Quality of High-Resolution 3-Dimensional Neck MRI Using CAIPIRINHA-VIBE and GRASP-VIBE: An Intraindividual Comparative Study. Invest Radiol. 2022;57(11):711–719.

6 Kim SG, Feng L, Grimm R, Freed M, Block KT, Sodickson DK, et al. Influence of temporal regularization and radial undersampling factor on compressed sensing reconstruction in dynamic contrast enhanced MRI of the breast. J Magn Reson Imaging. 2016;43(1):261–9.

7 Chandarana H, Feng L, Block TK, Rosenkrantz AB, Lim RP, Babb JS, et al. Free-breathing contrast-enhanced multiphase MRI of the liver using a combination of compressed sensing, parallel imaging, and golden-angle radial sampling. Invest Radiol. 2013;48(1):10–6.

8 Huber S, Balcacer De la Cruz P, Mahan M, Spektor M, Lo R, Block KT, et al. Comparison of image quality of subtracted and nonsubtracted breath hold VIBE and free breathing GRASP in the evaluation of renal masses. Clin Imaging. 2021;74:15–18.

9 Ream JM, Doshi A, Lala S V., Kim S, Rusinek H, Chandarana H. High Spatiotemporal Resolution Dynamic Contrast-Enhanced MR Enterography in Crohn Disease Terminal Ileitis Using Continuous Golden-Angle Radial Sampling, Compressed Sensing, and Parallel Imaging. AJR Am J Roentgenol. 2015;204(6):W663–9.

10 Rosenkrantz AB, Geppert C, Grimm R, Block TK, Glielmi C, Feng L, et al. Dynamic contrast-enhanced MRI of the prostate with high spatiotemporal resolution using compressed sensing, parallel imaging, and continuous golden-angle radial sampling: preliminary experience. J Magn Reson Imaging. 2015;41(5):1365–73.

11 Parikh N, Ream JM, Zhang HC, Block KT, Chandarana H, Rosenkrantz AB. Performance of simultaneous high temporal resolution quantitative perfusion imaging of bladder tumors and conventional multi-phase urography using a novel free-breathing continuously acquired radial compressed-sensing MRI sequence. Magn Reson Imaging. 2016;34(5):694–8.

12 Yoon JH, Nickel MD, Peeters JM, Lee JM. Rapid Imaging: Recent Advances in Abdominal MRI for Reducing Acquisition Time and Its Clinical Applications. Korean J Radiol. 2019;20(12):1597–1615.

13 Feng L, Chandarana H. Accelerated Abdominal MRI: A Review of Current Methods and Applications. J Magn Reson Imaging. 2025;62(3):654–672.

14 Feng L, Axel L, Chandarana H, Block KT, Sodickson DK, Otazo R. XD-GRASP: Golden-angle radial MRI with reconstruction of extra motion-state dimensions using compressed sensing. Magn Reson Med. 2016;75(2):775–88.

15 Feng L. 4D Golden-Angle Radial MRI at Subsecond Temporal Resolution. NMR Biomed. 2022;e4844.

16 Feng L. Live-view 4D GRASP MRI: A framework for robust real-time respiratory motion tracking with a sub-second imaging latency. Magn Reson Med. 2023;90(3):1053–1068.

17 Feng L, Liu F, Soultanidis G, Liu C, Benkert T, Block KT, et al. Magnetization-prepared GRASP MRI for rapid 3D T1 mapping and fat/water-separated T1 mapping. Magn Reson Med. 2021;86(1):97–114.

18 Pei H, Chandarana H, Sodickson D, Feng L. DeepGrasp4D: A General Framework for Highly-Accelerated Real-Time 4D Golden-Angle Radial MRI Using Deep Learning. In: Proc Intl Soc Mag Reson Med. 2024;32:40.

19 Lustig M, Donoho D, Pauly JM. Sparse MRI: The application of compressed sensing for rapid MR imaging. Magn Reson Med. 2007;58(6):1182–95.

20 Lustig M, Donoho DL, Santos JM, Pauly JM. Compressed sensing MRI: A look at how CS can improve on current imaging techniques. IEEE Signal Process Mag. 2008;25(2):72–82.

21 Block KT, Uecker M, Frahm J. Undersampled radial MRI with multiple coils. Iterative image reconstruction using a total variation constraint. Magn Reson Med. 2007;57(6):1086–98.

22 Otazo R, Kim D, Axel L, Sodickson DK. Combination of compressed sensing and parallel imaging for highly accelerated first-pass cardiac perfusion MRI. Magn Reson Med. 2010 Sep;64(3):767–76.

23 Feng L, Xu J, Axel L, Sodickson DK, Otazo R. Combination of Compressed Sensing, Parallel Imaging & Partial Fourier for Highly-Accelerated 3D First-Pass Cardiac Perfusion MRI. In: Proc Intl Soc Mag Reson Med. 2011;19:4368.

24 Feng L, Srichai MB, Lim RP, Harrison A, King W, Adluru G, et al. Highly accelerated real-time cardiac cine MRI using k-t SPARSE-SENSE. Magn Reson Med. 2013;70(1):64–74.

25 Liu J, Feng L, Shen HW, Zhu C, Wang Y, Mukai K, et al. Highly-accelerated self-gated free-breathing 3D cardiac cine MRI: validation in assessment of left ventricular function. MAGMA. 2017;30(4):337–346.

26 Wang X, Uecker M, Feng L. Fast Real-Time Cardiac MRI: a Review of Current Techniques and Future Directions. Investig Magn Reson Imaging. 2021;25(4):252–256.

27 Kim D, Dyvorne HA, Otazo R, Feng L, Sodickson DK, Lee VS. Accelerated phase-contrast cine MRI using k-t SPARSE-SENSE. Magn Reson Med. 2012;67(4):1054–64.

28 Feng L, Otazo R, Jung H, Jensen JH, Ye JC, Sodickson DK, et al. Accelerated cardiac T2 mapping using breath-hold multiecho fast spin-echo pulse sequence with k-t FOCUSS. Magn Reson Med. 2011;65(6):1661–9.

29 Block K, Chandarana H, Fatterpekar G, Hagiwara M, Milla S, Mulholland T, et al. Improving the Robustness of Clinical T1-Weighted MRI Using Radial VIBE. MAGNETOM Flash. 2013;5:6–11.

30 Peters DC, Korosec FR, Grist TM, Block WF, Holden JE, Vigen KK, et al. Undersampled Projection Reconstruction Applied to MR Angiography. Magn Reson Med. 2000;43:91–101.

31 Feng L. Golden-Angle Radial MRI: Basics, Advances, and Applications. J Magn Reson Imaging. 2022;56(1):45–62.

32 Chandarana H, Block TK, Rosenkrantz AB, Lim RP, Kim D, Mossa DJ, et al. Free-breathing radial 3D fat-suppressed T1-weighted gradient echo sequence: A viable alternative for contrast-enhanced liver imaging in patients unable to suspend respiration. Invest Radiol. 2011;46(10):648–53.

33 Winkelmann S, Schaeffter T, Koehler T, Eggers H, Doessel O. An optimal radial profile order based on the golden ratio for time-resolved MRI. IEEE Trans Med Imaging. 2007;26(1):68–76.

34 Song H, Lin W, Dougherty L, Schnall M. A 3D golden-angle projection reconstruction technique for dynamic contrast-enhanced MRI. In: Proc Intl Soc Mag Reson Med. 2006;14:3364.

35 Chandarana H, Block TK, Ream J, Mikheev A, Sigal SH, Otazo R, et al. Estimating liver perfusion from free-breathing continuously acquired dynamic gadolinium-ethoxybenzyl-diethylenetriamine pentaacetic acid-enhanced acquisition with compressed sensing reconstruction. Invest Radiol. 2015;50(2):88–94.

36 Lauterbur PC. Image Formation by Induced Local Interactions: Examples Employing Nuclear Magnetic Resonance. Nature. 1973;242:190–1.

37 Glover GH, Pauly JM. Projection Reconstruction Techniques for Reduction of Motion Effects in MRI. Magn Reson Med. 1992;28(2):275–89.

38 Gmitro AF, Alexander AL. Use of a projection reconstruction method to decrease motion sensitivity in diffusion-weighted MRI. Magn Reson Med. 1993;29(6):835–8.

39 Rasche V, De Boer RW, Holz D, Proksa R. Continuous radial data acquisition for dynamic MRI. Magn Reson Med. 1995;34(5):754–61.

40 Rasche V, Holz D, Proksa R. MR fluoroscopy using projection reconstruction multi-gradient-echo (prMGE) MRI. Magn Reson Med. 1999;42(2):324–34.

41 Barger A V., Block WF, Toropov Y, Grist TM, Mistretta CA. Time-resolved contrast-enhanced imaging with isotropic resolution and

broad coverage using an undersampled 3D projection trajectory. Magn Reson Med. 2002;48(2):297–305.

42 Altbach MI, Outwater EK, Trouard TP, Krupinski EA, Theilmann RJ, Stopeck AT, et al. Radial fast spin-echo method for T2-weighted imaging and T2 mapping of the liver. J Magn Reson Imaging. 2002;16(2):179–89.

43 Gmitro AF, Kono M, Theilmann RJ, Altbach MI, Li Z, Trouard TP. Radial GRASE: implementation and applications. Magn Reson Med. 2005;53(6):1363–71.

44 Block KT, Uecker M, Frahm J. Model-based iterative reconstruction for radial fast spin-echo MRI. IEEE Trans Med Imaging. 2009;28(11):1759–69.

45 Li Z, Graff C, Gmitro AF, Squire SW, Bilgin A, Outwater EK, et al. Rapid Water and Lipid Imaging with T2 Mapping Using a Radial IDEAL-GRASE Technique. Magn Reson Med. 2009;61(6):1415–24.

46 Glover GH, Pauly JM, Bradshaw KM. Boron-11 imaging with a three-dimensional reconstruction method. J Magn Reson Imaging. 1992;2(1):47–52.

47 Bergin CJ, Pauly JM, Macovski A. Lung parenchyma: projection reconstruction MR imaging. Radiology. 1991;179(3):777–81.

48 Lu A, Grist TM, Block WF. Fat/water separation in single acquisition steady-state free precession using multiple echo radial trajectories. Magn Reson Med. 2005;54(5):1051–7.

49 Larson AC, White RD, Laub G, McVeigh ER, Li D, Simonetti OP. Self-gated cardiac cine MRI. Magn Reson Med. 2004;51(1):93–102.

50 Mistretta CA, Wieben O, Velikina J, Block W, Perry J, Wu Y, et al. Highly constrained backprojection for time-resolved MRI. Magn Reson Med. 2006;55(1):30–40.

51 Winkelmann S, Schaeffter T, Eggers H, Nielsen T, Doessel O. Single Shot T1-Mapping, using a Radial Look-Locker Sequence and an optimal Profile Order determined by the Golden Cut Rule. In: Proc Intl Soc Mag Reson Med. 2005;13:2196.

52 Feng L, Liu J, Block K, Xu J, Axel L, Sodickson D, et al. Compressed Sensing Reconstruction with an Additional Respiratory-Phase Dimension for Free-Breathing Imaging. In: Proc Intl Soc Mag Reson Med. 2013;21:0606.

53 Wundrak S, Paul J, Ulrici J, Hell E, Rasche V. A Small Surrogate for the Golden Angle in Time-Resolved Radial MRI Based on Generalized Fibonacci Sequences. IEEE Trans Med Imaging. 2015;34(6):1262–9.

54 Wundrak S, Paul J, Ulrici J, Hell E, Geibel MA, Bernhardt P, et al. Golden ratio sparse MRI using tiny golden angles. Magn Reson Med. 2016;75(6):2372–8.

55 Chan RW, Ramsay EA, Cunningham CH, Plewes DB. Temporal stability of adaptive 3D radial MRI using multidimensional golden means. Magn Reson Med. 2009;61(2):354–63.

56 Piccini D, Littmann A, Nielles-Vallespin S, Zenge MO. Spiral phyllotaxis: The natural way to construct a 3D radial trajectory in MRI. Magn Reson Med. 2011;66(4):1049–56.

57 Pang J, Sharif B, Fan Z, Bi X, Arsanjani R, Berman DS, et al. ECG and navigator-free four-dimensional whole-heart coronary MRA for simultaneous visualization of cardiac anatomy and function. Magn Reson Med. 2014;72(5):1208–17.

58 Piccini D, Littmann A, Nielles-Vallespin S, Zenge MO. Respiratory self-navigation for whole-heart bright-blood coronary MRI: Methods for robust isolation and automatic segmentation of the blood pool. Magn Reson Med. 2012;68(2):571–9.

59 Delacoste J, Chaptinel J, Beigelman-Aubry C, Piccini D, Sauty A, Stuber M. A double echo ultra short echo time (UTE) acquisition for respiratory motion-suppressed high resolution imaging of the lung. Magn Reson Med. 2018;79(4):2297–2305.

60 Jiang W, Ong F, Johnson KM, Nagle SK, Hope TA, Lustig M, et al. Motion robust high resolution 3D free-breathing pulmonary MRI using dynamic 3D image self-navigator. Magn Reson Med. 2018;79(6):2954–2967.

61 Song HK, Dougherty L. k-space weighted image contrast (KWIC) for contrast manipulation in projection reconstruction MRI. Magn Reson Med. 2000;44(6):825–32

62 Sodickson DK, Manning WJ. Simultaneous acquisition of spatial harmonics (SMASH): Fast imaging with radiofrequency coil arrays. Magn Reson Med. 1997;38(4):591–603.

63 Pruessmann KP, Weiger M, Scheidegger MB, Boesiger P. SENSE: Sensitivity encoding for fast MRI. Magn Reson Med. 1999;42(5):952–62.

64 Griswold MA, Jakob PM, Heidemann RM, Nittka M, Jellus V, Wang J, et al. Generalized Autocalibrating Partially Parallel Acquisitions (GRAPPA). Magn Reson Med. 2002;47(6):1202–10.

65 Pruessmann KP, Weiger M, Börnert P, Boesiger P. Advances in sensitivity encoding with arbitrary k-space trajectories. Magn Reson Med. 2001;46(4):638–51.

66 Yeh EN, Stuber M, McKenzie CA, Botnar RM, Leiner T, Ohliger MA, et al. Inherently self-calibrating non-Cartesian parallel imaging. Magn Reson Med. 2005;54(1):1–8.

67 Griswold M, Heidemann R, Jakob P. Direct parallel imaging reconstruction of radially sampled data using GRAPPA with relative shifts. Proc Intl Soc Magn Reson Med. 2003;11:2349.

68 Wright KL, Hamilton JI, Griswold MA, Gulani V, Seiberlich N. Non-Cartesian parallel imaging reconstruction. J Magn Reson Imaging. 2014;40(5):1022–40.

69 Cashen TA, Carroll TJ. Hybrid Radial-Parallel 3D Imaging. Proc Intl Soc Mag Reson Med. 2005;13:288.

70 Lustig M, Lee JH, Donoho DL, Pauly JM. Faster Imaging with Randomly Perturbed, Undersampled Spirals and |L|_1 Reconstruction. In: Proc Intl Soc Mag Reson Med. 2005;13:685.

71 Velikina JV. VAMPIRE: Variation Minimizing Parallel Imaging Reconstruction. In: Proc Intl Soc Mag Reson Med 2005;13:2424.

72 Lustig M, Donoho DL, Pauly JM. Rapid MR Imaging with "Compressed Sensing" and Randomly Under-Sampled 3DFT Trajectories. In: Proc Intl Soc Mag Reson Med. 2006;14:695.

73 Lustig M, Santos JM, Donoho DL, Pauly JM. k-t SPARSE: High frame rate dynamic MRI exploiting spatio-temporal sparsity. In: Proc Intl Soc Mag Reson Med. 2006;14:2420.

74 Chang TC, He L, Fang T. MR Image Reconstruction from Sparse Radial Samples Using Bregman Iteration. In: Proc Intl Soc Mag Reson Med. 2006;14:696.

75 Jong CY, Tak S, Han Y, Hyun WP. Projection reconstruction MR imaging using FOCUSS. Magn Reson Med. 2007;57(4):764–75.

76 Liang D, Liu B, Wang J, Ying L. Accelerating SENSE using compressed sensing. Magn Reson Med. 2009;62(6):1574–84.

77 Liu B, Zou YM, Ying L. Sparsesense: Application of compressed sensing in parallel MRI. In: 5th Int Conference on Information Technology and Applications in Biomedicine, ITAB 2008 in conjunction with 2nd Int Symposium and Summer School on Biomedical and Health Engineering, IS3BHE 2008. 2008. p. 127–30.

78 Tsao J, Boesiger P, Pruessmann KP. k-t BLAST and k-t SENSE: Dynamic MRI With High Frame Rate Exploiting Spatiotemporal Correlations. Magn Reson Med. 2003;50(5):1031–42.

79 Adluru G, Awate SP, Tasdizen T, Whitaker RT, DiBella EVR. Temporally constrained reconstruction of dynamic cardiac perfusion MRI. Magn Reson Med. 2007;57(6):1027–36.

80 Adluru G, McGann C, Speier P, Kholmovski EG, Shaaban A, Dibella EVR. Acquisition and reconstruction of undersampled radial data for myocardial perfusion magnetic resonance imaging. J Magn Reson Imaging. 2009;29(2):466–73.

81 Feng L, Chandarana H, Xu J, Block K, Sodickson DK. K-T Radial SPARSE-SENSE: Combination of Compressed Sensing and Parallel Imaging with Golden Angle Radial Sampling for Highly Accelerated Volumetric Dynamic MRI. In: Proc Intl Soc Mag Reson Med. 2012;20:81.

82 Block KT, Grimm R, Feng L, Otazo R, Chandarana H, Bruno M, et al. Bringing Compressed Sensing to Clinical Reality: Prototypic Setup for Evaluation in Routine Applications. In: Proc Intl Soc Mag Reson Med. 2013;21:3809.

83 Xue Y, Yu J, Kang HS, Englander S, Rosen MA, Song HK. Automatic coil selection for streak artifact reduction in radial MRI. Magn Reson Med. 2012;67(2):470–6.

84 Zaitsev M, Maclaren J, Herbst M. Motion artifacts in MRI: A complex problem with many partial solutions. J Magn Reson Imaging. 2015;42(4):887–901.

85 Piccini D, Feng L, Bonanno G, Coppo S, Yerly J, Lim RP, et al. Four-dimensional respiratory motion-resolved whole heart coronary MR angiography. Magn Reson Med. 2017;77(4):1473–1484.

86 Chitiboi T, Muckley M, Dane B, Huang C, Feng L, Chandarana H. Pancreas deformation in the presence of tumors using feature tracking from free-breathing XD-GRASP MRI. J Magn Reson Imaging. 2019;50(5):1633–1640.

87 Feng L, Axel L, Latson LA, Xu J, Sodickson DK, Otazo R. Compressed sensing with synchronized cardio-respiratory sparsity for free-breathing cine MRI: initial comparative study on patients with arrhythmias. J Cardiovasc Magn Reson. 2014;16(Suppl 1): O17.

88 Piekarski E, Chitiboi T, Ramb R, Feng L, Axel L. Use of self-gated radial cardiovascular magnetic resonance to detect and classify arrhythmias (atrial fibrillation and premature ventricular contraction). J Cardiovasc Magn Reson. 2016;18(1):83.

89 Feng L, Delacoste J, Smith D, Weissbrot J, Flagg E, Moore WH, et al. Simultaneous Evaluation of Lung Anatomy and Ventilation Using 4D Respiratory-Motion-Resolved Ultrashort Echo Time Sparse MRI. J Magn Reson Imaging. 2019;49(2):411–422.

90 Chandarana H, Feng L, Ream J, Wang A, Babb JS, Block KT, et al. Respiratory motion-resolved compressed sensing reconstruction of free-breathing radial acquisition for dynamic liver magnetic resonance imaging. Invest Radiol. 2015;50(11):749–56.

91 Seiberlich N, Breuer FA, Blaimer M, Barkauskas K, Jakob PM, Griswold MA. Non-Cartesian data reconstruction using GRAPPA operator gridding (GROG). Magn Reson Med. 2007;58(6):1257–65.

92 Seiberlich N, Breuer F, Blaimer M, Jakob P, Griswold M. Self-calibrating GRAPPA operator gridding for radial and spiral trajectories. Magn Reson Med. 2008;59(4):930–5.

93 Benkert T, Tian Y, Huang C, DiBella EVR, Chandarana H, Feng L. Optimization and validation of accelerated golden-angle radial sparse MRI reconstruction with self-calibrating GRAPPA operator gridding. Magn Reson Med. 2018;80(1):286–293.

94 Feng L, Huang C, Shanbhogue K, Sodickson DK, Chandarana H, Otazo R. RACER-GRASP: Respiratory-weighted, aortic contrast enhancement-guided and coil-unstreaking golden-angle radial sparse MRI. Magn Reson Med. 2018;80(1):77–89.

95 Feng L, Chandarana H, Sodickson DK, Otazo R. Unstreaking: Radial MRI with Automatic Streaking Artifact Reduction. In: Proc Intl Soc Mag Reson Med. 2017;25:4001.

96 Feng L, Coppo S, Piccini D, Yerly J, Lim RP, Masci PG, et al. 5D whole-heart sparse MRI. Magn Reson Med. 2018;79(2):826–838.

97 Ma LE, Yerly J, Piccini D, Di Sopra L, Roy CW, Carr JC, et al. 5D Flow MRI: A Fully Self-gated, Free-running Framework for Cardiac and Respiratory Motion-resolved 3D Hemodynamics. Radiol Cardiothorac Imaging. 2020;2(6):e200219.

98 Feng L, Wen Q, Huang C, Tong A, Liu F, Chandarana H. GRASP-Pro: imProving GRASP DCE-MRI through self-calibrating subspace-modeling and contrast phase automation. Magn Reson Med. 2020;83(1):94–108.

99 Chen J, Huang C, Shanbhogue K, Xia D, Bruno M, Huang Y, et al. DCE-MRI of the liver with sub-second temporal resolution using GRASP-Pro with navi-stack-of-stars sampling. NMR Biomed. 2024;37(12):e5262

100 Solomon E, Bae J, Zan E, Moy L, Ge Y, Feng L, et al. GRASP-Pro+: GRASP reconstruction with locally low-rank subspace constraint for DCE-MRI. In: Proc Intl Soc Mag Reson Med. 2022;30:1603.

101 Li Z, Xu X, Yang Y, Feng L. Repeatability and robustness of MP-GRASP T1 mapping. Magn Reson Med. 2022;87(5):2271–2286.

102 Pei H, Xia D, Xu X, Yang Y, Wang Y, Liu F, et al. Rapid 3D T1 mapping using deep learning-assisted Look-Locker inversion recovery MRI. Magn Reson Med. 2023;90(2):569–582.

103 Zhao T, Tang J, Krumpelman C, Moum SJ, Russin JJ, Ansari SA, et al. Highly accelerated non-contrast-enhanced time-resolved 4D MRA using stack-of-stars golden-angle radial acquisition with a self-calibrated low-rank subspace reconstruction. Magn Reson Med. 2025;93(2):615–629.

104 Xu X, Leforestier R, Xia D, Block KT, Feng L. MRI of GlycoNOE in the human liver using GraspNOE-Dixon. Magn Reson Med. 2025;93(2):507–518.

105 Benkert T, Feng L, Sodickson DK, Chandarana H, Block KT. Free-breathing volumetric fat/water separation by combining radial sampling, compressed sensing, and parallel imaging. Magn Reson Med. 2017;78(2):565–576.

106 Armstrong T, Dregely I, Stemmer A, Han F, Natsuaki Y, Sung K, et al. Free-breathing liver fat quantification using a multiecho 3D stack-of-radial technique. Magn Reson Med. 2018;79(1):370–382.

107 Benkert T, Block KT, Heller S, Moccaldi M, Sodickson DK, Kim SG, et al. Comprehensive Dynamic Contrast-Enhanced 3D Magnetic Resonance Imaging of the Breast With Fat/Water Separation and High Spatiotemporal Resolution Using Radial Sampling, Compressed Sensing, and Parallel Imaging. Invest Radiol. 2017;52(10):583–589.

108 Benkert T, Feng L, Gerges L, Shanbhogue K, Huang C, Sodickson D, et al. Comprehensive T1-weighted dynamic liver MRI during free-breathing using fat/water separation, radial sampling, compressed sensing, parallel imaging, and motion-weighted reconstruction. In: Proc Intl Soc Mag Reson Med. 2017;25:902.

109 Li Z, Mathew M, Syed AB, Feng L, Brunsing R, Pauly JM, et al. Rapid fat-water separated T1 mapping using a single-shot radial inversion-recovery spoiled gradient recalled pulse sequence. NMR Biomed. 2022;35(12).e4803.

110 Feng L, Tyagi N, Otazo R. MRSIGMA: Magnetic Resonance SIGnature MAtching for real-time volumetric imaging. Magn Reson Med. 2020;84(3):1280–1292.

111 Han P, Chen J, Xiao J, Han F, Hu Z, Yang W, et al. Single projection driven real-time multi-contrast (SPIDERM) MR imaging using pre-learned spatial subspace and linear transformation. Phys Med Biol. 2022;67(13):10.1088/1361-6560/ac783e.

112 Huttinga NRF, Bruijnen T, Van Den Berg CAT, Sbrizzi A. Real-Time Non-Rigid 3D Respiratory Motion Estimation for MR-Guided Radiotherapy Using MR-MOTUS. IEEE Trans Med Imaging. 2022;41(2):332–346.

113 Pei H, Chen J, Huang Y, Xu X, Xia D, Wang Y, et al. Deep-Grasp-Quant: A General Framework for Deep Learning-Enabled Quantitative Imaging Based on Golden-Angle Radial Sparse Parallel MRI. In: Proc Intl Soc Mag Reson Med. 2024;32:1072.

114 Campbell-Washburn AE, Ramasawmy R, Restivo MC, Bhattacharya I, Basar B, Herzka DA, et al. Opportunities in interventional and diagnostic imaging by using high-performance low-field-strength MRI. Radiology. 2019;293(2):384–393.

115 Xia D, Tian Y, Benkert T, Feng L. Spiral-GRASP-UTE: 4D Real-Time MRI of the Lung with Sub-Second Temporal Resolution. In: Proc Intl Soc Mag Reson Med. 2023;31;4656.

116 Chen J, Pei H, Bruno M, Wen Q, Maier C, Sodickson D, et al. Joint Denoising and Reconstruction of T2-Weighted PROPELLER MRI of the Lung at 0.55T Using Self-Supervised Deep Learning. In: Proc Intl Soc Mag Reson Med. 2025;33:92.

117 Chen J, Zhou K, Bruno M, Chandarana H, Sodickson D, Wen Q, et al. Distortion-Free Diffusion-Weighted Imaging of the Prostate Using TGSE-Based Golden-Angle PROPELLER Acquisition and Deep Learning Denoising.
In: Proc Intl Soc Mag Reson Med. 2025;33:664.

118 Pei H, Wang Y, Chandarana H, Feng L. Hybrid Learning: A Novel Combination of Self-Supervised and Supervised Learning for MRI Reconstruction without High Quality Training Reference.
In: Proc Intl Soc Mag Reson Med. 2025;33:390.

119 Janjusevic N, Pei H, Keerthivasan M, Sood T, Bruno M, Maier C, et al. SNAC-DL: Self-Supervised Network for Adaptive Convolutional Dictionary Learning of MRI Denoising.
In: Proc Intl Soc Mag Reson Med. 2024;32:2853.

120 Liu F, Feng L, Kijowski R. MANTIS: Model-Augmented Neural neTwork with Incoherent k-space Sampling for efficient MR parameter mapping. Magn Reson Med. 2019;82(1):174–188.

121 Feng L, Ma D, Liu F. Rapid MR relaxometry using deep learning: An overview of current techniques and emerging trends.
NMR Biomed. 2022;35(4):e4416.

122 Liu F, Kijowski R, Feng L, El Fakhri G. High-performance rapid MR parameter mapping using model-based deep adversarial learning. Magn Reson Imaging. 2020;74:152–160.

123 Liu F, Kijowski R, El Fakhri G, Feng L. Magnetic resonance parameter mapping using model-guided self-supervised deep learning. Magn Reson Med. 2021;85(6):3211–3226.

124 Stemkens B, Paulson ES, Tijssen RHN. Nuts and bolts of 4D-MRI for radiotherapy. Phys Med Biol. 2018;63(21):21TR01.

125 Paulson ES, Ahunbay E, Chen X, Mickevicius NJ, Chen GP, Schultz C, et al. 4D-MRI driven MR-guided online adaptive radiotherapy for abdominal stereotactic body radiation therapy on a high field MR-Linac: Implementation and initial clinical experience. Clin Transl Radiat Oncol. 2020;23:72–79.

Contact

Li Feng, Ph.D.
Center for Advanced Imaging Innovation and Research (CAI²R)
New York University Grossman School of Medicine
660 First Avenue
New York, NY, 10029
USA
Li.Feng@nyulangone.org

Kidney MR Elastography: Methods and Clinical Applications in Pediatric Kidney Transplantation

Suraj D. Serai, Ph.D.[1,3]; Bernarda Viteri, M.D., MSTR[2,3]; Hansel J. Otero, M.D.[1,3]

[1]Department of Radiology, Children's Hospital of Philadelphia, Philadelphia, PA, USA
[2]Division of Nephrology, Children's Hospital of Philadelphia, Philadelphia, PA, USA
[3]Perelman School of Medicine at the University of Pennsylvania, Philadelphia, PA, USA

Abstract

Magnetic resonance elastography (MRE) is well established for the evaluation of liver fibrosis. Our team now explores MRE as a promising non-invasive imaging technique for assessing the health of transplanted kidneys in children. This paper explains the principles, methodology, and clinical applications of MRE in evaluating kidney stiffness and its potential role in diagnosing and monitoring interstitial fibrosis and tubular atrophy (IFTA) in pediatric transplanted kidneys. Our study showed a correlation between kidney stiffness and histological fibrosis, with higher stiffness values observed in allografts with fibrosis compared to stable ones. This suggests that MRE could serve as a non-invasive tool for monitoring post-transplant kidney health, and thereby reduce the need for invasive biopsies and potentially enable more timely interventions.

Introduction

Dynamic elastography is a non-invasive imaging technique that uses shear waves to assess tissue stiffness by measuring its response to an applied force [1]. Magnetic resonance elastography (MRE) is a clinically validated, FDA-cleared method that provides a reliable estimate of soft tissue stiffness [2, 3], which is widely used in clinical practice for diagnosing and staging liver fibrosis [4, 5]. The technique works by applying low-frequency harmonic vibrations to a target tissue, then imaging the resulting propagating waves and processing the data to calculate mechanical parameters [6]. The result is a stiffness measurement displayed on an elastogram, a color-coded map that highlights variations in tissue stiffness and provides valuable objective quantitative information that helps identify disease presence and progression [7].

Kidney MRE

While a healthy kidney is typically soft and pliable, a diseased kidney may become stiffer due to inflammation, scarring, or fibrosis. Since the mechanical properties of renal tissues change with underlying pathologies, MRE can be used to spatially assess tissue stiffness and would potentially allow doctors to assess the health of the kidneys [6, 7]. For example, kidney MRE could assist in the management of patients with chronic kidney disease (CKD) to monitor progression. In the case of transplanted kidneys, MRE could help monitor for signs of rejection or other complications. MRE generates a color-coded map called an elastogram. The desired output is to measure the stiffness value from the elastogram. The elastogram that is generated from the acquired images indicates areas of tissue stiffness and can give objective quantitative information about the presence of disease.

Methods

MRE utilizes low-frequency sound waves to generate shear waves in the tissue or organ of interest (in this case, the kidneys). In the commercial version of MRE provided by Resoundant Inc. (Rochester, MN, USA), mechanical waves are produced by an "active driver" that is positioned outside the scanner room and controlled by the scanner. The pressure waves are transmitted through a plastic tube to a "passive driver" placed on the patient's body. While the original passive drivers were flat disks, they are now being replaced with soft, flexible models that adapt to the shape of the body. The passive driver is held in place by an elastic band. Patients can feel the vibration applied by the driver, but it is generally not uncomfortable.

Patient setup for kidney MRE

Instead of the single circular passive driver that is typically used for the liver, a Y-shaped splitter is used to connect two passive drivers placed on the back of the patient. The drivers should be positioned over the approximate location of the left and right kidneys (Fig. 1). For patients with single allograft kidney, a single passive driver is used.

Implementation of MRE

MRE data is acquired using special gradient-recalled echo (GRE) or spin-echo echo-planar imaging (SE-EPI) sequences. Both sequences work well on 1.5T systems, but the SE-EPI sequence has proven effective in reducing technical failures due to iron overload [8]. The SE-EPI MRE sequence is also recommended for 3T MRI systems, where T2* decay in the liver is more rapid [9].

The MRE implementation that is now widely used in clinical practice for evaluation of liver disease acquires individual cross-sectional images of propagating shear waves. The driver system is designed to generate shear waves in the liver that propagate mainly in directions parallel with the x-y plane and therefore can be accurately recorded with transverse images. In the standard liver MRE protocol, four transverse sections of the liver are acquired with through-plane motion encoding. The wave images are individually processed with a 2D inversion algorithm to generate elastograms. This approach, called 2D MRE, has been extensively validated and shown to efficiently provide reliable liver stiffness measurements. It is regarded as the most accurate non-invasive imaging-based method for detecting and staging liver fibrosis.

Method	MRE with 2D motion encoding	MRE with 3D motion encoding
Pulse sequence	2D SE-EPI	3D SE-EPI
Matrix size	100 × 100	96 × 96
Echo time, TE (msec)	35	36
Repetition time, TR (msec)	1200	4200
Bandwidth (Hz/px)	2174	2380
Slice thickness (mm)	8	3.6
Distance factor	25%	18%
No. of slices	4	14
No. of phases	4	3
Axis of MEG	Z	X, Y, and Z
Driver frequency (Hz)	60	60
Acceleration	GRAPPA	GRAPPA
Acceleration factor	2	3
No. of breath-holds	1	5
Imaging time (min: sec)	0:13	1:27

**Table 1:** Pulse sequence parameters for 2D and 3D MRE[1]. SE-EPI: spin-echo echo-planar imaging; 2D: two dimensional; 3D: three dimensional; MRE: magnetic resonance elastography; MEG: motion encoding gradients; msec: milliseconds; mm: millimeters; Hz: hertz; mT/m: millitesla/meter; Px: pixel; min: minutes; sec: seconds
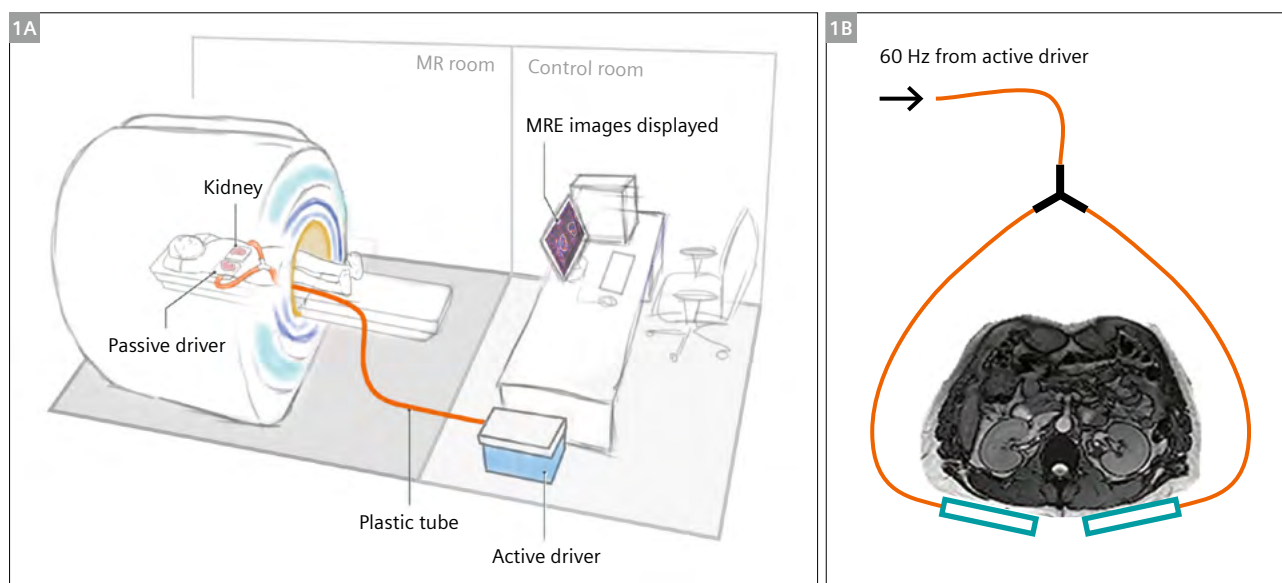
1 **(1A)** Kidney MRE passive driver positioning. The driver is positioned posteriorly so that it is relatively close to the kidney from the dorsal side. **(1B)** A Y-shaped splitter is used to position two paddles in parallel under both kidneys. Figure adapted and modified from [8].
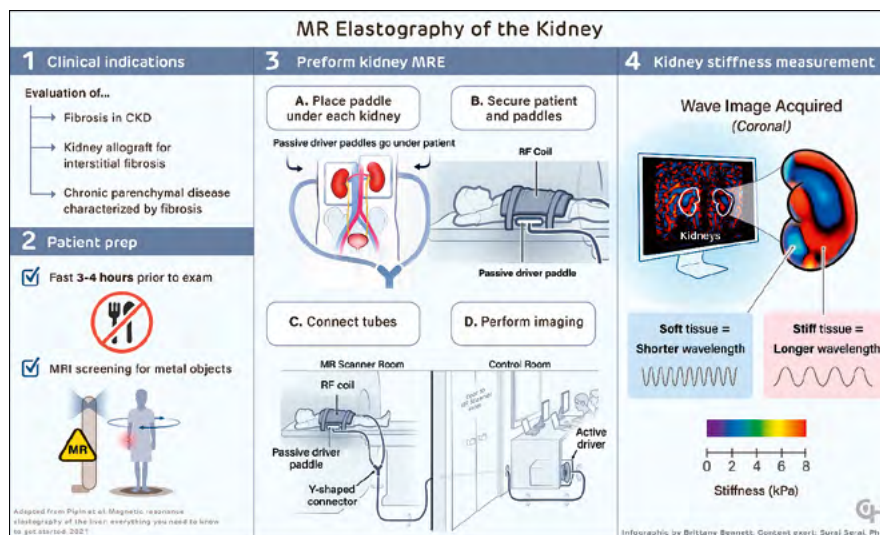
2 A visual roadmap to MR Elastography of the Kidney: from identifying clinical indications to capturing wave-based stiffness maps.
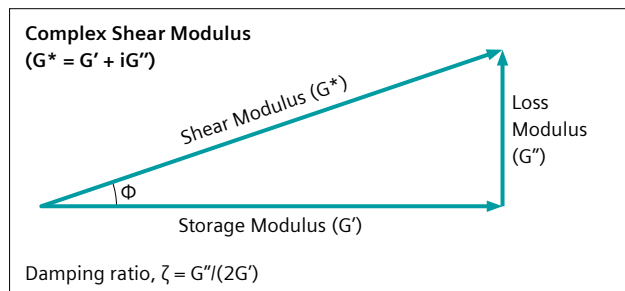
3 By encoding shear wave propagation in all three dimensions, 3D MRE enables independent measurement of the complex shear modulus ($G^* = G' + iG''$), where the real part (G') is the storage modulus and the imaginary part (G'') is the loss modulus; the damping ratio, defined as $G''/(2G')$, quantifies the relative magnitude of the loss modulus, while overall stiffness, represented by the shear modulus, can be measured using either 2D or 3D MRE.

Today, 2D MRE is widely available on clinical MRI scanners and can be relatively easily translated to the kidney (Fig. 2) [8]. A detailed protocol for kidney MRE acquisition is provided in Table 1.

3D MRE[1]

When MRE is used to evaluate the kidneys and other organs, the pattern of wave propagation is often much more complex than in the liver application. This can be addressed with an implementation of MRE that encodes the wavefield in all three dimensions. This implementation is known as 3D MRE, and often includes encoding for cyclic motion in X, Y, and Z directions rather than just in one direction. It is important not to confuse 3D MRE with 3D volumetric imaging in the common meaning. The 3D MRE data are processed with a special 3D MRE inversion

algorithm that considers wave propagation in all directions in 3D space. By capturing and processing wave data throughout a volume and in all directions of propagation, and by measuring cyclic motion in all directions, the 3D vector MRE technique can provide a more accurate measurement of tissue stiffness in complex anatomy. Moreover, 3D vector MRE processing can yield additional biomarkers such as the individual components of the complex shear modulus [11].

Given the kidney's small size and relatively deep location in comparison to the liver, accurate and reproducible stiffness measurement may benefit from 3D analysis of wave field data. Due to its enhanced accuracy and ability to measure wave motion in all three directions, 3D MRE is expected to outperform 2D MRE in kidney assessment.

Shear stiffness, (G^*), also called the magnitude of the complex shear modulus, $|G^*| = \sqrt{((G')^2 + (G'')^2)}$, is the commonly used MRE parameter; it reflects both elastic and viscous (or damping) elements of tissue stiffness. 3D MRE evaluates additional mechanical properties related to the dynamic aspects of stiffness, including storage modulus (G', elastic behavior), loss modulus (G'', viscous behavior), and damping ratio (loss modulus divided by 2 × storage modulus) (Fig. 3). Preclinical and clinical studies suggest that these parameters are differentially impacted by fibrosis and inflammation [9, 10]. Although 2D MRE is highly effective for detecting and staging fibrosis, tissue stiffness is only a surrogate marker influenced not only by fibrosis but also by other factors like inflammation, and portal hypertension, which can make it challenging to differentiate inflammation from fibrosis when both coexist.

The more comprehensive data set from 3D MRE enables advanced processing techniques, allowing for the reliable calculation of new markers.

Image acquisition

First, scout images: 3 to 5 slices in all three orthogonal planes are obtained in a single breath-hold during end-expiration to match MRE acquisition. MRE slices are acquired in an oblique coronal plane aligned to the long axis of the kidneys (Fig. 4). For our study, both 2D and a 3D MRE acquisition sequences were run on the same scanner and in the same imaging session. The MRE acquisitions were performed back-to-back. The spatial resolution, bandwidth, and motion-encoding gradient frequency were optimized to keep the imaging time to approximately 15 seconds per breath-hold. For the 2D SE-EPI image acquisition, all data are acquired in a single breath-hold at end-expiration (Fig. 5). Pulse sequence parameters for 2D and 3D SE-MRE are detailed in Table 1.
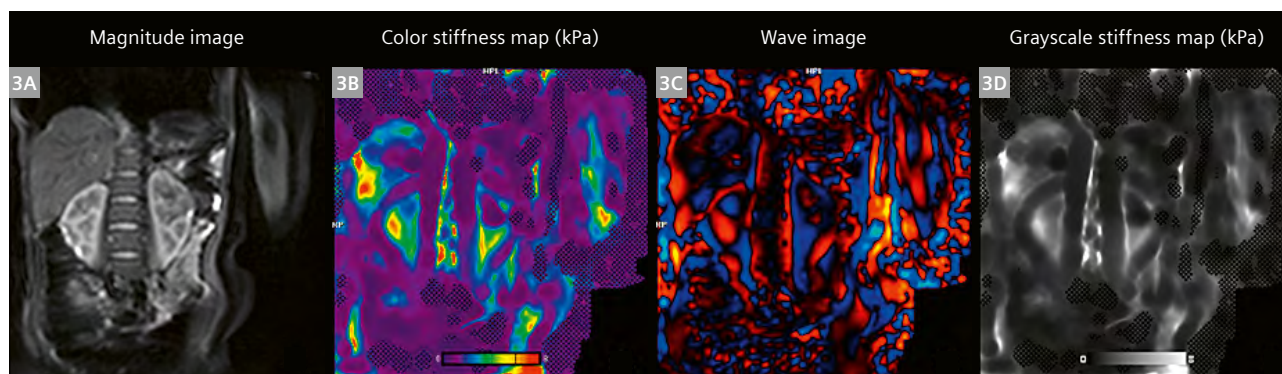
Stiffness measurement

Analogous to liver MRE, the stiffness maps and the 95% confidence maps are generated on the scanner. All MRE images must be reviewed for any breathing or motion artifacts that could render the images undiagnostic. Regions of interest (ROI) for measurement of stiffness are drawn within the regions bound by the confidence maps to include as much of the kidney parenchyma as possible, staying within the outer kidney capsule. A weighted mean shear stiffness is calculated. For 3D MRE, ROIs are carefully matched to record measurements of stiffness, storage modulus, and loss modulus.

## Clinical applications in children post-kidney transplant

MR imaging can characterize kidney structures. However, biopsies remain the primary method for diagnosing kidney pathologies, despite their associated risks and complications. A non-invasive method such as MRE can
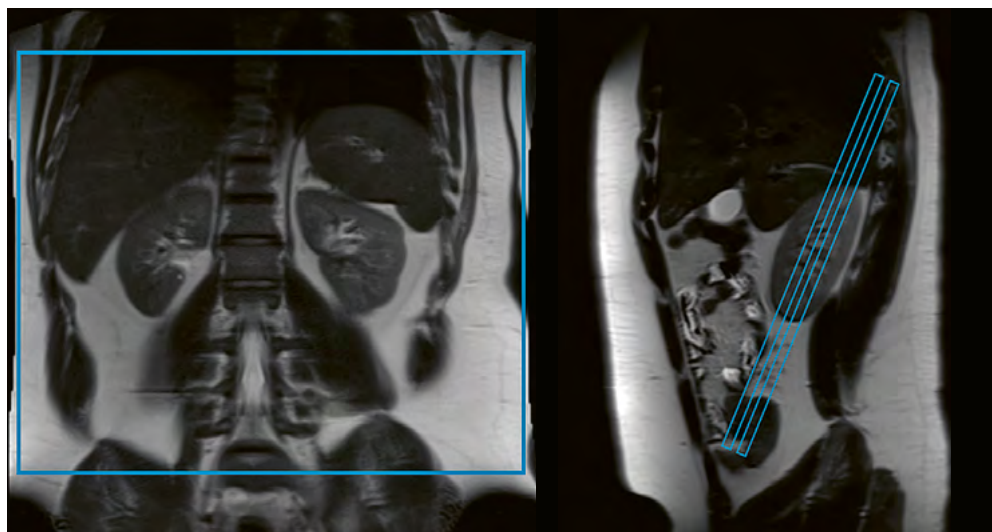
4 T2W coronal and sagittal slices showing the MRE slice setup.

5 Representative MRE images (2D SE-EPI) of an 8-year-old girl recruited as a healthy control. Mean kidney stiffness was measured as 3.9 kPa.
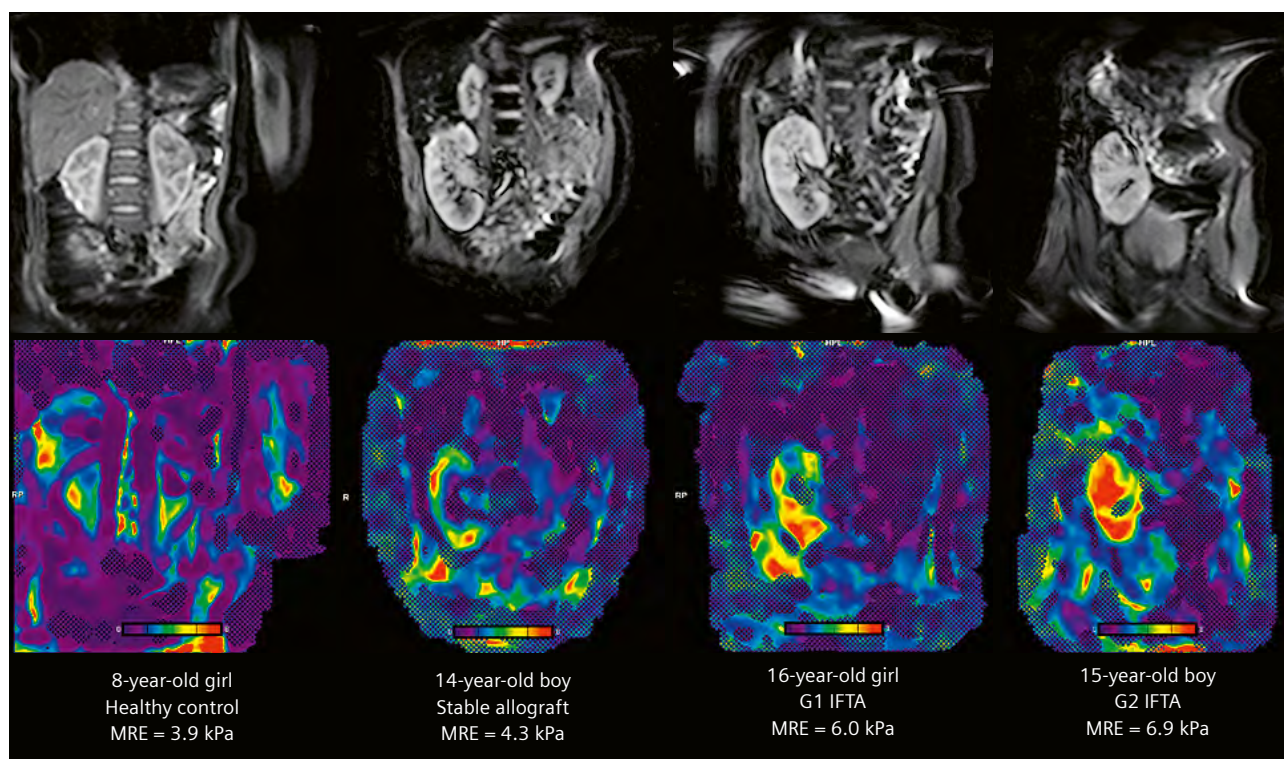
6 Representative MRE (2D SE-EPI) images of an 8-year-old girl recruited as a healthy control; a 14-year-old boy with stable allograft; a 16-year-old girl with Grade 1 IFTA; and a 15-year-old boy with Grade 2 IFTA. Mean kidney stiffness was measured as 3.9 kPa, 4.3 kPa, 6.0 kPa, and 6.9 kPa, respectively.

help identify and monitor kidney parenchymal abnormalities with the potential to spare or at least space out the need for biopsies. In patients with a transplanted kidney, interstitial fibrosis and tubular atrophy (IFTA) are major histopathologic factors in kidney allograft failure. IFTA progresses in two phases: The early phase, within the first year post-transplant, is characterized by fibrogenesis and tubulointerstitial injury due to ischemic or immunological damage. The late phase, beyond the first year, involves severe graft injury, including fibrosis, tubular atrophy, glomerulosclerosis, and arteriolar hyalinosis, leading to irreversible graft loss. Currently, percutaneous biopsy remains the gold standard for diagnosing and evaluating IFTA. In their pilot study, Kirpalani et al. showed the potential for MRE as a novel non-invasive measure of whole-allograft fibrosis burden, as it may predict future changes in kidney function [11].

In our study, we observed a positive correlation between kidney elasticity and histological fibrosis, with stiffness values generally being higher in fibrosed allografts compared to stable ones and also compared to normal native kidneys [8]. Mean kidney stiffness was higher for IFTA allografts (5.6 kPa) than stable allografts (4.4 kPa) and controls (3.6 kPa) (Fig. 6) [8].

Discussion

Application of MRE for non-invasive evaluation of renal fibrosis has great potential for non-invasive assessment in patients with kidney transplant. Although MRE is a well-established technique for imaging liver fibrosis; only a limited number of high-quality studies have assessed its use in human kidney allografts [11, 12]. Imaging the kidneys presents unique challenges due to their heterogeneous structure, deep anatomical location, hydration status, and respiratory motion, all of which can reduce image quality and complicate analysis [6]. However, further development and testing of these applications are necessary, primarily to validate the measurement against gold-standard invasive methods, to establish the discriminatory limits of MRE, and to better understand the physiology and pathophysiology of the observed changes in stiffness. On a technical note, MRE in patients with kidney transplants is relatively easy to perform, as the graft is usually located in the lower abdomen, where it is subject to less movement from respiration, and is closer to the skin surface, which would facilitate relatively easier transmission of the shear wave (Fig. 7). For kidney MRE, a recent study by Liu et al., found that a cortical stiffness
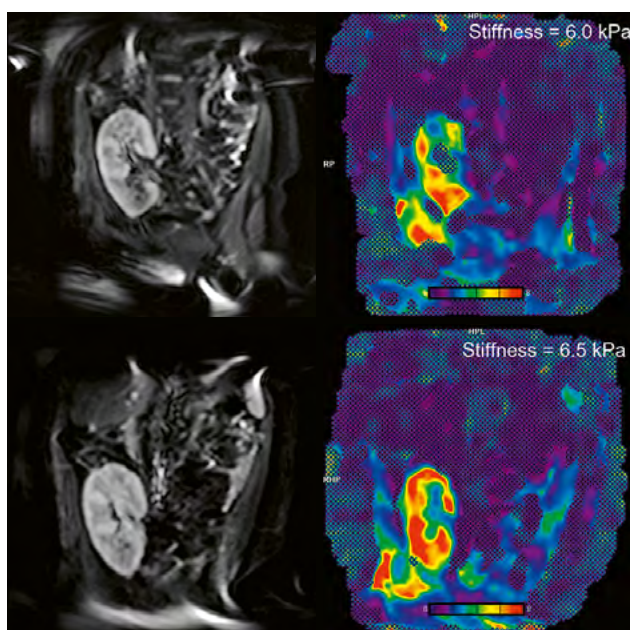
7 Longitudinal scan of a 16-year-old girl with Grade 1 IFTA. A mean kidney stiffness of 6.0 kPa was measured at baseline, and an increase in stiffness is seen on the scan performed 18 months later.

cutoff of approximately 3.6 kPa could distinguish serious interstitial fibrosis (≥ 30% extracellular matrix) with about 70% sensitivity and specificity [13]. Our preliminary results showed that MRE has the potential to be used as a non-invasive tool for quantitative measurement of the degree of fibrosis in renal allografts with a strong correlation with histopathology [8]. We think this is because the diffuse interstitial fibrosis increases tissue stiffness similar to the increased stiffness in liver fibrosis. We found normal mean kidney stiffness to be 3.6 kPa. Moreover, MRE has shown that it can help discriminate between the different IFTA groups with 4.4 kPa as the mean kidney stiffness for stable allografts [8].

While 3D MRE offers advantages in generating additional tissue parameters (Fig. 8), 2D MRE, which is more widely available, still holds significant potential in the basic application of detecting IFTA in patients with kidney transplant.

Conclusion

Kidney MRE shows promise in detecting low-grade IFTA in allografts. If clinically implemented, elastography would be useful for early detection of IFTA in renal transplants. This would individualize the need for immunosuppression therapy with the added benefit of reducing the need for invasive biopsies.
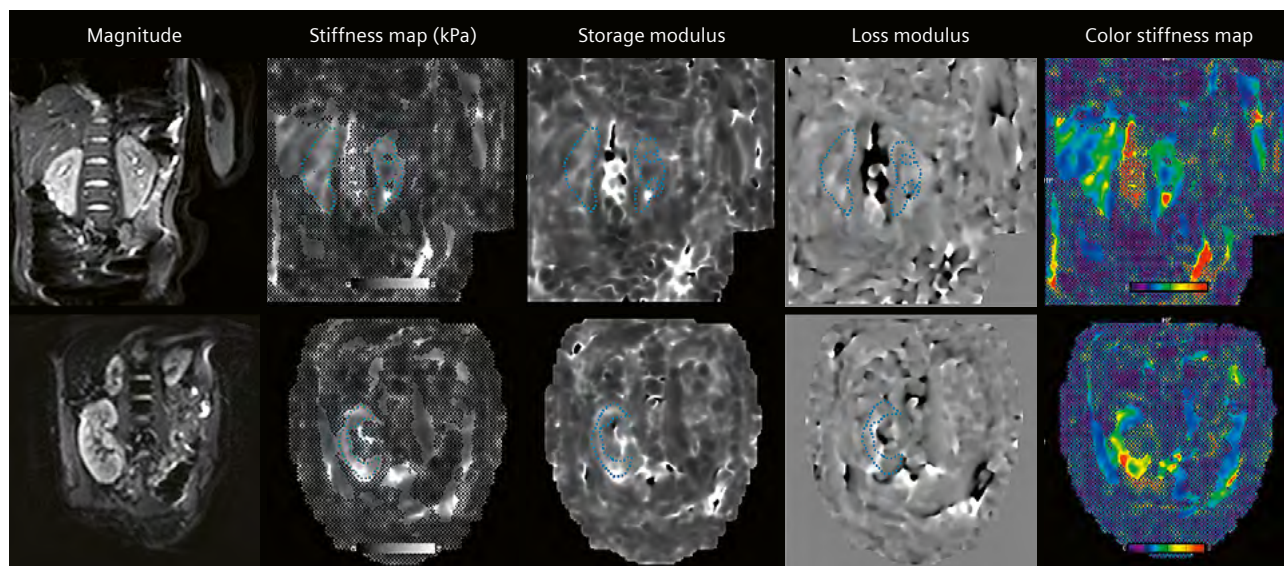
8 In addition to stiffness maps, 3D MRE allows the generation of storage modulus, loss modulus, and damping ratio. ROIs were carefully matched to record measurements. The top row shows representative images of 3D MRE on the same 8-year-old girl (stiffness = 3.8 kPa; storage modulus = 3.6 kPa; loss modulus = 2.0 kPa; damping ratio = 0.2). The bottom row shows representative images of 3D MRE on the same 14-year-old boy with stable allograft (stiffness = 4.6 kPa; storage modulus = 4.2 kPa; loss modulus = 0.85 kPa; damping ratio = 0.1).

References

1 Serai SD, Trout AT, Sirlin CB. Elastography to assess the stage of liver fibrosis in children: Concepts, opportunities, and challenges. Clin Liver Dis (Hoboken). 2017;9(1):5–10.
2 Towbin AJ, Serai SD, Podberesky DJ. Magnetic resonance imaging of the pediatric liver: imaging of steatosis, iron deposition, and fibrosis. Magn Reson Imaging Clin N Am. 2013;21(4):669–80.
3 Serai SD, Towbin AJ, Podberesky DJ. Pediatric liver MR elastography. Dig Dis Sci. 2012;57(10):2713–9.
4 Joshi M, Dillman JR, Towbin AJ, Serai SD, Trout AT. MR elastography: high rate of technical success in pediatric and young adult patients. Pediatr Radiol. 2017;47(7):838–843.
5 Serai SD, Obuchowski NA, Venkatesh SK, Sirlin CB, Miller FH, Ashton E, et al. Repeatability of MR Elastography of Liver: A Meta-Analysis. Radiology. 2017;285(1):92–100.
6 Serai SD, Yin M. MR Elastography of the Abdomen: Basic Concepts. Methods Mol Biol. 2021;2216:301–323.
7 Serai SD, Yin M. MR Elastography of the Abdomen: Experimental Protocols. Methods Mol Biol. 2021;2216:519–546.
8 Elsingergy MM, Viteri B, Otero HJ, Bhatti T, Morales T, Roberts TPL, et al. Imaging fibrosis in pediatric kidney transplantation: A pilot study. Pediatr Transplant. 2023;27(5):e14540.
9 Yin M, Glaser KJ, Manduca A, Mounajjed T, Malhi H, Simonetto DA, et al. Distinguishing between Hepatic Inflammation and Fibrosis with MR Elastography. Radiology. 2017;284(3):694–705.
10 Qu Y, Middleton MS, Loomba R, Glaser KJ, Chen J, Hooker JC, et al. Magnetic resonance elastography biomarkers for detection of histologic alterations in nonalcoholic fatty liver disease in the absence of fibrosis. Eur Radiol. 2021;31(11):8408–8419.
11 Kirpalani A, Hashim E, Leung G, Kim JK, Krizova A, Jothy S, et al. Magnetic resonance elastography to assess fibrosis in kidney allografts. Clin J Am Soc Nephrol. 2017;12(10):1671–9.
12 Lee CU, Glockner JF, Glaser KJ, Yin M, Chen J, Kawashima A, et al. MR elastography in renal transplant patients and correlation with renal allograft biopsy: a feasibility study. Acad Radiol. 2012;19(7):834–41.
13 Zhang J, Yu Y, Liu X, Tang X, Xu F, Zhang M, et al. Evaluation of renal fibrosis by mapping histology and magnetic resonance imaging. Kidney Dis (Basel). 2021;7(2):131–42.

Contact

Suraj D. Serai, Ph.D.
Children's Hospital of Philadelphia
3401 Civic Center Blvd.
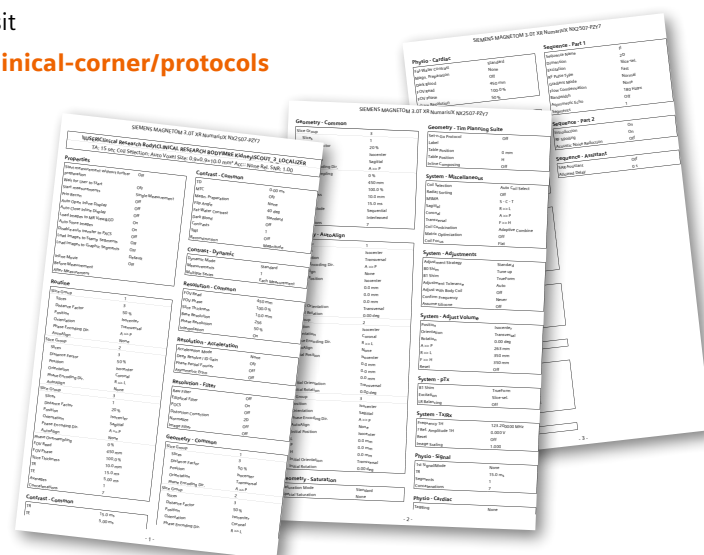Philadelphia, PA 19104
USA
serais@chop.edu

Suraj D. Serai   Bernarda Viteri   Hansel J. Otero

To download the protocol **(exar.1 file and PDF)**, please visit

www.magnetomworld.siemens-healthineers.com/clinical-corner/protocols

What happens when you have an MRI scan?

Help your little patients lose their fear – with Lottie

Lottie is an adventurous little lamb that loves to skateboard. But poor Lottie had an accident and may have broken her ankle. Now instead of leaping, she can only limp. Lottie is off to the hospital for an MRI scan. This engaging story by Professor Rolf Vosshenrich and Sylvia Graupner explains to children what it's like to have an MRI scan in a way they can understand.

We offer Lotti's story as a children's book in 21 languages (PDF) and as video in 6 languages. You can also order hard copies of the book in German, English, and Spanish.

The material is available at
www.siemens-healthineers.com/ magnetom-world

Go to **> Publications > MR Basics**

Ultra-Fast Pediatric Brain MRI for Toddlers and Young Children Using Deep Learning Acceleration

Sebastian Altmann, M.D.; Vanessa Schöffling, M.A.; Ahmed Othman, M.D., MHBA

Johannes Gutenberg University (JGU) Medical Center Mainz, Department of Neuroradiology, Center for Imaging, Minimally Invasive and Molecular Therapy, Mainz, Germany

Introduction

The rapid advancement of deep learning-based reconstruction techniques has led to significant changes in medical imaging, most notably in magnetic resonance imaging (MRI). These developments, which currently focus primarily on the acquisition of 2D datasets, have enabled substantial reductions in scan time [1–3]. This opens up new possibilities, especially in the fields of pediatric radiology and neuroradiology.

In neonates and infants[1] during the first months of life, the feed-and-wrap technique has proven to be highly effective. In this approach, the child is fed immediately before the MRI examination in an attempt to induce a natural sleep phase. This, combined with immobilization in a vacuum mattress, is usually sufficient for successful image acquisition [4].

However, for young children aged 6 months[1] to about 6 years, sedation or general anesthesia remain the most reliable options for acquiring diagnostic MRI datasets. This necessity presents multiple challenges, particularly in emergency settings or during recurrent follow-up examinations (e.g., in patients with ventriculoperitoneal shunts). In addition to the significant healthcare costs, sedation carries a low but not negligible risk for pediatric patients.

Furthermore, the logistical and staffing requirements for anesthesia often limit its availability, especially in acute care scenarios, where trained anesthesiology personnel may not be immediately accessible [5, 6].

These limitations can, in extreme cases, result in delayed or insufficient MRI diagnostics, forcing clinicians to rely on computed tomography (CT) instead. While CT offers speed and accessibility, it also involves ionizing radiation exposure, which is particularly undesirable for this vulnerable patient population [7].

Until recently, the technical capacity to significantly accelerate MRI acquisition was limited. However, emerging technologies, including real-time imaging and deep learning-based reconstruction algorithms, are now providing viable solutions to these challenges [8].

In this article, we describe the successful clinical implementation of an ultra-fast, T2-weighted, deep learning-enhanced MRI protocol tailored to pediatric patients, especially to those aged from 6 months[1] to 6 years. We provide a detailed overview of our workflow, with practical recommendations for patient preparation, positioning, and scan execution aimed at optimizing outcomes in both routine follow-ups and emergency pediatric imaging scenarios.
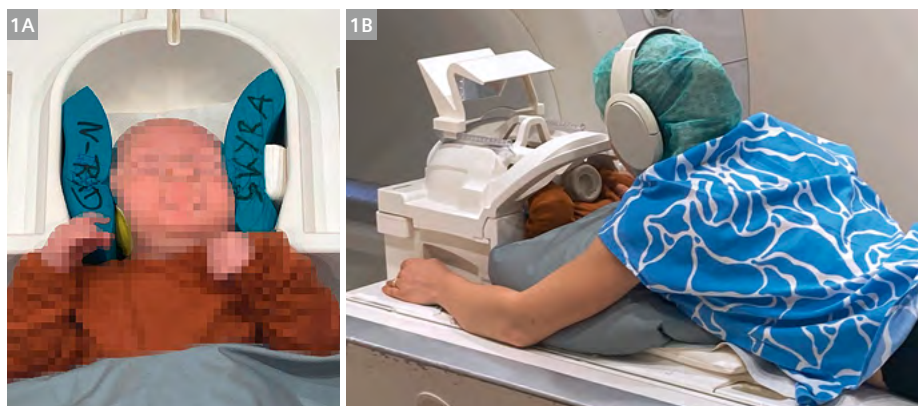
1 **(1A)** Positioning of an infant in the head coil for MRI examination: The infant wears adequate hearing protection. The head is securely stabilized within the coil using soft padding, and the body is additionally supported with a vacuum cushion. **(1B)** The mother lies in a prone position with forearms propped up to soothe the infant, maintains eye contact via a mirror, and can also hold the bottle. Both wear adequate hearing protection.

[1]MR scanning has not been established as safe for imaging fetuses and infants less than 2 years of age. The responsible physician must evaluate the benefits of the MR examination compared to those of other imaging procedures.

Weighting	T2	T2	T2
Orientation	Transversal	Coronal	Sagittal
Averages	1	1	1
Total time (sec)	17	15	15
Time of acquisition (sec)	5	5	5
FOV (mm²)	240	240	240
Matrix size	384 × 384	384 × 384	384 × 384
Phase resolution	80%	80%	80%
TE (ms)	97	97	97
TR (ms)	3850	3470	3470
Reconstructed voxel size (mm³)	0.3 × 0.3 × 5 (i)	0.3 × 0.3 × 5 (i)	0.3 × 0.3 × 5 (i)
Parallel imaging acceleration	4	4	4
SMS factor	2	2	2
Slice thickness (mm)	5	5	5
Slice distance factor	10%	10%	10%

Table 1: Sequence parameters for the ultra-fast deep learning-based protocol. Interpolation = i; time to echo = TE; repetition time = TR; Simultaneous Multi-Slice = SMS

Technical aspects

Sequences are accelerated using the CE-certified Deep Resolve techniques (Siemens Healthineers, Erlangen, Germany) and acquired in all three planes: axial, sagittal, and coronal, with a slice thickness of 5 mm using a 1.5T clinical scanner (MAGNETOM Sola; Siemens Healthineers, Erlangen, Germany) with a 20-channel head-neck coil. The total acquisition time for all three planes was less than one minute. The parameters for the sequences are provided in Table 1.

Patient preparation, positioning, and scan execution

Thorough preparation of both the child and the accompanying caregiver is crucial for successfully performing MRI examinations without sedation in children. In our clinical setting, parents receive detailed written information about the examination procedure at an early stage. Additionally, a standardized MRI safety questionnaire is provided to and discussed with the parents. The MRI compatibility of the accompanying person is systematically checked using a structured checklist to reliably rule out ferromagnetic implants or other contraindications.

A central element of the information provided is specific information about potential dangers in the MR tunnel, especially regarding the presence of a caregiver. These include restricted movement, emergency procedures, and the increased risk of RF-induced heating due to close

physical contact. Parents are informed in detail about these aspects to set realistic expectations and actively define their role.

Once safety clearance has been obtained and written consent has been given, the child is placed in a supine position directly on the scanner table. A vacuum-fixable mattress is then placed over the child to reduce involuntary movements during the examination and ensure stable positioning. In our setting, this positioning primarily serves to secure the infant or toddler during imaging. Additionally, soft positioning aids such as pillows and foam wedges are used to stabilize the position further and enhance comfort.

This form of positioning significantly optimizes image quality by minimizing motion artifacts. At the same time, however, wrapping the child in the vacuum mattress can impair heat dissipation and lead to increased thermal stress due to restricted ventilation. This effect is particularly noteworthy in very young patients. Due to the very short total duration of the examination in our protocol – typically only a few minutes – this risk is considered acceptable. For more protracted examinations, however, targeted monitoring of heat regulation would be necessary to prevent overheating.

The child's head is carefully positioned in the head coil and fixed in place with cushions inserted at the sides to severely restrict head movement.

To promote compliance and reduce anxiety, a child-friendly mirror is mounted inside the MRI tunnel. This allows the child to maintain constant visual contact with the accompanying caregiver. This measure has proven

particularly effective in younger children to minimize restlessness and movement. However, it is essential to ensure that the caregiver only looks at the child through the mirror. Lifting the head or looking directly down can lead to motion artifacts. The caregiver is therefore specifically instructed to maintain constant eye contact from a fixed position and not to change it during the examination.

A key feature of our protocol is the option of positioning a parent inside the MRI tunnel. Provided that safety clearance has been obtained and risk-specific consent has been given, the parent is positioned in a prone position inside the tube. The caregiver supports themselves on their elbows, gently embraces the child's upper body with their arms, and places their hands on either side of the child's head. This position allows for reassuring physical closeness and can, if necessary, contribute to additional manual stabilization of the head.

If in-bore positioning is refused or impractical, the caregiver remains at the entrance to the MRI tunnel. There, they can maintain reassuring tactile contact with the child's leg or abdomen. This form of support also has an anxiety-reducing effect, but is associated with an increased frequency of motion artifacts in children under three years of age.

In our institutional setting, we use the 1.5T MAGNETOM Sola scanner, because the examination room provided more space and a child-friendly environment, and the 70 cm bore diameter facilitated greater comfort for both child and caregiver. These infrastructural aspects, however, may vary between institutions.

The examination protocol was kept as short as possible. To this end, state-of-the-art AI-supported image reconstruction methods, the Simultaneous Multi-Slice technique, and targeted sequence optimizations such as increasing the turbo factor (echo train length) were employed. These measures significantly reduced acquisi-tion time while maintaining diagnostic accuracy. Short-ened protocols are particularly advantageous in pediatric imaging, as they minimize motion-related artifacts, improve patient comfort, and facilitate the feasibility of performing scans without sedation or anesthesia.

Our standardized methodology consistently enables the acquisition of high-resolution T2-weighted images in all three spatial planes, ensuring comprehensive representation of the child's neurocranial anatomy. Figure 2 illustrates the image quality achieved in a 2-year-old boy who was successfully examined without sedation following a fall against a door frame.

Direct skin-to-skin contact between the child and the caregiver may be necessary in exceptional cases, for instance when the child needs to be calmed or repositioned at short notice. Such contact should be limited to a few seconds and avoided whenever possible. As a rule, non-conductive, MRI-compatible materials such as thick foam layers or metal-free blankets are placed between the child and the caregiver to prevent RF loop formation and local overheating [9]. In our setting, standard metal-free positioning aids are routinely used, including two flat wedges, small triangular wedges, small wedge fillers, and two universal insert cushions (Siemens Healthineers, Erlangen, Germany). In addition, MRI-compatible pediatric thermal blankets may be employed, for example the ConRad™ MRI Safe Thermal Blanket (Patterson Veterinary, Loveland, CO, USA) or the MRI-Safe Pediatric Thermal Blanket (MRI Equip, Nisswa, MN, USA). These aids contribute to patient comfort and safety while minimizing the risk of RF loops and local heating during MRI examinations. In addition, a clear signal is agreed upon with the caregiver before the examination begins, which they can use to request a brief interruption of image acquisition – for example, by wiggling or lifting their foot. This arrangement allows the caregiver to calm or reposition the child

2 Images of a 2-year-old boy with head trauma. **(2A)** Axial T2 TSE with Deep Resolve, **(2B)** coronal T2 TSE with Deep Resolve, **(2C)** sagittal T2 TSE with Deep Resolve.

in a targeted manner while no image sequence is running that would be affected by movement.

To protect against acoustic stress, all pediatric patients receive combined hearing protection. Our facility uses individually adapted OHROPAX® Classic wax earplugs (OHROPAX GmbH, Wehrheim, Germany), which provide a particularly effective seal. In addition, child-friendly Natus MiniMuffs® ear muffs (Ewimed Switzerland AG, Bern, Switzerland) are applied to further reduce noise exposure from loud MRI sequences. For additional relief, sequences that are particularly low noise (e.g., single-shot T2) are placed at the beginning of the examination protocol, while louder gradient sequences are moved to the end of the examination whenever medically justifiable [10]. However, diagnostically necessary sequences always take priority, and repeat sequences are only performed if absolutely necessary after all essential acquisitions have been completed.

Infants and toddlers can also be calmed with a pacifier or a small bottle of familiar liquid (breast milk, infant formula, or mild tea), provided they tolerate this well. Slight motion artifacts caused by swallowing are acceptable as long as they do not significantly impair image quality. All drinking aids used must be completely metal-free and made of MRI-compatible plastic.

To increase motion robustness, our examination protocol specifically uses fast T2-weighted 2D sequences in three orthogonal planes (axial, coronal, sagittal). Longer 3D sequences with isotropic resolution are deliberately avoided, as they are significantly more susceptible to motion artifacts. The use of short-cycled 2D sequences increases the likelihood of obtaining usable image data even with slight movement.

In our workflow, the total duration of image acquisition for all three planes is less than one minute. The coronal plane provides an excellent representation of subdural fluid accumulations and the anterior skull base. The sagittal plane allows for a differentiated assessment of cerebrospinal fluid spaces, the ventricular system, and midline structures. The axial plane complements the dataset with a detailed image of cortical and subcortical structures. The total duration of the examination is therefore very short. By far the most time-consuming part is the careful preparation of the child and caregiver, and these efforts are directly related to image quality and the avoidance of repeat images.

Finally, it should be emphasized that non-sedation strategies do not necessarily reduce the overall examination time. While rapid acquisition techniques shorten scan duration, the time saved is largely invested in comprehensive preparation, including calming the child and positioning. Sedation-free strategies may allow some of this preparation to be performed outside the scanner room, potentially reducing the total time the patient spends in the scanner. The primary aim remains to avoid the risks associated with sedation – such as respiratory complications, circulatory instability, and post-anesthetic monitoring – while still obtaining high-quality diagnostic images.

Challenges in daily routine and limitations

These ultra-fast MRI sequences and the resulting significantly shortened scan times substantially reduce the risk of patient movement and associated motion artifacts. However, if movement occurs during this short scanning window, it can still result in pronounced artifacts. Therefore, despite all advancements in AI-assisted image reconstruction, this novel imaging protocol is not immune to motion-related artifacts.

3 Images from a 19-month-old male infant[1]. **(3A)** and **(3B)** demonstrate impaired image quality of initial scans due to motion artifacts. As the acquisition time per sequence is less than 20 seconds, sequences can easily be repeated; **(3A, 3B)** axial T2 TSE with Deep Resolve, **(3C)** axial T2 TSE with Deep Resolve after calming the toddler.

However, due to the very short acquisition time of approximately 15–17 seconds per sequence, individual sequences can be easily repeated if temporary agitation results in relevant motion artifacts.

Figure 3 is an example of a 19-month-old male infant[1] who was accidentally dropped by his mother as she was going up the stairs. In this case, several brief repetitions of the scan were necessary, due to relevant motion artifacts. They resulted in significantly improved diagnostic quality. Nevertheless, some examinations cannot be completed entirely free of artifacts. While image quality may be compromised in such cases, it is often still sufficient for a confident diagnostic assessment. Figure 4 illustrates persistent motion artifacts in a 7-year-old boy, who underwent a regular control examination due to shunted congenital hydrocephalus.

Up to now, preparing children and their parents for the child's MRI examination has taken place in the anteroom of our MRI scanner. From there, the child can be introduced to the scanner and examination room through the open door. However, a significantly more effective approach – currently in planning – involves gradually and playfully familiarizing especially young children with the examination over multiple sessions. This includes a separate informational and preparation appointment using a pediatric MRI dummy, which allows for trial positioning.

This setup offers several advantages: First, it reduces stress for staff, as it takes place outside of regular clinical operations and does not interfere with the ongoing examination schedule. Second, it allows radiology technologists to assess in advance whether a child might be too agitated for this examination technique.

For children, this stepwise process under protected conditions offers the opportunity to become gently accustomed to the procedure, helping to reduce the fear associated with an MRI scan. From our perspective, this type of preparation has the potential to improve image quality further, reduce the need for sequence repetition, and potentially lessen the emotional burden on parents, especially in cases where they may need to help stabilize their child's head during the scan.

Conclusion

Ultra-fast, non-sedated pediatric brain MRI using Simultaneous Multi-Slice (SMS) acquisition and deep learning-accelerated image reconstruction is feasible in children aged 6 months[1] to 6 years. Successful implementation requires meticulous preparation of both the child and the accompanying caregiver to ensure high-quality diagnostic images. In our protocol, rapid acquisition across three orthogonal planes, combined with AI-supported reconstruction, enables T2-weighted imaging, often within a total scan time of less than one minute.

These accelerated non-sedated protocols may, in selected cases, serve as a robust first-line imaging technique, potentially replacing CT in situations where radiation exposure is a concern, such as mild head trauma. By minimizing the need for sedation, this approach reduces periprocedural risks, enhances patient comfort, and may lower overall healthcare costs. The integration of structured pediatric preparation and gradual familiarization with the MRI environment further improves the likelihood of successful examinations and may decrease the need for repeat sequences.
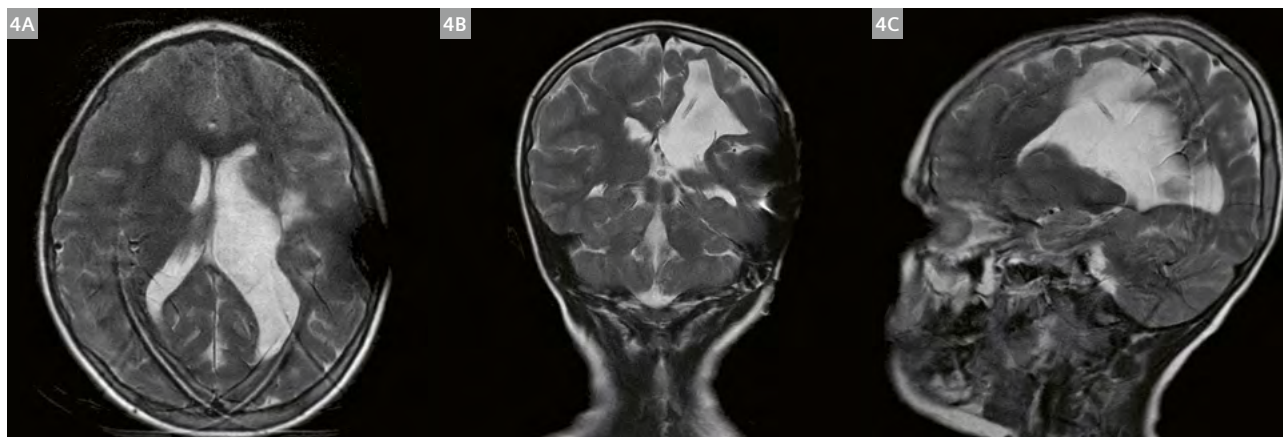
4 Even after repetition due to severe artifacts, motion artifacts remain. Image quality is still impaired, but relevant intracranial pathology can be excluded. **(4A)** axial T2 TSE with Deep Resolve, **(4B)** coronal T2 TSE with Deep Resolve, **(4C)** sagittal T2 TSE with Deep Resolve.

References

1 Altmann S, Grauhan NF, Brockstedt L, Kondova M, Schmidtmann I, Paul R, et al. Ultrafast Brain MRI with Deep Learning Reconstruction for Suspected Acute Ischemic Stroke. Radiology. 2024;310(2):e231938.

2 Altmann S, Abello Mercado MA, Brockstedt L, Kronfeld A, Clifford B, Feiweier T, et al. Ultrafast Brain MRI Protocol at 1.5 T Using Deep Learning and Multi-shot EPI. Acad Radiol. 2023;30(12):2988–98.

3 Schuhholz M, Ruff C, Burkle E, Feiweier T, Clifford B, Kowarik M, et al. Ultrafast Brain MRI at 3 T for MS: Evaluation of a 51-Second Deep Learning-Enhanced T2-EPI-FLAIR Sequence. Diagnostics (Basel). 2024;14(17):1841.

4 Antonov NK, Ruzal-Shapiro CB, Morel KD, Millar WS, Kashyap S, Lauren CT, et al. Feed and Wrap MRI Technique in Infants. Clin Pediatr (Phila). 2017;56(12):1095–1103.

5 Artunduaga M, Liu CA, Morin CE, Serai SD, Udayasankar U, Greer MC, et al. Safety challenges related to the use of sedation and general anesthesia in pediatric patients undergoing magnetic resonance imaging examinations. Pediatr Radiol. 2021;51(5):724–735.

6 Suliman M, Saleh W, Al-Shiekh H, Taan W, AlBashtawy M. The Incidence of Peripheral Intravenous Catheter Phlebitis and Risk Factors among Pediatric Patients. J Pediatr Nurs. 2020;50:89–93.

7 Hauptmann M, Byrnes G, Cardis E, Bernier MO, Blettner M, Dabin J, et al. Brain cancer after radiation exposure from CT examinations of children and young adults: results from the EPI-CT cohort study. Lancet Oncol. 2023;24(1):45–53.

8 Hirsch FW, Frahm J, Sorge I, Klee D, Prenzel F, Krause M, et al. Real-time MRI: a new tool of radiologic imaging in small children. Eur J Pediatr. 2023;182(8):3405–3417.

9 Baker C, Nugent B, Grainger D, Hewis J, Malamateniou C. Systematic review of MRI safety literature in relation to radiofrequency thermal injury prevention. J Med Radiat Sci. 2024;71(3):445–460.

10 Barkovich MJ, Xu D, Desikan RS, Williams C, Barkovich AJ. Pediatric neuro MRI: tricks to minimize sedation. Pediatr Radiol. 2018;48(1):50–55.

To download 1.5T MAGNETOM Sola and 3T MAGNETOM Skyra protocols **(exar.1 file and PDF)**, please visit

www.magnetomworld.siemens-healthineers.com/clinical-corner/protocols

Contact

Sebastian Altmann, M.D.
Johannes Gutenberg University (JGU)
Medical Center Mainz
Department of Neuroradiology
Center for Imaging, Minimally Invasive and Molecular Therapy
Langenbeckstr. 1
55131 Mainz
Germany
Tel.: +49 (0) 6131 17-6256
Sebastian.Altmann@unimedizin-mainz.de

Vanessa Schöffling, M.A
Johannes Gutenberg University (JGU)
Medical Center Mainz
Department of Neuroradiology
Center for Imaging, Minimally Invasive and Molecular Therapy
Langenbeckstr. 1
55131 Mainz
Germany
Vanessalnes.Schoeffling@unimedizin-mainz.de

Professor Ahmed Othman, M.D., EBIR
Johannes Gutenberg University (JGU)
Medical Center Mainz
Department of Neuroradiology
Center for Imaging, Minimally Invasive and Molecular Therapy
Langenbeckstr. 1
55131 Mainz
Germany
Ahmed.Othman@unimedizin-mainz.de

Photography by Dominik Gruszczyk

Advanced Imaging-Based Medicolegal Death Investigation: Postmortem MRI and CT

Chris O'Donnell, MB BS[1,2]; Aoife Reid, BRadMedImag (Hons)[3]; Miranda Northey, Grad. Dip. MRT[1];
Catherine Vincent, BMedRadSci[1]; Felicity Barnes, MB BS (Hons)[1]; Joanna Glengarry, MB ChB (Dist.)[1,2]

[1]Victorian Institute of Forensic Medicine, Melbourne, Australia
[2]Department of Forensic Medicine, Monash University, Australia
[3]Siemens Healthcare Pty. Ltd., Australia

Abstract

Postmortem computed tomography (PMCT) is well established for medicolegal death investigation. There are deficiencies in PMCT that can be overcome with postmortem magnetic resonance imaging (PMMRI) especially in the brain, spinal cord, and heart, and in young children. MRI sequences need to be adapted to the deceased, mostly to compensate for body cooling. In this case of hypoxic ischemic brain injury, both PMCT and PMMRI provided information about the deceased. This included iodine leak into the basal ganglia following high-dose antemortem CT scanning confirmed on dual energy PMCT, and swelling and T2 hyperintensity in gray matter of the basal ganglia and cortex on PMMRI. These findings were confirmed as hypoxic ischemic encephalopathy at autopsy examination.

Introduction

Postmortem computed tomography (PMCT) has become the standard of practice at many forensic institutions for investigating cause and manner of death. All admissions to our institution are scanned from head to toe. PMCT is used to triage the body to decide if there is a probable cause of death or to exclude traumatic injury, and to aid in determining if autopsy is necessary to advance the diagnosis and further characterize pathology. PMCT-guided procedures can also be undertaken and include angiography, specimen sampling such as bladder aspiration or orogastric tube insertion, and organ biopsy. Pathologists use PMCT to guide the autopsy dissection, concentrating on the areas of suspected pathology and avoiding the need to open all body cavities such as the skull if CT findings are negative. Retrospective review of PMCT can aid in interpreting findings at autopsy. Magnetic resonance imaging (MRI) is rarely used in postmortem practice due to difficulties in access. However, it can provide more information as long as sequences are adapted to the deceased to compensate for reduced body temperature, decomposition, and absence of blood flow. Image interpretation in both PMCT and postmortem MRI (PMMRI) differs from clinical imaging due to changes that occur in the body after death, and requires specialized postmortem imaging experience.

Although PMCT is useful for the analysis of bones, chest, abdomen, and hemorrhage, it has limited application as intravenous radiographic contrast agent is not administered after death. Major areas of deficiency include the brain, spinal cord, heart, and young children, where there is minimal abdominal and peripheral fat to separate organs and other structures. MRI has excellent contrast resolution in these areas. It is therefore complementary to CT and can provide a complete analysis of the body contents for forensic purposes.

Case report

A middle-aged adult was found unconscious on the floor. Prolonged resuscitation ensued and they were transferred to a hospital emergency department. Imaging in hospital included a CT brain scan with angiography and a CT pulmonary angiogram (CTPA) with abdomen and pelvis examination using a total of 150 cc radiographic contrast (Omnipaque 350 iohexol: 113.25 g/150 mL, GE Healthcare Australia Pty Ltd, Melbourne, Australia). The CT brain scan showed diffuse brain swelling and no hemorrhage. The CTPA showed no pulmonary embolism, and examination of the abdomen/pelvis was otherwise normal. Clinical testing subsequently confirmed brain death, and the patient was extubated. Given the sudden and unexpected nature of the death, it was referred to the coroner for medicolegal death investigation, and the decedent was transferred to the Victorian Institute of Forensic Medicine (VIFM). A whole-body CT was performed on admission, followed by dedicated dual energy CT of the brain based on initial findings. A postmortem brain MRI was performed after the body had been stored in refrigeration at ~ 4 °C. A full autopsy examination was undertaken after the MRI.

Technique

The institute's mortuary-based CT scanner is a SOMATOM Drive with software version VB20A. The PMCT technique included whole-body imaging from head to toe, and dedicated imaging with a smaller field of view through the head and neck (see Table 1).

Dual energy PMCT of the head was performed (see Table 2) and analyzed on *syngo*.via (version VB80D) using the CT Dual Energy workflow and the Virtual Unenhanced application profile.

The institute's mortuary-based MRI system is a 3T MAGNETOM Vida with software version XA60. Images were analyzed on *syngo*.via (version VB80D) using the MR Basic workflow. For imaging parameters, see Table 3.

After review of the whole-body CT scan to exclude internal metallic hardware, the body bag is opened, and an external examination is undertaken to detect and remove any metallic devices or other accoutrements on the skin. The body bag is then closed, with any metallic zips moved to the foot end. The body is carefully transferred with a ceiling hoist onto the eDrive dockable table. The head is positioned in the 64-channel head/neck coil, and the table is maneuvered to the scanner and docked.

Scan parameter	Routine head	Routine whole body
Scan range	Vertex to T1	Vertex to toes
Slice thickness	1 mm	1.5 mm
Slice increment	0.8 mm	1.0 mm
FOV	300 mm	500 mm
Soft Tissue		
Kernel	H31s	B30f
Window	Base orbita	Abdomen
Bone		
Kernel	H70h	Vertex to toes
Window	Bone	
Lung		
Kernel		B70f
Window		Lung
Eff mAs	420	280
kV	120	120
Pitch	0.55	0.6
Care Dose4D	off	off
Care kV	off	off
Rotation time	1 sec	0.5 sec
Detector config.	128 x 0.6	128 x 0.6

Table 1: PMCT whole-body imaging.

Parameter	Dual energy head
Care kV	Tube A 100 / Tube B Sn 140
Quality ref mAs	119
Pitch	0.6
FOV	300
Detector config.	32 x 0.6
Slice thickness	1.5 mm
Slice increment	1.0 mm
Reconstruction kernel (s)	Qr 40
Reconstruction window	Cerebrum

Table 2: Dual energy PMCT of the head

Sequence	MPRAGE	T2 TSE axial	T2 TSE coronal	T2 TSE dark-fluid axial_fs	PD TSE axial	T2 SWI	Resolve (segmented DWI) axial
Echo time (ms)	2.32	87	87	80	11	20	TE1: 75 TE2: 125
Repetition time (ms)	2300	3600	3600	9000	2290	30	5650
Slice thickness (mm)	0.9	3.0	3.5	3.0	3.0	2.0	3.0
Acquisition matrix	256 x 256	312 x 512	312 x 512	174 x 304	243 x 400	270 x 352	200 x 200
Imaged field of view (mm)	240 x 240	187 x 230	187 x 230	187 x 230	187 x 230	196 x 230	230 x 230
Receiver bandwidth (Hz/pixel)	200	222	222	289	223	100	781
Acquisition time (min:sec)	5.21	2.18	2.47	1.50	2.00	1.45	3.48
Acceleration	GRAPPA 2	GRAPPA 4	GRAPPA 4	GRAPPA 2	GRAPPA 2	Wave CAIPI: 6	SMS:2,: GRAPPA 2
AI (Deep Resolve Boost, Deep Resolve Sharp)	n/a	DRB:med; DRS	DRB:med;	50, 800	0.5 × 0.5 × 3.0	1.5 × 1.5 × 4.0	1.0 × 1.0 × 3.0
Inversion time (ms)*	900	n/a	n/a	Variable*	n/a	n/a	n/a
Flip angle	8	150	150	150	150	15	180
b values (s/mm^2)	n/a	n/a	n/a	n/a	n/a	n/a	b0; b1500; Calc b2000

Table 3: Imaging parameters
* = depends on body temperature (see Fig. 4)
n/a = not applicable

Image review

The PMCT of the brain shows bilateral symmetrical hyper-density in the basal ganglia, including caudate heads and lentiform nuclei. On dual energy CT (DECT), this hyper-density is shown to represent iodine and disappears on the virtual non-contrast reconstruction (Fig. 1).

The PMMRI of the brain demonstrates swelling and increased T2 signal in the basal ganglia (Fig. 2). Further swelling and increased T2 signal indicative of edema is present within the cortical gray matter of both the frontal and parietal lobes, indicative of diffuse hypoxic ischemic brain injury. This was confirmed at autopsy.

Superimposition of colorized axial T2 TSE PMMRI and axial PMCT using *syngo*.via (Fig. 3).

Series of FLAIR sequences with differing inversion times (constant TR and TE) showing varying effects on T2 contrast and signal within the cerebrospinal fluid (CSF) to find the null point, i.e., net zero transverse magnetization of water (Fig. 4).

Discussion

Hypoxic ischemic injury to the brain occurs when there is generalized inadequate oxygenation leading to cell swelling and death (so-called hypoxic ischemic encepha-lopathy or HIE). This is often associated with cardiac arrest. Gray matter is more metabolically active than white, making it sensitive to hypoxemia and more likely to be affected. This includes the basal ganglia and cortical gray matter. On CT imaging, hypoxemia is manifested as edema within gray matter and the resultant swelling. Normally, intravenously injected radiographic contrast does not enter the brain tissue due to an intact blood-brain barrier that restricts it to the meninges and blood vessels. If the barrier is disrupted, as it is in hypoxic injury, the radiographic contrast can leak into the brain, especially the basal ganglia, leading to a phenomenon known as hyperdense basal ganglia (HBG).
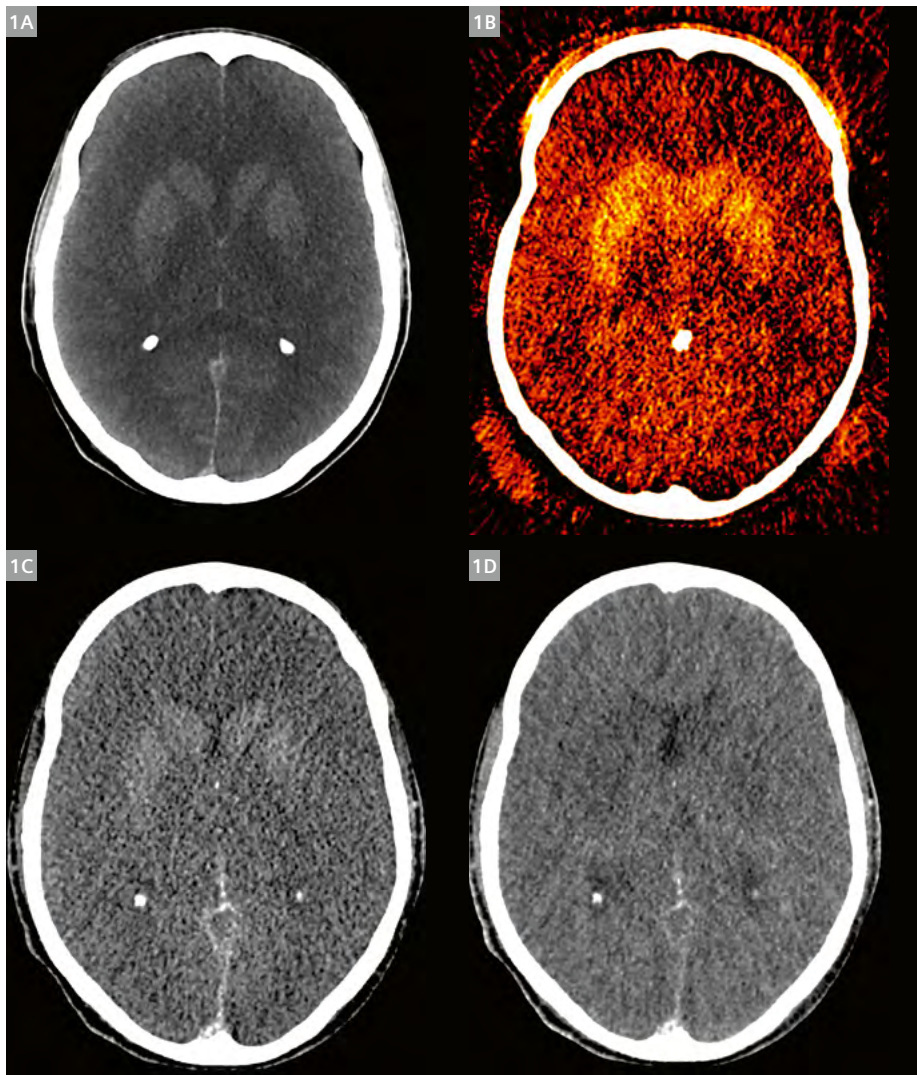
1 Axial PMCT brain **(1A)** showing bilateral symmetrical hyperdensity of basal ganglia. Axial PM DECT brain with iodine overlay **(1B)** shows that this hyperdensity is iodine deposition with a concentration of 1.5 mg/mL. Side-by-side comparison of DECT with iodine **(1C)** and virtual non-contrast **(1D)** showing loss of hyperdensity in the basal ganglia indicating the presence of iodine. Note how high-density blood in the superior sagittal sinus does not show loss of density on virtual non-contrast (VNC).
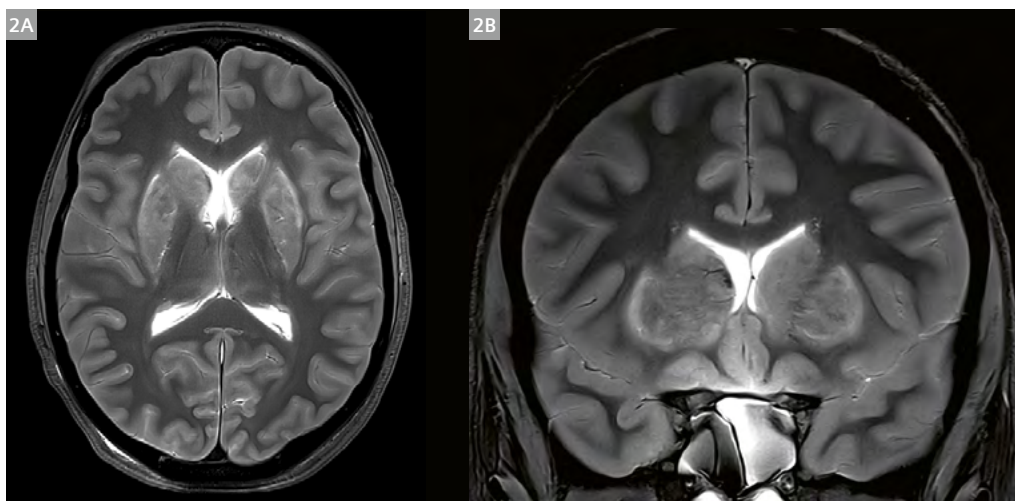
2 T2 TSE axial **(2A)** and coronal **(2B)** PMMRI showing bilateral symmetrical hyperintensity and swelling in basal ganglia indicative of hypoxic ischemic encephalopathy (HIE).
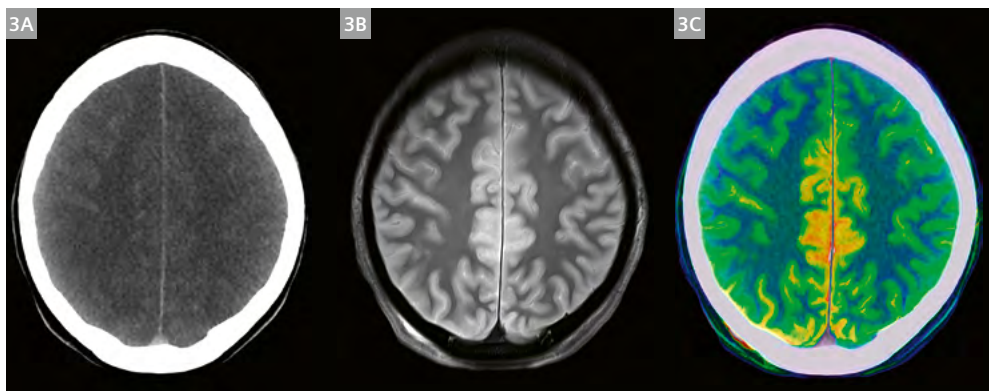
3 Axial PMCT **(3A)** shows minor swelling of the medial cortex. T2 TSE axial PMMRI **(3B)** shows significant swelling and abnormal T2 signal in the medial cortices. Fused colorized T2 TSE axial PMMRI and PMCT **(3C)**.
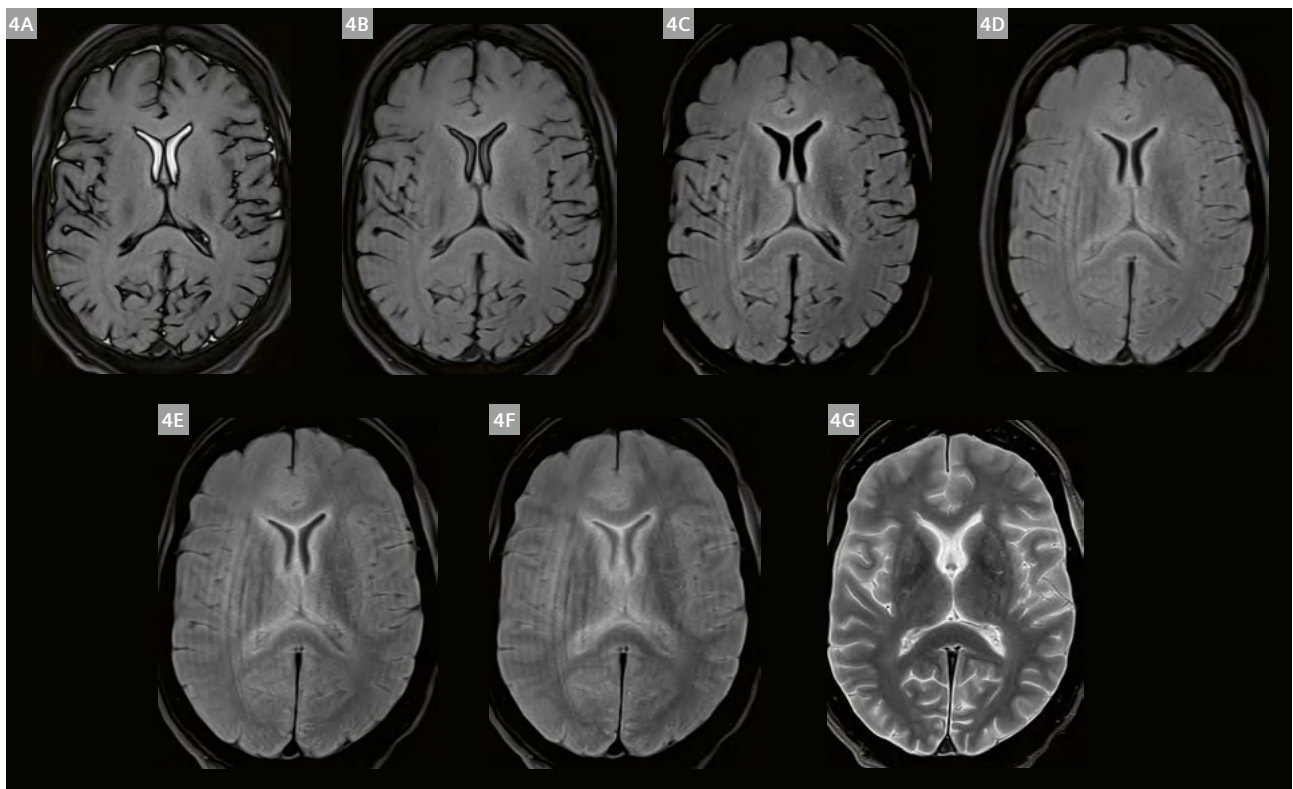
4 Axial T2 TSE dark-fluid FLAIR sequences with a TR of 9000, a TE of 80 ms, and a TI of **(4A)** 1000, **(4B)** 1200, **(4C)** 1400, **(4D)** 1600, **(4E)** 1800, **(4F)** 2000, and **(4G)** 2500 msec. The TI of 1400 ms produces the best signal suppression in CSF.

On PMCT, HBG is detected if an individual has an episode of severe hypoxic injury, is resuscitated to reestablish blood flow and oxygen to the brain, and then undergoes post collapse radiological imaging using large volumes of IV radiographic contrast (e.g., coronary angiography or a CT pan scan). Although not necessarily seen at the time of the antemortem CT, the contrast will progressively leak into the brain at sites where the blood-brain barrier is disrupted, such as the basal ganglia, and can be detected on PMCT as HBG.

Dual energy CT can detect iodine in tissues and can be used to confirm that this hyperdensity is iodine, distinguishing it from other causes such as nonketotic hyperglycemia, calcification, hemorrhage, and copper deposition (Wilson disease).

MR imaging is temperature sensitive, especially for T1-weighted sequences, leading to low signal intensity and tissue contrast [1]. T2 contrast and signal intensity are less affected. Deceased persons are routinely stored in fridges at ~ 4 °C. The temperature of the decedent at the time of scanning varies depending on body habitus and duration of refrigeration. If necessary, this can be quantified using rectal or forehead temperature measurements [2]. Limited T1-weighted sequences are performed in PMMRI and are not relied upon for diagnosis, apart from detection of methemoglobin and fat. T2-weighted sequences on PMMRI are most useful without flow artifacts. This means that time-of-flight MR angiography is not possible, but CSF is always universally white and brain edges are extremely sharp as there is no brain pulsation. FLAIR imaging is problematic due to temperature sensitivity, meaning inversion times differ from clinical practice [3]. We routinely perform a series of rapid preliminary FLAIR sequences with variable TI (1000–1600 ms) to determine the "sweet spot" or null point of CSF signal (Fig. 4). Once determined, this TI is then used for a full diagnostic sequence. A TI of 1400 ms is most commonly used on our magnet at 3T on bodies taken directly from refrigeration. This contrasts with the typical TI of 2500 ms used in clinical cases at body temperature.

Despite immediate changes to the body that occur following death, swelling and abnormal T2 signal in the brain on MRI are not a feature until decomposition progresses. It is somewhat counterintuitive that pathology such as HIE can be readily detected as swelling and increased T2 signal on PMMRI, although diffusion-weighted imaging is more problematic. This means that PMMRI of the brain is a particularly useful investigative tool for many fatal neurological conditions such as infarction, mass lesions, hemorrhage, and HIE.

Conclusion

Postmortem imaging is now highly sophisticated. It uses all the CT and MRI techniques available in clinical radiology, albeit with adjustments to allow for changes in the body after death and refrigeration. In medicolegal practice, interpretation must also be tempered by the requirements of investigators and the criminal justice system to answer questions, which may not always be obvious to clinically trained medical specialists, whose focus is diagnostic and therapeutic rather than forensic. Imaging specialists must therefore be experts in interpreting imaging of deceased persons, have an understanding of the law, and be able to engage with legal professionals and investigators, including providing expert evidence in court.

References

1 Berger C, Bauer M, Scheurer E, Lenz C. Temperature correction of post mortem quantitative magnetic resonance imaging using real-time forehead temperature acquisitions. Forensic Sci Int. 2023;348:111738.
2 Berger C, Bauer M, Wittig H, Gerlach K, Scheurer E, Lenz C. Investigation of post mortem brain, rectal and forehead temperature relations. J Therm Biol. 2023;115:103615.
3 Bruguier C, Magnin V, Knebel JF, Grabherr S, Dunet V, Genet P. Inversion time optimization in postmortem 1.5 tesla FLAIR brain imaging: a pilot study. Int J Legal Med. 2025. doi: 10.1007/s00414-025-03571-6. Epub ahead of print.

Contact

Dr. Chris O'Donnell, MB BS, FRANZCR, MMed, GradDipForMed, FFFPMI (RCPA)
Forensic Radiologist
Victorian Institute of Forensic Medicine
65 Kavanagh St
Southbank VIC 3006
Australia
chris.odonnell@vifm.org

DANTE Pulse Changed Our Clinical Routine and Research

Yasutaka Fushimi[1], Sachi Okuchi[1], Akihiko Sakata[1], Satoshi Nakajima[1], Takayuki Yamamoto[1], John Grinstead[2], Sinyeob Ahn[3], Yuji Nakamoto[1]

[1]Department of Diagnostic Imaging and Nuclear Medicine, Graduate School of Medicine, Kyoto University, Kyoto, Japan
[2]Siemens Healthineers, MR Research and Development, Portland, OR, USA
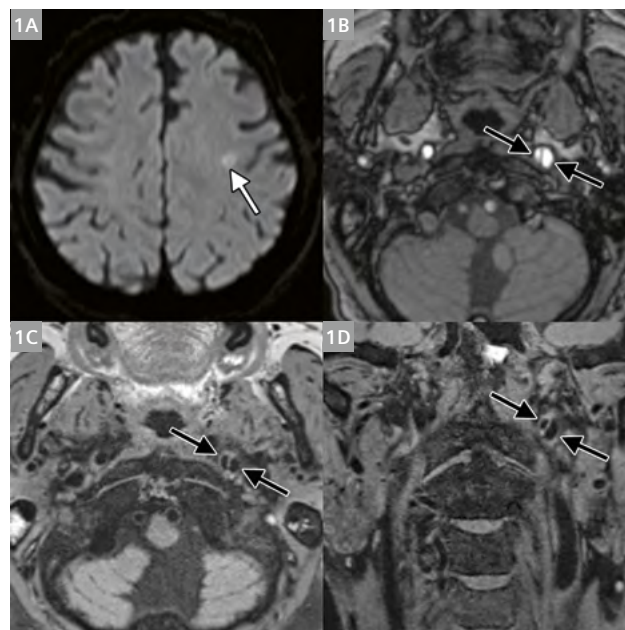[3]Siemens Healthineers, MR Research and Development, San Francisco, CA, USA

Introduction

Vessel wall MRI (VW-MRI) has become an essential tool for characterizing pathological features of the vessel wall (VW) in clinical practice [1]. Its clinical importance has been primarily established in the evaluation of atherosclerotic diseases, both extracranially and intracranially. With the introduction of additive pre-pulses such as motion-sensitized driven equilibrium (MSDE) and delay alternating with nutation for tailored excitation (DANTE), VW-MRI has gained potential applications beyond atherosclerosis and has improved the assessment quality of atherosclerotic lesions.

Although MSDE is widely used in VW-MRI, its low diffusion-sensitizing capability can cause blurring and T2-weighted effects. In contrast, the DANTE pulse attenuates signals from flowing spins by applying a train of low flip-angle pulses along the flow direction [2]. Compared to MSDE, DANTE causes less attenuation of signals from static tissue [3].

We have encountered various clinical cases in which non-contrast and contrast-enhanced DANTE T1-SPACE imaging helped visualize abnormal findings. In this narrative review, we present representative cases, acquired on a 3T scanner, to illustrate the clinical utility of DANTE T1-SPACE imaging.

1 An 80-year-old male. **(1A)** DWI showed mild hyperintensity in the left centrum semiovale (white arrow), suggesting subacute cerebral infarction. **(1B)** TOF-MRA revealed an intimal flap in the extracranial internal carotid artery (ICA), indicating ICA dissection. **(1C, 1D)** Axial and coronal DANTE T1-SPACE images demonstrated patent true and false lumens of the left ICA. Although the source of infarction was not definitively determined, a diagnosis of ipsilateral ICA dissection was established.

Application of DANTE pulse

DANTE pulses can be combined with T1-SPACE sequences using optimized CAIPIRINHA acceleration (4×), enabling high-resolution imaging with 0.6 mm isotropic voxels in under six minutes. Both non-contrast and contrast-enhanced DANTE T1-SPACE can be applied to a variety of intracranial and extracranial lesions [4]. Additionally, DANTE T1-SPACE can be used with Compressed Sensing and/or deep learning-based reconstruction techniques, which enhance signal-to-noise ratio (SNR) and reduce acquisition time. Careful optimization is required to avoid the loss of critical contrast and to detect small enhancing lesions, but the reduction of acquisition time will be beneficial in clinical practices.

## Arterial wall evaluation of internal carotid artery and vertebral artery

VW-MRI, also known as plaque imaging, is frequently employed for assessing vulnerable plaques. DANTE T1-SPACE can be applied to both cervical and intracranial arterial plaques. Hyperintense signals on this sequence may reflect intraplaque hemorrhage, a known risk factor for stroke [5, 6]. Another key application of VW-MRI is in the evaluation of arterial dissection. DANTE T1-SPACE can clearly depict arterial patency and differentiate true and false lumens by focusing on intraluminal signal intensity (Figs. 1 and 2).

Additionally, we focus on the plasticity of the bony carotid canal, which may reflect remodeling of the internal carotid artery (ICA). The canal can become narrower, even in adulthood, corresponding to ICA narrowing. DANTE

T1-SPACE allows longitudinal assessment of carotid canal morphology and may serve as a surrogate marker for ICA remodeling [7].

Pre- and post-treatment evaluation of aneurysms

VW-MRI is clinically useful for both pre- and post-treatment evaluation of large cerebral aneurysms, particularly those treated with flow-diverter stents [8, 9]. DANTE T1-SPACE can clearly delineate patent aneurysms and detect thrombus formation. Its ability to suppress signals from flowing spins enables visualization of early thrombosis shortly after stent placement, indicating effective treatment (Fig. 3). VW-MRI also aids in the evaluation of rare vascular diseases by ruling out vasculitis, plaque formation, and dissection [10].
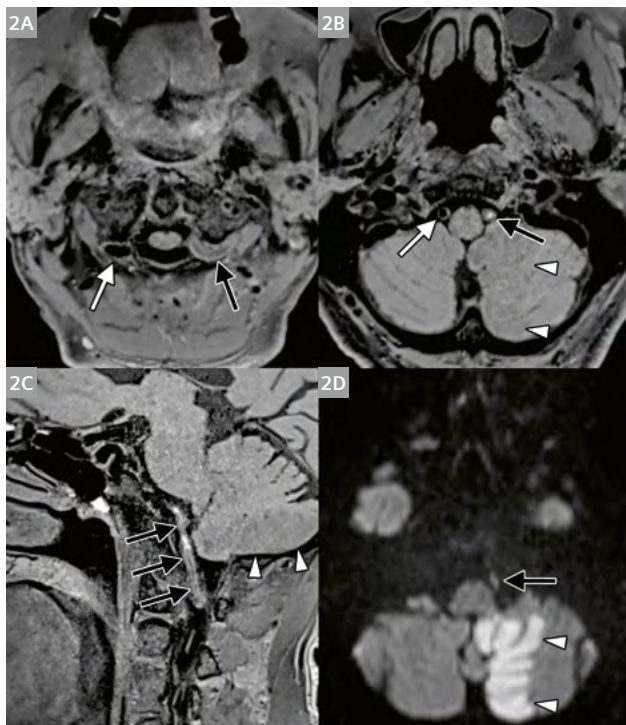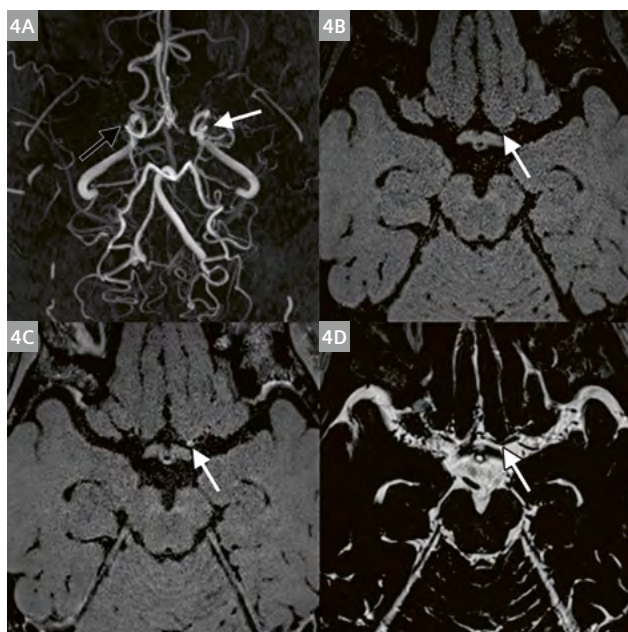

2 A 60-year-old male. **(2A, 2B)** Axial DANTE T1-SPACE images showed intermediate to high signal in the left vertebral artery (VA) (black arrow), while the right VA showed intraluminal signal suppression, suggesting flow (white arrow). **(2C)** Sagittal DANTE T1-SPACE depicted a long segment of high-intermediate signal along the left VA, suggestive of acute thrombus formation in the false lumen associated with left VA dissection. **(2D)** DWI revealed hyperintensity in the territory of the left posterior inferior cerebellar artery (PICA), indicating subacute cerebellar infarction. Mild hypointensity in the corresponding region was also seen on DANTE T1-SPACE (2B, 2C, arrowheads). DWI also showed intermediate signal in the left VA, suggesting the presence of thrombus.
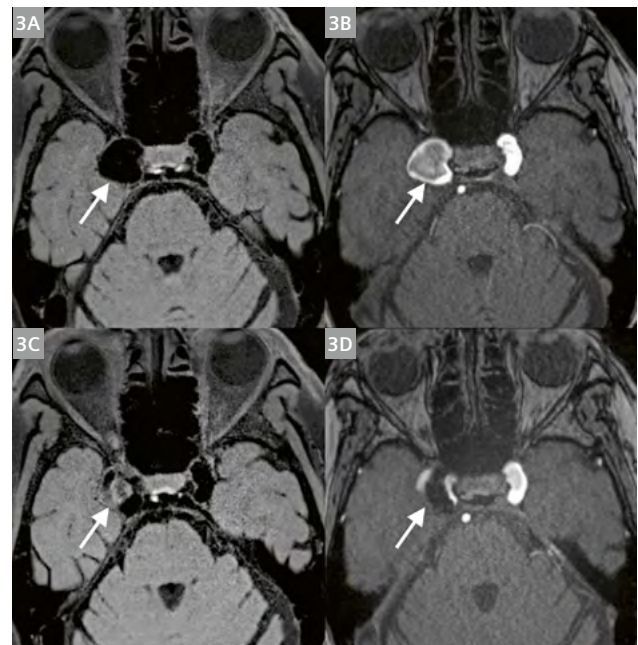
3 A 70-year-old female. **(3A)** DANTE T1-SPACE showed signal suppression within a large internal carotid artery (ICA) aneurysm located in the right cavernous sinus. **(3B)** TOF-MRA revealed an inhomogeneous high signal within the aneurysm. **(3C)** DANTE T1-SPACE obtained on Postoperative Day 1 (POD1) following flow diverter stent placement demonstrated an intermediate signal area, suggestive of thrombus formation within the aneurysm. **(3D)** TOF-MRA on POD1 showed residual inflow along the aneurysmal wall (arrow).

Arterial wall enhancement

Arterial wall enhancement on VW-MRI can be observed in various forms of vasculitis or vasculopathy, including moyamoya disease (MMD). Although the pathological basis of arterial wall enhancement in MMD remains unclear, contrast-enhanced DANTE T1-SPACE has revealed that the degree and distribution of enhancement vary depending on patient age, arterial location, and disease stage. Moreover, the extent of arterial wall enhancement tends to increase with disease progression in MMD (Fig. 4) [11]. Accurate assessment of arterial wall enhancement may be clinically important not only in MMD, but also in other types of intracranial inflammation.

Venous thrombosis

VW-MRI is also valuable for evaluating venous pathologies. Venous thrombosis can be difficult to diagnose, partly because thrombi are often inconspicuous. However, DANTE pulses suppress signals from flowing blood in veins as well, making it easier to detect abnormal signal intensities suggestive of thrombus formation (Fig. 5).

Arteriovenous malformation

A brain arteriovenous malformation (AVM) is a critical vascular condition caused by abnormal connections between arteries and veins in the brain that would normally be connected by a capillary network. AVM can lead to serious complications, including hemorrhage associated with nidal
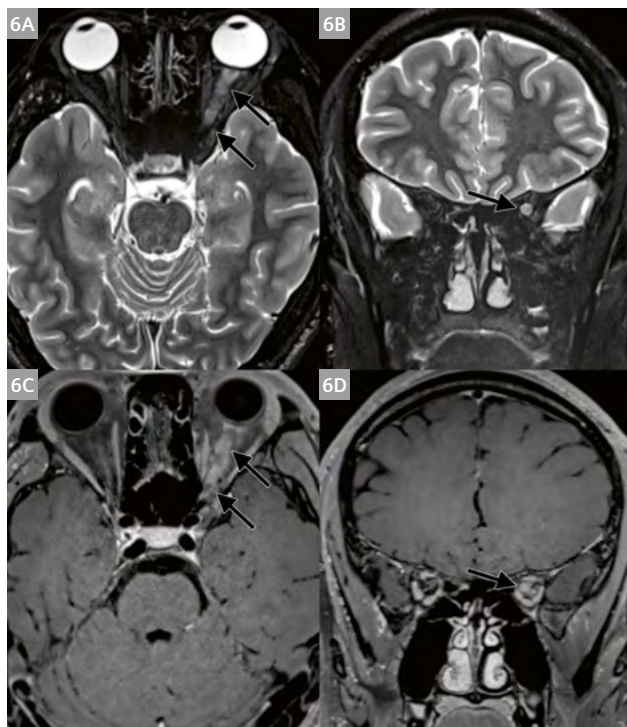

4 A 50-year-old female presented with mild right-sided motor weakness. **(4A)** MIP images of TOF-MRA suggested occlusion at the terminal portions of the bilateral ICAs (black and white arrows). **(4B)** Non-contrast DANTE T1-SPACE showed faint signal in the proximal left M1 segment (white arrow). **(4C)** CE DANTE T1-SPACE revealed clear enhancement of the left M1. No enhancement was observed in the right MCA (not shown). **(4D)** T2-SPACE delineated the contour of the proximal left M1. Enhancement of the left M1 segment may reflect progressive disease activity, which could be responsible for the right-sided motor weakness.

5 A 30-year-old female presented with headache and seizures during pregnancy. **(5A)** FLAIR imaging showed hyperintensity in the left temporal lobe. **(5B–5D)** DANTE T1-SPACE revealed high signal intensity in the cortical vein along the left temporal lobe, suggestive of cortical vein thrombosis. A diagnosis of venous infarction due to cortical vein thrombosis was established.

rupture. Since non-infectious inflammation may occur at the nidal wall, ruptured intranidal aneurysm of AVM could be determined by enhanced nidal wall on contrast-enhanced DANTE T1-SPACE [12].

Cranial nerve enhancement

Cranial nerve enhancement suggests abnormal inflammation, carcinomatous meningitis, or CSF space dissemination. Optic neuritis and optic perineuritis are commonly experienced clinical situations, and the accurate evaluation of inflammation of the optic nerve and/or surrounding optic nerve sheath is crucial in the diagnosis (Fig. 6) [13]. Other cranial nerve inflammation and malignancy can be evaluated with contrast-enhanced DANTE T1-SPACE [14].

Neuromelanin contrast

DANTE pulse may induce a slight magnetization transfer effect, which can enhance neuromelanin contrast in the substantia nigra [15, 16]. Thus, DANTE T1-SPACE can serve not only as a vessel-wall imaging sequence (VW-MRI) but also as a high-resolution neuromelanin-sensitive imaging sequence (Fig. 7). To further enhance neuromelanin contrast, denoising approaches have been proposed for neuromelanin-sensitive MRI [17].

Conclusion

We hope this article shows that DANTE T1-SPACE has the potential to enhance the quality of routine clinical imaging and to serve as a valuable tool for future clinical research.
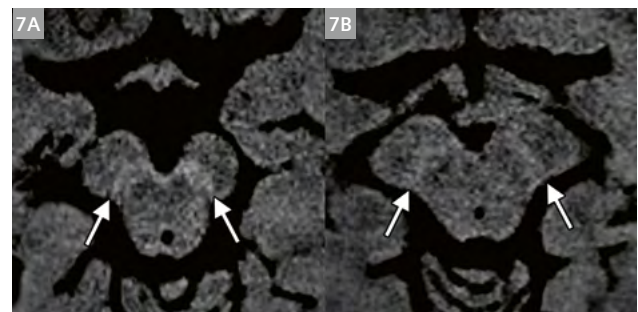
7 DANTE T1-SPACE images of a 59-year-old healthy male control **(7A)** and a 54-year-old male patient with Parkinson's disease (PD) **(7B)**. In the healthy control, the substantia nigra exhibits slightly higher signal intensity, whereas no distinct high signal is observed in the PD patient. This contrast may assist in differentiating PD from healthy individuals.

6 A male in his teens with left visual impairment. **(6A, 6B)** STIR showed high intensity along the left optic nerve. **(6C, 6D)** CE DANTE T1-SPACE showed enhancement of the left optic nerve and surrounding the nerve sheath, which was consistent with myelin oligodendrocyte glycoprotein (MOG) antibody-associated disease (MOGAD).

References

1   Mandell DM, Mossa-Basha M, Qiao Y, Hess CP, Hui F, Matouk C, et al. Intracranial Vessel Wall MRI: Principles and Expert Consensus Recommendations of the American Society of Neuroradiology. AJNR Am J Neuroradiol. 2017;38(2):218–229.

2   Li L, Miller KL, Jezzard P. DANTE-prepared pulse trains: a novel approach to motion-sensitized and motion-suppressed quantitative magnetic resonance imaging. Magn Reson Med. 2012;68(5):1423–38.

3   Li L, Chai JT, Biasiolli L, Robson MD, Choudhury RP, Handa AI, et al. Black-blood multicontrast imaging of carotid arteries with DANTE-prepared 2D and 3D MR imaging. Radiology. 2014;273(2):560–9.

4   Fushimi Y, Yoshida K, Okawa M, Maki T, Nakajima S, Sakata A, et al. Vessel wall MR imaging in neuroradiology. Radiol Med. 2022;127(9):1032–1045.

5   Okuchi S, Fushimi Y, Okada T, Yamamoto A, Okada T, Kikuchi T, et al. Visualization of carotid vessel wall and atherosclerotic plaque: T1-SPACE vs. compressed sensing T1-SPACE. Eur Radiol. 2019;29(8):4114–4122.

6   Takayama N, Maki T, Fushimi Y, Okawa M, Mineharu Y, Yamada K, et al. Association between ischemic stroke and hyperintense plaques detected by high-resolution vessel wall MRI in Japanese patients with intracranial atherosclerotic disease. Front Stroke. 2025; 4: 2025.

7   Oichi Y, Mineharu Y, Agawa Y, Morimoto T, Funaki T, Fushimi Y, et al. Plasticity of the bony carotid canal and its clinical use for assessing negative remodeling of the internal carotid artery. PLoS One. 2021;16(12):e0261235.

8   Matsukawa S, Ishii A, Fushimi Y, Grinstead J, Ahn S, Kikuchi T, et al. Efficacy of high-resolution vessel wall MRI in the postoperative assessment of intracranial aneurysms following flow diversion treatment. J Neurosurg. 2024;142(1):88–97.

9   Matsukawa S, Ishii A, Fushimi Y, Terada Y, Natsuhara H, Kikuchi T, et al. Ruptured thrombosed vertebral artery dissecting aneurysm treated with staged flow diverter after prediction of the rupture point by vessel wall MRI. Neuroradiol J. 2024;37(6):772–775.

10 Tokunaga S, Yamao Y, Maki T, Ishii A, Miyake T, Yasuda K, et al. Vessel wall imaging and carotid artery stenting for recurrent cervical internal carotid artery vasospasm syndrome: illustrative case. J Neurosurg Case Lessons. 2023;5(23):CASE2341.

11 Tagawa H, Fushimi Y, Funaki T, Nakajima S, Sakata A, Okuchi S, et al. Vessel wall MRI in moyamoya disease: arterial wall enhancement varies depending on age, arteries, and disease progression. Eur Radiol. 2024;34(4):2183–2194.

12 Komatsu K, Takagi Y, Ishii A, Kikuchi T, Yamao Y, Fushimi Y, et al. Ruptured intranidal aneurysm of an arteriovenous malformation diagnosed by delay alternating with nutation for tailored excitation (DANTE)-prepared contrast-enhanced magnetic resonance imaging. Acta Neurochir (Wien). 2018;160(12):2435–2438.

13 Shimada A, Suda K, Nakano E, Tagawa M, Miyata M, Kashii S, et al. Accuracy of Diagnosing Optic Neuritis Using DANTE T1-SPACE Imaging. Eye Brain. 2024;16:65–73.

14 Tsubouchi R, Ohira J, Sawamura M, Fushimi Y, Grinstead J, Ahn S, et al. Multiple cranial neuritis depicted with DANTE-prepared contrast-enhanced MRI. Neurology and Clinical Neuroscience. 2020;8:220–1.

15 Oshima S, Fushimi Y, Okada T, Nakajima S, Yokota Y, Shima A, et al. Neuromelanin-Sensitive Magnetic Resonance Imaging Using DANTE Pulse. Mov Disord. 2021;36(4):874–882.

16 Park S, Sung YH, Kim WR, Noh Y, Kim EY. Correlation Between Neuromelanin-Sensitive MRI and ^{18}F-FP-CIT PET in Early-Stage Parkinson's Disease: Utility of a Voxel-Wise Analysis by Using High-Spatial-Resolution MRI. J Clin Neurol. 2023;19(2):156–164.

17 Oshima S, Fushimi Y, Miyake KK, Nakajima S, Sakata A, Okuchi S, et al. Denoising approach with deep learning-based reconstruction for neuromelanin-sensitive MRI: image quality and diagnostic performance. Jpn J Radiol. 2023;41(11):1216–1225.

Contact

Associate Professor Yasutaka Fushimi, M.D., Ph.D.
Department of Diagnostic Imaging
and Nuclear Medicine
Graduate School of Medicine, Kyoto University
54 Shōgoin Kawaharachō, Sakyo-ku
Kyoto 606-8507
Japan
yfushimi@kuhp.kyoto-u.ac.jp

From left to right:
Dr. Sakata, Dr. Fushimi, Dr. Okuchi
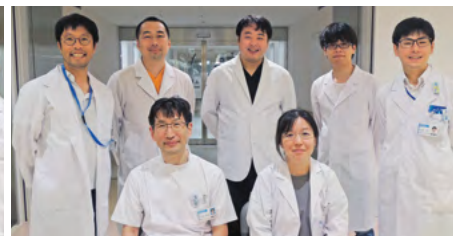
Front row left to right: Dr. Fushimi and Dr. Okuchi
Back row left to right: Dr. Yamamoto, Dr. Nakajima, and colleagues

From Routine to Rapid: Implementing Two-Minute Deep-Learning-Enabled Protocols for Enhanced Clinical Efficiency

T.B.S Buxi, M.D.[1]; Seema Sud, D.N.B.[1]
Yatin Sharma, B.Sc.[2]; Rishi Awasthi[2]

[1]Department of Imaging, Sir Ganga Ram Hospital, New Delhi, India
[2]Siemens Healthineers, Gurugram, India

Introduction

Deep learning reconstruction in MRI enables high-resolution imaging while significantly reducing scan times, thereby striking a balance between speed and image quality [1]. This study explores the clinical deployment of the Deep Resolve image reconstruction technique on a 3T MAGNETOM Vida MRI scanner (Siemens Healthineers, Erlangen, Germany) in combination with both conventional and the latest acceleration techniques. We performed a multi-anatomy comparative analysis between Deep-Resolve-based protocols and traditional acceleration techniques like GRAPPA on the 3T MAGNETOM Verio scanner (Siemens Healthineers, Erlangen, Germany). Our focus was to examine the diagnostic viability, spatial resolution, and workflow impact.

Protocol strategy and acceleration techniques

Image data selection on the MAGNETOM Verio was done retrospectively from the available database, which was limited to conventional acceleration techniques such as parallel imaging (e.g., iPAT and GRAPPA) that rely on coil sensitivity profiles and undersampling of *k*-space data to reduce scan time.

On the MAGNETOM Vida, two protocol strategies were evaluated:

Set 1 included routine Deep Resolve protocols that were optimized to acchieve very high image quality and efficiency;

Set 2 included ultra-fast protocols that were optimized to combine Deep Resolve with Simultaneous Multi-Slice (SMS, parallel excitation of more than one slice at a time) and PAT acceleration to reduce total acquisition times to

approximately 2 to 3 minutes per anatomy while preserving diagnostic image quality.

The latest deep-learning-based reconstruction technologies from Siemens Healthineers are collectively referred to as Deep Resolve. They include Deep Resolve Boost (DRB) and Deep Resolve Sharp (DRS). Deep Resolve is a sophisticated reconstruction algorithm that uses deep learning to enhance image quality and denoise undersampled acquisitions. It enables faster scans while simultaneously improving spatial resolution [2]. Together, these techniques leverage the full potential of modern hardware and deep learning software, helping to push the boundaries of fast, high-quality imaging.

We compared scans from the two MRI systems, focusing on six anatomies that represent a major portion of routine clinical workload (> 75% of MRI scans as per the IMV MR Market Outlook Report [3]): brain, spine (cervical, dorsal, and lumbar), shoulder, and knee joint.

Results

MAGNETOM Vida with routine deep learning image reconstruction protocols vs. MAGNETOM Verio with conventional image recon

Comparing images from the two scanners, it was consistently observed that the Deep Resolve protocols on the MAGNETOM Vida delivered superior image quality and spatial resolution across all anatomies studied. Structures that typically require high detail – such as cortical gray matter (Figs. 1–3), spinal nerve roots (Figs. 4 and 5), and cartilage, meniscus, and ligamentous structures (Figs. 6–10) were more clearly visualized on MAGNETOM Vida scans in both protocols, courtesy of higher resolution, higher signal-to-noise ratio (SNR), and improved image contrast.

Figures 1 through 10 are direct comparisons of individual sequences from the MAGNETOM Verio (Image A) and from the MAGNETOM Vida with routine Deep Resolve protocols (Image B) and ultra-fast protocols of 2–3 minutes enabled by Deep Resolve (Image C). Scanner identification can be verified at the top right of each image with the orange arrow, while the acquisition time (TA) can be verified at the bottom left of each image with the petrol arrow.

We observed that the images acquired on the MAGNETOM Vida, even with ultra-fast protocols, were crisper and had better edge definition and lower background noise compared to those acquired on the MAGNETOM Verio. This suggests that the deep-learning-based reconstruction capabilities do more than just match conventional methods – they enhance them to a degree that redefines diagnostic clarity, even in shorter scans.
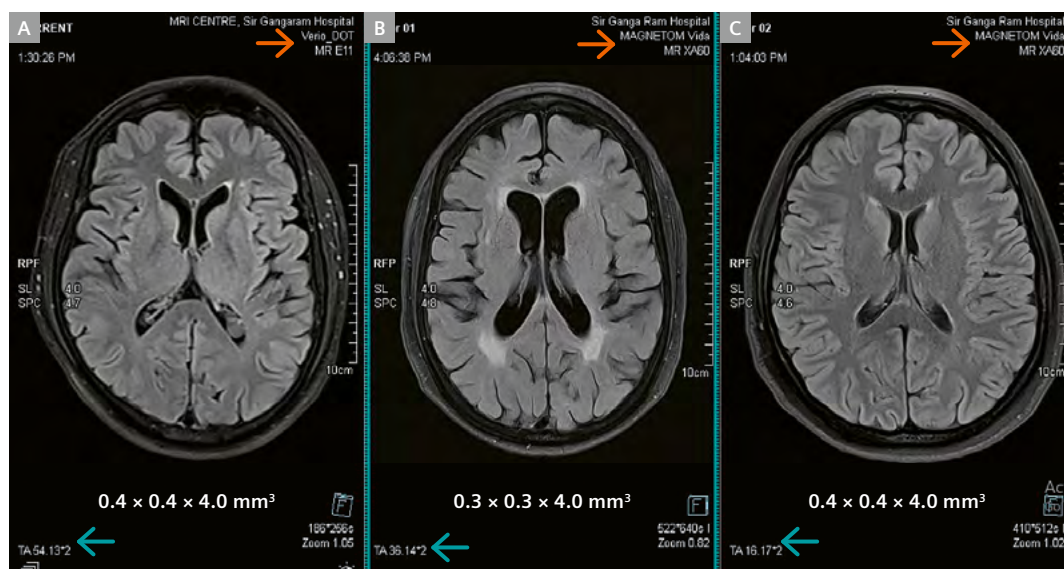
1 Image B has finer in-plane resolution than A, suggesting improved resolution. Images A and C have the same voxel size, but the image acquisition speed of C is 69% faster than A.
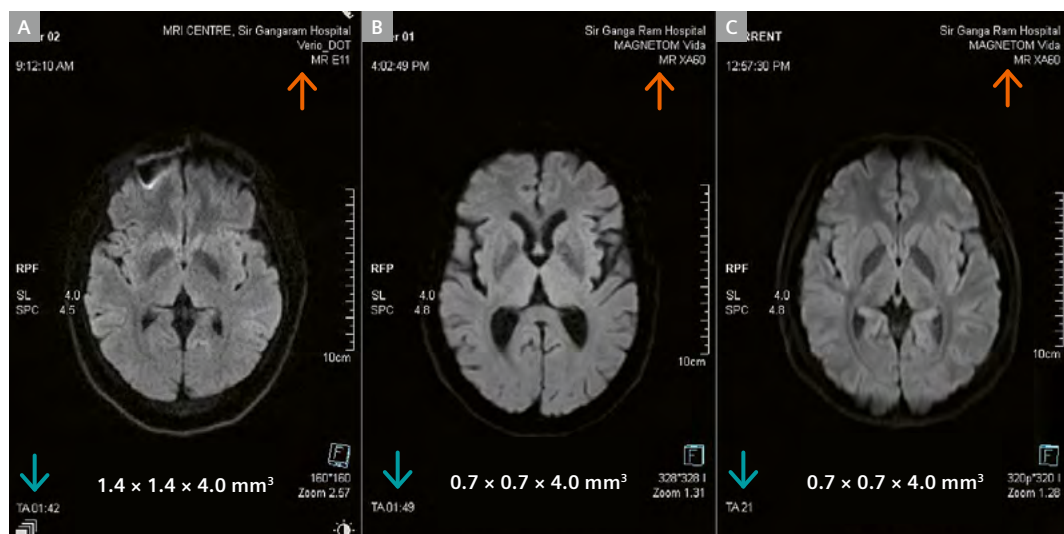
2 Both MAGNETOM Vida scans (images B and C) double the resolution compared to the MAGNETOM Verio scan (A), implying significant resolution gain. Meanwhile, the scan time for C is 79% shorter than for A.
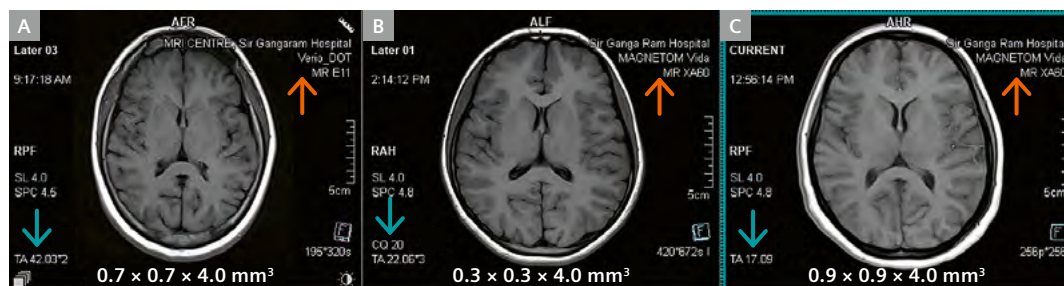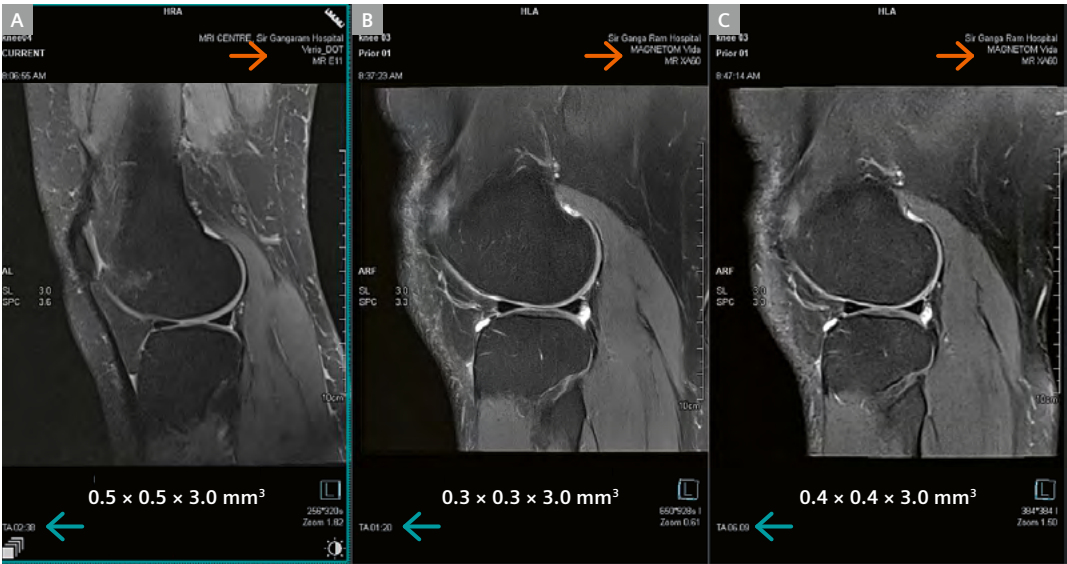
3 Image B shows higher resolution here, while the acquisition time for C is 79% faster than for A.
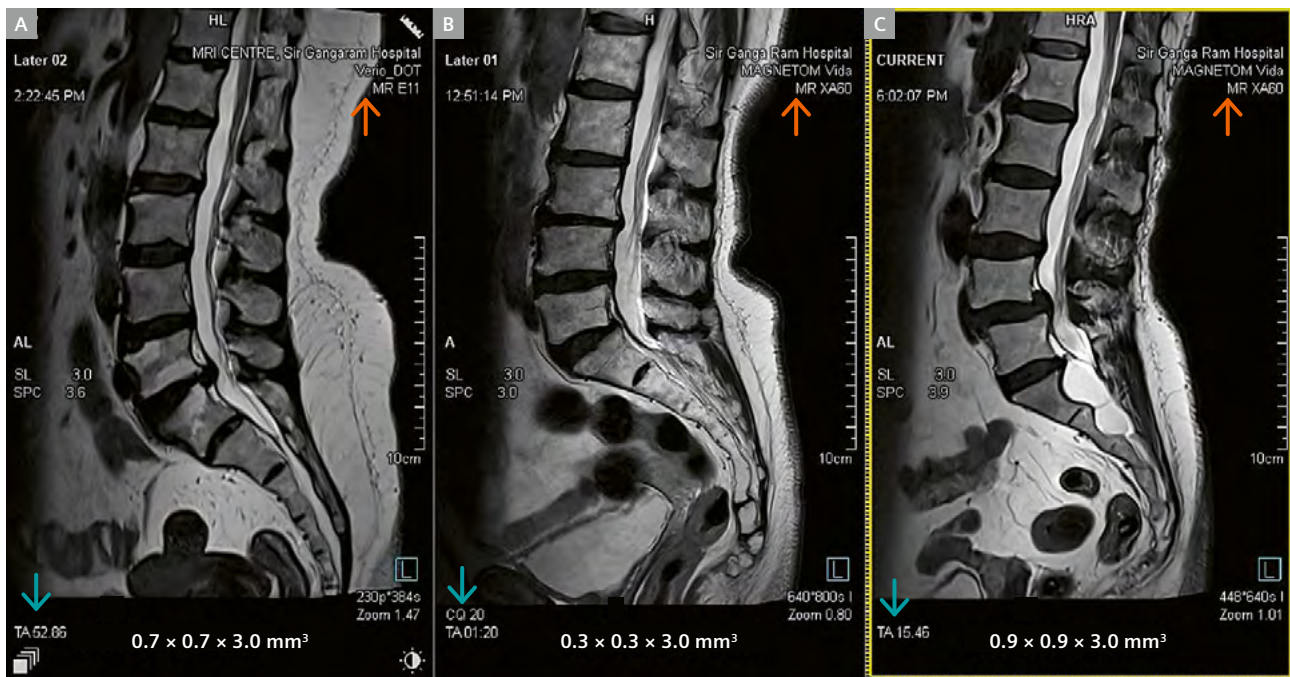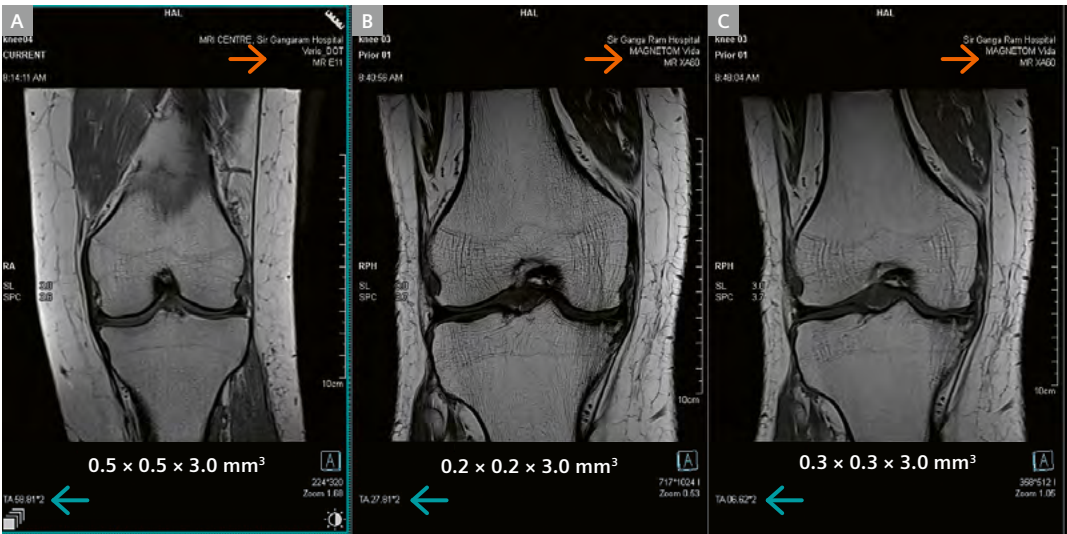
4 Images B and C offer higher resolution than A. The acquisition time for C is 70% faster than for A.
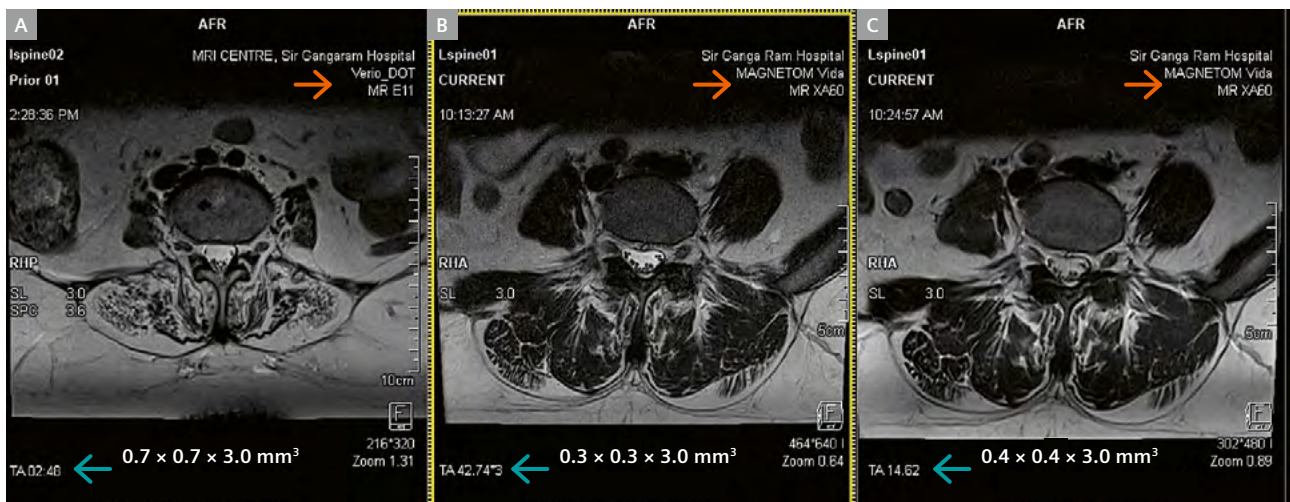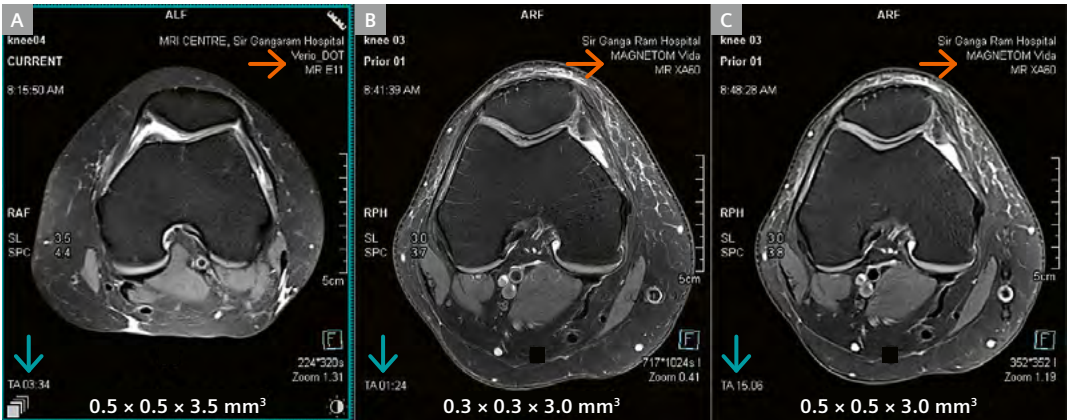

5 Images B and C have markedly better resolution than A. The acquisition time for C is 91% faster than for A.
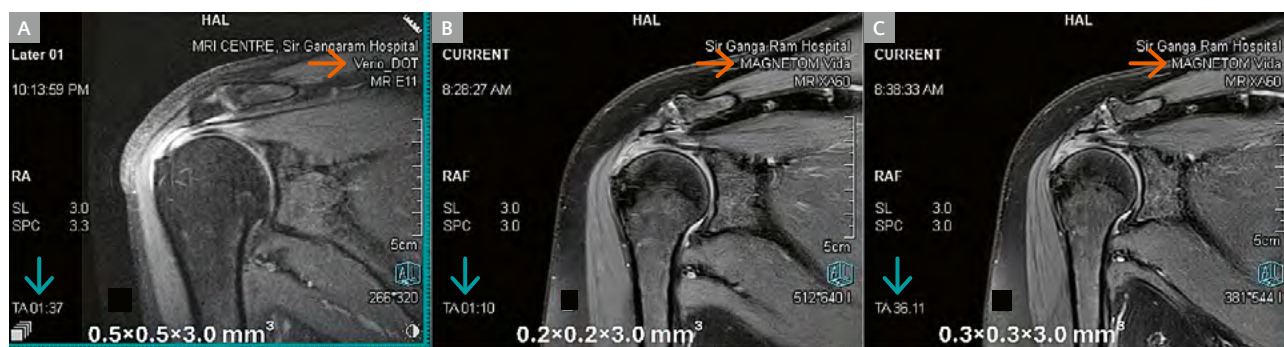
6 The acquisition time for C is 95% faster than for A.
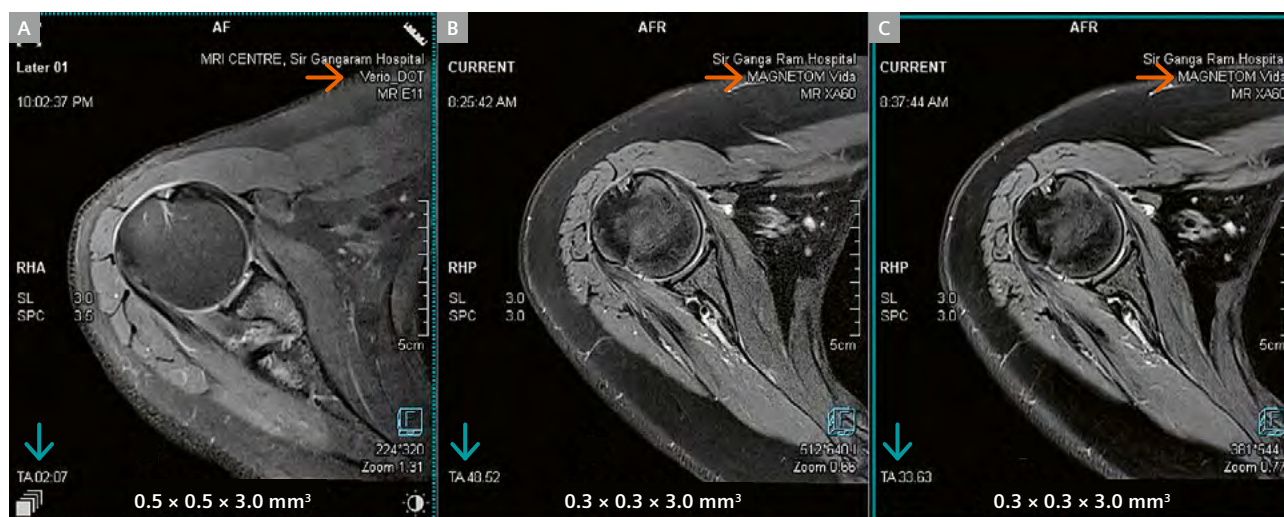

7 Substantial voxel gain in B and C compared to A, with scan time efficiency. The acquisition time for C is 88% faster than for A.

8 The acquisition time for C is 92% faster than for A.

9 Images B and C outperform A in resolution and scan time efficiency. The acquisition time for C is 61% faster than for A.

10 Images B and C outperform A in terms of resolution. The acquisition time for C is 73% faster than for A.

Routine deep learning reconstruction protocols vs. ultra-fast 2-minute protocols on the MAGNETOM Vida
Comparing the routine deep learning protocols with ultra-fast 2-minute protocols produced compelling results. Although the ultra-fast protocols were designed with aggressive SMS acceleration factors, they maintained a surprisingly high level of diagnostic integrity. There was only a marginal difference in image sharpness and noise. Importantly, there was also no significant loss in the ability to interpret clinical findings accurately (Figs. 1–10).

These 2-minute protocols offer a strategic advantage in real-world clinical settings. For instance, they are highly beneficial for imaging pediatric[1] and elderly patients, two groups who often struggle with long MR scan times (Fig.11). Similarly, claustrophobic individuals can benefit from dramatically shortened scan durations (Fig. 12). Perhaps most critically, these protocols open up the possibility of avoiding general anesthesia or sedation in patients who would otherwise require it to undergo MRI (Fig 13). In high-throughput or emergency settings, where scan time is often a bottleneck, ultra-fast protocols enabled by Deep Resolve provide a game-changing opportunity to increase patient turnover without sacrificing diagnostic quality. These use cases strongly position 2-minute protocols not merely as a backup, but also as a primary option for specific patient populations and workflow scenarios.

---

[1]MR scanning has not been established as safe for imaging fetuses and infants less than two years of age. The responsible physician must evaluate the benefits of the MR examination compared to those of other imaging procedures.
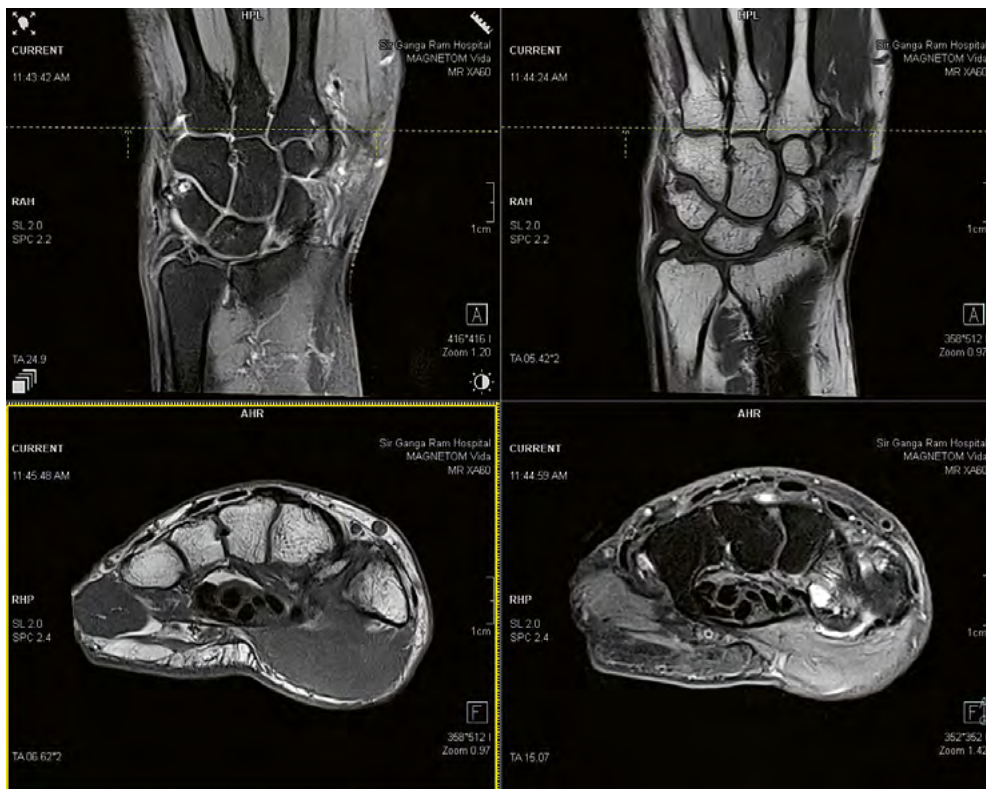
11 A wrist MR scan of a 53-year-old patient, done in under three minutes. Longer scan times often result in motion.
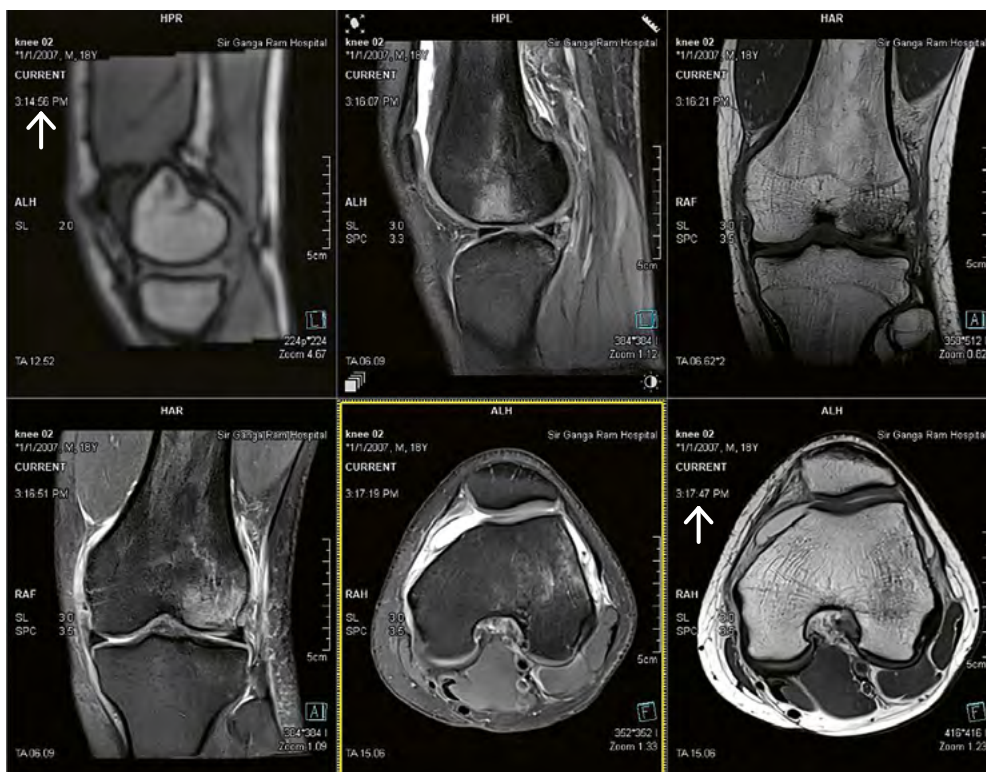
12 A knee MR scan of a claustrophobic patient. The white arrow shows the first localizer acquisition time at 03:14:56 p.m., with a scan time of 12 seconds, followed by a Pd_fs_sag of 7 seconds, a T1 cor of 13 seconds, a Pd_fs_cor of 7 seconds, a Pd_fs_tra of 16 seconds, and a PD_tra of 16 seconds. The knee exam was completed at 03:17:47 p.m., meaning it took less than three minutes. A 3-minute knee scan was previously a dream wish in clinical practice.

Sequence	TA (seconds)
Scout	19
T2 sag	21
T1 sag	25
STIR sag	25
T2 ax	26
T1 ax	19

Total: 02:05 min
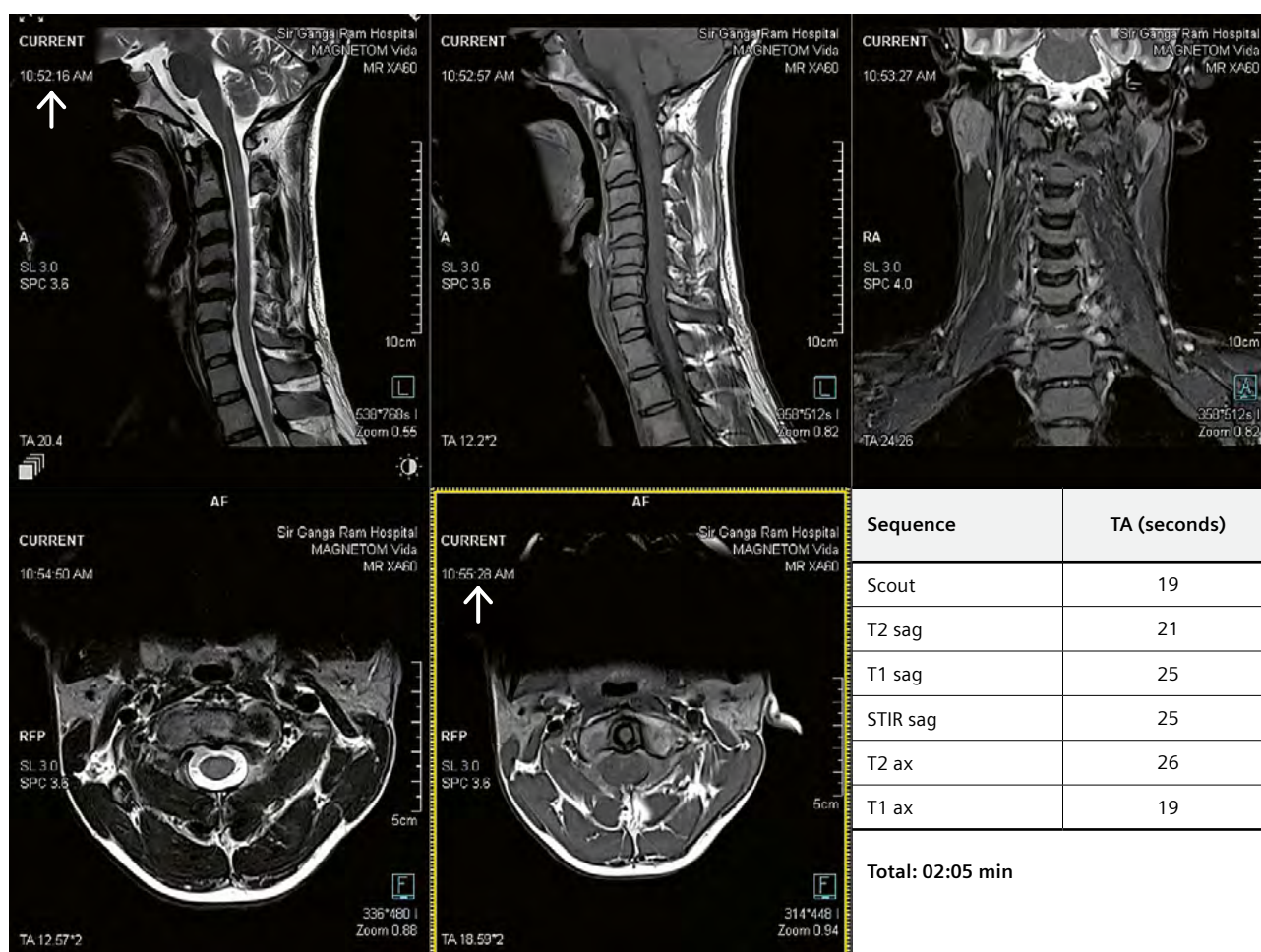
13 A cervical spine scan done in under three minutes, with a highly uncooperative patient. The white arrow shows the clock time stamp from the console. TA for T2 sag was 21 seconds, T1 sag was 25 seconds, Stir Cor was 25 seconds, T2 axial was 26 seconds, T1 axial was 19 seconds, and the localizer was 19 seconds. This makes a total scan time of just 2 minutes 5 seconds.

Conclusion

This study highlights the advantages of the Deep Resolve technique on 3T MAGNETOM Vida over the conventional acceleration methods on 3T MAGNETOM Verio. The combination of four distinct features (Deep Resolve Boost + Deep Resolve Sharp + Simultaneous Multi-Slice + GRAPPA) in the ultra-fast protocols can potentially transform MR imaging with less need for sedation and with the possibility of scanning uncooperative patients.

Acknowledgments

References

1 Rastogi A, Brugnara G, Foltyn-Dumitru M, Mahmutoglu MA, Preetha CJ, Kobler E, et al. Deep-learning-based reconstruction of undersampled MRI to reduce scan times: a multicentre, retrospective, cohort study. Lancet Oncol. 2024;25(3):400-410.
2 Behl N. Deep Resolve – Mobilizing the Power of Networks. MAGNETOM Flash. 2021;78(1):29-35. https://marketing.webassets. siemens-healthineers.com/2efe552ddbfa9372/3bcd31c 7597b/Behl_DeepResolve_MAGNETOM_Flash_78_ISMRM_2021.pdf
3 IMV Medical Information Division. IMV MR Market Outlook Report. 2024.

Contact

Seema Sud, D.N.B.
Department of Imaging
Sir Ganga Ram Hospital
Old Rajinder Nagar
New Delhi 110060
India
Tel.: +11 42251909
sudseema@gmail.com

Unlocking the Potential of Arterial Spin Labeling at 7T: Overcoming Challenges and Advancing Clinical and Neuroscience Applications

Jianxun Qu[1], Jinhao Lyu[2], Chenyang Zhao[3], Xin Lou[2], Danny JJ Wang[3,4]

[1]Siemens Healthineers, MR Research and Collaboration Team, Beijing, China
[2]Department of Radiology, The First Medical Center, Chinese PLA General Hospital (PLAGH), Beijing, China
[3]Laboratory of Functional MRI Technology (LOFT), Mark & Mary Stevens Neuroimaging and Informatics Institute, Keck School of Medicine, University of Southern California, Los Angeles, CA, USA
[4]Department of Neurology, Keck School of Medicine, University of Southern California, Los Angeles, CA, USA

Among the various functional imaging techniques, arterial spin labeling (ASL) has emerged as a powerful tool, not only in neuroscience and cognitive research but also in clinical practice. By using water as an endogenous tracer, ASL delivers quantitative perfusion information with high spatial specificity. Over the years, ASL has demonstrated its clinical value in diagnosing and monitoring a range of neurological conditions, from stroke and brain tumors to neurodegenerative disease, and has been extensively practiced at 3T and 1.5T [1]. Today, ASL is routinely practiced in numerous hospitals and research institutes worldwide. In 2017, the MAGNETOM Terra 7T scanner (Siemens Healthineers, Erlangen, Germany) received FDA approval for clinical use [2]. The advent of ultra-high-field (UHF) 7T in clinical practice has opened new opportunities for ASL while also presenting significant technical challenges [3]. The Laboratory of Functional MRI Technology (LOFT) at the University of Southern California (USC) has spearheaded the development and optimization of 7T ASL, which was applied to clinical studies through the collaboration with the PLA General Hospital (PLAGH), paving the way for its large-scale clinical adoption and for neuroscience applications.

The promise and challenges of ASL at 7T

ASL operates by magnetically labeling arterial blood water, which then serves as an endogenous tracer. After labeling, a delay is introduced to allow the labeled blood to flow into the tissue, generating perfusion contrast. The amount of labeled blood accounts for 1%–2% of the total tissue volume, making ASL a technique with an intrinsically low signal-to-noise ratio (SNR). Additionally, during the waiting period, the labeled water undergoes T1 relaxation, which further reduces the SNR [4]. In theory, higher field strengths like 7T offer significant advantages for ASL. The increased SNR and prolonged T1 relaxation times

at 7T promise a huge improvement in perfusion measurement. This has led to high expectations for ASL at UHF [5]. However, the road to realizing these benefits has been far from straightforward.

UHF MRI presents its own set of challenges. Increased magnetic field strength accentuates B0 and radio frequency (RF) field inhomogeneities, increases specific absorption rate (SAR), and markedly reduces transverse relaxation time (T2). These challenges, which are less pronounced at 3T or lower fields, demand systematic innovations and modifications to the ASL sequence to ensure robust and reliable performance at 7T. In 2009, a review article titled "Arterial spin labeling at ultra-high field: all that glitters is not gold" summarized the hurdles for the translation of ASL to UHF [6]. The title aptly reflects the difficulties.

Collaboration between USC and PLAGH

LOFT at USC has long been at the forefront of advancing ASL for clinical applications. USC was the first site in North America to install a MAGNETOM Terra scanner following FDA approval, and the lab has played a pivotal role in the development and optimization of ASL techniques at ultra-high fields. A series of publications from USC has documented the iterative improvements in ASL at 7T, addressing challenges such as B0/B1 field inhomogeneities, SAR limitations, and T2/T2* relaxation penalty [7–9]. For example, the RF and gradient in the labeling unit of pseudo-continuous ASL (pCASL) were optimized for 7T to achieve robust labeling in the presence of B0/B1 field inhomogeneities. Additionally, the widely used turbo-gradient and spin-echo readout at 3T was replaced with turbo gradient echo to mitigate transverse relaxation penalties and image distortions. The end product is a robust, whole-cerebrum, distortion-free 3D pseudo-continuous ASL sequence for 7T perfusion imaging with high resolution and quality [7, 10], as shown in Figure 1,

and the sequence can be acquired from the C2P exchange platform.

PLAGH was one of the first hospitals to deploy a 7T MRI scanner for clinical research in China. It played a critical role in evaluating the optimized 7T ASL sequence in clinical use and providing valuable feedback to USC for further refinement. In 2021, after the installation of the MAGNETOM Terra, a prototype ASL sequence was installed at PLAGH via a C2P agreement to explore its clinical utility in patients with moyamoya disease, brain tumors, and other neurological disorders. This collaboration, also supported by the collaboration team from Siemens Healthineers, led to the refinement of ASL at 7T for clinical applications, achieving spatial resolution as fine as 2.0 mm isotropic or even higher – a significant improvement over the 3.5 to 4.0 mm isotropic resolution typically achieved on conventional clinical scanners. This advancement allows for the clear visualization of small lesions and enhances the conspicuity of important imaging markers, such as arterial transit artifacts (ATA), as shown in Figure 2, which are clinically useful in identifying collateral perfusion in cerebrovascular disorders [4, 11].

In 2022, at the ISMRM Perfusion Study Group virtual meeting, Dr. Lou, director of the Radiology Department at PLAGH, shared the preliminary findings on the clinical applications of 7T ASL in a talk titled "Clinical Translations of UHF ASL Perfusion MRI" [12]. This presentation highlighted the advantages of 7T ASL, including its ability to provide higher spatial resolution and more accurate perfusion maps, offering clinicians unprecedented insights into cerebral blood flow alterations in a number of brain disorders.

While the clinical applications of ASL at 7T are pioneering, its potential in neuroscience research is equally compelling. The enhanced SNR and resolution at 7T enable researchers to delve deeper into the laminar functional activity of the cortex, uncovering subtle changes in perfusion across cortical layers. This capability opens new avenues for studying brain function and connectivity. For example, LOFT has been using 7T ASL to investigate hemodynamic parameters, such as perfusion and arrival time, across cortical layers in task functional MRI [13]. These advancements not only enhance our understanding of the brain's functional organization, but also hold promise for addressing complex neurological and psychiatric disorders.

Below are several examples showcasing the advantages of UHF ASL.
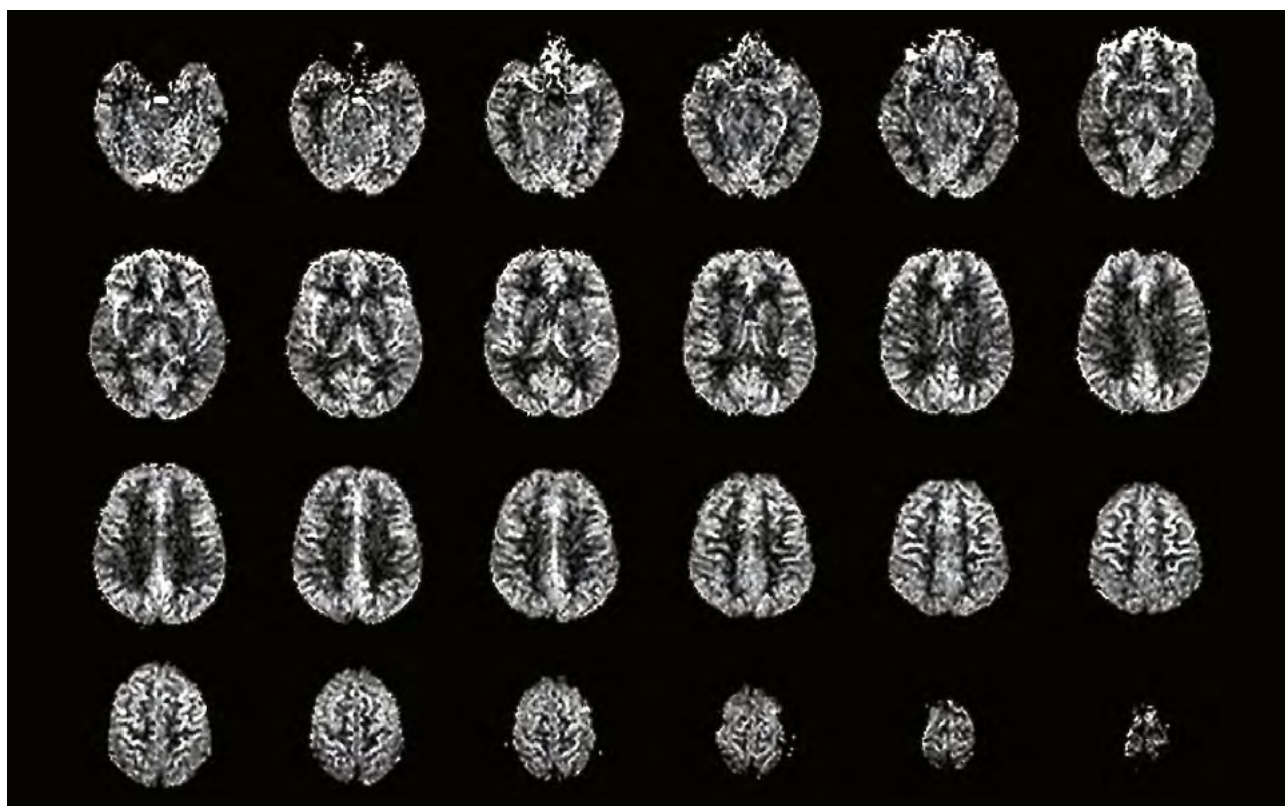
1 7T high-resolution (iso-2.0 mm) 3D TFL pCASL at 7T acquired with the following parameters: effective TR = 6.0 s, labeling duration = 1.0 s, post-labeling delay (PLD) of 2.0, TE = 1.65 ms, FOV = 224 × 192 × 112 mm³, matrix size = 112 × 96 × 56, FA = 8°, in-plane resolution = 2 × 2 mm², slice thickness = 2.0 mm, 56 slices, centric ordering, bandwidth = 490 Hz/pixel, 2 OPTIM background suppression (BS) pulses, 2D-CAIPIRINHA undersampling (R = 2 × 2) with GRAPPA reconstruction, number of repetitions = 24, and scanning time = 10 min [7].
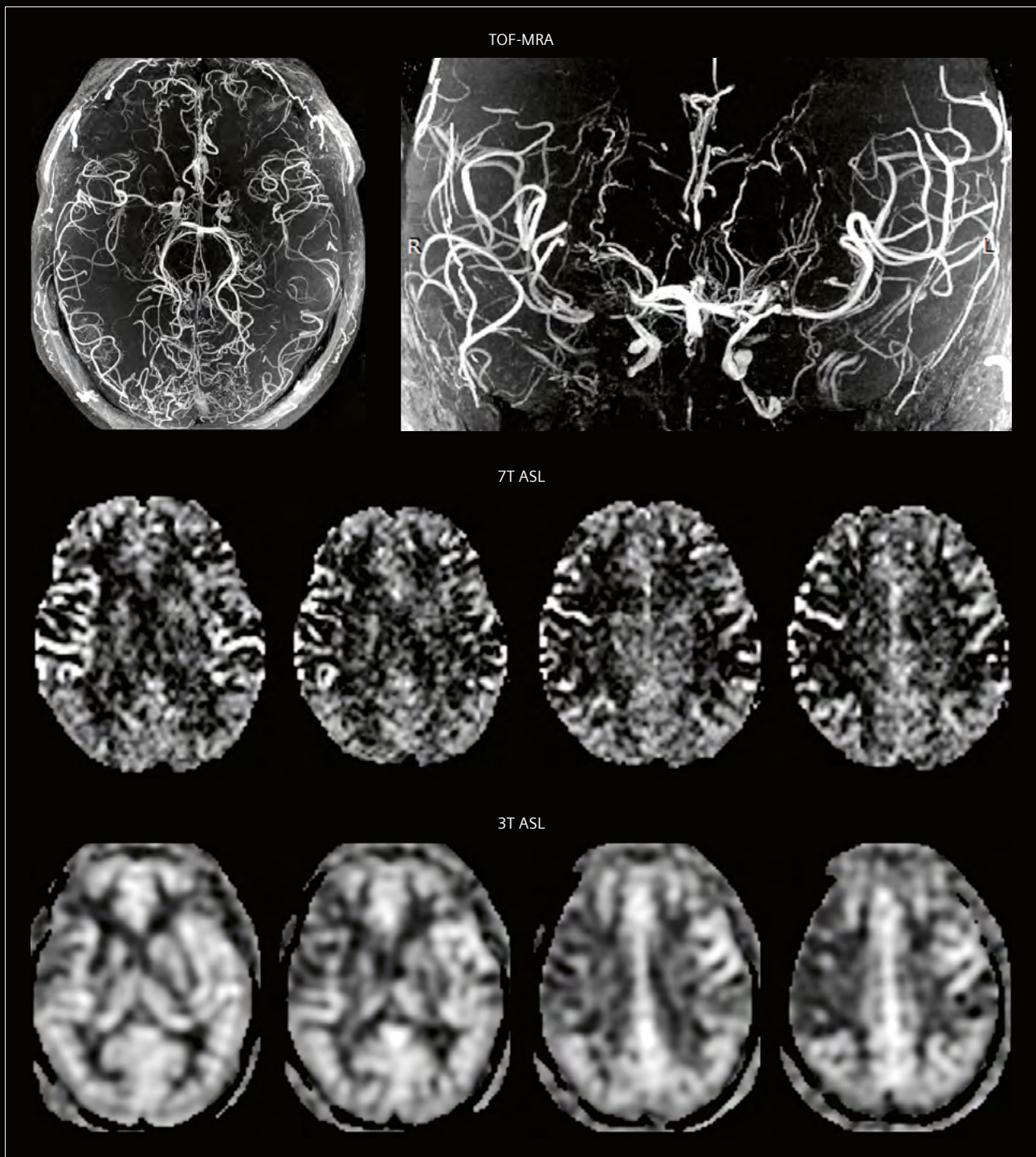
2 A 67-year-old female patient diagnosed with moyamoya disease. The 7T ASL imaging demonstrates a pronounced arterial transit artifact (ATA), whereas no significant ATA expression was detected on the 3T ASL images [11]. The in-plane resolution is 2.2 × 2.2 mm².
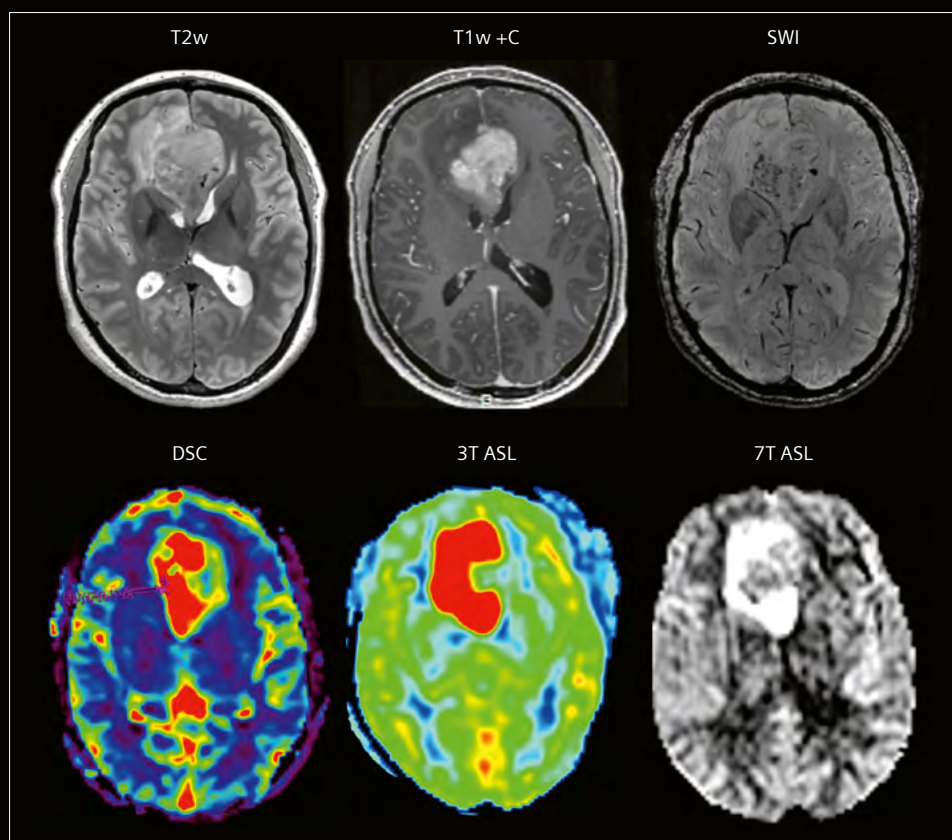
3 This is a 45-year-old woman with pathologically confirmed oligodendroglioma. A mass with predominantly mild heterogeneous hyperintensity on T2-weighted imaging (T2w) was observed in the right frontal lobe, extending into the knee of the corpus callosum, with small areas of hypointensity. Susceptibility-weighted imaging (SWI) sequences revealed signs of bleeding or calcification within the mass, and significant enhancement was noted. ASL sequences demonstrated hyperperfusion in most regions of the lesion.
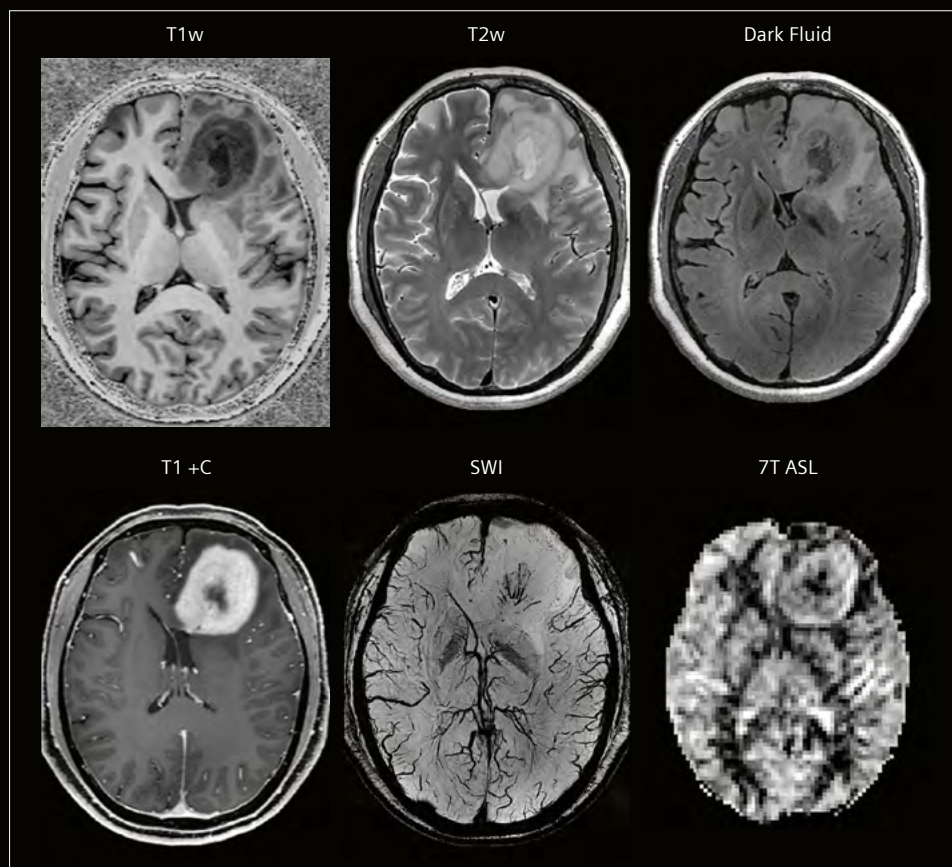
4 A 56-year-old female patient with pathologically confirmed glioblastoma. Masses were observed in both frontal lobes, exhibiting low signal on T1-weighted imaging (T1w) and high signal on T2-weighted imaging (T2w). Necrosis was noted in the center of the left frontal mass, which showed low signal on the dark fluid sequence. The SWI sequence revealed microbleeding and dilated venous vessels within the lesion, along with marked enhancement after contrast administration. ASL demonstrated hypoperfusion in the necrotic areas and hyperperfusion in the solid portion corresponding to enhanced portion.

Conclusion

The journey to harness the full potential of ASL at 7T has been marked by both challenges and breakthroughs. Thanks to the collaborative efforts of USC, PLAGH, and Siemens Healthineers, significant progress has been made in overcoming technical barriers, enabling the clinical translation of ASL at UHF and its application in neuroscience research. The theme of the 2022 ISMRM Perfusion Study Group meeting was aptly formulated: "Ultra-High Field Perfusion MRI: Reality, Not Fantasy." As a workhorse for perfusion imaging, ASL has undergone advancements that have transformed it into a practical and powerful tool for both clinical and research applications at 7T. Undoubtedly, there is much to be expected for UHF ASL in the future.

Contact

Danny J.J. Wang, Ph.D., MSCE
Professor of Neurology, Radiology, and Biomedical Engineering
University of Southern California
Stevens Hall for Neuroimaging
2025 Zonal Ave.
Los Angeles, CA 90033
USA
dannyjwa@usc.edu

Xin Lou, M.D.
Professor and Chair of
the Radiology Department
Chinese PLA General Hospital
No.28 Fuxing Road
Beijing
China
louxin@301hospital.com.cn

Jianxun Qu, M.Eng.
Collaboration Scientist
Siemens Healthineers
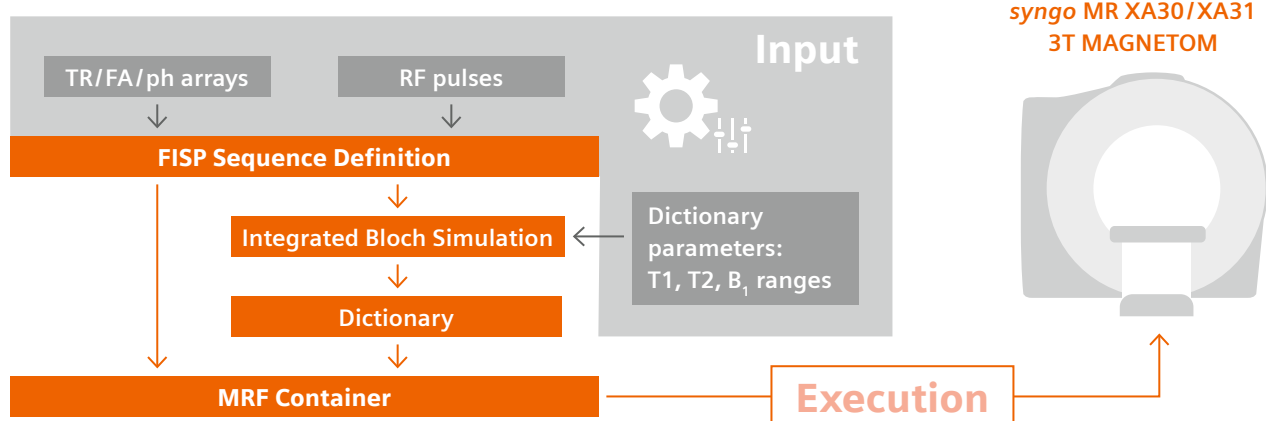Beijing
China
jianxun.qu@siemens-healthineers.com
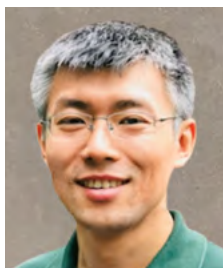
References

1   Woods JG, Achten E, Asllani I, Bolar DS, Dai W, Detre JA, et al. Recommendations for quantitative cerebral perfusion MRI using multi-timepoint arterial spin labeling: Acquisition, quantification, and clinical applications. Magn Reson Med. 2024;92(2):469–495.
2   U.S. Food & Drug Administration. FDA clears first 7T magnetic resonance imaging device [Internet]. FDA; 2017 Oct. 12 [updated 2018 Mar 2022; cited 2025 Mar 26]. Available from: https://www.fda.gov/news-events/press-announcements/fda-clears-first-7t-magnetic-resonance-imaging-device
3   Shao X, Yan L, Ma SJ, Wang K, Wang DJJ. High-Resolution Neurovascular Imaging at 7T: Arterial Spin Labeling Perfusion, 4-Dimensional MR Angiography, and Black Blood MR Imaging. Magn Reson Imaging Clin N Am. 2021;29(1):53–65.
4   Alsop DC, Detre JA, Golay X, Günther M, Hendrikse J, Hernandez-Garcia L, et al. Recommended implementation of arterial spin-labeled perfusion MRI for clinical applications: A consensus of the ISMRM perfusion study group and the European consortium for ASL in dementia. Magn Reson Med. 2015;73(1):102–16.
5   Zuo Z, Wang R, Zhuo Y, Xue R, Lawrence KSSt, Wang DJJ. Turbo-FLASH Based Arterial Spin Labeled Perfusion MRI at 7 T. PLoS One. 2013;8(6):e66612.
6   Teeuwisse WM, Webb AG, Van Osch MJP. Arterial spin labeling at ultra-high field: All that glitters is not gold. Int J Imaging Syst Technol. 2010;20(1):62–70.
7   Zhao C, Shao X, Shou Q, Ma SJ, Gokyar S, Graf C, et al. Whole-Cerebrum distortion-free three-dimensional pseudo-continuous arterial spin labeling at 7T. Neuroimage. 2023;277:120251.
8   Wang K, Ma SJ, Shao X, Zhao C, Shou Q, Yan L, et al. Optimization of pseudo-continuous arterial spin labeling at 7T with parallel transmission B1 shimming. Magn Reson Med. 2022;87(1):249–262.
9   Wang K, Shao X, Yan L, Ma SJ, Jin J, Wang DJJ. Optimization of adiabatic pulses for pulsed arterial spin labeling at 7 tesla: Comparison with pseudo-continuous arterial spin labeling. Magn Reson Med. 2021;85(6):3227–3240.
10 Zhao C, Guo F, Shou Q, Shao X, Li Y, Huang S, et al. Iso-1.25mm Whole-cerebrum pCASL at 7T for Mapping Depth-dependent Cortical Gray Matter and Tract-specific White Matter Cerebral Blood Flow. In: Proc Intl Soc Mag Reson Med. 2024 In Toronto, ON, Canada; [cited 2025 Mar 15]. Abstract #1264 [cited 2025 Mar 15]. Available from: https://archive.ismrm.org/2024/1264.html
11 Lyu J, Duan Q, Duan C, Bian X, Wang D, Zhao C, et al. Pseudo-continuous arterial spin labeling evaluation of collateral circulation at 7T and 3T MRI in Moyamoya disease. In: Proc Intl Soc Mag Reson Med. 2023. Abstract #0887 [cited 2025 Mar 15]. Available from: https://archive.ismrm.org/2023/0887.html
12 Lou X. Clinical Translations of UHF ASL Perfusion MRI. ISMRM & ISMRT Virtual Meeting Archives [Internet]. ISMRM.org [cited 2025 Mar 15]. Available from: https://www.ismrm.org/virtual-meetings/archive/
13 Shao X, Guo F, Shou Q, Wang K, Jann K, Yan L, et al. Laminar perfusion imaging with zoomed arterial spin labeling at 7 Tesla. Neuroimage. 2021;245:118724.

MR Fingerprinting Development Kit

for Tailored Research Applications

Input

TR/FA/ph arrays

RF pulses

FISP Sequence Definition

Integrated Bloch Simulation

Dictionary parameters: T1, T2, B$_1$ ranges

Dictionary

MRF Container

syngo MR XA30/XA31
3T MAGNETOM

Execution

The MR Fingerprinting Development Kit[1] takes files describing the input parameters T1, T2, RF- flip angles and pulse phases. This input generates a customized MR Fingerprinting[1] sequence. The input also serves as the basis for a Bloch simulation, which creates a MR Fingerprinting dictionary unique to its input parameters.

In a final step, the new MR Fingerprinting sequence and its unique dictionary are bundled in the so-called MR Fingerprinting container. This container can be transferred and executed on a qualified MAGNETOM 3T scanner from Siemens Healthineers[2] with a valid MR Fingerprinting license.

The sequence generation, the Bloch simulation, and the creation of the MR Fingerprinting container are performed by running a Windows command line tool[3] provided with the MR Fingerprinting Development Kit.

The MR Fingerprinting Development Kit is available for download to all users of MR Fingerprinting at **www.magnetomworld.siemens-healthineers.com/ hot-topics/mr-fingerprinting/mrf-developer-kit**

This unique MRF Development Kit empowers you to tailor the research application to your needs.

[1]*The product / feature is not for sale in the U.S. Its future availability cannot be guaranteed.*
[2]*syngo MR XA30: MAGNETOM Prisma, MAGNETOM Prisma Fit, MAGNETOM Skyra; syngo MR XA31: MAGNETOM Vida*
[3]*The user needs to install the MR Fingerprinting Development Kit on a standalone Windows 10 PC. Installation on the host computer is not possible.*

SIEMENS
Healthineers

Managing Head Exams in Claustrophobic Patients Undergoing MRI: Challenges and Strategies Using MAGNETOM Free.Max

Marcelo Fernandes Arêas

Siemens Healthineers, Erlangen, Germany

Magnetic resonance imaging (MRI) is one of the most efficient diagnostic methods, providing detailed images of the body's internal structures. However, the procedure can be distressing for claustrophobic patients due to the confined space of the MRI scanner. This article addresses claustrophobia in MRI patients and presents strategies for improving the patient experience.

The impact of claustrophobia is profound, often requiring the use of sedation, which can increase healthcare costs and delay diagnosis.

With its ultra-wide 80 cm bore, the 0.55T MAGNETOM Free.Max scanner is designed to enhance the patient experience. The wider bore provides a less confining environment, making the experience more comfortable. The system has a compact design with a shorter magnet length and is designed to allow for more flexible patient positioning. Measures such as using Contour coils, music during the scan, and cushions for positioning can further increase comfort.

The MAGNETOM Free.Max Head/Neck coil has a 12-channel design with 12 integrated pre-amplifiers with three rungs of 4 elements. The coil is tilted to 9 degrees to give patients the feeling of lying on a pillow. The upper part, with 6 elements, can be easily removed. The lower part, also with 6 elements, is usable without the upper part for highly claustrophobic patients.

When using only the lower part of the coil, the AutoAlign option still works even with the open coil. Deep learning-based image reconstruction using Deep Resolve Boost helps denoise the image and achieve good quality. We also need to make some changes on the protocol side, such as selecting prescan normalize, increasing the FOV, and changing the iPAT factor and average. The aim is to increase SNR when you scan without the upper part of the Head/Neck coil.

Another approach is to use the flexible Contour coils. The system can be configured with all three Contour coils: large (L), medium (M), and small (S). The Contour S coil with 6 channels is typically used for knee, shoulder, elbow, and other MSK exams. The high flexibility of the coil means we can set it up as a "hat" and produce a great image while the patient benefits from more comfort. This approach does not require any further changes to the protocol. AutoAlign works as usual and you can keep using the same parameters and achieve the same image quality as the standard brain examination with the Head/Neck coil. This method can also be used on 1.5T and 3T systems using the Flex or UltraFlex coil.

1 Positioning a claustrophobic patient for a head exam on a 0.55T MAGNETOM Free.Max. **(1A)** Both parts of the Head/Neck coil; **(1B)** lower part of the Head/Neck coil only; **(1C)** adding the Contour S coil.

2A Head/Neck coil

2B Lower part of Head/Neck coil only

2C Lower part of Head/Neck coil + Contour S coil
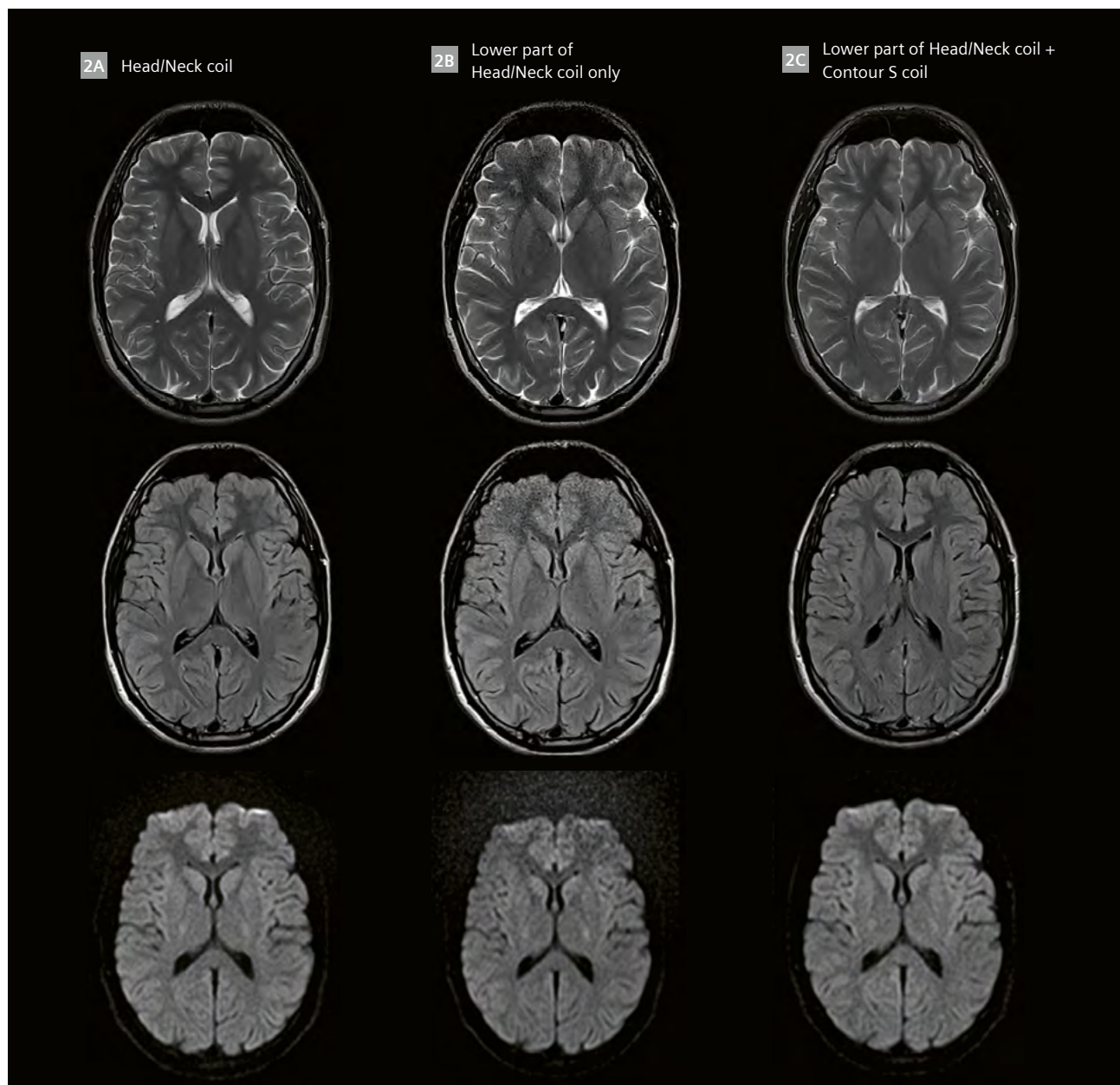
Study ID 7aaaa0862

2 The sequences in **(2A)** and **(2C)** are the same: field of view 230 × 201, BW 100, average 2, TE 114, Grappa 4. The sequence in **(2B)** was acquired without the upper part of the coil and differs slightly: field of view 240 × 240, Grappa 3, and turbo factor 17. Of note, in **(2B)** the frontal region shows reduced image quality compared to temporal and okzipital regions. This is certainly a limitation of this coil setup.

Contact

Marcelo Fernandes Arêas
Siemens Healthineers
SHS DI MR M&S S CVP
Allee am Roethelheimpark 2
91052 Erlangen
Germany
marcelo.areas@siemens-healthineers.com

Examining Musculoskeletal Implants with Lower-Field MRI

Bianca Samsula[1], Simon Balzer[2], Mathias Nittka, Ph.D.[2]; Markus Lentschig, M.D.[1]

[1]ZEMODI - MVZ Zentrum für moderne Diagnostik, Bremen, Germany
[2]Siemens Healthineers, Erlangen, Germany

Implant surgery for musculoskeletal diseases has been progressing steadily in recent years, and the number of operations is continually growing. In Germany alone, some 200,000 hip replacements are performed each year, along with roughly 150,000 knee replacements. Improvements and new developments in implant technology mean that other joint replacement surgeries (such as for the shoulder, elbow, ankle, or knuckles) are also being performed increasingly frequently [1].

This is leading to rising demand for diagnostic imaging connected to pathologies at or around these implants*. Since the established methods of X-ray and CT imaging are of limited diagnostic value, patients are increasingly being referred to MRI.

With conventional high-field MRI scanners, it is difficult to examine body regions that contain metallic implants: The large difference in magnetic susceptibility between metal and the surrounding tissue causes significant local distortion of the magnetic field, which produces the familiar image artifacts in the region of the implant. Even when using advanced applications like WARP and SEMAC, the image quality on conventional 1.5T and 3T MRI systems remains limited, making it difficult to diagnose the pathology.

With a low field strength of 0.55T, the systems of the MAGNETOM Free. Platform have the advantage of producing significantly fewer susceptibility artifacts than is commonly the case with high-field systems. With far fewer distortions and artifacts in the direct vicinity of implants, these lower-field scanners make it possible to identify pathologies better than with high-field systems, despite the lower resolution and signal-to-noise ratio. Like imaging at higher field strengths, these examinations use turbo spin echo (TSE) sequences with optimized acquisition parameters that are activated via the WARP option in the sequence. Increased excitation and readout bandwidths are crucial here, especially in combination with STIR technology as a more robust alternative to conventional spectral fat saturation for fat suppression.

In addition to established advanced acceleration techniques (parallel imaging and Simultaneous Multi-Slice acquisition), deep-learning-based image reconstruction methods offer enormous potential – now also at lower field strengths. This means that, even at these lower field strengths, it is possible to produce high-quality diagnostic MR images in very acceptable acquisition times.

The combination of lower field strength and deep learning therefore lends itself particularly well to imaging implants using 0.55T systems in clinical routine.

This article will present our experience using a selection of case studies. Full protocols for the hip and knee regions are available on MAGNETOM World: www.magnetomworld.siemens-healthineers.com/clinical-corner/protocols

The patients were examined on a 0.55T MAGNETOM Free.Max using only TSE sequences with the WARP option and Deep Resolve reconstruction. The main parameters are presented in the tables. We did not use more advanced WARP techniques such as VAT[1] and SEMAC[2]. Since there were already so few distortions compared to high-field imaging, these techniques offered us no diagnostically relevant advantage that would have justified the disadvantages.

For hip examinations, patients were positioned on their back and head first. The Spine coil and the Contour M/L coil were used for imaging.

For knee examinations, patients were positioned on their back and feet first. The Contour Knee coil was used for imaging.

---

[1]View-angle tilting (VAT): Slices are acquired at a tilt angle to partially compensate for the metal distortions. This can cause some blurring, but VAT is essential for the SEMAC technique.

[2]Slice encoding for metal artifact correction (SEMAC): This technique can at least partially correct even very severe distortions. However, it is very time-consuming and therefore generally associated with a loss of resolution and contrast.

---

*The MRI restrictions (if any) of the metal implant must be considered prior to patient undergoing MRI exam. MR imaging of patients with metallic implants brings specific risks. However, certain implants are approved by the governing regulatory bodies to be MR conditionally safe. For such implants, the previously mentioned warning may not be applicable. Please contact the implant manufacturer for the specific conditional information. The conditions for MR safety are the responsibility of the implant manufacturer, not of Siemens Healthineers.

## Example images showing the advantage of lower field over high field
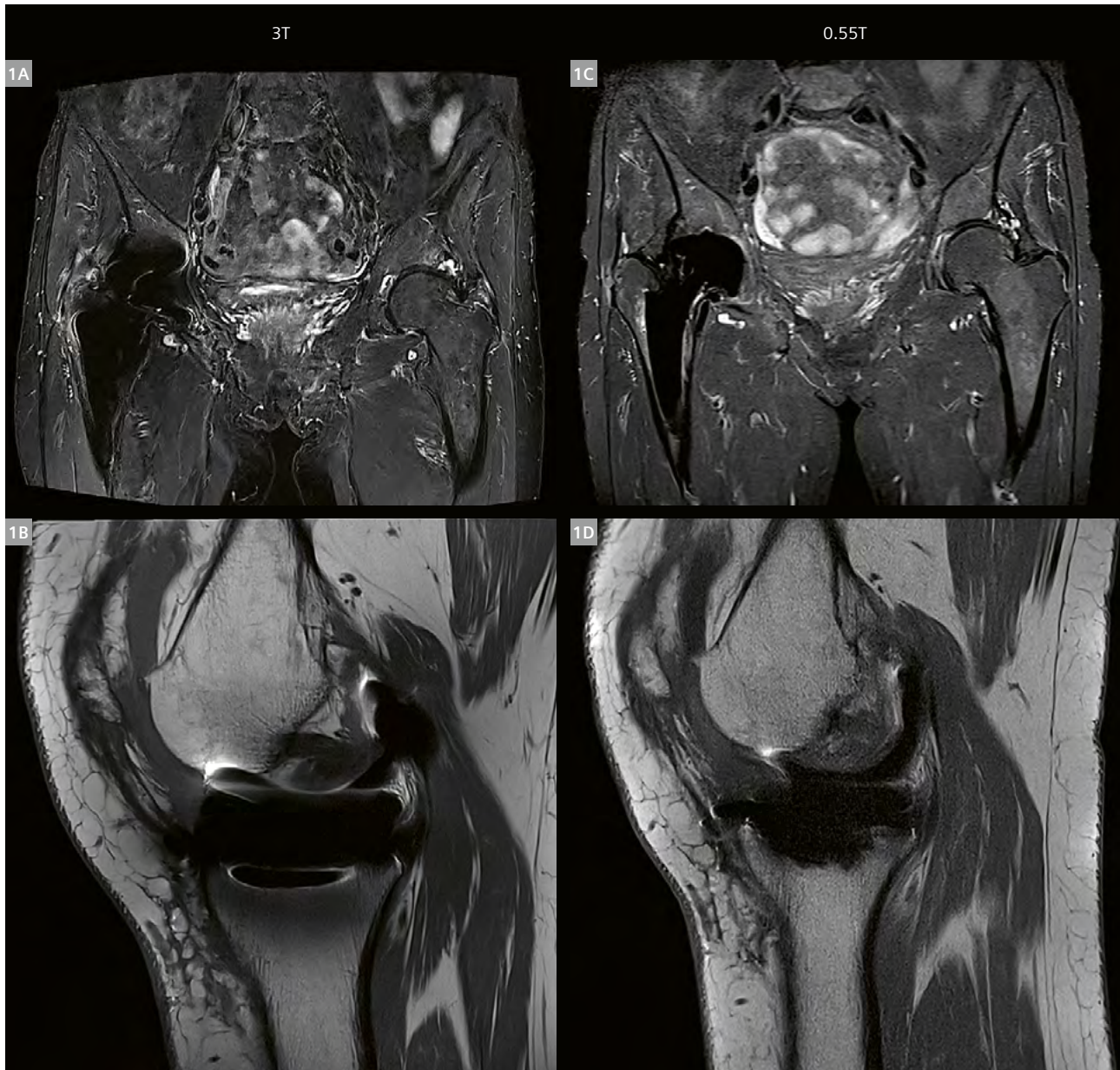
1 Left **(1A)** STIR cor and **(1B)** T1 TSE sag on a 3T system. Right **(1C)** STIR cor and **(1D)** T1 TSE sag on a 0.55T system.

Clinical case studies

Knee

Increasing pain after a partial knee replacement. Loosening? A Dual Energy CT scan showed no evidence of loosening. Bone marrow edema of the medial femoral condyle; stress reaction with joint effusion.
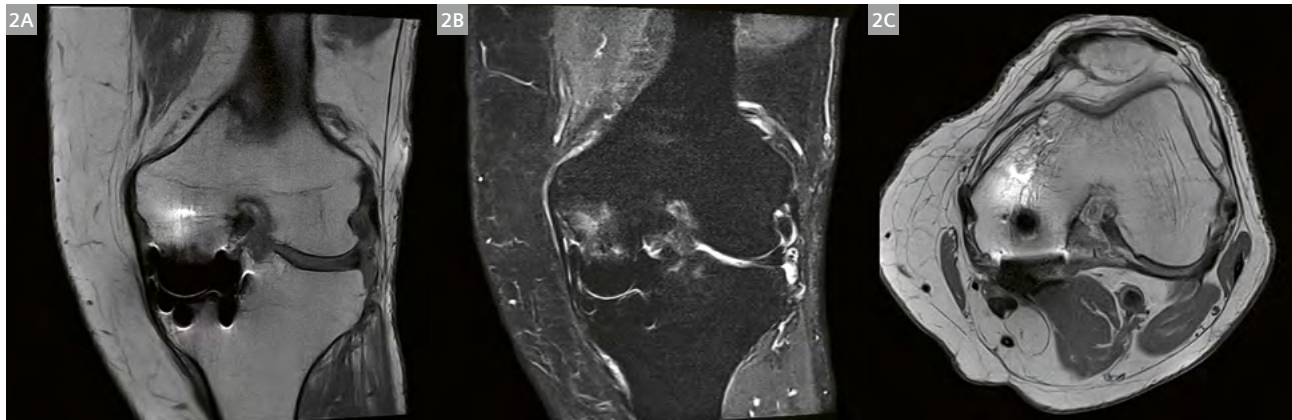
2 (2A) PD cor. (2B) STIR cor, bone marrow edema clearly visible. (2C) PD tra.

Knee

Increasing pain following partial knee replacement; establishing cause of pain. An examination on the 3T system was discontinued due to artifacts. Implant appears normal on MRI. Pronounced arthritic changes in the lateral joint cavity, Grade 3 lateral meniscus tear and Grade 4 chondromalacia at the lateral femoral condyle.

3 (3A) STIR cor, visible bone marrow edema with arthritic changes. (3B) STIR sag, visible bone marrow edema with arthritic changes. (3C) PD tra.

Hip

Pain after implantation of a gamma nail following femoral neck fracture approximately 12 months ago.
Material intact. Fracture line still visible with significant soft tissue buildup.

4 **(4A)** T1 cor. **(4B)** STIR cor, clearly visible soft tissue buildup. **(4C)** PD tra, clearly visible fracture line with soft tissue buildup.

Hip

Bilateral total hip replacement followed by recurring dislocation of the right hip prosthesis. Increasing pain in the right hip since falling eight months ago. No fracture, no loosening of the endoprosthesis, no bone lesion. Extensive joint effusion leaking into the trochanteric bursa.
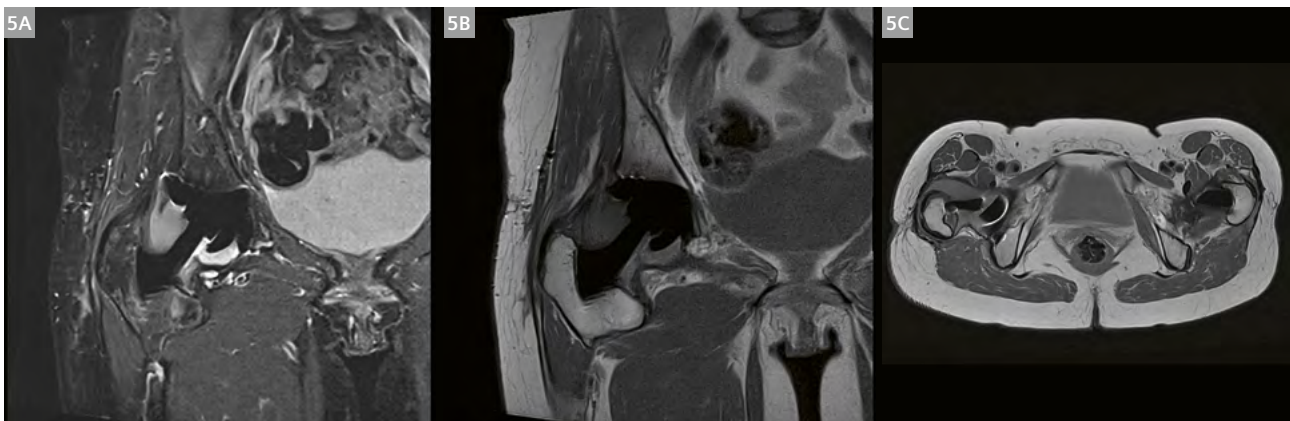
5 **(5A)** STIR cor, clearly visible effusion and hematoma. **(5B)** PD cor. **(5C)** PD tra, clearly visible effusion.

	T1 TSE sag	T1 TSE cor	STIR cor	STIR tra	STIR sag	PD TSE cor	PD TSE tra
Voxel size [mm³]	0.3 × 0.3 × 3.0	0.3 × 0.3 × 3.0	0.3 × 0.3 × 3.0	0.4 × 0.4 × 4.0	0.4 × 0.4 × 3.0	0.2 × 0.2 × 3.0	0.3 × 0.3 × 3.0
TR/TE [ms]	420 / 8.2	440 / 8.4	3800 / 39	3600 / 39	3500 / 38	2830 / 26	2710 / 25
PE-direction	H>>F	R>>L	R>>L	R>>L	H>>F	R>>L	R>>L
Phase oversampling [%]	150	150	130	200	200	140	150
Avg./Conc.	3 / 2	3 / 2	3 / 2	2 / 2	4 / 1	3 / 1	3 / 1
BW [Hz/px]	305	300	301	300	302	302	300
TA [min]	3:37	3:57	4:43	3:30	3:49	3:03	2:47

Table 1: Scan parameters, knee.

	PD TSE cor	T1 TSE cor	STIR cor
Voxel size [mm³]	0.5 × 0.5 × 3.0	0.5 × 0.5 × 3.0	0.6 × 0.6 × 3.0
TR/TE [ms]	2500 / 31	386 / 7.2	5000 / 45
PE-direction	R>>L	R>>L	R>>L
Phase oversampling [%]	100	200	200
Avg./Conc.	2 / 1	2 / 2	2 / 1
BW [Hz/px]	395	352	300
TA [min]	2:04	2:26	2:57

Table 2: Scan parameters, bilateral hip.

	PD TSE cor	T1 TSE cor	STIR cor	PD TSE sag	STIR sag
Voxel size [mm³]	0.5 × 0.5 × 3.0	0.5 × 0.5 × 3.0	0.7 × 0.7 × 3.0	0.5 × 0.5 × 3.0	0.7 × 0.7 × 3.0
TR/TE [ms]	2600 / 24	482 / 8	6100 / 35	3000 / 24	7100 / 35
PE-direction	R>>L	R>>L	R>>L	H>>F	H>>F
Phase oversampling [%]	170	170	200	200	200
Avg./Conc.	2 / 1	2 / 2	2 / 1	2 / 1	2 / 1
BW [Hz/px]	391	349	352	391	352
TA [min]	1:59	2:06	2:46	2:29	3:13

Table 3: Scan parameters, unilateral hip.

Hip

Total hip replacement in 2016. Increasing hip pain for roughly the past three years. Slight bone marrow edema along the stem of the prosthesis, markedly lateral, indicating loosening of the prosthesis.
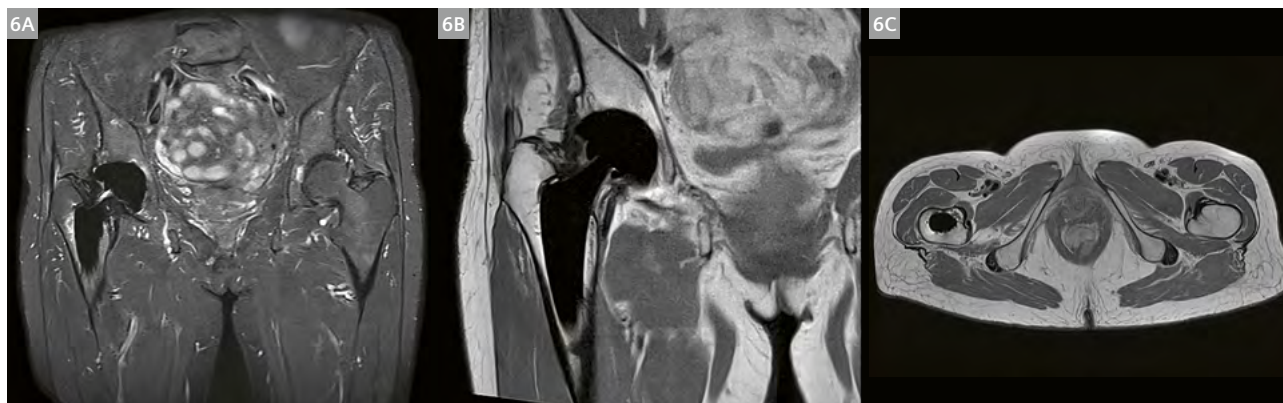
6 **(6A)** STIR cor, with visible bone marrow edema bordering the implant. **(6B)** PD cor. **(6C)** PD tra.

Conclusion

It has been three and a half years since our MAGNETOM Free.Max was installed, and we see the system as the perfect complement to our high-field scanners (a 3T MAGNETOM Skyra, a 3T MAGNETOM Lumina, a 1.5T MAGNETOM Altea, a 1.5T MAGNETOM Avanto Fit, and our PET/MR scanner, Biograph mMR). Thanks partly to its wide-bore design, our MAGNETOM Free.Max is ideal for examining claustrophobic or extremely over-weight patients and is very popular among these popula-tions. Particularly when it comes to examining patients with musculoskeletal implants, we find our lower-field system to be at a great advantage over the high-field systems. This means that diagnosing pathologies following implants is no longer limited to Dual Energy CT scanning: MR imaging can now supply crucial additional information for these cases.

References

1 Feuerriegel GC, Sutter R. Managing hardware-related metal artifacts in MRI: current and evolving techniques. Skeletal Radiol. 2024;53(9):1737–1750.

Contact

Bianca Samsula
ZEMODI - MVZ Zentrum für moderne Diagnostik
Schwachhauser Heerstraße 63a
28211 Bremen
Germany
bianca.samsula@zemodi.de

Markus Lentschig, M.D.
ZEMODI - MVZ Zentrum für moderne Diagnostik
Schwachhauser Heerstraße 63a
28211 Bremen
Germany
markus.lentschig@zemodi.de

Download the 0.55T MAGNETOM Free.Max protocols (**.exar1 and PDF**) at
**www.magnetomworld.siemens-healthineers.com/
clinical-corner/protocols**
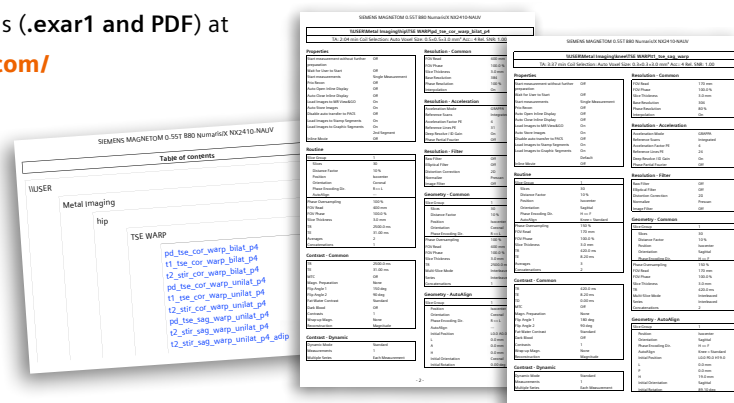
MSK MRI on MAGNETOM Free.Max: Initial Experience

Thomas M. Link, M.D., Ph.D. and Daehyun Yoon, Ph.D.

University of California, San Francisco (UCSF), Department of Radiology and Biomedical Imaging, San Francisco, CA, USA

Introduction

The unveiling of the MAGNETOM Free. Platform, with its unique field strength of 0.55T, by Siemens Healthineers has opened new possibilities for MRI. While low field strengths have been explored in past, the combination of 0.55T with new hardware and state-of-the-art deep-learning reconstruction techniques offers the potential for using this system reliably in many clinical conditions.

In this article, we document our experience in using a MAGNETOM Free.Max for musculoskeletal (MSK) applications. Specifically, we focus on situations where the MAGNETOM Free.Max (i) provides comparable diagnostic quality to conventional field strengths and (ii) improves our current imaging capabilities in patients with metal hardware, such as spinal fusions and total joint replacements, where traditional high-field scanners often fall short.

At our institution at UCSF, the MAGNETOM Free.Max is located in an outpatient facility with a high volume of MSK cases, and next to other scanners with conventional field strengths of 1.5T and 3T. This offers a convenient way to directly compare and optimize our experience across field strengths.

Initial findings have shown that the MAGNETOM Free.Max scanner is quite promising in routine spine imaging, where the image quality is quite good. We have a large majority of spine cases that are routinely scanned on the MAGNETOM Free.Max. Our radiology practice, however, still favors 1.5T and 3T for other joints such as knee or ankle, which require imaging with high spatial resolution for detailed visualization of the cartilage and ligaments.

One area where the MAGNETOM Free.Max particularly excels is metal-artifact-suppressed imaging, especially in the spine and in areas around total joint replacements.

Most importantly, in patients with multi-level spine fusion, our experience with conventional field strengths of 1.5T and 3T has been quite mixed. Our MAGNETOM Free.Max, on the other hand, has consistently provided better image quality and diagnostic information in this cohort. We believe that the substantially reduced off-resonance and radio-frequency specific-absorption-rate (SAR) burden at 0.55T may provide unique opportunities to enhance visualization of the metal-tissue interface and enable contrasts (e.g., diffusion and post gadolinium) that were previously excluded for patients with extensive spine hardware.

The larger bore size has also facilitated imaging for larger patients, although our experience is limited due to the demography of the community that we serve.

Protocol adaptation for 0.55T

We started with our standard protocols from 3T systems and tweaked them in an iterative process to get our optimized set of parameters at 0.55T. For turbo spin-echo (TSE) protocols, we adjusted the spatial resolution where necessary to maintain the signal-to-noise ratio (SNR). All the protocols had Deep Resolve Boost turned on. Implant[1] protocols for joint arthroplasty applied the TSE WARP feature, which optimizes the sequence to reduce metal-induced distortions employing high bandwidth and View Angle Tilting (VAT).

To remove the fat signal, we used a prototype research TSE-Dixon sequence[2] that supports Deep Resolve Boost, instead of fat-saturated TSE or STIR TSE sequences. The preferred method for fat suppression near metal at 1.5T or 3T is STIR, as fat suppression methods based on chemical shift, such as fat saturation using a spectrally selective

---

[1] The MRI restrictions (if any) of the metal implant must be considered prior to patient undergoing MRI exam. MR imaging of patients with metallic implants brings specific risks. However, certain implants are approved by the governing regulatory bodies to be MR conditionally safe. For such implants, the previously mentioned warning may not be applicable. Please contact the implant manufacturer for the specific conditional information. The conditions for MR safety are the responsibility of the implant manufacturer, not of Siemens Healthineers.

[2] Although the TSE-Dixon sequence is commercially available, it is not yet available with deep learning-based image reconstruction in our scanner software version. The deep learning based reconstruction of TSE-Dixon is work in progress. The sequence is still under development and not commercially available. Its future availability cannot be ensured.

RF pulse and fat-water separation using a Dixon-based approach, become unreliable near metal due to strong off-resonance. However, STIR significantly lowers the SNR, making it challenging to incorporate into TSE at 0.55T that employs high pixel bandwidth for metal artifact mitigation. It is because the sequence configuration already has two factors (high pixel bandwidth and 0.55T) that substantially lower the SNR. On the other hand, 0.55T limits the area of strong off-resonance near metal, giving it a second chance for conventional chemical-shift-based fat suppression methods. Unfortunately, the reduced resonance frequency difference between fat and water at 0.55T makes selective fat saturation more challenging than at 1.5T or 3T. TSE-Dixon, although it exhibited fat-water swap artifacts near metal in some cases, shows the best SNR among other options, with Deep Resolve Boost, and

has the potential to achieve more accurate fat-water separation later with retrospective application of a more advanced fat-water separation algorithm. Additionally, the in-phase images of TSE-Dixon can serve as simple TSE images without fat suppression. Advanced metal suppression techniques such as SEMAC were not included in the final protocol. This is because our initial scans suggested a lack of additional benefits for the extra scan time. We believe further optimization is needed to develop relevant protocols for the metals known to cause more severe off-resonance, such as cobalt-chromium and stainless steel.

Case studies

We present a selection of clinical cases that demonstrate our experience with MSK MRI on our MAGNETOM Free.Max.

Case 1
Clinical spine study of the lumbar spine with no significant imaging abnormalities.
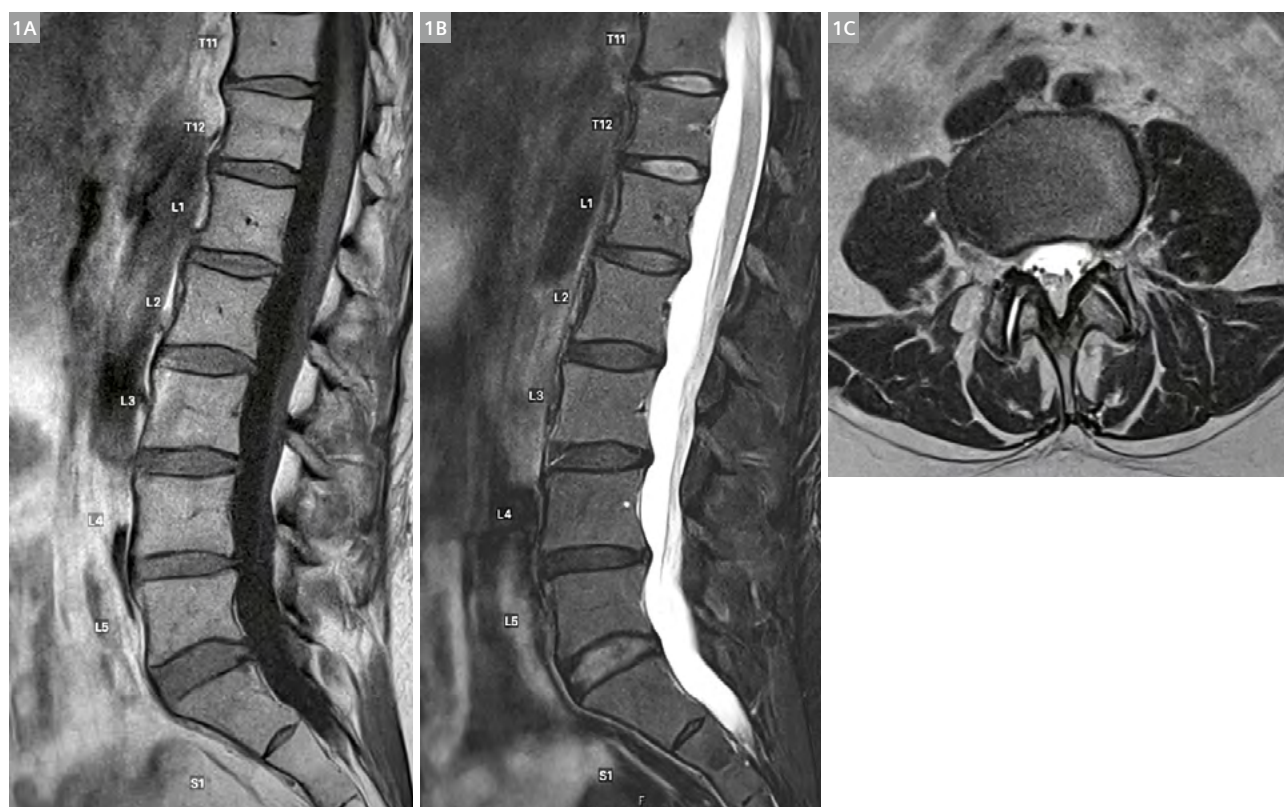
1 Lumbar spine 0.55T MRI, **(1A)** sag T1-weighted TSE, **(1B)** sag T2-weighted TSE-water from fast-Dixon, and **(1C)** axial T2-weighted TSE sequences.
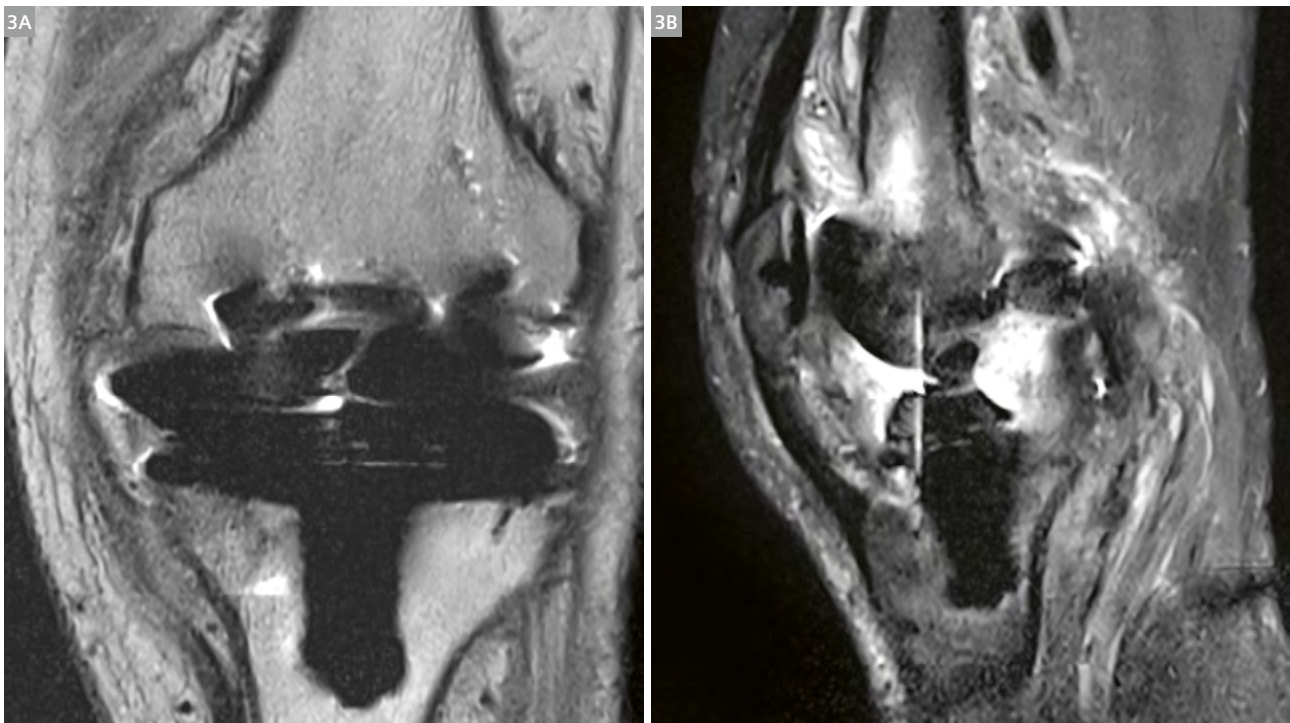
Case 2
Status post left total hip resurfacing (cobalt-chromium, metal on metal)
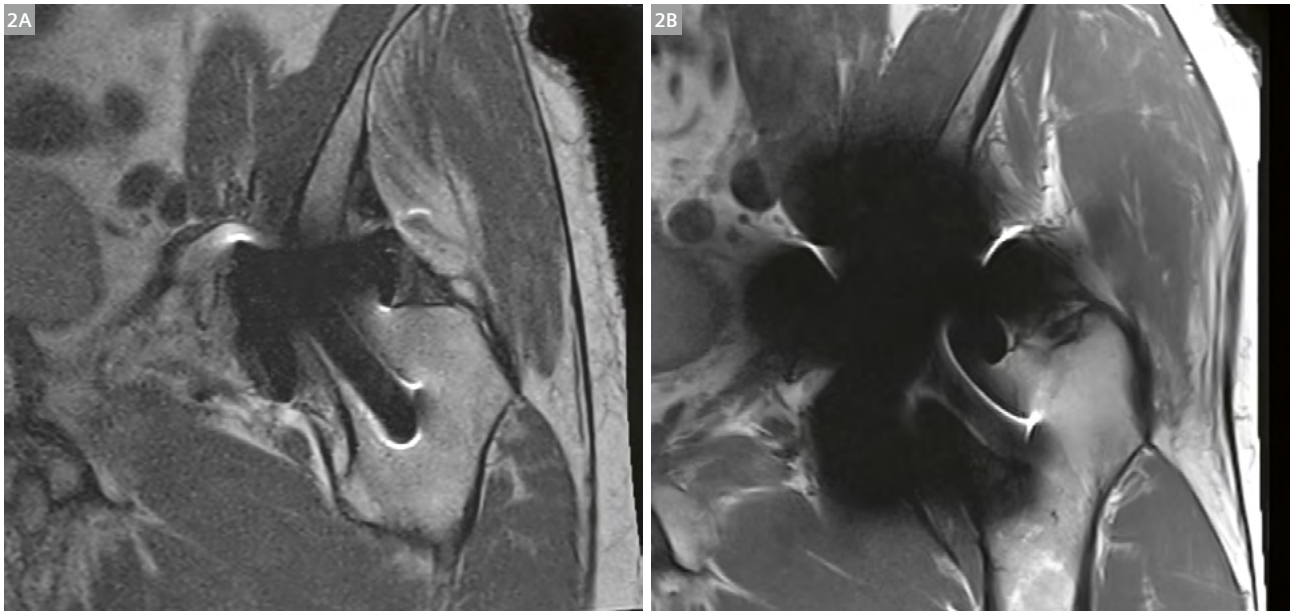
2 **(2A)** PD-weighted WARP TSE imaging at 0.55T and **(2B)** at 3T.

Case 3
Status post total left knee replacement (titanium alloy).

3 Images obtained at 0.55T with WARP TSE, **(3A)** PD-weighted and **(3B)** STIR. Bone marrow signal abnormalities and synovitis are clearly shown on the STIR sequence.

Case 4
Status post lumbar spinal fusion (titanium).

4 Sagittal T2-weighted TSE sequences at **(4A)** 0.55T and **(4B)** 1.5T.
Note: as explained above, TSE-Dixon (fast-Dixon option) was used at 0.55T. The image shown here is the in-phase image, which is equivalent to TSE.

Summary

The MAGNETOM Free.Max has been a great addition to our fleet of MR scanners for MSK applications. While we handle routine spine cases using any of the three available field strengths (0.55T, 1.5T, 3T) at our outpatient center, our imaging practice has developed a preference for the MAGNETOM Free.Max when it comes to patients with metal hardware – specifically, multi-level spinal fusions. This is because of the improved image quality that we have been able to achieve with this platform. As of this writing, we are also actively encouraging and educating our clinicians to consider scheduling their patients with metal hardware on the MAGNETOM Free.Max, due to its superior and consistent image quality, shorter scan protocol, and shorter imaging times.

　　　　Overall, the MAGNETOM Free.Max scanner has demonstrated its potential to significantly improve imaging outcomes in challenging MSK cases, making it a valuable asset in the diagnostic toolkit at UCSF.

Contact

Professor Thomas M. Link, M.D., Ph.D.
Chief of the Musculoskeletal Imaging Section and Clinical Director of the Musculoskeletal and Quantitative Imaging Research Group
Department of Radiology & Biomedical Imaging
University of California, San Francisco
505 Parnassus Avenue, M-391
San Francisco, CA 94143-0628
USA
thomas.link@ucsf.edu

Daehyun Yoon, Ph.D.
Assistant Professor of Radiology
Department of Radiology & Biomedical Imaging
University of California, San Francisco
505 Parnassus Avenue, M-391
San Francisco, CA 94143-0628
USA
daehyun.yoon@ucsf.edu

Wideband Black-Blood Cardiac Magnetic Resonance in Patients with Implantable Cardiac Devices

Pauline Gut, M.Sc.[1,2,3]; Hubert Cochet, Ph.D.[1,4]; Matthias Stuber, Ph.D.[1,2,5]; Aurélien Bustin, Ph.D.[1,2,4]

[1]IHU LIRYC, Heart Rhythm Disease Institute, Université de Bordeaux – INSERM U1045, Pessac, France
[2]Department of Diagnostic and Interventional Radiology, Lausanne University Hospital and University of Lausanne, Switzerland
[3]Faculty of Biology and Medicine, University of Lausanne, Switzerland
[4]Department of Cardiovascular Imaging, Hôpital Cardiologique du Haut-Lévêque, CHU de Bordeaux, Pessac, France
[5]CIBM Center for Biomedical Imaging, Lausanne, Switzerland

Introduction

The use of implantable cardiac devices (ICDs), such as implantable cardioverter defibrillators and pacemakers, is the most effective treatment for ventricular tachycardia, for heart failure, and for preventing sudden cardiac death [1, 2]. Use of these devices has been increasing over the past decades [3, 4], with approximately 1.4 million implantations occurring worldwide each year [5]. Cardiovascular magnetic resonance imaging (MRI) has become an essential diagnostic tool, due to its ability to generate high-resolution images of soft tissues without ionizing radiation. With the development of modern MR-compatible ICDs [6], the prevalence of patients with ICDs undergoing cardiovascular MRI has increased in recent decades. About 50%–70% of these patients will require follow-up MRI scans during their lifetime [7].

Bright-blood late gadolinium enhancement (LGE) imaging, such as phase-sensitive inversion recovery (PSIR) [8], is clinically routinely applied in patients for myocardial scar assessment, as it provides an excellent scar-myocardium contrast. However, the poor scar-blood contrast can challenge the detection and assessment of subendocardial, small, or focal scars. This scar-blood contrast can be improved using black-blood LGE imaging [9], which simultaneously darkens healthy myocardium and blood signals while enhancing scar signal using an appropriate inversion time (TI).

Thanks to technological advances, most implantable devices such as ICDs are now designed to be MR compatible[1], enabling wider clinical use of cardiac MRI in this patient population. However, the presence of ferromagnetic materials in the generator of these devices creates strong field inhomogeneities around the device. This results in bright-blood LGE images and black-blood LGE images that are heavily impacted by signal loss, hyperintensity artifacts, and image distortion, often resulting in non-diagnostic images [10]. In this article, we present the "wideband" MRI technique for reducing ICD-related artifacts, and its application to black-blood LGE imaging.

Theory

The inversion recovery pulse used in the PSIR and black-blood sequences and discussed in this article is an adiabatic hyperbolic secant radiofrequency (RF) pulse. An adiabatic hyperbolic secant pulse of duration T_p, amplitude modulation $A(t)$, phase modulation $\phi(t)$, and frequency modulation $\omega(t)$ is described by the following equations:

$$B_1(t) = A(t)\, e^{-i\phi(t)}$$

$$A(t) = A_0\, sech(\beta t)$$

$$\phi(t) = \mu\, ln(sech(\beta t))$$

$$\omega(t) = \frac{d\phi(t)}{dt} = -\mu\beta\, tanh(\beta t)$$

with $-T_p/2 \leq t \leq T_p/2$ (seconds), A_0 the maximum B_1 field amplitude (micro tesla), β the frequency modulation parameter (radians per second), and μ the degree of phase modulation (dimensionless). The RF spectral bandwidth Δf of an adiabatic hyperbolic secant is determined by:

$$\Delta f = \frac{\mu\beta}{\pi}$$

---

[1]The MRI restrictions (if any) of the metal implant must be considered prior to patient undergoing MRI exam. MR imaging of patients with metallic implants brings specific risks. However, certain implants are approved by the governing regulatory bodies to be MR conditionally safe. For such implants, the previously mentioned warning may not be applicable. Please contact the implant manufacturer for the specific conditional information. The conditions for MR safety are the responsibility of the implant manufacturer, not of Siemens Healthineers.

Finally, to fulfil the adiabatic passage, the maximum B_1 field amplitude must satisfy the following condition:

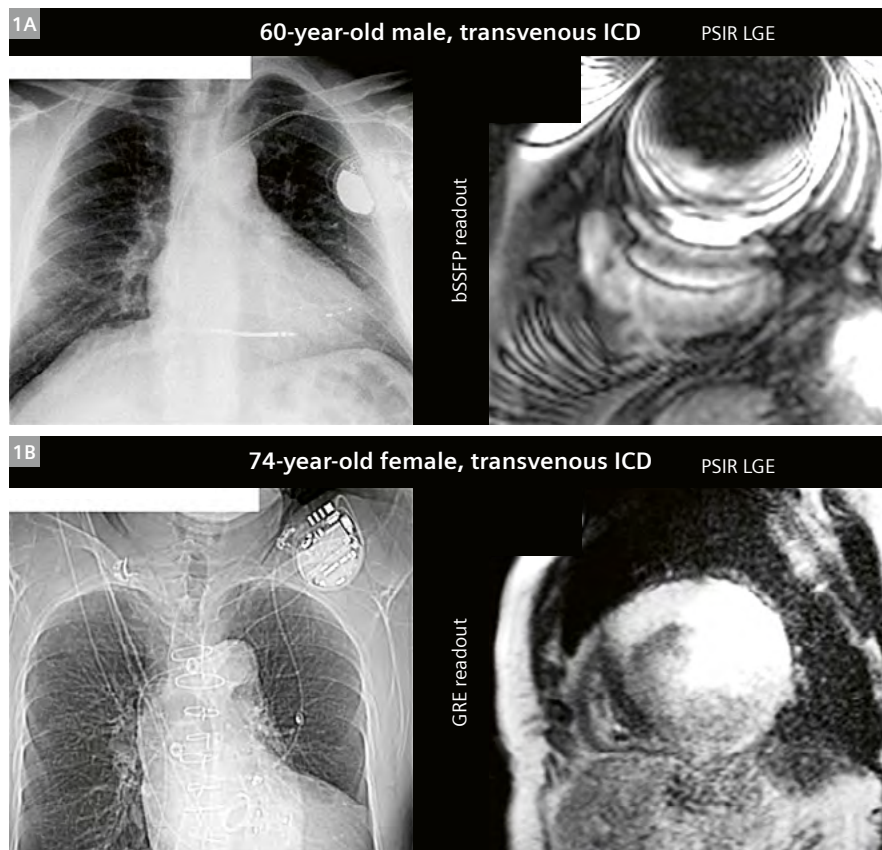$$A_0 \geq \frac{\mu\sqrt{\beta}}{\gamma}$$

with γ being the gyromagnetic ratio in Hz/Gauss. A smaller increase in μ and a larger increase in β can achieve a certain RF spectral bandwidth without a dramatic increase in the B_1 amplitude A_0.

ICD-related artifacts on LGE images

Implantable cardiac devices have ferromagnetic components with positive magnetic susceptibility. When placed in a magnetic field environment, the field lines are distorted around the cardiac device. This generates local field inhomogeneities, resulting in off-resonant spins (≠ Larmor frequency) with a frequency shift of 2 to 6 kHz of tissues located at 5 to 10 cm from the device generator [11]. When applying a bright-blood LGE sequence such as PSIR, the inversion recovery pulse used in the sequence will correctly invert spins at the Larmor frequency, but not off-resonant spins, as the frequency shift caused by the device may exceed the spectral bandwidth of the inversion pulse, typically around 0.8–1.1 kHz. This incorrect inversion results in a region of high signal intensity (bright region) caused by the mismapping of a disproportionate number of spins (MR signal) to this location during image reconstruction (Fig. 1). This abnormally bright region is known as a hyperintensity artifact, which often obscures the myocardium and compromises image quality and diagnosis. In addition, dephasing of protons on either side of the device generator boundary results in signal loss (dark region) (Fig. 1).

Banding artifacts can also be seen on PSIR LGE images in the presence of an ICD, and are associated with balanced steady-state free-precession (bSSFP) readout (Fig. 1A). The bSSFP readout relies on steady-state magnetization, which is achieved by rapidly repeating RF pulses with very short repetition times (TRs). The signal in bSSFP is a function of off-resonance frequency and varies periodically with off-resonance with a period of 1/TR. Field inhomogeneities (B0) cause phase accumulation between RF pulses. When the accumulation is a multiple of π, the signal nulls and dark bands appear [12]. A gradient recalled echo (GRE) readout can be used instead to avoid the banding artifacts when a cardiac implant is present (Fig. 1B). The GRE readout is much less sensitive to off-resonance since its signal does not periodically null with frequency offsets.

1A   **60-year-old male, transvenous ICD**   PSIR LGE   bSSFP readout

1B   **74-year-old female, transvenous ICD**   PSIR LGE   GRE readout

1 ICD-related artifacts on PSIR LGE images. **(1A)** Hyperintensity, signal loss, and bSSFP-associated banding artifacts. **(1B)** Hyperintensity and signal-loss artifacts, no banding artifacts with gradient echo readout.

Wideband bright-blood LGE

In 2014, Rashid et al. [11] introduced the concept of wideband PSIR LGE. They showed in their study a frequency shift of 2 to 6 kHz of tissues located at 5 to 10 cm from the device generator, which is well outside the standard spectral bandwidth of the 1.1 kHz inversion pulse. They therefore proposed to broaden the RF spectral bandwidth of the inversion pulse in the PSIR sequence from 1.1 to 3.8 kHz ($\mu = 16$, $\beta = 750$ rad/s) (Figs. 2A, 2B). They showed that this RF spectral bandwidth broadening, known as wideband, enables the correct inversion of off-resonant spins, reducing or even eliminating hyperintensity artifacts that obscure the myocardium (Figs. 2C, 2D).

Wideband black-blood LGE

A black-blood LGE sequence can be achieved using inversion recovery followed by T2 preparation [13–15]. In this article, we present a 2D GRE black-blood sequence with inversion recovery (pulse duration = 10.24 ms) and T2 preparation (duration = 27 ms) (Fig. 3). The T2 preparation used is B1-insensitive and adiabatic, and consists of a 90°
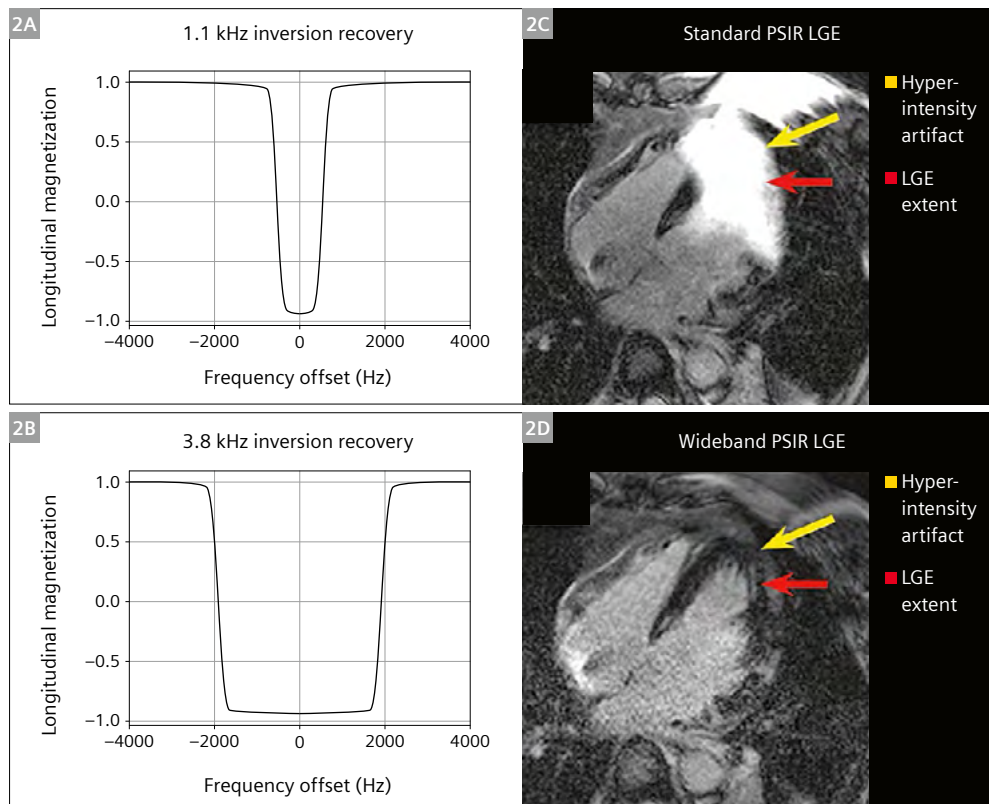
2 **(2A)** Standard spectral bandwidth of 1.1 kHz and **(2B)** wideband spectral bandwidth of 3.8 kHz of the inversion recovery pulse in the PSIR sequence, providing **(2C)** images with severe ICD-related hyperintensity artifacts and **(2D)** images with a net reduction in hyperintensity artifacts.
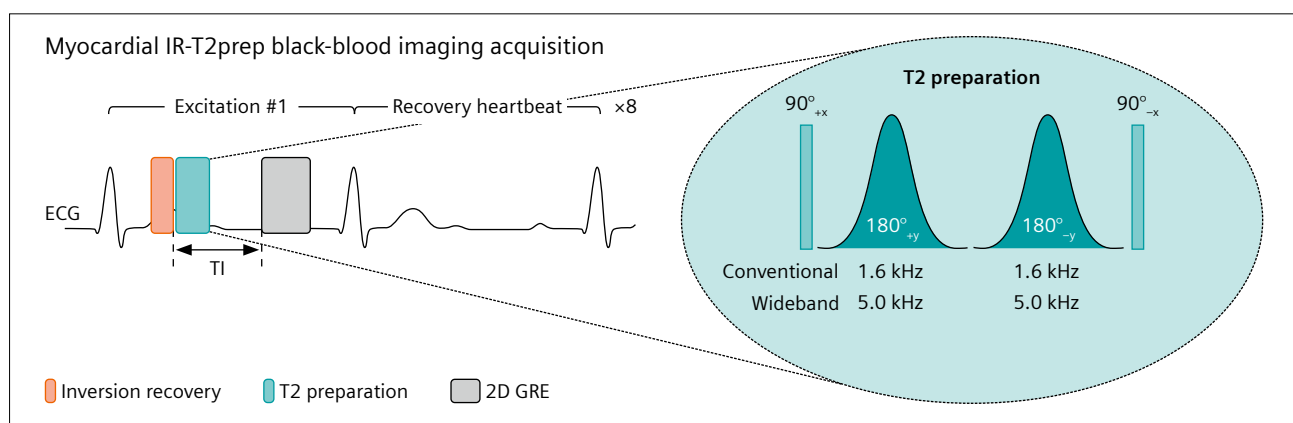

3 Myocardial IR-T2prep black-blood imaging framework, inversion recovery (IR) and T2 preparation pulses employed.
Abbreviations: TI = inversion time; ECG = electrocardiogram; GRE = gradient echo.

tip-down RF pulse, two hyperbolic secant 180° refocusing RF pulses, and a 90° tip-up RF pulse [16] (Fig. 3). A spoiling gradient is then applied to suppress any residual transverse magnetization.

Similarly to PSIR, the spectral bandwidths used in the inversion recovery pulse (0.8 kHz), and the T2 preparation refocusing pulses (1.6 kHz) in the standard black-blood sequence are too narrow to properly prepare the magnetization in the presence of cardiac implants, resulting in LGE images with hyperintensities, signal loss, and image distortion (Figs. 4, 5). In 2024, wideband RF pulses were integrated into this black-blood LGE imaging to allow better LGE detection with reduced hyperintensity artifacts that obscure the myocardium in ICD patients [17] (Figs. 4, 5). It was proposed to broaden the spectral bandwidth of the inversion recovery from 0.8 to 3.8 kHz ($\mu = 16$, $\beta = 750$ rad/s, $A_0 = 19$ µT), as proposed for wideband PSIR, and to broaden the spectral bandwidth of the T2 preparation refocusing pulses from 1.6 to 5.0 kHz ($\mu = 25$, $\beta = 785$ rad/s, $A_0 = 30$ µT).
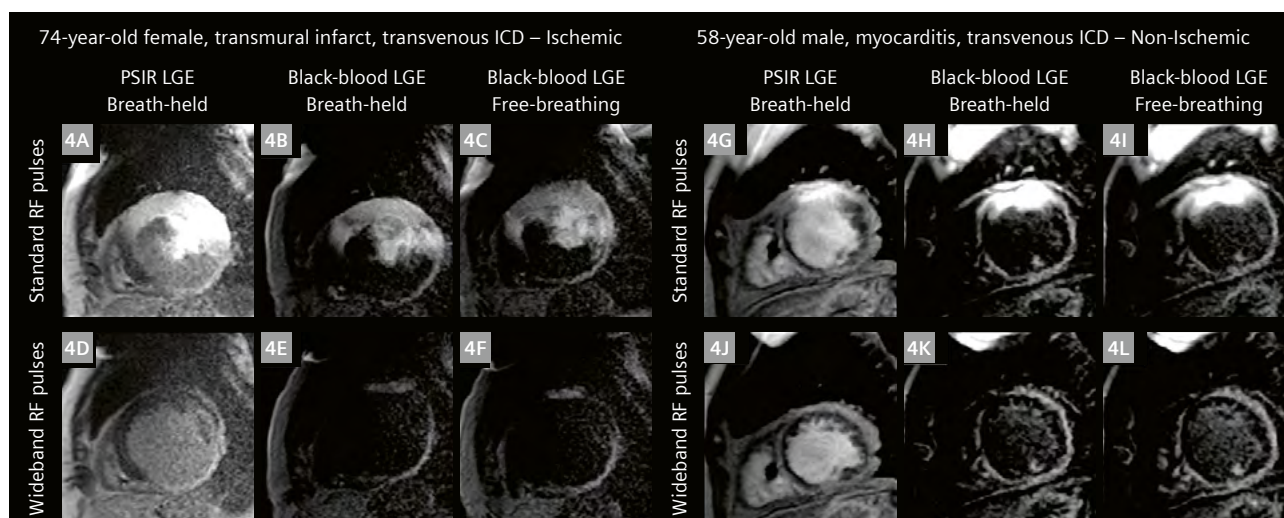
4 Cases 1 and 2. One female patient with ischemic infarct and one male patient with dilated cardiomyopathy with heart failure and reduced ejection fraction on probable myocarditis scar imaged at CHUV Lausanne University Hospital on a 1.5T MAGNETOM Sola system. Severe hyperintensities obscure the myocardium using standard PSIR LGE **(4A, 4G)** and standard black-blood LGE **(4BC, 4HI)**. These are suppressed using wideband PSIR LGE **(4D, 4J)** and wideband black-blood LGE **(4EF, 4KL)**.
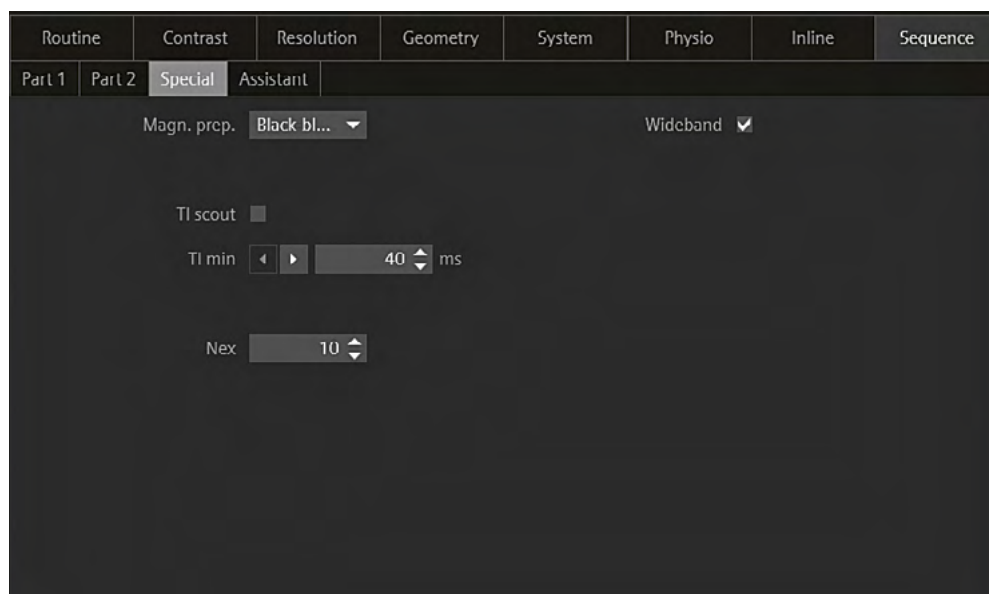

5 The Special card of the wideband black-blood sequence on a 1.5T MAGNETOM Sola system. Either PSIR or black-blood imaging can be chosen under "Magn. prep," not under "Contrast." Wideband RF pulses can be selected if the patient has an ICD. A TI scout can be performed for PSIR and black blood with or without wideband RF pulses. The number of excitations (Nex) is manually set and corresponds to the number of collected images for each slice position.

Tips and tricks for successful black-blood LGE imaging

Since its introduction, the 2D wideband black-blood GRE LGE sequence has been applied in a breath-hold study [17] and in a free-breathing study [18] with nonrigid motion correction at 1.5T (MAGNETOM Aera and MAGNETOM Sola, Siemens Healthineers, Erlangen, Germany). The protocol used is described in Table 1. It employs an electrocardiogram-triggered pulse to capture multiple single-shot images for each slice location during mid-diastole. In the special card of the protocol of the sequence at the MRI machine, PSIR or black-blood imaging can be chosen and wideband RF pulses can be activated or deactivated.

A dedicated TI scout can be performed with or without wideband RF pulses for both PSIR and black-blood LGE imaging. The optimal TI is then set to cancel to tissue of interest: black healthy myocardium for PSIR, and both black myocardium and black blood for black-blood imaging. The number of excitations (Nex) per slice location is determined manually (Fig. 5). A single short-axis slice is acquired within a single breath-hold or in free breathing with advanced non-rigid motion correction (Fig. 6), producing Nex images per slice position. The Nex images are then averaged, after motion correction if acquired in free breathing, into one high-quality image. A one-heart-beat gap between acquisitions allows for magnetization recovery. Below are some protocol recommendations:
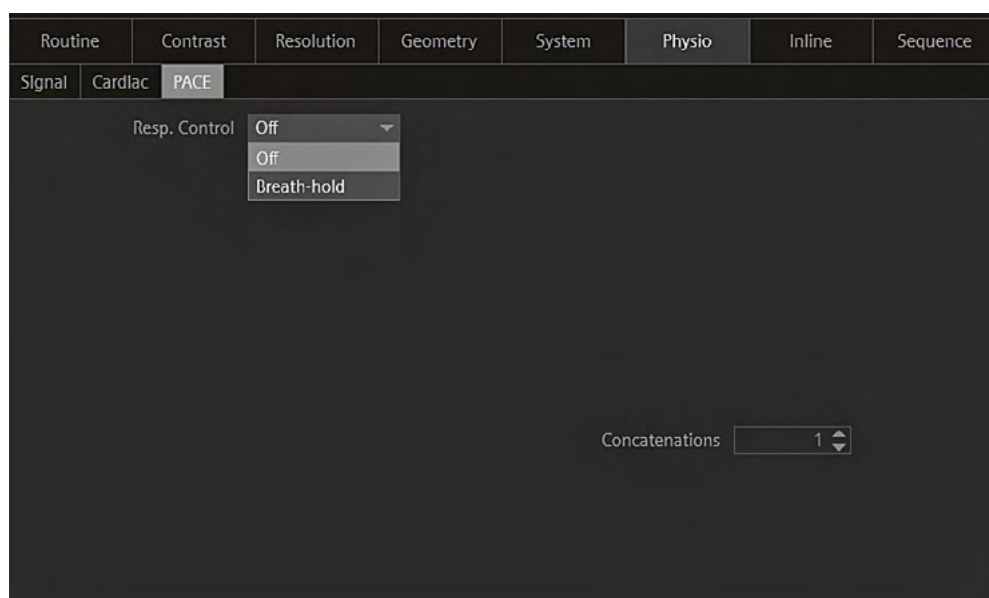
6 The Physio-PACE card of the black-blood imaging sequence on a 1.5T MAGNETOM Sola system. Images can be collected either during breath-hold or free breathing ("Resp. Control: Off"). In the case of free breathing, images will be delivered with motion correction (embedded in the reconstruction of the sequence).
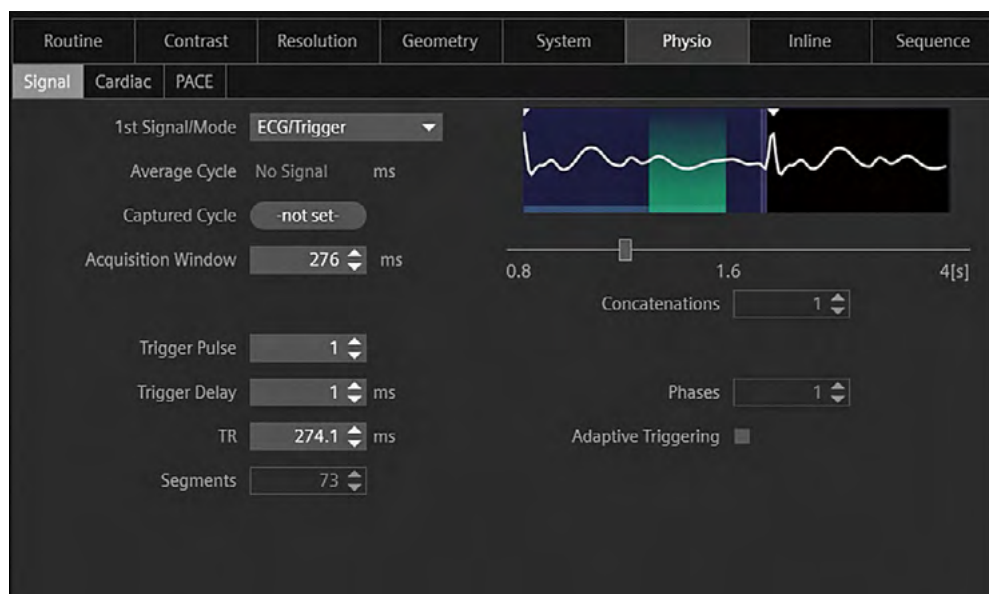
7 The Physio-Signal card of the black-blood imaging sequence on a 1.5T MAGNETOM Sola system. Images are collected during mid-diastole, and repetition time (TR) is set to the minimum.

1) We recommend collecting the images in mid-diastole (Fig. 7).
2) To achieve simultaneous darkening of healthy myocardium and blood signals, the correct TI needs to be determined with a dedicated wideband black-blood TI scout sequence (Fig. 5).
3) Regularly review the image contrast during acquisition (single-shot images are reconstructed and sent back to the operator on a beat-to-beat basis) and adjust the TI if necessary. Monitor the heart rate and adjust the trigger delay if necessary. Check for ghosting artifacts if performed in breath-hold, and check for wrapping artifacts.
4) Check for residual ICD-related hyperintensity artifacts obscuring the myocardium. If they are not completely suppressed, we recommend acquiring images with breath-hold during full inspiration to increase the heart-ICD distance. If this is not sufficient, the distance can be further increased by raising the patient's left arm and placing it next to their head.

MRI safety considerations

Before the 2000s, MRI was contraindicated in patients with any kind of cardiac implants (pacemaker, ICD, etc.). With the development of modern, smaller cardiac implants [6] with fewer magnetic components and improved electromagnetic interference safety, cardiac MRI has been shown to be safe at 1.5T with both MR-conditional and nonconditional cardiac implants [19–21] when following specific protocols and intraprocedural programming of the device [22–24]. The presence of fractured, abandoned, or epicardial leads still remains a contraindication to MRI.

Another aspect that has to be considered is the specific absorption rate (SAR). Wideband black-blood imaging is more SAR intensive than standard black-blood imaging, due to the increased B_1 amplitude in the inversion recovery and T2 preparation refocusing pulses. Wideband black-blood imaging is also more SAR intensive than wideband PSIR, due to the four additional RF pulses of the T2 preparation. For this prototype wideband black-blood imaging sequence at 1.5T, the proposed parameters (see Table 1) remained below the acceptable limit of 2 W/kg for clinical application, although SAR values were around 24 times higher than those of wideband PSIR. Nevertheless, a reassessment of the SAR deposit will be necessary for 3D applications.

Clinical applications

All images shown in this article were acquired by the Lausanne University Hospital on a 1.5T MAGNETOM Sola (software version *syngo* MR XA31 and XA51, Siemens Healthineers, Erlangen, Germany) and the University Hospital of Bordeaux on a 1.5T MAGNETOM Aera (software version *syngo* MR E11C) using a 32-channel spine coil and an 18-channel body coil.

Sequence setting	Parameter range
Acquisition	2D single-shot GRE
Cardiac control	ECG triggering
Respiratory control	Breath-holding
Spatial resolution	1.4 × 1.4 mm²
Slice thickness	8 mm
Acquisition window	170–200 ms
Receiver bandwidth	751 Hz/pixel
Flip angle	15°
Paralell imaging	GRAPPA 2 with 36 reference lines
Phase FOV	75%
Phase resolution	76%
Partial Fourier	6/8
Asymmetric echo	Weak or Strong
Dummy heartbeats	0
k-space encoding	Linear
IR duration	10.24 ms
IR bandwidth	Conventional: 0.8 kHz; Wideband: 3.8 kHz
T2prep module	$90_x – 180_y – 180_{-y} – 90_{-x}$
T2prep duration	27 ms
T2prep refoc. bandwidth	Conventional: 1.6 kHz; Wideband: 5.0 kHz
Nex	5–10
Scan time	Nex * 2 heartbeats

Table 1: Wideband black-blood imaging sequence parameters. Abbreviations: ECG, electrocardiogram; FOV, field of view; GRAPPA, generalized autocalibrating partially parallel acquisitions; GRE, gradient recalled echo; Nex, number of excitations.

Findings in ischemic patients

In individuals with subendocardial or transmural infarct, wideband black-blood could improve LGE detection by 58% compared to wideband PSIR. This is explained by the contrast improvement at the scar-blood interface with the simultaneous darkening of healthy myocardium and blood. The improved scar detection was associated with an improvement in image quality of 5% [17, 18]. ICD-related hyperintensity artifacts were suppressed as well as with wideband PSIR, revealing LGE areas that may have been obscured.

Case 1: A 74-year-old female patient presenting with reduced left ventricular ejection fraction (20%), preserved right ventricular ejection fraction (48%), and a transvenous ICD. Severe hyperintensity artifacts hide half of the myocardium when using standard PSIR (Fig. 4A) and standard black-blood (Figs. 4B, 4C) LGE imaging, potentially masking the scar. Wideband sequences (Figs. 4D–4F) drastically reduced these artifacts, revealing all scarred segments with the presence of LGE in the inferior and inferolateral segments. The transmural LGE could be better manually segmented using wideband black-blood imaging than wideband PSIR. The application of nonrigid motion correction to black-blood LGE images obtained during free breathing resulted in sharp images (Fig. 4F).

Findings in non-ischemic patients

Dilated cardiomyopathy, hypertrophic cardiomyopathy, myocarditis, calmodulinopathy, and unknown-origin cardiomyopathy have been inspected with wideband black-blood LGE imaging, with midwall and subepicardial LGE findings. Overall, wideband black-blood LGE improved scar detection by 31%, with the same efficacy as wideband PSIR in suppressing ICD-associated hyperintensity artifacts. However, image quality was decreased by 8% compared to wideband PSIR, due to the lack of anatomical information [17, 18]. Scar localization with respect to the myocardial wall is challenged in black-blood imaging, due to the black healthy myocardium and blood signal. Therefore, especially for non-ischemic patients, bright-blood imaging remains essential to localize the LGE segments, whereas black-blood imaging is essential to detect the LGE segments. It is worth mentioning that these two acquisitions can be combined into a single sequence that provides coregistered bright- and black-blood LGE images.

Case 2: A 58-year-old male patient presenting with dilated cardiomyopathy with heart failure and reduced left and right ventricular ejection fraction (26% and 38%, respectively) on probable myocarditis scar. The patient was implanted with a transvenous ICD. Standard PSIR (Fig. 4G) and standard black-blood (Figs. 4H, 4I) LGE imaging revealed hyperintensity artifacts in the anteroseptal, anterior, and anterolateral segments. Wideband sequences (Figs. 4J–4L) were able to remove hyperintensity artifacts that masked the myocardium and LGE. Scar depiction was challenging with wideband PSIR, but improved markedly with wideband black-blood LGE imaging. The latter suggested strong evidence of subepicardial LGE in all segments. As in Case 1, the application of nonrigid motion correction to black-blood LGE images obtained during free breathing resulted in sharp images without ghosting artifacts (Figs. 4K, 4L).

What does the future look like?

Black-blood LGE imaging offers a significant advantage by improving LGE detection. However, as previously mentioned, accurate scar localization is essential for differentiating between ischemic and nonischemic cardiomyopathy, as well as for comprehensive pathological assessment. Bright-blood LGE plays a critical role in providing this spatial context but is acquired independently from black-blood LGE. A promising future direction involves combining these two techniques into a single integrated bright- and black-blood LGE sequence that enables coregistered imaging [25–27], as well as its 3D application.

Beyond distinguishing acute from chronic myocardial injuries with LGE, risk stratification in various myocardial diseases is vital for enhancing diagnostic and prognostic capabilities in structural heart disease. Cardiac parametric mapping, particularly T1 and T2 mapping, shows considerable promise in refining risk stratification in patients being evaluated for ICD therapy. These techniques may also enable longitudinal monitoring of myocardium post-ICD implantation, offering valuable insights into arrhythmic risk progression and supporting the tailoring of adjunctive therapies. The integration of parametric mapping with wideband RF pulses could be pivotal for quantitative cardiac MRI in ICD patients. Wideband T1 mapping has been proposed as a solution to the limitations of conventional T1 mapping in the presence of ICDs, though further clinical validation is needed [28, 29]. The feasibility of wideband T2 mapping in ICD patients has also been recently introduced but remains at an early stage of investigation [30]. Future preclinical and clinical studies are required to assess its sensitivity and specificity for detecting myocardial edema, acute inflammation, myocarditis, and takotsubo cardiomyopathy.

Conclusion

Magnetic resonance myocardial black-blood LGE imaging with wideband RF pulses holds significant promise for better LGE identification and characterization in ICD patients. The release of this C2P sequence could contribute to better LGE assessment in myocardial disorders in ICD patients and offer better access to cardiac MRI for this population.

Sequence availability

Our C2P sequence is currently available for sharing in *syngo* MR E11C, XA20, XA30, XA31, XA51, XA60, and XA61 on the C2P platform. The .exar1 protocol for the 1.5T MAGNETOM Sola (software version *syngo* MR XA61) is available to download on the MAGNETOM World website.

Acknowledgments

References

1 Priori SG, Blomstrom-Lundqvist C, Mazzanti A, Blom N, Borggrefe M, Camm J, et al. 2015 ESC Guidelines for the management of patients with ventricular arrhythmias and the prevention of sudden cardiac death: The Task Force for the Management of Patients with Ventricular Arrhythmias and the Prevention of Sudden Cardiac Death of the European Society of Cardiology (ESC). Endorsed by: Association for European Paediatric and Congenital Cardiology (AEPC). Eur Heart J. 2015;36(41):2793–2867.

2 Ponikowski P, Voors AA, Anker SD, Bueno H, Cleland JGF, Coats AJS, et al. 2016 ESC Guidelines for the diagnosis and treatment of acute and chronic heart failure: The Task Force for the diagnosis and treatment of acute and chronic heart failure of the European Society of Cardiology (ESC)Developed with the special contribution of the Heart Failure Association (HFA) of the ESC. Eur Heart J. 2016;37(27):2129–2200.

3 Vaidya VR, Asirvatham R, Kowlgi GN, Dai MY, Cochuyt JJ, Hodge DO, et al. Trends in Cardiovascular Implantable Electronic Device Insertion Between 1988 and 2018 in Olmsted County. JACC Clin Electrophysiol. 2022;8(1):88–100.

4 Patel NJ, Edla S, Deshmukh A, Nalluri N, Patel N, Agnihotri K, et al. Gender, Racial, and Health Insurance Differences in the Trend of Implantable Cardioverter-Defibrillator (ICD) Utilization: A United States Experience Over the Last Decade. Clin Cardiol. 2016;39(2):63–71.

5 Kusumoto FM, Schoenfeld MH, Wilkoff BL, Berul CI, Birgersdotter-Green UM, Carrillo R, et al. 2017 HRS expert consensus statement on cardiovascular implantable electronic device lead management and extraction. Heart Rhythm. 2017;14(12):e503–e551.

6 Roguin A, Zviman MM, Meininger GR, Rodrigues ER, Dickfeld TM, Bluemke DA, et al. Modern pacemaker and implantable cardioverter/defibrillator systems can be magnetic resonance imaging safe: In vitro and in vivo assessment of safety and function at 1.5 T. Circulation. 2004;110(5):475–82.

7 Kalin R, Stanton MS. Current clinical issues for MRI scanning of pacemaker and defibrillator patients. Pacing Clin Electrophysiol. 2005;28(4):326–8.

8 Kellman P, Arai AE, McVeigh ER, Aletras AH. Phase-sensitive inversion recovery for detecting myocardial infarction using gadolinium-delayed hyperenhancement. Magn Reson Med. 2002;47(2):372–83.

9 Sridi S, Nuñez-Garcia M, Sermesant M, Maillot A, Hamrani DE, Magat J, et al. Improved myocardial scar visualization with fast free-breathing motion-compensated black-blood T1-rho-prepared late gadolinium enhancement MRI. Diagn Interv Imaging. 2022;103(12):607–617.

10 Gut P, Cochet H, Stuber M, Bustin A. Magnetic Resonance Myocardial Imaging in Patients With Implantable Cardiac Devices: Challenges, Techniques, and Clinical Applications. Echocardiography. 2024;41(11):e70012.

11 Rashid S, Rapacchi S, Vaseghi M, Tung R, Shivkumar K, Finn JP, et al. Improved late gadolinium enhancement MR imaging for patients with implanted cardiac devices. Radiology. 2014;270(1):269–74.

12 Bieri O, Scheffler K. SSFP signal with finite RF pulses. Magn Reson Med. 2009;62(5):1232–41.

13 Basha T, Roujol S, Kissinger KV, Goddu B, Manning WJ, Nezafat R. Black blood late gadolinium enhancement using combined T2 magnetization preparation and inversion recovery. J Cardiovasc Magn Reson. 2015;17(Suppl 1):O14.

14 Kellman P, Xue H, Olivieri LJ, Cross RR, Grant EK, Fontana M, et al. Dark blood late enhancement imaging. J Cardiovasc Magn Reson. 2016;18(1):77.

15 Basha TA, Tang MC, Tsao C, Tschabrunn CM, Anter E, Manning WJ, et al. Improved dark blood late gadolinium enhancement (DB-LGE) imaging using an optimized joint inversion preparation and T2 magnetization preparation. Magn Reson Med. 2018;79(1):351–360.

16 Nezafat R, Ouwerkerk R, Derbyshire AJ, Stuber M, McVeigh ER. Spectrally selective B1-insensitive T2 magnetization preparation sequence. Magn Reson Med. 2009;61(6):1326–35.

17 Gut P, Cochet H, Caluori G, El-Hamrani D, Constantin M, Vlachos K, et al. Wideband black-blood late gadolinium enhancement imaging for improved myocardial scar assessment in patients with cardiac implantable electronic devices. Magn Reson Med. 2024;92(5):1851–1866.

18 Gut P, Cochet H, Antiochos P, Caluori G, Durand B, Constantin M, et al. Improved myocardial scar visualization using free-breathing motion-corrected wideband black-blood late gadolinium enhancement imaging in patients with implantable cardiac devices. Diagn Interv Imaging. 2025;106(5):169–182. Epub 2024 Dec 12.

19 Nazarian S, Hansford R, Rahsepar AA, Weltin V, McVeigh D, Gucuk Ipek E, et al. Safety of Magnetic Resonance Imaging in Patients with Cardiac Devices. N Engl J Med. 2017;377(26):2555–2564.

20 Kim D, Collins JD, White JA, Hanneman K, Lee DC, Patel AR, et al. SCMR expert consensus statement for cardiovascular magnetic resonance of patients with a cardiac implantable electronic device. J Cardiovasc Magn Reson. 2024;26(1):100995.

21 Indik JH, Gimbel JR, Abe H, Alkmim-Teixeira R, Birgersdotter-Green U, Clarke GD, et al. 2017 HRS expert consensus statement on magnetic resonance imaging and radiation exposure in patients with cardiovascular implantable electronic devices. Heart Rhythm. 2017;14(7):e97–e153.

22 Nazarian S, Roguin A, Zviman MM, Lardo AC, Dickfeld TL, Calkins H, et al. Clinical utility and safety of a protocol for noncardiac and cardiac magnetic resonance Imaging of patients with permanent pacemakers and implantable-cardioverter defibrillators at 1.5 tesla. Circulation. 2006;114(12):1277–84.

23 Nazarian S, Halperin HR. How to perform magnetic resonance imaging on patients with implantable cardiac arrhythmia devices. Heart Rhythm. 2009;6(1):138–43.

24 Nazarian S, Hansford R, Roguin A, Goldsher D, Zviman MM, Lardo AC, et al. A prospective evaluation of a protocol for magnetic resonance imaging of patients with implanted cardiac devices. Ann Intern Med. 2011;155(7):415–24.

25 Bustin A, Sridi S, Kamakura T, Jais P, Stuber M, Cochet H. Free-breathing joint bright- and black-blood cardiovascular magnetic resonance imaging for the improved visualization of ablation-related radiofrequency lesions in the left ventricle. EP Europace. 2022;24(Supplement_1).

26 de Villedon de Naide V, Maes JD, Villegas-Martinez M, Ribal I, Maillot A, Ozenne V, et al. Fully automated contrast selection of joint bright- and black-blood late gadolinium enhancement imaging for robust myocardial scar assessment. Magn Reson Imaging. 2024;109:256–263.

27 Richard T, de Villedon de Naide V, Nogues V, Génisson T, Narceau K, He K, et al. Improved and Automated Detection of Papillary Muscle Infarction Using Joint Bright- and Black-Blood Late Gadolinium Enhancement MRI. J Magn Reson Imaging. 2025. Online ahead of print.

28 Shao J, Rashid S, Renella P, Nguyen KL, Hu P. Myocardial T1 mapping for patients with implanted cardiac devices using wideband inversion recovery spoiled gradient echo readout. Magn Reson Med. 2017;77(4):1495–1504.

29 Hong K, Jeong EK, Wall TS, Drakos SG, Kim D. Wideband arrhythmia-Insensitive-rapid (AIR) pulse sequence for cardiac T1 mapping without image artifacts induced by an implantable-cardioverter-defibrillator. Magn Reson Med. 2015;74(2):336–45.

30 Gut P, Kim D, Cochet H, Sacher F, Jaïs P, Stuber M, et al. Wideband myocardial T2 mapping with implantable cardiac device: A preliminary evaluation in healthy volunteers at 1.5T. J Cardiovasc Magn Reson. 2025;27(Supplement 1):101276.

Contact

Aurélien Bustin, Ph.D.
IHU LIRYC, Heart Rhythm Disease Institute
Avenue du Haut Lévêque
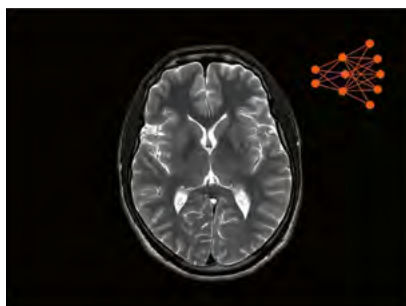33000, Bordeaux
France
aurelien.bustin@ihu-liryc.fr

Optimization of Petrous Internal Carotid Artery Imaging in 7T Ultra-High-Field TOF-MRA

Hui Liu, Ph.D.

Siemens Healthineers, Zhengzhou, China

Introduction

Ultra-high-field time-of-flight magnetic resonance angiography (TOF-MRA) at 7T significantly enhances the accuracy of cerebrovascular disease diagnosis and image quality by leveraging the benefits of ultra-high magnetic field strength. Compared to conventional 1.5T or 3T MRI, the 7T TOF-MRA offers the following key advantages:

1. Ultra-high spatial resolution, enabling clear visualization of tiny blood vessels (e.g., lenticulostriate arteries (LSA))
2. Exceptional signal-to-noise ratio (SNR) and contrast-to-noise ratio (CNR), significantly enhancing the contrast between blood vessels and surrounding tissues

To date, 7T TOF-MRA has demonstrated significant value in the study of cerebrovascular malformations, atherosclerosis, and neurodegenerative diseases, and is expected to become the gold standard for precision neurovascular imaging in the future.

However, 7T TOF-MRA also faces challenges such as susceptibility artifacts at the air-bone interface of the sella turcica region, and physiological motion (e.g., vascular pulsation), which lead to suboptimal imaging of the petrous segment of the internal carotid artery. This paper aims to optimize imaging of the petrous internal carotid artery (ICA) through several key parameter modifications.

The petrous segment of the internal carotid artery is located in the parasellar region, where the large susceptibility difference between air and bone leads to susceptibility artifacts. These artifacts affect the homogeneity of both the B0 and B1 fields, which can result in asymmetry of TOF signals between the two sides. Even B0 shimming and volume-specific parallel-transmit (pTX) B1 shimming could not fully resolve the signal loss at the ICA.

The optimization strategy was revised by altering the flow compensation scheme and increasing the acquisition bandwidth, therefore shortening the echo time (TE) and reducing the influence of T2* effects. Furthermore, changing the phase-encoding direction redirected pulsation artifacts away from critical vascular structures. Together, these approaches minimized the impact of susceptibility and pulsation artifacts in this region and led to a better display of the ICA on the TOF-MRA.

Methods and materials

All examined cases were acquired using a 7T MAGNETOM Terra MR scanner equipped with an 8-channel transmit/32-channel receive head coil (8Tx/32Rx Nova coil; Nova Medical, Wilmington, MA, USA), operating on the *syngo* MR E12 software platform.

Group	TE	Phase encoding	Bandwidth	Flow compensation	TA	TR/FA	Voxel size	TONE
Ref (A)	3.57 ms	L>>R	531 Hz/Px	Slice/Read	8:15 min	25 ms/25°	0.4 × 0.4 × 0.4 mm³	70%
Ctrl (B)	3.57 ms	P>>A	531 Hz/Px	Slice/Read	8:15 min	25 ms/25°	0.4 × 0.4 × 0.4 mm³	70%
Ctrl (C)	1.79 ms	L>>R	531 Hz/Px	Slice/Read	8:15 min	25 ms/25°	0.4 × 0.4 × 0.4 mm³	70%
Opt (D)	1.79 ms	P>>A	531 Hz/Px	Slice/Read	8:15 min	25 ms/25°	0.4 × 0.4 × 0.4 mm³	70%

Table 1: Experimental parameters.

Case 1: A 17-year-old healthy male volunteer.

A comparison of the original TOF-MRA images and maximum intensity projection (MIP) reconstructions across the four groups revealed the following findings:

1. Shorter TE values (groups C and D) resulted in significantly less distortion in the cross-sectional shape of the petrous segment of the internal carotid artery compared to longer TE values (groups A and B).
2. When vascular pulsation artifacts were minimal, the phase-encoding direction had no noticeable impact on the appearance of the vessel in this region.
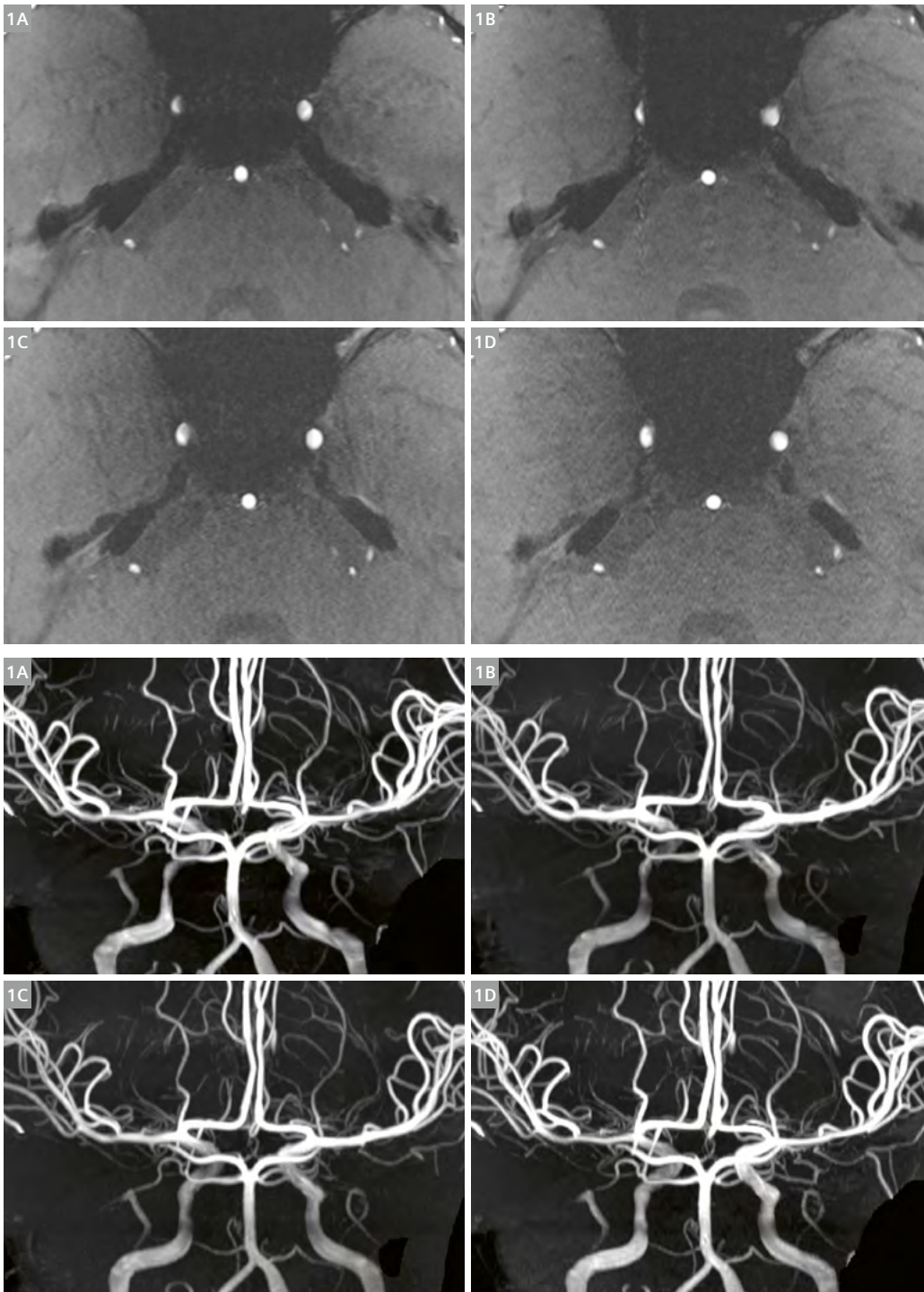
Case 2: A 35-year-old healthy female volunteer.

Comparison of original TOF-MRA images:
1. When the phase-encoding direction is P>>A (posterior-to-anterior), vascular pulsation artifacts align along the posterior-anterior direction, thereby avoiding interference between bilateral vessels and resulting in a more uniform blood flow signal.
2. Shorter TE values (comparison between Group A and Group C) significantly reduce vascular pulsation artifacts.
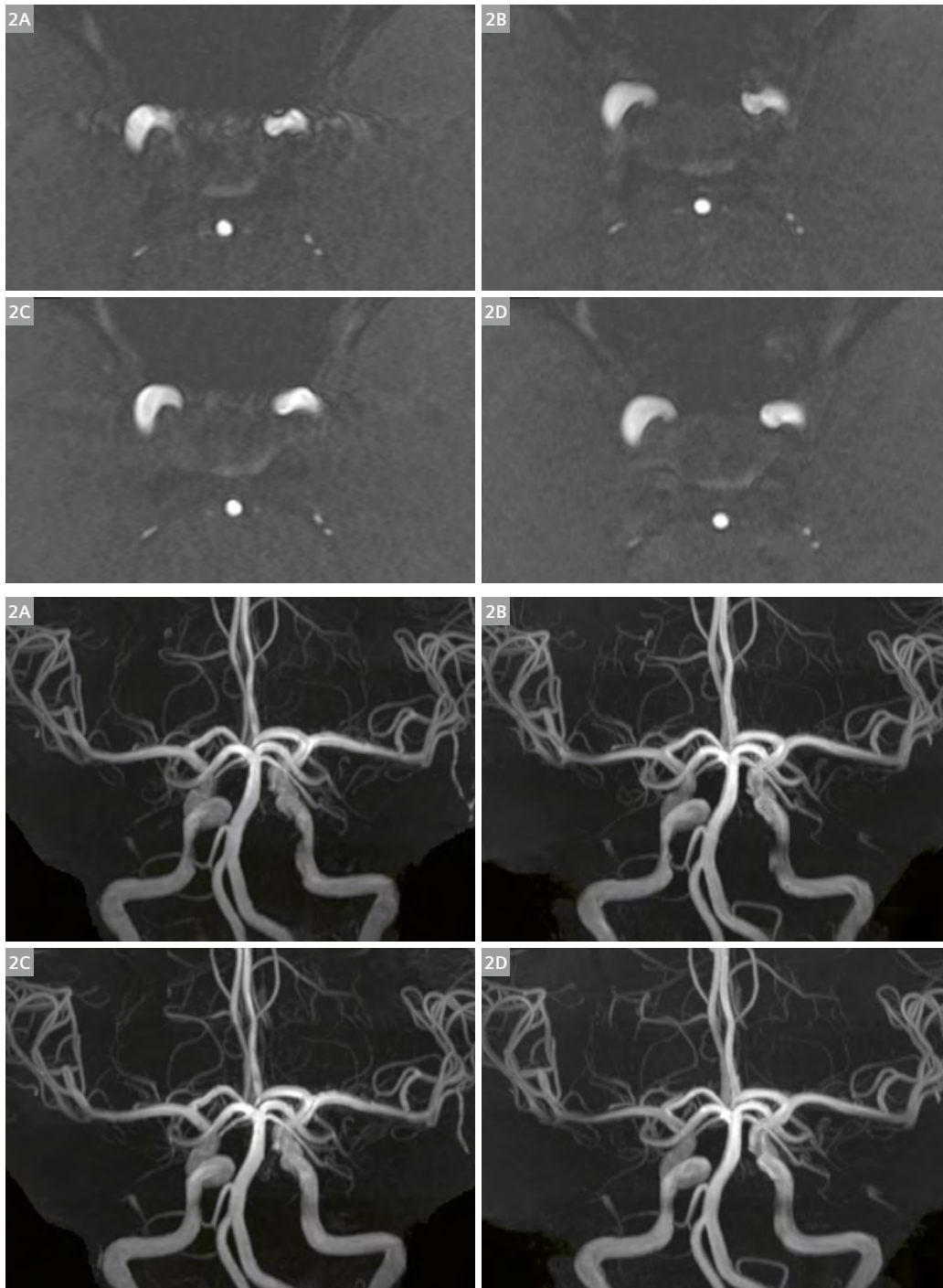
Case 3: A 77-year-old male with atherosclerosis.

Visual inspection of the original TOF-MRA images revealed the following findings:
1. Shorter TE values exhibit superior efficacy in suppressing vascular pulsation artifacts.
2. Reduced TE improved homogeneity of the blood flow signal.
3. Under conditions of pronounced pulsation artifacts, P>>A (posterior-to-anterior) phase-encoding orientation effectively prevents cross-vessel interference induced by pulsation-related artifacts.
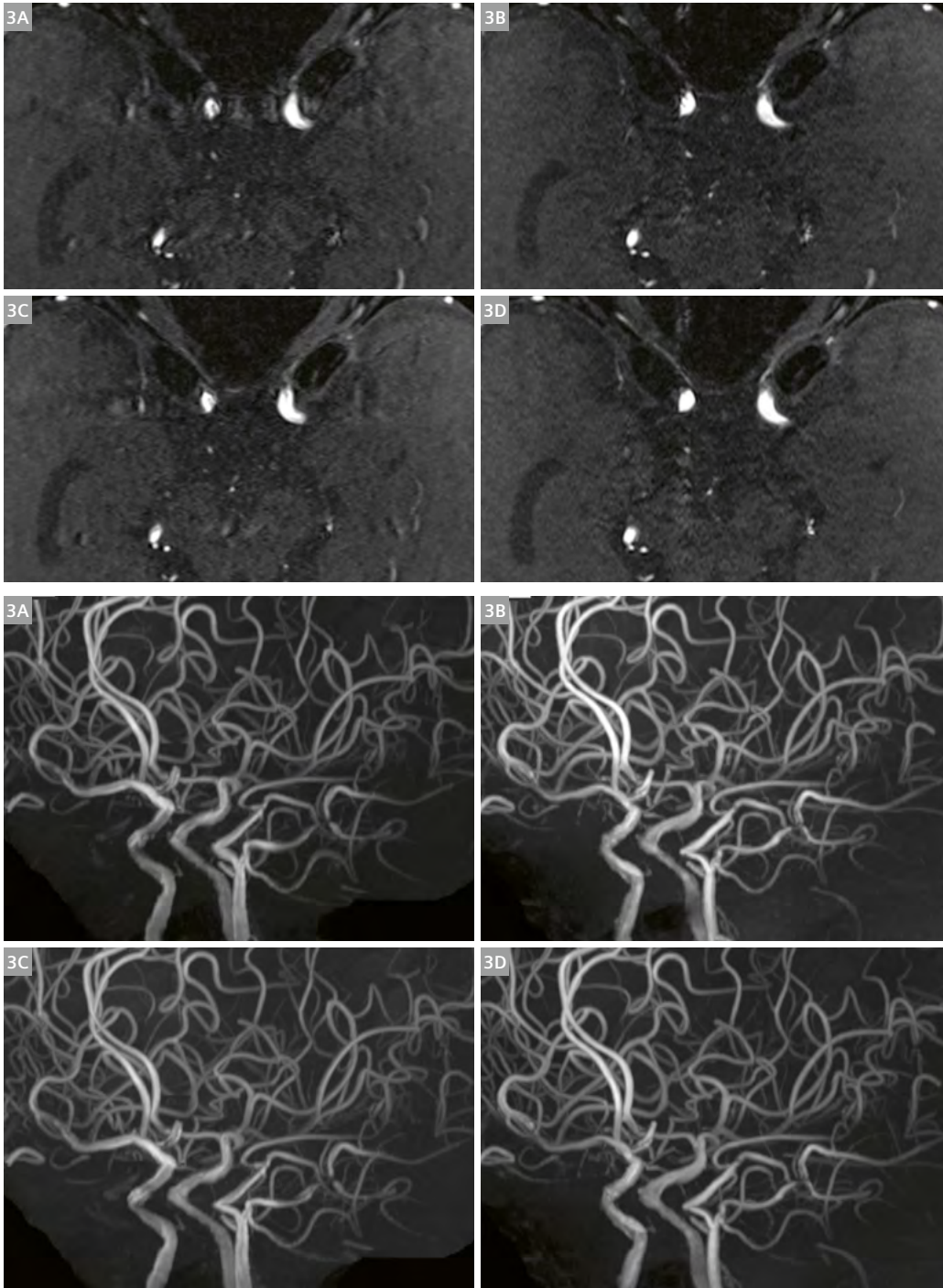
The original TOF-MRA sequence with a voxel size of $0.4 \times 0.4 \times 0.4$ mm³ has a phase-encoding direction of L>>R, a bandwidth of 254 Hz/Px, and flow compensation set to "Yes". These parameters constrain the minimum TE value. Additionally, based on the conventional imaging practices of TOF-MRA at 3T, the TE value for TOF-MRA is typically set to the opposed-phase value (3.57 ms) to achieve optimal vessel-to-background contrast.

To achieve the shortest possible TE of 1.79 ms, the acquisition bandwidth was increased to its maximum value of 531 Hz/pixel, and the flow compensation scheme was modified to "Slice/Read". All parameters were kept the same except for the TE and phase-encoding direction. Therefore, the bandwidth and flow compensation settings in Group A (reference) are adjusted to match those of the other groups.

Conclusion

In 7T ultra-high-field TOF-MRA imaging, shorter TE values demonstrate the following:
1. Reduced vascular distortion in the petrous segment of the internal carotid artery
2. More homogeneous blood flow signal
3. Significantly diminished pulsation artifacts

Additionally, employing a P>>A (posterior-to-anterior) phase-encoding direction effectively prevents mutual interference between bilateral internal carotid arteries caused by pulsation-related artifacts.

The minimum achievable TE value is inherently constrained by the imaging voxel size: Larger voxels permit shorter TE values. In this study, we employed an isotropic $0.4 \times 0.4 \times 0.4$ mm³ voxel to optimize visualization of small intracranial vessels. However, when specifically targeting the ICA, increasing the voxel size could allow for further TE reduction, thereby improving image quality of the artery.

Regarding the phase-encoding direction, our findings indicate that for patients with mild vascular pulsation, the choice between left-right (L>>R) and posterior-anterior (P>>A) encoding has minimal impact on ICA image quality. In cases of severe vascular pulsation, P>>A encoding is preferred to mitigate cross-interference artifacts between bilateral internal carotid arteries.

References

1 Kang CK, Hong SM, Han JY, Kim KN, Kim SH, Kim YB, et al. Evaluation of MR angiography at 7.0 Tesla MRI using birdcage radio frequency coils with end caps. Magn Reson Med. 2008;60(2):330–8.
2 von Morze C, Xu D, Purcell DD, Hess CP, Mukherjee P, Saloner D, et al. Intracranial time-of-flight MR angiography at 7T with comparison to 3T. J Magn Reson Imaging. 2007;26(4):900–4.
3 Cho ZH, Kang CK, Han JY, Kim SH, Kim KN, Hong SM, et al. Observation of the lenticulostriate arteries in the human brain in vivo using 7.0T MR angiography. Stroke. 2008;39(5):1604–6.
4 De Cocker LJ, Lindenholz A, Zwanenburg JJ, van der Kolk AG, Zwartbol M, Luijten PR, et al. Clinical vascular imaging in the brain at 7T. Neuroimage. 2018;168:452–458.
5 Liu J, Chen F, Wang X, Zhang X, Sun K, Xue R, et al. A comparative analysis framework of 3T and 7T TOF-MRA based on automated cerebrovascular segmentation. Comput Med Imaging Graph. 2021;89:101830.
6 Grochowski C, Staśkiewicz G. Ultra high field TOF-MRA: A method to visualize small cerebral vessels. 7T TOF-MRA sequence parameters on different MRI scanners - Literature review. Neurol Neurochir Pol. 2017;51(5):411–418.

Contact

Hui Liu, Ph.D.
Siemens Healthineers
SHS CHN CS-CRM APP MR NS
76, Kangning Street
Zhengzhou, HA
Zhengzhou 450000
China
hui.hilu.liu@siemens-healthineers.com

Optimized Protocols for Uterus and Ovaries Guided by Recommendations from the European Society of Urogenital Radiology

Oleg Shagalov, Ph.D.; Elisa Roccia, Ph.D.

Siemens Healthineers, Erlangen, Germany

Female pelvic disorders

Female pelvic disorders have a profound impact on women's quality of life and overall health outcomes. Among the most prevalent and clinically significant female pelvic disorders are endometriosis, ovarian cancer, and uterine and cervical cancer.

Endometriosis is a chronic condition characterized by the presence of endometrial-like tissue outside the uterine cavity, which leads to inflammation and scar tissue forming in the pelvic region and sometimes elsewhere in the body. It affects an estimated 10% of women of reproductive age globally. Endometriosis often leads to debilitating pelvic pain, infertility, and a reduced quality of life. Accurate diagnosis remains challenging due to its variable presentation and non-specific symptoms, contributing to diagnostic delays that can span years [1].

Ovarian cancer, one of the leading causes of cancer-related deaths in women, is frequently diagnosed at advanced stages due to the asymptomatic nature of early disease. Timely and precise imaging is essential for differentiating benign from malignant lesions and for guiding surgical and therapeutic interventions [2, 3].

Cervical cancer, which is preventable through vaccination and screening, continues to impact women globally, particularly in regions with limited access to preventive healthcare. Imaging plays a critical role in staging the disease, assessing tumor extent, and evaluating treatment response, all of which are key determinants of patient outcomes [4].

MRI is a key tool for assessing female pelvic disorders: It provides a comprehensive evaluation of the pelvis, helps detect features of malignancy, and enables assessment of extrapelvic involvement. This article reviews current MRI techniques for female pelvic disorders, emphasizing protocol optimization guided by the recommendations of the European Society of Urogenital Radiology (ESUR) [5, 6].

Guidelines from the European Society of Urogenital Radiology

As for many other body regions, specialized professional organizations provide guidance on how to perform pelvic imaging examinations. With the *syngo* MR XB10 software from Siemens Healthineers, we introduce some new pelvic MRI protocols and workflows that were developed according to the ESUR guidelines [5, 6]. As far as gynecological examinations are concerned, there are two new dedicated workflows in the Siemens protocol tree: A uterus workflow and an ovaries workflow. Both workflows include a set of T1W, T2W, DWI, and various protocols for contrast agent usage, where the parameters have been optimized for gynecological imaging, as recommended by the ESUR.
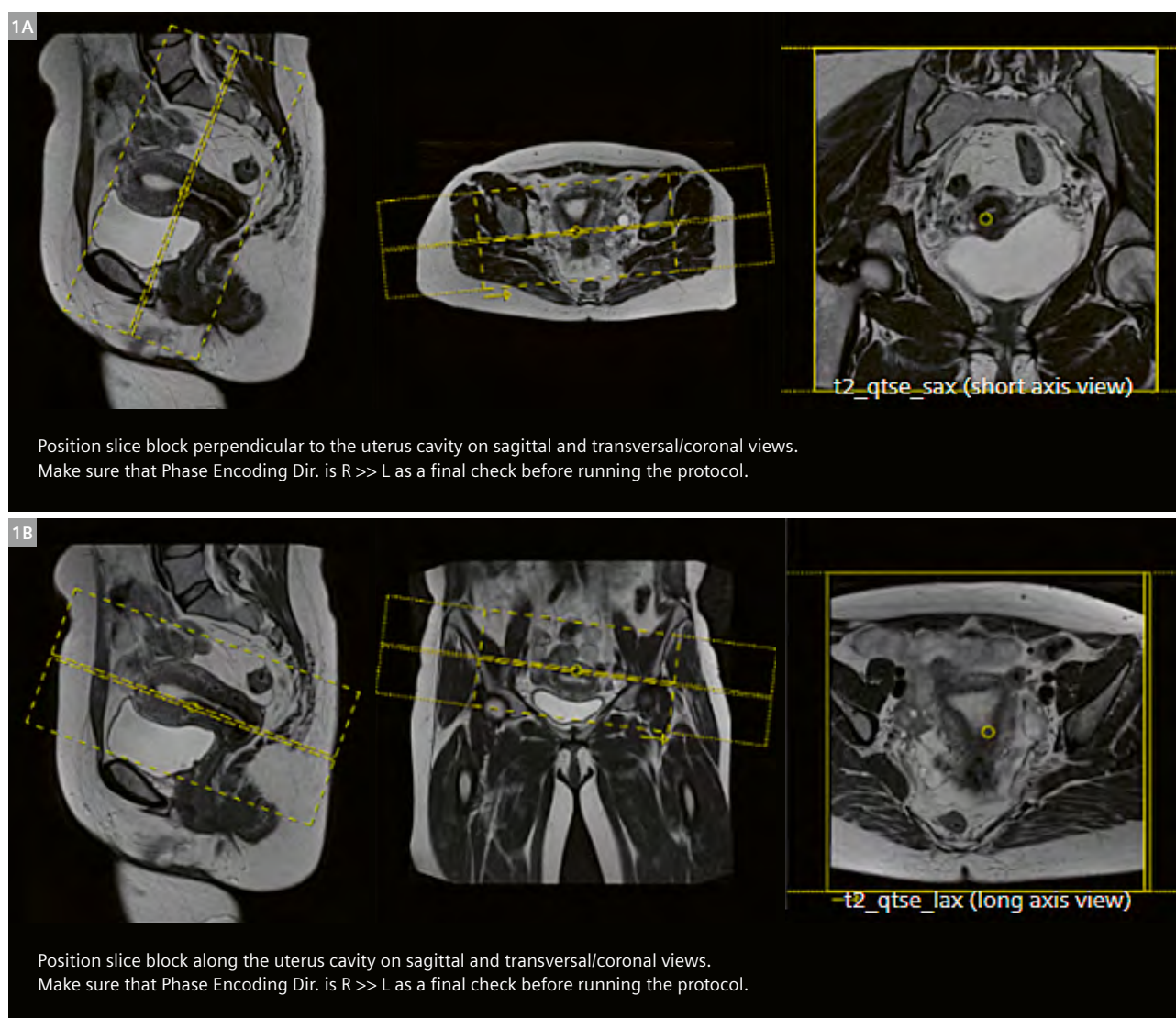
On the one hand, the Siemens tree is intended to provide users with robust protocols with a reasonable scan time that can be used out-of-the-box without further adaptations. On the other hand, whenever possible, protocols are developed in a way that allows them to be easily adapted – to increase resolution or decrease acquisition time, for example.

Uterus workflow

Proper angulation that follows the anatomy of the uterus is important in gynecological imaging to allow for reliable image interpretation. Instead of the transversal and coronal orientations, we decided to use a long-axis (LAX) and a short-axis (SAX) approach in the uterus workflow. In the uterus coordinate system, LAX means that the slices are positioned along the uterus body, whereas SAX means that the slices are positioned perpendicular to the uterus body. To make the examinations more reproducible, we introduced guidance images for all protocols utilizing these new orientations (Fig. 1).

After the conventional three-plane localizer, the uterus workflow (Fig. 2A) continues with a focused sagittal T2W protocol, which also helps position LAX and SAX protocols more precisely. The next protocol is T2W SAX, which, together with the sagittal protocol, is mandatory according to the ESUR guidelines for endometrial cancer staging. The T2W LAX protocol is provided as an option in the same protocol folder. The DWI series should mirror the T2W SAX protocol positioning, so a copy reference with the "slices" option is used. The contrast-enhanced series are represented by a dynamic protocol with a time resolution of 10 seconds and a single-phase high-resolution post-contrast protocol. The ESUR also recommends T2W and DWI protocols with a bigger coverage for lymph-node evaluation. These are available in a separate library folder [5].

Position slice block perpendicular to the uterus cavity on sagittal and transversal/coronal views.
Make sure that Phase Encoding Dir. is R >> L as a final check before running the protocol.

Position slice block along the uterus cavity on sagittal and transversal/coronal views.
Make sure that Phase Encoding Dir. is R >> L as a final check before running the protocol.

1 **(1A)** Protocol guidance for short-axis (SAX) positioning of the uterus. **(1B)** Protocol guidance for long-axis (LAX) positioning of the uterus.

Ovaries workflow

The ovaries workflow (Fig. 2B) also starts with a conventional three-plane localizer and a sagittal T2W protocol. As there is no specific recommendation on the orientation for the remainder of the protocols, we use transversal by default, but this can be changed by the user. A T2W and a T1W Dixon series follow, the latter providing in-phase and opposed-phase images for microscopic fat definition. The DWI utilizes a higher b-value (1000 s/mm²) compared to the uterus DWI protocol in order to enable higher contrast of lesions [7]. The dynamic and single-phase high-resolution post-contrast series are the same as in the uterus workflow.

Deep Resolve

All T2W and DWI protocols from both the uterus and ovaries workflows are also provided in their accelerated version using the AI-accelerated technique Deep Resolve[1] and are stored in the Deep Resolve library. In a nutshell, Deep Resolve allows to reduce scan times while maintaining, or even improving, image quality.

Further protocol details

The protocols described above are also provided without a specific orientation. These can be rotated as required, with guidance on how to select the appropriate phase-encoding direction.

In software version *syngo* MR XB10, we also introduced new large field of view protocols (overview protocols) for the whole pelvis with different contrasts, fat suppression techniques, and orientations. These are available in a separate library folder. Most of the overview protocols have a slice thickness of 4 mm, whereas the focus protocols have 3 mm slices for both 1.5T and 3T.

T2W protocols use a high parallel imaging factor of 4, even in the versions without deep-learning acceleration. The high parallel imaging factor, combined with the high number of averages (4 or even 5 for certain systems) helps to significantly reduce motion artifacts, which are typically induced by bowel movement. Whenever possible, the phase resolution is kept at (or close to) 100%. Although
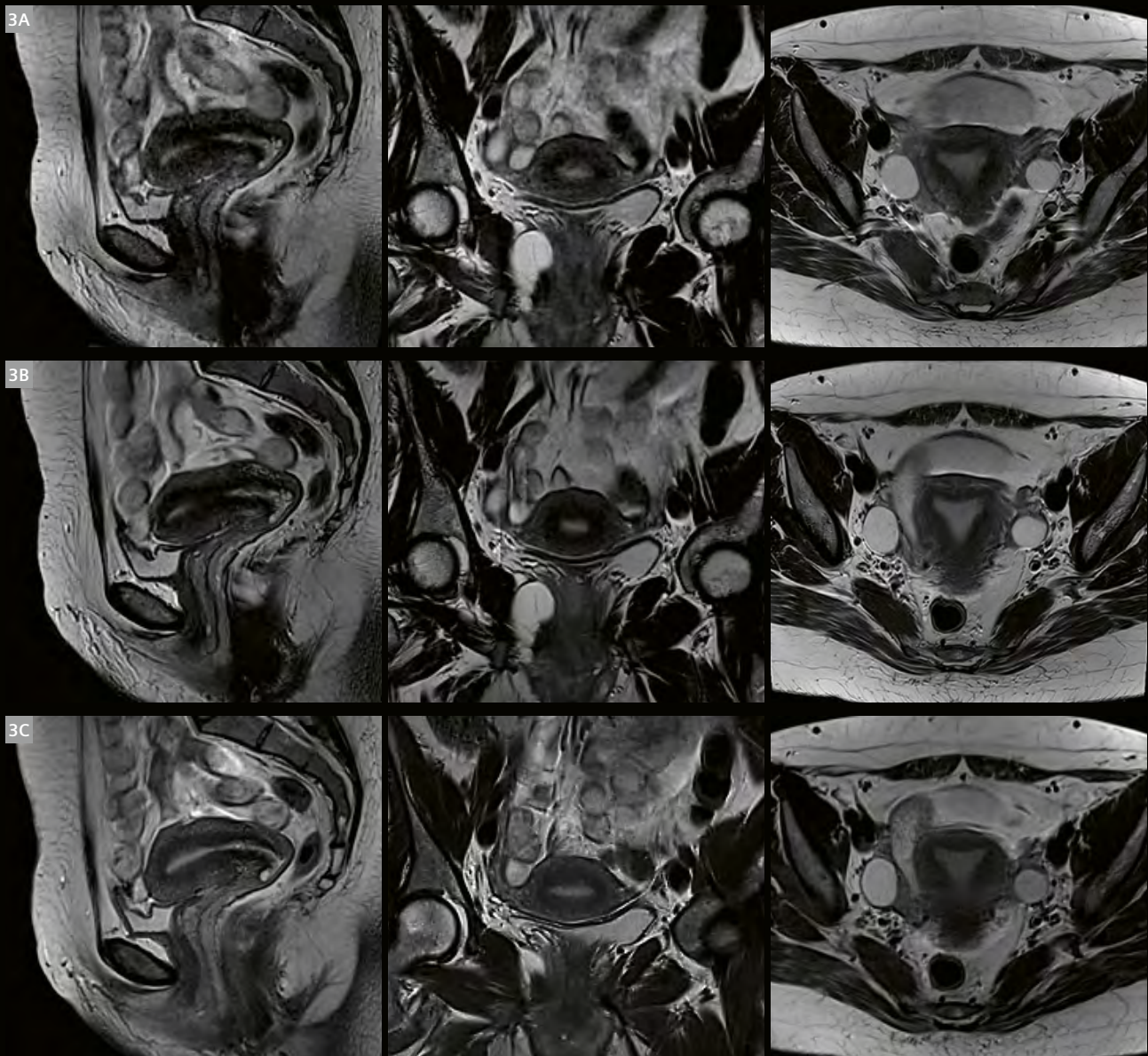
---

[1]*Deep Resolve requires a dedicated software license.*

	Uterus	Uterus with Deep Resolve	Ovaries	Ovaries with Deep Resolve
MAGNETOM Sola (1.5T)	14:06 min	10:46 min	15:49 min	12:10 min
MAGNETOM Vida (3T)	13:53 min	9:07 min	15:23 min	11:09 min

Table 1: Acquisition time reduction enabled by Deep Resolve for the uterus and ovaries protocols at both 1.5T and 3T.
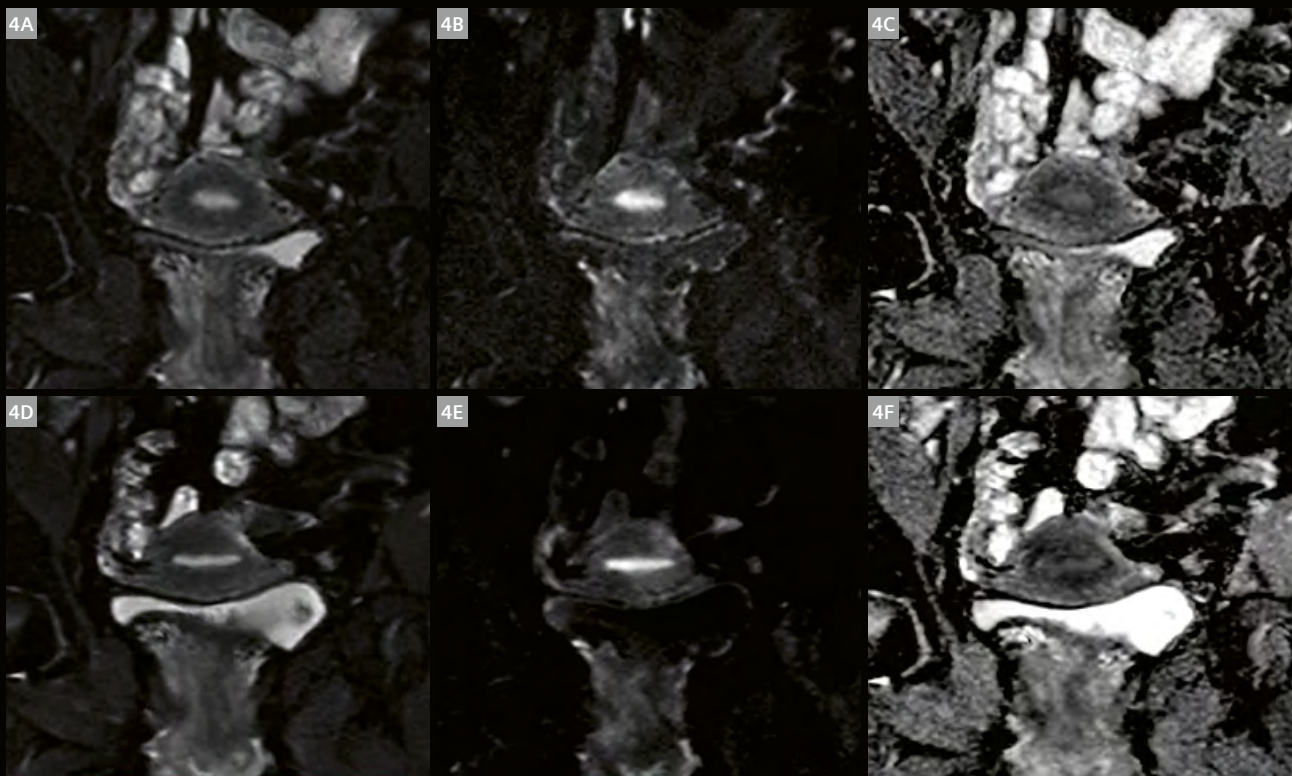

2 (2A) Overview of the uterus workflow.
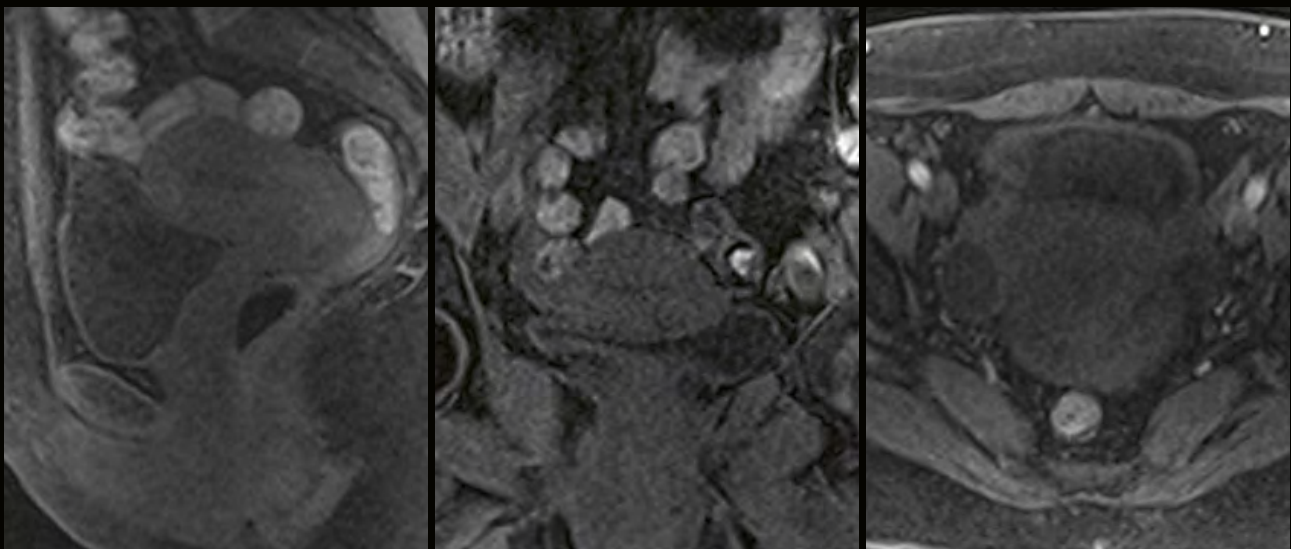(2B) Overview of the ovaries workflow.

Study ID 2aaaa3398

3 T2W imaging of the uterus body (sagittal, short axis, and long axis): conventional TSE, 3:36 min **(3A)**, TSE with Deep Resolve, 1:54 min **(3B)**, TSE BLADE, 3:29 min **(3C)**.

4 DWI of the uterus body/ovaries (short-axis view, **(4A)** b50, **(4B)** b1000, **(4C)** ADC): conventional echo planar imaging (EPI), 4:06 min **(4A–4C)**; EPI with Deep Resolve, 3:06 min **(4D–4F)**.

Study ID 2aaaa3398

5 T1W imaging for dynamic contrast enhancement of the uterus body and ovaries (sagittal, short axis, and long axis), 10 seconds per phase.

Study ID 2aaaa3398

using reduced phase resolution would help increase the signal-to-noise ratio (SNR) and reduce scan times simultaneously, we found that this has a significant negative impact on image sharpness. Since pelvic examinations often suffer from artifacts due to bowel motion, focus T2W protocols are also offered using the BLADE technique, which is more robust towards motion.

All **DWI** protocols use a 3D diagonal scheme to increase image sharpness, since there is no indication of anisotropic diffusion in the pelvic region, except in the prostate. For the same reason, when scan time allows, the phase resolution is kept at 100%, and partial Fourier is either off or set to the minimum. Deep Resolve protocols should always be used with maximum phase oversampling to avoid aliasing induced by the SENSE-based reconstruction. To compensate for the echo time increase of the increased phase oversampling, a parallel imaging factor of 3 is used.

Protocols for **dynamic** contrast enhancement must have a time resolution below 10 seconds while preserving a reasonable spatial resolution. The main change compared to previous protocol versions is a new CAIPI scheme using only 1 in the phase-encoding direction, but 4 in the slice direction with a shift of 2. This approach helps avoid aliasing in the phase-encoding direction, which usually appears in the middle of the image in correspondence with the region of interest. To reduce motion and third-arm

artifacts, the flip angle was slightly decreased, and the receiver bandwidth set to the maximum. To improve SNR, reduced by fat suppression and by the high temporal and spatial resolution, prescan normalize was switched off. Even though this might result in imperfect fat suppression in the periphery of the image, it does not affect the region of interest.

Conclusion

Accurate and timely diagnosis of female pelvic disorders is essential for improving patient outcomes and quality of life. MRI plays a pivotal role in this effort, offering detailed anatomical and functional information that supports diagnosis, staging, and treatment planning. By aligning with ESUR recommendations, the new uterus and ovaries workflows introduced in the *syngo* MR XB10 software provide standardized, high-quality imaging protocols tailored to gynecological needs. In addition, Deep Resolve can be applied to further accelerate scan times while maintaining high image quality – enhancing patient comfort and workflow efficiency. With these advancements, MRI continues to evolve as a key pillar in the evaluation and management of female pelvic health.

References

1   World Health Organization. Endometriosis [Internet]. Geneva, Switzerland: World Health Organization; 2023 March 24 [accessed 2025 July 07]. Available from: https://www.who.int/news-room/fact-sheets/detail/endometriosis

2   Doubeni CA, Doubeni AR, Myers AE. Diagnosis and Management of Ovarian Cancer. Am Fam Physician. 2016;93(11):937–44.

3   Engbersen MP, Van Driel W, Lambregts D, Lahaye M. The role of CT, PET-CT, and MRI in ovarian cancer. Br J Radiol. 2021;94(1125):20210117.

4   Mansoori B, Khatri G, Rivera-Colón G, Albuquerque K, Lea J, Pinho DF. Multimodality Imaging of Uterine Cervical Malignancies. AJR Am J Roentgenol. 2020;215(2):292–304.

5   Nougaret S, Horta M, Sala E, Lakhman Y, Thomassin-Naggara I, Kido A, et al. Endometrial Cancer MRI staging: Updated Guidelines of the European Society of Urogenital Radiology. Eur Radiol. 2019;29(2):792–805

6   Thomassin-Naggara I, Dolciami M, Chamie LP, Guerra A, Bharwani N, Freeman S, et al. ESUR consensus MRI for endometriosis: indications, reporting, and classifications. Eur Radiol. 2025. Epub ahead of print.

7   Reinhold C, Rockall A, Sadowski EA, Siegelman ES, Maturen KE, Vargas HA, et al. Ovarian-Adnexal Reporting Lexicon for MRI: A White Paper of the ACR Ovarian-Adnexal Reporting and Data Systems MRI Committee. J Am Coll Radiol. 2021;18(5):713–729.

Contact

Elisa Roccia, Ph.D.
Global Clinical Marketing Manager Oncology
SHS DI MR M&S CSM
Park View, Watchmoor Park
Camberley
Surrey GU15 3YL
United Kingdom
elisa.roccia@siemens-healthineers.com

Oleg Shagalov, Ph.D.
Senior Applications Developer
SHS DI MR R&D SWI AFT APPL
Allee am Roethelheimpark 2
91052 Erlangen
Germany
oleg.shagalov@siemens-healthineers.com

Mobile MRI: Revolutionizing Access to Advanced Imaging

Jakob Krebs Christensen

Agito Medical A/S, Nørresundby, Denmark

Historical development of mobile MRI units

The evolution of mobile MRI units represents a remarkable convergence of medical imaging technology and transportation engineering, driven by the fundamental challenge of bringing diagnostic capabilities to underserved populations and remote locations.

Early conceptualization (1980s)
The concept of mobile MRI emerged in the 1980s, shortly after magnetic resonance imaging became clinically established in major medical centers. As hospitals recognized the diagnostic value of MRI but faced significant capital investment barriers, the idea of shared mobile units began to take shape. Early pioneers faced considerable technical challenges: MRI systems needed precise magnetic field stability, extensive shielding from external electromagnetic interference, and substantial amounts of power, all of which seemed incompatible with mobile platforms.

The American FONAR Corporation tackled these obstacles with success and introduced the world's first mobile MRI unit in 1983. It received FDA approval in 1985 and began serving multiple separate hospital sites from 1986 [1].

The magnetic field strength on these first-generation mobile systems was typically limited to 0.5 Tesla or less, and image quality was compromised by vibrations and electromagnetic interference from the vehicle's systems.

Technological breakthroughs (1990s–2000s)
The mid-1990s marked a turning point, with several key technological advances. Improved superconducting magnet designs allowed for more compact systems while maintaining high field strength. Advanced shielding techniques, including both active and passive electromagnetic shielding, enabled mobile units to operate in various environments without significant image degradation. Vibration isolation systems were developed to minimize the impact of road transport and environmental factors on image quality.

During this period, manufacturers began producing purpose-built mobile MRI trailers with integrated power generation systems, patient areas, and operator consoles. The development of helium recapture systems (zero boil-off) reduced the operational costs associated with cryogenic coolant loss, making mobile units more economically viable and practical for routine clinical use.

Meeting current global healthcare challenges

Mobile radiology units provided by private companies are emerging as crucial solutions to one of the many pressing healthcare challenges facing the world today.

The World Health Organization (WHO) reports that over two-thirds of the global population lack access to radiology services [2]. This reflects a massive gap in diagnostic capabilities that mobile units are uniquely positioned to address. These flexible, transportable imaging solutions tackle inequities in healthcare access by bringing advanced diagnostic capabilities to underserved communities, rural hospitals, and regions with limited infrastructure.

The momentum gained during the last 10 years is attributed to the rising demand for decentralized healthcare, reflecting a broader shift toward more accessible, patient-centered care delivery models.

The growth of the mobile radiography industry is primarily driven by an increase in chronic diseases, necessitating more frequent diagnostic imaging. Another factor is its ability to address critical shortages in the healthcare workforce by providing imaging services without requiring investments in permanent facilities and long-term staffing commitments.

Mobile units offer rapid deployment capabilities for emergency situations, temporary coverage during equipment maintenance, and scalable solutions for varying patient volumes. In doing so, they provide a strategic response to the dual challenges of expanding healthcare access while maintaining cost-effectiveness in an increasingly resource-constrained global healthcare environment.

Operational models

Trailer units are true mobile MRI systems housed in large semi-trailers that operate as scanning rooms. They are magnetically shielded and can be transported with the magnet fully energized to minimize setup time at each location.

Trailer units are designed for maximum mobility and can be easily moved between facilities on a regular schedule. With an overall size of approximately 15 × 3 meters, the units are typically used in route-based operations. This means they follow predetermined routes between multiple healthcare facilities, spending days or weeks at each location before moving to the next site. They are ideal for serving rural areas, smaller hospitals, or facilities that need temporary MRI access during equipment maintenance, replacement, or surges in demand.

Relocatable units are oversized trailers that can be semi-permanently parked at a hospital or imaging facility and function as a bridge between mobile trailer units and fixed installations.

A relocatable unit provides ground-level access and a spacious environment for patients and staff. It is a good option if a facility is considering a long-term imaging solution, as the unit can be fully integrated into the hospital infrastructure, maintaining the patient pathway.

These units are typically deployed for months or years at a single location. Compared to the capital investment for a permanent installation, a relocatable MRI unit can provide the most cost-effective way of meeting increasing clinical demand.

Relocatable units are commonly used when facilities need expanded capacity but want to avoid the time and expense of permanent construction, or when testing market demand before committing to a permanent installation.

Each model has distinct advantages in terms of cost-effectiveness, scheduling flexibility, and resource utilization. The optimal choice will depend on factors such as patient volume, geographic distribution of facilities, and local healthcare infrastructure requirements.

1 A 1.5T MAGNETOM Viato.Mobile deployed in a trailer unit in Spain.

2 A 1.5T MAGNETOM Sola deployed in a relocatable unit in the UK.

Current state of mobile MRI technology

Mobile MRI technology has reached a significant level of maturity and adoption. The field has seen important technological breakthroughs, particularly in sustainability and operational efficiency.

In February 2024, we at Agito Medical received the world's first helium-free mobile MRI scanner for our fleet. It reduces environmental impact and operational costs and marks a significant step forward in sustainable healthcare technology. This development addresses one of the major operational and financial challenges of traditional MRI systems: helium dependency.

These sealed MRI systems also have practical advantages, allowing safe transport thanks to simple ramp-up/ramp-down procedures. They also enable optimized positioning, as they are not constrained by a quench pipe, which traditionally requires careful distancing from structures and personnel.

Another breakthrough concerns innovative measures for reducing power consumption, such as switching MRI units off and enabling power-save mode. The power-save mode works by cycling cooling components on and off when the MRI is not in use, rather than keeping all systems running continuously. This maintains the magnet's superconducting state while reducing energy consumption during idle periods. The technology is especially effective for facilities and mobile units that operate during specific hours, allowing significant energy savings overnight and during weekends.

These power-saving technologies are a win-win solution for healthcare providers: They substantially reduce costs while contributing to environmental sustainability goals without compromising imaging quality or patient care.

In addition, optimized system reliability and remote service capabilities enable real-time diagnostics, predictive maintenance, and instant technical support. This signifi-

cantly reduces downtime through proactive issue resolution and by eliminating the need for on-site technician visits for routine troubleshooting. In turn, this maximizes scanner availability and operational efficiency while lowering service costs.

All the above features are ideal for mobile MRI systems, which must operate reliably in challenging environments characterized by vibrations, frequent transportation between locations and regions, support from multiple technicians, and deployment across diverse clinical applications.

Outlook and emerging trends

The future of MRI technology is rapidly evolving, driven by several transformative trends that promise to continue revolutionizing mobile imaging over the next decade.

More helium-free systems
As mentioned above, the first "helium-free" unit was deployed in our fleet in 2024. We are excited to see other vendors either developing or offering such technology now too, as it is truly a match made in heaven for mobile MRI units.

The question now is whether and when the recent research into next-generation superconductivity with more-accessible nitrogen-cooled copper-free and nickel-based superconductors, or perhaps even the new LK-99 superconductor [3] that South Korean researchers claim can operate at room temperature, will become a reality in MRI technology.

Artificial intelligence
AI has significantly transformed clinical radiology by enhancing image quality, reducing scan times, and improving diagnostic accuracy and patient safety in MRI. These applications are streamlining workflows and increasing acquisition efficiency and speed, while maintaining superior image quality.

This is probably only the beginning of the AI evolution. In the near future, we are likely to encounter AI technology that can transform both the patient experience and diagnostic capabilities through, for instance, advanced Compressed Sensing and deep learning-based reconstruction that enable faster image acquisition without compromising quality. We are also likely to see AI technology offer fully automated image reconstruction, protocol optimization, and preliminary analysis to help radiologists focus on complex diagnostic decisions.
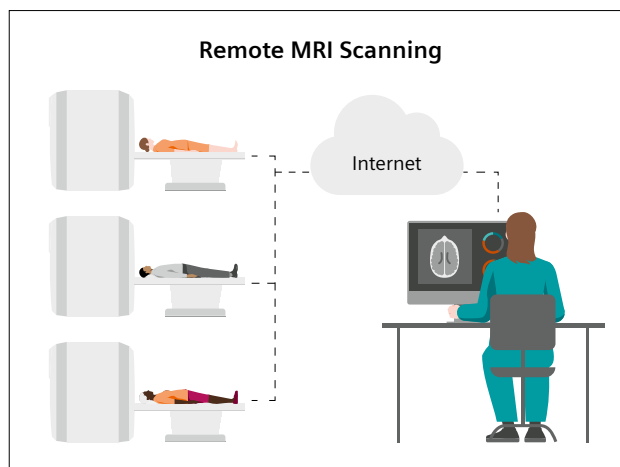
3 The concept of remote scanning.

Remote scanning

Remote MR and CT scanning has evolved significantly. Several key technological advances are now FDA approved and have been clinically implemented by both independent vendors and major MRI manufacturers. One such solution is *syngo* Virtual Cockpit from Siemens Healthineers, which reflects the broader trend toward remote scanning capabilities across the industry.

This infrastructure is very well suited for mobile scanners. It expands the reach of skilled technologists, especially in rural and underserved areas where these units are often in operation.

Assuming regulatory and compliance barriers are addressed, and the concept is optimized and fully adopted, we might very well see new mobile MRI or CT units developed specifically for remote use. They would have a different and optimized layout: Since less space would be needed for the technologist, patients would have a larger and better environment.

Patient-centric innovations

The industry is increasingly focusing on patient comfort and accessibility. Patient-centered technology, such as wide-bore systems, in-system entertainment, low-acoustic-noise scanning, lightweight coils, and free-breathing scanning, will continue to be an important goal for MRI in the 21st century and will greatly impact the mobile environment as well.
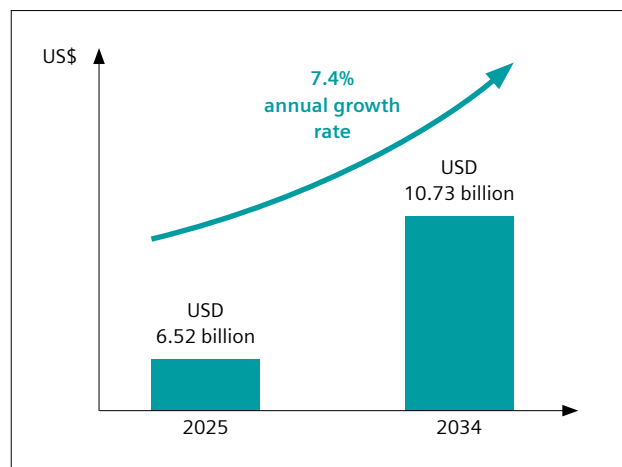
Conclusion

Today's mobile MRI units serve diverse populations worldwide, from rural communities in high-income nations to underserved regions in low- and middle-income countries. These systems have proven particularly valuable in disaster response scenarios, military medical support, and population health screening programs. The concept of mobile units continues to evolve with advances in artificial intelligence, power and helium optimization, and remote scanning.

Research estimates that the global mobile scan market will reach US$ 10.73 billion by 2034, up from US$ 6.52 billion in 2025, which represents a 7.4% annual growth rate [3]. Growth drivers include rising demand in underserved areas, and screening programs. North America and Europe currently dominate adoption, while Asia-Pacific markets are expanding rapidly.

4 The global mobile scan market is estimated to reach US$ 10.73 billion by 2034, up from US$ 6.52 billion in 2025 – a 7.4% annual growth rate. *Figure reprinted with permission from [4].*

References

1 FONAR Corporation. FONAR History [Internet]. Melville, NY, USA: FONAR Corporation. [cited 2025 Sept 25]. Available from: https://www.fonar.com/history.html

2 Mariani G, Kasznia-Brown J, Paez D, Mikhail MN, H Salama D, Bhatla N, et al. Improving women's health in low-income and middle-income countries. Part II: the needs of diagnostic imaging. Nucl Med Commun. 2017;38(12):1024-1028.

3 Kim E, Luo W, Jho H. Perception and argumentation in the LK-99 superconductivity controversy: a sentiment and argument mining analysis. Sci Rep. 2025;15(1):13254.

4 Research and Markets. Mobile Scan Radiology Room Market Size, Share, Trends, Analysis, and Forecasts, 2024-2025 & 2026-2034 | Global Industry Growth, Competitive Landscape, Opportunities, and Challenges [Internet]. Dublin, Ireland: GlobeNewswire; 2025 [cited 2025 Sept 25]. Available from: https://www.globenewswire.com/news-release/2025/06/24/3103984/28124/en/Mobile-Scan-Radiology-Room-Market-Size-Share-Trends-Analysis-and-Forecasts-2024-2025-2026-2034-Global-Industry-Growth-Competitive-Landscape-Opportunities-and-Challenges.html

Contact

Jakob Krebs Christensen
Sales Manager, Nordics, Iberia, and CEE
AGITO Medical A/S
Bejlerholm 3B
9400 Nørresundby
Denmark
Tel.: +45 25 37 68 59
Jakob.Krebs@AgitoMedical.com

Real-Life Considerations and Benefits of the AutoResponse Feature in MRI Systems with DryCool Technology

Yatin Sharma[1], Benjamin Schmitt[2], Matthias Fenchel[3]

[1]Siemens Healthcare Pvt Ltd, India
[2]Siemens Healthcare Pty Ltd, Australia
[3]Siemens Healthineers, Erlangen, Germany

Introduction

Magnetic resonance imaging (MRI) is a cornerstone of modern diagnostic medicine, providing non-invasive insights into the human body. However, the availability of MRI services, particularly in geographically challenging or remote locations, is often restricted due to infrastructure limitations. In some countries, the most significant issue with infrastructure is the lack of a consistent and reliable electricity supply. This can range from full outages of varying duration to regular fluctuations in the available power. Conventional MRI scanners rely heavily on an uninterrupted and steady power supply to maintain the cryogenic systems that stabilize the liquid helium needed for the low temperatures that enable superconductivity in the magnet.

When electricity is interrupted for an extended period, it can disrupt the cryogenic system. This can lead to suspended cooling and, as the temperature rises, impact the superconducting capacity of the magnet. Depending on the duration and impact of the interruption, the static magnetic field may be lost entirely in a rapid event known as "magnet quench," where the entire magnetic field is converted into thermal energy. As a result, most of the helium within the magnet vessel is lost to evaporation. Recovering the magnet is highly resource-intensive: The process requires replenishing the liquid helium (which is a sparse and expensive resource with challenging logistics), and demands highly trained engineers with specialized tools to restore the functionality of the cryogenic system and the magnet. The resulting downtime, which can span multiple days, impairs patient care and escalates operational costs, rendering MRI systems less viable, especially in remote areas where access to the necessary resources is limited.

To address this shortage of resources, Siemens Healthineers introduced a revolutionary solution in the form of DryCool technology in its 0.55T MAGNETOM Free. and 1.5T MAGNETOM Flow. Platform. These systems have a cryostat with a closed magnet vessel and a practically negligible helium inventory of 0.7 liters. In addition, the low magnetic field does not cause a loss of helium, so there is no need for liquid cryogen refilling. The helium remains in the vessel and can be liquidized again once power and cooling have been reestablished. Most importantly, the system is equipped with an auto-recovery feature that reestablishes the magnetic field without the need for specialized and costly intervention. This article explores the significance of this feature, its role in improving MRI accessibility in resource-limited settings, and its potential to transform diagnostic healthcare delivery in geographically challenging regions.

Key features and discussion

1. The role of AutoResponse

AutoResponse is an automatic ramp-up feature in all systems with DryCool technology, including the MAGNETOM Flow. Platform at 1.5T and the MAGNETOM Free. Platform at 0.55T. It eliminates the dependence on manual intervention for restoring magnet functionality after a ramp-down event caused by a severe interruption to the power supply. In conventional MRI systems, this event would require replenishing of the liquid helium, specialized tools, and engineers. Systems with DryCool technology employ an innovative mechanism to automatically restore the magnetic field. Key benefits include:

No need for helium refilling: The system operates with a small amount of helium (0.7 liters). The helium deposit is sealed for life, so evaporating helium can be captured and recondensed upon restoration of the power supply.

Self-sufficient operation: Even in the event of extended power outages, the system can autonomously return to operational status once power is restored, without requiring specialized engineers or equipment.

Case study:
Power outage at AIIMS in Ballabhgarh, India

At the All India Institute of Medical Sciences (AIIMS) campus in Ballabhgarh, India, the 0.55T MAGNETOM Free.Star system demonstrated its resilience during a prolonged power outage.

Ballabhgarh is a regional center, located approximately two hours from New Delhi. There, AIIMS has established a comprehensive rural health services project (CRHSP), which is supplied with staff from the main campus in Delhi to provide a basic healthcare service to the population of Ballabhgarh.

Around five or six extended power cuts were recorded at AIIMS Ballabhgarh during an observation window in the peak summer months: A 16-hour power cut was recorded from roughly 3:50 p.m. on Sunday, July 7, 2024, to 8:10 a.m. on Monday, July 8, 2024. In general, MRI systems are backed up with a diesel generator to maintain the electricity supply, and this setup was in place during the outage. However, the diesel generator ceased operation after consuming all its diesel, cutting all power to the MRI system and causing it to ramp down at approximately 2:00 a.m. on July 8. This type of scenario can result in significant downtime for conventional MRI systems that require manual ramp-up.

However, once power was restored, the AutoResponse ramp-up mechanism on our MAGNETOM Free.Star system seamlessly activated, autonomously restoring the magnet to full operational status within roughly 4.5 hours as per the log file (Fig. 1).

Figure 1: Log file showing AutoResponse.

This automatic recovery to operational state happened without liquid helium refilling, specialized tools, or expert intervention. As a result, patient imaging services resumed on the same day, minimizing disruption to the clinical workflow. The event highlighted the system's efficiency in mitigating operational challenges, making it a possible MRI solution for healthcare facilities in regions prone to power outages.

2. Impact on resource-limited settings

Geographically challenging regions
Many remote and rural areas, particularly in low income countries, suffer from unstable electricity supply. Operating traditional MRI systems in these areas often requires investment in expensive and extensive power-backup solutions to safeguard the operation of the magnet. As well as adding to the cost, these measures provide no guarantee that a magnet quench and loss of helium can be avoided entirely. The helium safety combined with the AutoResponse ramp-up feature ensures that scanners with DryCool technology can maintain continuity in operations, providing reliable diagnostic imaging to underserved populations.

Cost savings and time efficiency
Cost savings: Avoiding the need for cryogen refills and reducing costly service needs translates into substantial upfront operational savings, planning certainty, and investment security.
Time efficiency: The AutoResponse feature reduces system downtime even in areas with an unstable power supply, ensuring that diagnostic services are available when needed. This is particularly vital in time-sensitive scenarios such as trauma or stroke cases.

3. Comparison with conventional systems

Downtime and service continuity
In conventional MRI systems, magnet quenches result in significant downtime due to the complexity of restoring the magnet. This downtime disrupts patient care and creates bottlenecks in diagnostic workflows due to cost and time. By contrast, DryCool technology and the AutoResponse feature minimize service interruptions, enabling practically continuous scanning and maximizing patient throughput.

Impact on the environment and resources
In conventional systems, the reliance on liquid helium not only imposes logistical challenges but also contributes to environmental concerns and costs. Liquid helium is a finite resource, and its extraction and transportation are resource intensive with a large carbon footprint. In addition, helium is a common by-product of fossil gas production. The ability of systems with DryCool technology to operate without the need for helium refills aligns with sustainable healthcare practices, reducing the ecological footprint of MRI operations and making MRI more sustainable.

4. Advancing diagnostic equity

The introduction of the MAGNETOM Free. Platform with AutoResponse has far-reaching implications for healthcare equity. By enabling reliable diagnostic imaging in areas with unreliable infrastructure, the platform bridges the gap between urban and rural healthcare access. Patients in remote areas can now benefit from timely diagnoses, which can improve health outcomes and reduce the need for costly referrals to distant healthcare facilities. Availability of and access to MRI are key factors in improving healthcare in developing countries.

Conclusion

The 0.55T MAGNETOM Free. and 1.5T MAGNETOM Flow. Platforms with AutoResponse and a sealed-for-life helium deposit that requires no refilling represent a significant leap forward in MRI technology. By addressing the challenges of power dependency, cryogen management, and operational downtime, these systems are uniquely suited for deployment in resource-constrained and geographically challenging settings.

The ability to autonomously restore magnet functionality without requiring specialized tools, engineers, or cryogen refills ensures cost-effectiveness, sustainability, and reliability. These attributes not only enhance the feasibility of MRI operations in underserved regions, but also contribute to the broader goal of equitable healthcare delivery and access to MRI for everyone, everywhere.

As healthcare systems worldwide strive to extend diagnostic services to the most remote areas, innovations to deal with infrastructural challenges are needed. By reducing costs, improving operational efficiency, and ensuring consistent service delivery, the MAGNETOM Free. Platform has the potential to transform diagnostic imaging, bringing the benefits of MRI closer to those who need it most.
References

Probability case for power outages in a remote MRI installation	
Frequency of power outages	Assume long power outages occur three to four times per month, or seven to eight times per quarter.
Probability of system ramp-down during long power outages	Estimate that **20%** of these outages last long enough to trigger a ramp-down event. Note that it is possible to safeguard against longer outages, but this comes at the expense of managing fuel supply to the generator.
Probability of cryogen refill and manual intervention	With conventional MRI systems (at AIIMS Ballabhgarh), every ramp-down requires a manual ramp-up that involves helium refilling, specialized tools, and trained engineers. Assume that all ramp-down cases require cryogen refilling for traditional systems.
Costs and downtime	
Helium refilling cost	Approx. $40,000 per incident (including helium and labor).
Engineering cost, and downtime	$2,000 per incident; average downtime of one to two days.
Calculation	
Incidents per quarter	Total power outages: Seven to eight times per quarter. Ramp-down events (20% of outages): 7 × 0.2 = 1.4 incidents per quarter
Cost for a conventional MRI system	Quarterly cost due to ramp-down (helium refilling + labor): **1.4 incidents × ($40,000 + $2,000) = $58,800 per quarter** Annual cost: $58,800 × 4 = $235,200 per year
Cost for a 0.55T MRI system with AutoResponse	No helium refilling or manual intervention required, so ramp-down recovery costs are **$0**.
Savings due to AutoResponse	For a remote MRI installation experiencing regular power outages: The AutoResponse feature eliminates the need for helium refilling and engineer intervention, saving **$58,800 quarterly** or **$235,200 annually.** It also reduces downtime, enabling continuous scanning and avoiding disruptions in patient care, which could otherwise result in lost revenue and cause delays in diagnosis.

Parameter	Conventional MRI scanner	MRI scanner with DryCool technology and AutoResponse
Power outages (per quarter)	7–8	7–8
Ramp-down events (per quarter)	1.4	1.4
Helium refill cost (quarterly)	$40,000	$0
Labor cost (quarterly)	$2,000	$0
Total quarterly cost	$58,800	$0

Disclaimer: The cost estimates provided above – including helium refilling, labor, and system downtime – are approximate values based on general market observations. Actual costs may vary significantly depending on geographic location, local helium supply chains, service provider fees, and regulatory considerations.

Abbreviations: $ = U.S. dollars (consider local currency exchanges for regional currency calculation)

1 Lamichhane B, Neupane N. Improved Healthcare Access in Low-resource Regions: A Review of Technological Solutions. arXiv. 2022; arXiv:2205.10913.

2 Hilabi, BS, Alghamdi SA, Almanaa M. Impact of Magnetic Resonance Imaging on Healthcare in Low- and Middle-Income Countries. Cureus. 2023;15(4): e37698.

3 Arnold TC, Freeman CW, Litt B, Stein JM. Low-field MRI: Clinical promise and challenges. Journal of Magnetic Resonance Imaging. J Magn Reason Imaging. 2023;57(1):25-44.

4 Chaban YV, Vosshenrich J, McKee H, Gunasekaran S, Brown MJ, Atalay MK, et al. Environmental Sustainability and MRI: Challenges, Opportunities, and a Call for Action. J Magn Reason Imaging. 2024;59(4):1149-1167. Epub 2023 Sep 11.

5 Murali S, Ding H, Adedeji F, Qin C, Obungoloch J, Asllani I, et al. Bringing MRI to low- and middle-income countries: Directions, challenges and potential solutions. NMR Biomed. 2024;37(7):e4992.
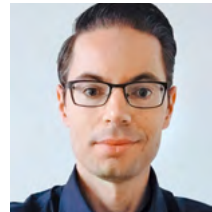
Contact

Yatin Sharma
SHS APJ IND DI
Tower A, Infinity Tower
28, DLF Tower 8th Road
Gurugram 122002
India

Yatin Sharma, B.Sc.   Benjamin Schmitt, Ph.D.   Matthias Fenchel, Ph.D.

Empowering you

Learn more about the
1.5T MAGNETOM Flow. Platform

Breaking barriers

Learn more about the
0.55T MAGNETOM Free. Platform

Meet Siemens Healthineers

Siemens Healthineers: Our brand name embodies the pioneering spirit and engineering expertise that is unique in the healthcare industry. The people working for Siemens Healthineers are totally committed to the company they work for, and are passionate about their technology. In this section we introduce you to colleagues from all over the world – people who put their hearts into what they do.

André Fischer, Ph.D.

André Fischer studied physics at the University of Würzburg in Germany, graduating in 2006 with a thesis on non-contrast perfusion MRI of the lung. In 2012, he earned his doctorate in physics with a thesis on compressed sensing in MRI, also from the University of Würzburg. As a postdoc, he worked at University Hospital Würzburg in functional lung imaging from 2010 to 2013. He then took a position as a cardiac scientist at GE HealthCare in Munich, Germany. In 2019, he joined the business line MR at Siemens Healthineers in Erlangen, Germany, where he worked in scientific marketing as global segment manager for neurological MRI. In October 2025, André moved into the role of associate editor MAGNETOM Flash.

Erlangen, Germany

How did you first come into contact with MRI?
I studied physics at the University of Würzburg in Germany. In 2005, I had to pick a topic for my diploma thesis. As I was also interested in medicine, I picked a project that looked at how to measure lung perfusion without contrast agents using MRI. The machine I was working on was a MAGNETOM Vision 1.5T system. The project was successful and a lot of fun, so I could imagine building a career in this field. Eventually, I pursued a Ph.D. and worked as a postdoc before moving into industry.

What do you find motivating about your job?
As a physicist who has been working in predevelopment, entering the marketing arena was not a straightforward move. However, to my own big surprise, interacting with customers and understanding more deeply how the clinical and research community uses our equipment is a huge motivation for me. As I'm now supporting MAGNETOM Flash, it is a bit like coming full circle, back to where I started. Like many former Ph.D. students, I have read and learned a lot from articles published in MAGNETOM Flash. It is my firm belief that this is the big strength of MAGNETOM Flash and what differentiates it from other magazines: It provides relevant content for the clinical and research community, and it is not primarily a device to convey marketing messages, as this would not resonate well. Hence, my motivation is to continue on this path with Antje Hellwich, editor-in-chief of MAGNETOM Flash, and learn as much as I can from her.

What are the biggest challenges in your job?
When I entered the MRI field 20 years ago, everyone collected and read the print editions of MAGNETOM Flash.

And while many readers still like the haptics of a printed journal, most prefer to read the articles online. Moreover, print is of course expensive and requires lots of natural resources. It is also not particularly sustainable to send printed journals around the world. So we are currently working on setting up a digital subscription to notify subscribers about new editions. Another challenge is to reach the younger community on social media and get them excited about the peer-to-peer community of MAGNETOM World.

What are the most important developments in healthcare?
With the advent of deep learning-based image reconstruction, imaging speed in MRI has seen the biggest gains since the advent of parallel imaging 25 years ago. Now our clinical customers are less concerned about the imaging time, and more interested in the workflow aspects. On top of this, there is a substantial shortage of qualified personnel to operate the MR scanner and to read the resulting images. As a healthcare company, we have to provide solutions to these challenges.

What would you do if you could spend a month doing whatever you wanted?
One thing I would very much like to learn is Spanish, so I would probably book myself into a language school in the Spanish countryside to be fully immersed in the language and forced to use it. This would open up the possibility of traveling through South America – a part of the world I really want to see – without such a big language barrier.

Mariappan S. Nadar, Ph.D.

Mariappan S. Nadar received his M.S. and Ph.D. in Electrical Engineering with a minor in Optical Sciences from the Department of Electrical and Computer Engineering at the University of Arizona, Tucson, AZ, USA. During his graduate studies, he developed scientific interests in image science, digital imaging, and digital signal processing. His thesis was on the topic of inverse problems in imaging, specifically super-resolving astronomical images beyond the diffraction limit. Mariappan owes his scientific interests and formative research-career years to two highly influential and inspirational mentors: Professor Bobby R. Hunt, Ph.D., who was his thesis advisor, and Professor Harrison H. Barrett, Ph.D., his optical sciences advisor. The classic text "Introduction to Fourier Optics" by Joseph W. Goodman, and the more recent epic tome, "Foundations of Image Science" by Harrison H. Barrett and Kyle J. Myers have both played an outsized role in his scientific interests and research career path. After his Ph.D., Mariappan joined Siemens Corporate Research Inc. in Princeton, NJ, USA, as a postdoc. Since then, he has held multiple roles in the department, and is currently Vice President at the AI Center, Digital Technology and Innovation, part of Siemens Healthineers in Princeton, NJ, USA. Under his leadership, his team has pioneered several innovative algorithms in multiple products from Siemens Healthineers. These include the Deep Resolve AI-based MRI reconstruction algorithms, Compressed Sensing algorithms for MRI, and the *syngo* Neuro 3D application. This work was conducted jointly with colleagues from the Clinical Fields teams and the R&D teams at MR.

Princeton, USA

How did you first come into contact with MRI?

It was via the Neuro 3D application that I first came into contact with MRI and the brilliant minds at MR in Erlangen, Germany. I became fascinated with the flexible soft tissue contrasts provided by the varied MRI sequences, specifically the DWI contrasts in neuroimaging. My learning in the MRI field has never stopped. I continue to be fascinated by this amazing medical imaging modality with rich underlying physical laws governing the MR contrast mechanisms and image formation process.

What do you find motivating about your job?

After my Ph.D., I joined the technology and innovation center of Siemens AG, now Siemens Healthineers in Princeton, NJ. What I enjoy most in building my career is the highly innovative environment and the fact that I get to interact with highly talented and motivated scientists who come from around the world and have varied cultural backgrounds. Most importantly, I enjoy conducting research on a multitude of topics for a multitude of modalities and seeing innovative solutions from the research phase making their way into products that directly impact patient care. In addition to the innovative solutions, the process of moving these solutions to clinical prototypes, then to clinical works-in-progress, and finally to a product with relevant regulatory clearances provides a tremendous sense of satisfaction, accomplishment, and motivation.

What are the biggest challenges in your job?

Progress in AI technologies is happening at breakneck speed. Interest in and contributions to the AI community are at an all-time high. Sifting through the AI "advancements" in publications, forums, etc., every day and sorting out key contributions from noise is like drinking water out of a fire hose! However, this has also been the most active, fertile, and fun research period in AI. Identifying key clinical needs in the healthcare industry and identifying

pragmatic AI solutions has made it a super exciting period in my career at the AI Center at Siemens Healthineers.

What are the most important developments in healthcare?

The impact of AI in different aspects of patient twinning, precision therapy, workflow orchestration, automation, etc., will be tremendous. AI-based image reconstruction is making a significant impact on medical scanners. The confluence of AI models (diffusion foundation models), physical laws (from first principles) governing the formation of an image, and the increasing availability of inexpensive high compute-power in desktops will enable the design of low-cost scanners at one end of the spectrum, push the limits of current scanners at the other end, and drive the development of specialized scanners with unconventional designs.

What would you do if you could spend a month doing whatever you wanted?

From a scientific-curiosity and learning perspective, I would love to spend a month or more (per modality) being embedded in teams to learn the complex process of developing a new scanner: from the requirements/concept phase to a final built prototype scanner, focusing on the design aspects of hardware systems and sub-systems. I have always been fascinated to see my friends all the way back in graduate school, working on both the hardware and the software aspects of pre-clinical scanners for their Ph.D. dissertations. The recent MRI4ALL hackathon has re-ignited this curiosity.

On a personal level, I would like to spend a month (during the appropriate season) gardening. I'd like to design and create a vibrant, colorful garden with plants that are native to New Jersey and pollinator friendly, and with an efficient rainwater-supplemented irrigation system. I would also expand our current small organic vegetable garden to include a broader variety of heirloom vegetables.

The entire editorial staff at Beijing Hospital, Beijing, China and at Siemens Healthineers extends their appreciation to all the radiologists, technologists, physicists, experts, and scholars who donate their time and energy – without payment – in order to share their expertise with the readers of MAGNETOM Flash.

Details about the processing of your personal data can be found on the Siemens Healthineers Website (www.siemens-healthineers.com) under "Privacy Policy" and "Marketing Privacy Policy".

MAGNETOM Flash includes reports in the English language on magnetic resonance: diagnostic and therapeutic methods and their application as well as results and experience gained with corresponding systems and solutions. It introduces from case to case new principles and procedures and discusses their clinical potential. The statements and views of the authors in the individual contributions do not necessarily reflect the opinion of the publisher.

The information presented in these articles and case reports is for illustration only and is not intended to be relied upon by the reader for instruction as to the practice of medicine. Any health care practitioner reading this information is reminded that they must use their own learning, training and expertise in dealing with their individual patients. This material does not substitute for that duty and is not intended by Siemens Healthcare to be used for any purpose in that regard. The drugs and doses mentioned herein are consistent with the approval labeling for uses and/or indications of the drug. The treating physician bears the sole responsibility for the diagnosis and treatment of patients, including drugs and doses prescribed in connection with such use. The Operating Instructions must always be strictly followed when operating the MR system. The sources for the technical data are the corresponding data sheets. Results may vary.

Partial reproduction in printed form of individual contributions is permitted, provided the customary bibliographical data such as author's name and title of the contribution as well as year, issue number and pages of MAGNETOM Flash are named, but the editors request that two copies be sent to them. The written consent of the authors and publisher is required for the complete reprinting of an article.

We welcome your questions and comments about the editorial content of MAGNETOM Flash. Please contact us at magnetomworld.team@siemens-healthineers.com

Manuscripts as well as suggestions, proposals and information are always welcome; they are carefully examined and submitted to the editorial board for attention. MAGNETOM Flash is not responsible for loss, damage, or any other injury to unsolicited manuscripts or other materials. We reserve the right to edit for clarity, accuracy, and space. Include your name, address, and phone number and send to the editors, address above.

MAGNETOM Flash is also available online:

www.siemens-healthineers.com/magnetom-world

Not for distribution in the US

On account of certain regional limitations of sales rights and service availability, we cannot guarantee that all products included in this brochure are available through the Siemens Healthineers sales organization worldwide. Availability and packaging may vary by country and is subject to change without prior notice. Some/All of the features and products described herein may not be available in the USA.

The information in this document contains general technical descriptions of specifications and options as well as standard and optional features which do not always have to be present in individual cases, and which may not be commercially available in all countries.

Due to regulatory reasons their future availability cannot be guaranteed. Please contact your local Siemens Healthineers organization for further details.

Siemens Healthineers reserves the right to modify the design, packaging, specifications, and options described herein without prior notice. Please contact your local Siemens Healthineers sales representative for the most current information.

Note: Any technical data contained in this document may vary within defined tolerances. Original images always lose a certain amount of detail when reproduced.